

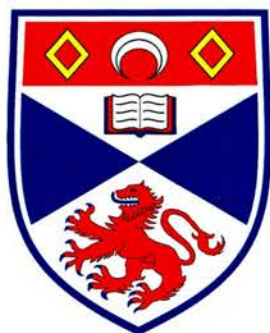
University of St Andrews



Full metadata for this thesis is available in
St Andrews Research Repository
at:

<http://research-repository.st-andrews.ac.uk/>

This thesis is protected by original copyright



University
of
St Andrews

***Synthesis and Characterisation of Iron
and Copper Complexes for Carbon-
Hydrogen Bond Activation Catalysis.***

A thesis presented by Sneh Lata Jain
to the University of St Andrews in application for
the Degree of Doctor of Philosophy.

November 2002



TL
E 314

Declarations

I, Sneh Lata Jain, hereby certify that this thesis, which is approximately 42000 words in length, has been written by me, that it is the record of work carried out by me and that it has not been submitted in a previous application for a higher degree.

Signature of candidate :

Date 12th November 2002

I was admitted as a research student in October 1999 as a candidate for the degree of PhD in Chemistry in October 2000; the higher study for which this is a record was carried out in the University of St Andrews between October 1999 and October 2002.

Signature of candidate :

Date 12th November 2002

I hereby certify that the candidate has fulfilled the conditions of the Resolution and Regulations appropriate for the degree of Ph.D in the University of St Andrews and that the candidate is qualified to submit this thesis for that degree.

Signature of supervisor

Date

12 November 2002

In submitting this thesis to the University of St Andrews I understand that I am giving permission for it to be made available for use in accordance with the regulations of the University Library for the time being in force, subject to any copyright vested in the work not being affected thereby. I also understand that the title and abstract will be published, and that a copy of the work may be made and supplied to any *bona fide* library or research worker.

Signature of candidate

Date 12th November 2002

Dedication

*To my older sister Kusum,
Thank you for inspiring me.*

Acknowledgements

I would firstly like to thank my family, especially my parents who have provided me with much needed support throughout.

I am hugely indebted to Professor Derek Woollins, Dr Pravat Bhattacharyya and Professor David Cole-Hamilton who have stood at the end of the tunnel with the all-alluring light.

Others I would like to thank are Dr Alex Slawin for the exquisite crystal structures and all the advice, Dr Joe Crayston for the invaluable time he has spent on electrochemistry with me, Dr Rona Ramsey for use of her UV-Vis spectrometer, Professor John Walton and Dr John Ingledew for their help with EPR, Dr Paul Webb for his help with GC analysis and Dr Martin Smith for running magnetic measurements. I am also thankful to the BBSRC for providing me with funding. I would like to thank Dr David Richens for providing me with such a challenging project.

Finally, I would like to thank all of my friend and colleagues for creating a wonderful atmosphere, leaving space only for fond memories in years to come.

Abstract

A series of pyridine dicarboxamide ligands have been prepared by dehydrative condensation reactions between pyridyl-containing amines and carboxylic acids which show interesting coordination properties when reacted with copper(II) and iron(III) precursors. X-ray crystallography reveals that the copper complexes can be mono-, bi-, tri- or tetranuclear. For a number of the multinuclear complexes prepared electrochemistry and magnetic measurements have been used to understand the metal-metal interactions.

We have then made use of these complexes in the Gif^{dV} systems (Zinc/acetic acid/pyridine/catalyst) and tested their catalytic activity towards the oxygenation of cyclohexane to cyclohexanol and cyclohexanone under ambient conditions. Turnover numbers of up to 300 have been achieved after 10 hr periods. We have noted that the iron complexes tested under these conditions are far more active than their copper analogues. Another interesting observation is that the initial oxidation state of the iron is not critical to its oxygenating activity.

We have monitored the reaction of [Fe(pic)₃] (pic = 2- pyridinecarboxylate anion) in pyridine with varying concentrations of hydrogen peroxide as a function of time and followed the formation and degradation of a high-spin iron(III)-hydroperoxy species using UV-vis, EPR and NMR spectroscopies. From this we tentatively conclude that under pseudo first order conditions an active Gif catalyst is formed, which over longer time periods (*ca.* 10 hrs) leads to a distinct difference in the absorbance profile when the substrate, cyclohexane, is added.

We report the synthesis and characterisation of two polyaza macrocycles and their reaction with iron(II) chloride. X-ray crystallography and NMR reveal that when *trans*-6,13-dimethyl-6,13-diamino-1,4,8,11-tetraaza-cyclotetradecane (*trans*-diammac) is reacted with pyridine-2-carboxaldehyde a ring closed tautomer of the expected Schiff base is produced.

List of Contents

List of Figures		ii
List of Tables		vi
List of Schemes		viii
Abbreviations		ix
General Experimental Conditions		xi
Chapter One	Oxidation Catalysis by Transition Metal Complexes	1
Chapter Two	Kinetic and EPR Spectroscopic Study of the Reaction of Hydrogen Peroxide in Pyridine With Iron Picolinate Complexes	50
Chapter Three	Iron Complexes Containing Multidentate Nitrogen Donor Ligands	84
Chapter Four	Coordination Chemistry of Copper(II) With Polydentate Nitrogen Donor Ligands	118
Chapter Five	Catalytic Studies of Iron and Copper Complexes Under $G_{\text{if}}^{\text{IV}}$ Conditions	157
Chapter Six	Polyaza Macrocycles And Their Iron(II),(III) Complexes	173
Appendix One	Crystal Structure Data	191
Appendix Two	Kinetic Analysis of $[\text{Fe}(\text{pic})_3]/$ Hydrogen Peroxide System	201

List of Figures

1.1	General structure of bleomycins	20
1.2	Simple chemical models of bleomycin	21
1.3	An iron(II)-imine complex which cleaves DNA in the presence of hydrogen peroxide	22
1.4	A diiron(III) complex which cleaves DNA but not phosphate esters	23
1.5	Two possible manifolds of Gif Chemistry: $\text{Fe}^{\text{III}}\text{-Fe}^{\text{V}}$, the non-radical forming manifold and $\text{Fe}^{\text{II}}\text{-Fe}^{\text{IV}}$, the radical forming manifold	27
1.6	Selective oxidation of (+)-car-3-ene (upper path = Gif, lower path = radical autoxidation)	33
1.7	Lee's reaction scheme for Gif (GoAgg) chemistry	34
2.1	Molecular structure of $[\text{Fe}(\text{pic})_3]$	52
2.2	Molecular structure of $[\text{pyH}][\text{Fe}(\text{pic})_2\text{Cl}_2]$ (hydrogen atoms omitted for clarity)	55
2.3	Molecular structure of $[\text{Fe}_2(\mu_2\text{-OMe})_2(\text{pic})_4]$ (C-H bonds omitted for clarity)	58
2.4	Time resolved spectra ($\Delta t = 2$ mins) for reaction of $[\text{Fe}(\text{pic})_3]$ (5×10^{-4} mol dm ⁻³) with 165 fold excess hydrogen peroxide in pyridine at 5 °C.	63
2.5	Absorbance vs time trace at 520 nm, $[\text{Fe}] = 5 \times 10^{-4}$ mol dm ⁻³ , $[\text{H}_2\text{O}_2] = 0.016 - 0.124$ mol dm ⁻³ , $T = 20$ °C	66
2.6	Absorbance vs time trace at 520 nm with cyclohexane added: $[\text{Fe}] = 5 \times 10^{-4}$ mol dm ⁻³ , $[\text{H}_2\text{O}_2] = 0.016 - 0.124$ mol dm ⁻³ , $T = 20$ °C	66
2.7	Plot of k_{obs} vs $[\text{H}_2\text{O}_2]$ for $[\text{Fe}(\text{pic})_3]$ -hydrogen peroxide system at 520 nm in the presence and absence of cyclohexane (triangles represent data with cyclohexane added, filled circles are data without cyclohexane)	68
2.8	Absorbance vs. time trace for $[\text{Fe}] = 5 \times 10^{-4}$ mol dm ⁻³ , $[\text{H}_2\text{O}_2] = 0.016 - 0.124$ mol dm ⁻³ , $T = 20$ °C at 430 nm	69

2.9	Plot of $k_{2(\text{obs})}$ vs $[\text{H}_2\text{O}_2]$ for $[\text{Fe}] = 5 \times 10^{-4} \text{ mol dm}^{-3}$, $[\text{H}_2\text{O}_2] = 0.016 - 0.124 \text{ mol dm}^{-3}$, $T = 20 \text{ }^\circ\text{C}$ at 430 nm	70
2.10	Absorbance vs. time trace for $[\text{Fe}] = 5 \times 10^{-4} \text{ mol dm}^{-3}$, $[\text{H}_2\text{O}_2] = 0.016 - 0.124 \text{ mol dm}^{-3}$, $T = 20 \text{ }^\circ\text{C}$ at 430 nm, with the addition of a tenfold molar excess of Hpic over $[\text{Fe}]$	73
2.11	Absorbance vs time trace for $[\text{Fe}(\text{pic})_3]$ with $[\text{H}_2\text{O}_2] = 0.042$ and $0.126 \text{ mol dm}^{-3}$, $T = 20 \text{ }^\circ\text{C}$, 520 nm. Dotted line = $0.126 \text{ mol dm}^{-3}$, full line = $0.042 \text{ mol dm}^{-3}$. Within each pair of curves the lower line represents the rates when cyclohexane is added.	74
2.12	EPR spectra at 110 K for (a) $5 \times 10^{-4} \text{ mol dm}^{-3}$ solution of $[\text{Fe}(\text{pic})_3]$ in pyridine. (b) Solution (a) with 170-fold excess of hydrogen peroxide after 2 mins (purple species). (c) Solution (b) warmed for a further 2 mins and then refrozen. (d) Solution (c) warmed for a further 2 mins and then refrozen.	78
2.13	EPR spectra at 110 K for (a) $5 \times 10^{-4} \text{ mol dm}^{-3}$ solution of $[\text{Fe}(\text{pic})_3]$ in pyridine. (b) Solution (a) with 170-fold excess of <i>t</i> -BuOOH after 2 mins (purple species)	80
3.1	Reaction of H_2dipic or pyridine-2,6-dicarbonyl dichloride with (i) 2-aminopyridine, (ii) 2-(aminomethyl)pyridine, (iii) 2-(aminoethyl)pyridine, (iv) 2-(aminomethyl)naphthalene, (v) 2-amino-4-methylpyridine, (vi) 2-amino-5-chloropyridine, (vii) 2-aminothiazole, (viii) 2-aminopyrimidine, (ix) 2-pyrazinecarboxylic acid and (x) Hpic	87
3.2	Molecular structure of $\text{H}_2\text{L}^9 \cdot \text{H}_2\text{O}$	88
3.3	(a) Molecular structure of H_2L^{10} , (b) Hydrogen-bonded dimer formation in H_2L^{10}	89
3.4	Molecular structure of $\text{H}_2\text{L}^{11} \cdot \text{H}_2\text{O}$ (C-H bonds omitted for clarity)	90
3.5	Structures of L^{12-15} , bppH and pyterpy	93
3.6	Molecular structure of the anion in $[\text{pyH}][\text{Fe}(\text{dipic})(\text{Hdipic})-(\text{py})_2] \cdot 3\text{py}$ (C-H bonds, cation and pyridine solvate molecules omitted for clarity)	95
3.7	Molecular structure of $[\{\text{Fe}(\text{dipic})(\text{py})_2\}_2(\mu_2\text{-O})] \cdot 2\text{py} \cdot \text{H}_2\text{O}$	

	(C-H bonds and pyridine solvate omitted for clarity)	97
4.1	Molecular structure of $[\text{Cu}_3(\text{L}^7)_2(\mu_2\text{-OAc})_2]\cdot\text{CHCl}_3$ (C-H bonds and chloroform solvate molecule omitted for clarity)	120
4.2	Molecular structure of $[\text{Cu}_3(\text{L}^6)_2(\mu_2\text{-OAc})_2]$ (C-H bonds and solvent molecules omitted for clarity)	123
4.3	Cyclic voltammogram (100 mV s^{-1}) of $[\text{Cu}_3(\text{L}^7)_2(\mu_2\text{-OAc})_2]$ in acetonitrile at a glassy carbon electrode (area = 0.071 cm^2). Potential referenced to ferrocene	125
4.4	Cyclic voltammogram (100 mV s^{-1}) of $[\text{Cu}_3(\text{L}^6)_2(\mu_2\text{-OAc})_2]$ in acetonitrile at a glassy carbon electrode (area = 0.071 cm^2). Potential referenced to ferrocene	126
4.5	Cyclic voltammogram (100 mV s^{-1}) of $[\text{Cu}(\text{pic})_2]\cdot 2\text{H}_2\text{O}$ in acetonitrile at a glassy carbon electrode (area = 0.071 cm^2). Inner trace (bold) shows two scans between -1.8 and $+0.25 \text{ V}$. Potential referenced to ferrocene.	129
4.6	Magnetic susceptibility data for $[\text{Cu}_3(\text{L}^7)_2(\mu_2\text{-OAc})_2]$. Circles represent data points, line is best fit to model	130
4.7	Molecular structure of H_2L^{18}	132
4.8	Molecular structure of $[\text{CuL}^{18}]$. C(12) and C(12A) are 50 % occupancy atoms	133
4.9	Cyclic voltammograms (2 V s^{-1}) for $[\text{CuL}^{17}]$ (full line) and $[\text{CuL}^{18}]$ (dashed line) in $0.1 \text{ M } [\text{Bu}_4\text{N}][\text{PF}_6]/\text{dmf}$ showing quasi-reversible copper(II/I) and copper(III/II) waves	136
4.10	Spectroelectrochemical data during oxidation of $[\text{CuL}^{18}]$ in $0.1 \text{ M } [\text{Bu}_4\text{N}][\text{PF}_6]/\text{dmf}$ showing the reversible appearance of the copper(III) species with λ_{max} near 370 and 630 nm	137
4.11	Molecular structure of $[\{\text{Cu}(\text{L}^9)(\text{OH}_2)\}_2]\cdot 2\text{H}_2\text{O}$ (C-H bonds omitted for clarity)	139
4.12	Molecular structure of $[\text{Cu}_4(\text{L}^7)_2(\text{L}^7\text{-O})_2]$ (C-H bonds and solvate molecules omitted for clarity)	142
4.13	Cyclic voltammogram (100 mV s^{-1}) of $[\text{CuL}^{19}]$ in acetonitrile at a glassy carbon electrode (area = 0.071 cm^2). Potential referenced to ferrocene (reversible peak at 0.0 V)	148

5.1	Product formation as a function of time for cyclohexane oxygenation in pyridine using metal picolinate complexes	166
5.2	Calibration curve for cyclohexanol	170
5.3	Calibration curve for cyclohexanone	170
6.1	Molecular structure of <i>trans</i> -diammac.6HCl.2H ₂ O	176
6.2	Reaction of <i>trans</i> -diammac with iron(II) chloride tetrahydrate	178
6.3	Proposed structure of iron(II)-monoammac complex	179
6.4	Expected structure for L ²⁰	180
6.5	L ²⁰ formation from <i>trans</i> -diammac	180
6.6	Molecular structure of L ²⁰ (C-H bonds omitted for clarity)	181
6.7	¹ H and ¹³ C{ ¹ H} NMR spectra of L ²⁰ (CDCl ₃ solution)	183
6.8	Proposed structure for L ²¹	183

List of Tables

1.1	Main industrial catalytic oxidation processes	3
1.2	Characteristics of homolytic and heterolytic oxidations	5
1.3	The nomenclature of the Gif family of oxidants	25
2.1	Selected bond lengths (Å) and angles (°) for [Fe(pic) ₃], [Fe(pic) ₃].0.5py and [Fe(pic) ₃].H ₂ O (esd's in parentheses)	53
2.2	Selected bond lengths (Å) and angles (°) for [pyH][Fe(pic) ₂ Cl ₂] (esd's in parentheses)	55
2.3	Selected bond lengths (Å) and angles (°) for [Fe ₂ (μ ₂ -OMe) ₂ (pic) ₄] (esd's in parentheses)	58
2.4	Kinetic data for [Fe(pic) ₃]-hydrogen peroxide system at 520 nm	68
2.5	Values of k_1 and k_{-1} for [Fe(pic) ₃]-hydrogen peroxide system at 520 nm	69
2.6	Kinetic data at 430 nm for the reaction of [Fe(pic) ₃] (5×10^{-4} mol dm ⁻³) with excess hydrogen peroxide in pyridine at 20 °C	71
2.7	Kinetic data for the reaction of [Fe(pic) ₃] (5×10^{-4} mol dm ⁻³) with excess hydrogen peroxide in pyridine at 20 °C followed at 430 nm	71
3.1	Selected bond lengths (Å) and angles (°) for H ₂ L ⁹ .H ₂ O, H ₂ L ¹⁰ and H ₂ L ¹¹ .H ₂ O (esd's in parentheses)	90
3.2	Hydrogen bonding distances (Å) and angles (°) for H ₂ L ⁹ .H ₂ O, H ₂ L ¹⁰ and H ₂ L ¹¹ .H ₂ O (esd's in parentheses). The hydrogen bond donor atoms are denoted as <i>D</i> and the acceptors as <i>A</i>	91
3.3	Selected bond lengths (Å) and angles (°) for [pyH][Fe(dipic)(Hdipic)(py) ₂].3py (esd's in parentheses)	95
3.4	Selected bond lengths (Å) and angles (°) for [{Fe(dipic)(py) ₂ }] ₂ (μ ₂ -O)].2py.H ₂ O (esd's in parentheses)	97
4.1	Selected bond lengths (Å) and angles (°) for [Cu ₃ (L ⁷) ₂ (μ ₂ -OAc) ₂].CHCl ₃ (esd's in parentheses)	120
4.2	Selected bond lengths (Å) and angles (°) for [Cu ₃ (L ⁶) ₂ (μ ₂ -OAc) ₂] (values for second independent molecule given in square brackets, esd's in parentheses)	124

4.3	Cyclic voltammetric data (100 mV s ⁻¹) for trimeric copper complexes and ligands (1 mM) in 0.1 M [Bu ₄ N][PF ₆] (V vs Fc ⁺⁰) using a glassy carbon electrode (area 0.071 cm ²).	128
4.4	Selected bond lengths (Å) and angles (°) for H ₂ L ¹⁸ (esd's in parentheses)	132
4.5	Selected bond lengths (Å) and angles (°) for [CuL ¹⁸] (esd's in parentheses)	134
4.6	Cyclic voltammetric data (2 V s ⁻¹) for [CuL ^{17,18}] in 0.1 M [Bu ₄ N][PF ₆] / dmf (V vs Fc/Fc ⁺)	135
4.7	Selected bond lengths (Å) and angles (°) for [{Cu(L ⁹)(OH ₂) ₂ }.2H ₂ O (esd's in parentheses)	140
4.8	Selected bond lengths (Å) and angles (°) for [Cu ₄ (L ⁷) ₂ (L ⁷ -O) ₂] (esd's in parentheses)	143
5.1	A comparison of the Gif ^{IV} oxygenation conditions employed by other Groups	160
5.2	GC analysis of product mixtures from Gif ^{IV} oxygenation reactions	163
5.3	Standard solution concentrations for GC analysis	169
6.1	Selected bond lengths (Å) and angles (°) for <i>trans</i> -diammac.6HCl.2H ₂ O (esd's in parentheses).	176
6.2	Hydrogen bonding distances (Å) and angles (°) for <i>trans</i> -diammac.6HCl.2H ₂ O (esd's in parentheses). The hydrogen bond donor atoms are denoted as <i>D</i> and the acceptors as <i>A</i> .	177
6.3	Selected bond lengths (Å) and angles (°) for L ²⁰ (esd's in parentheses)	182

List of Schemes

1.1	Catalytic reduction of dioxygen to hydrogen peroxide using anthraquinol	8
1.2	Nucleophilic attack by coordinated peroxo oxygen on an olefin	10
1.3	Catecholase induced oxidation of 3,5-di- ^t butylcatechol	11
1.4	Reaction intermediates in the oxidation of tartaric acid to dihydroxymaleic acid by iron(II) and hydrogen peroxide or hypochlorous acid	16
1.5	Oxidation of RH under Fenton conditions	17
1.6	Coupling of pyridine to adamantane during Gif reactions	25
1.7	Interconversions of iron-pic complexes	32
1.8	Photolysis of thione esters to generate <i>sec</i> - and <i>tert</i> -adamantyl radicals	35
1.9	Competition between dioxygen trapping and coupling to pyridinium cations by adamantyl radicals	36
1.10	Stoichiometric reductions of Gif ^{dV} catalyst precursors	38
4.1	Synthesis of H ₂ L ¹⁷ , H ₂ L ¹⁸	131
6.1	Preparation of <i>trans</i> -diammac	174
6.2	Preparation of monoammac	174

Abbreviations

Å	Angstrom unit, 10^{-10} m
Ad	adamantyl, $-C_{10}H_{15}$
BLM	Bleomycin
ⁿ Bu	<i>n</i> -butyl, $-(CH_2)_3CH_3$
^t Bu	<i>t</i> -butyl, $-C(CH_3)_3$
cm^{-1}	wavenumber
dmf	<i>N,N'</i> -dimethylformamide, Me_2NCHO
esd	estimated standard deviation
EI MS	electron impact mass spectrometry
ES MS	electrospray mass spectrometry
Et	ethyl, $-C_2H_5$
FAB MS	fast atom bombardment mass spectrometry
FT	Fourier transform (for IR or NMR spectroscopy)
GC	gas chromatography
H ₂ dipic	pyridine-2,6-dicarboxylic acid
Hpic	pyridine-2-carboxylic acid
Hquin	2-quinolinecarboxylic acid
Hz	Hertz
IR	infra-red
<i>J</i>	coupling constant, Hz
<i>k</i>	rate constant
KIE	kinetic isotope effect
Me	methyl, $-CH_3$
<i>m/z</i>	mass-to-charge ratio
3-NOBA	3-nitrobenzyl alcohol.
OAc	acetate, CH_3CO_2-
Ph	phenyl, $-C_6H_5$
ppm	parts per million
ⁿ Pr	<i>n</i> -propyl, $-(CH_2)_2CH_3$
py	pyridine, C_5H_5N
thf	tetrahydrofuran, C_4H_8O .
TON	turnover number

NMR: s = singlet, d = doublet, t = triplet, q = quartet, m = multiplet, br = broad.

IR: s = strong, m = medium, w = weak, br = broad.

General Experimental Conditions

Materials All commercially available solvents and reagents were purchased from Aldrich, Lancaster or Fisher Chemical Companies and used as received unless otherwise stated. Reactions were conducted under aerobic conditions unless stated otherwise, in which case standard Schlenk line techniques were employed under an argon or dinitrogen atmosphere using glassware which had been pre-dried in an oven at 100 °C overnight. Pyridine was dried and distilled from barium oxide, thf and diethyl ether were dried and distilled from sodium-benzophenone ketyl. Hexane and dichloromethane were dried and distilled from sodium and calcium hydride respectively.

Physical Measurements ^1H (300.0 and 270.0 MHz) and $^{13}\text{C}\{^1\text{H}\}$ (75.4 MHz) NMR spectra were recorded on Gemini 2000 and JEOL GSX 270 NMR spectrometers. Chemical shifts are referenced to internal tetramethylsilane (δ 0) using the high frequency positive convention. Infra-red spectra (pressed KBr discs) were recorded on a Perkin-Elmer System 2000 FTIR/Raman spectrometer. Microanalyses were carried out on a Carlo-Erba 1108 instrument by the University of St Andrews Microanalytical Service. UV-visible spectra were recorded on a Shimadzu W-2101 PC UV-visible scanning spectrophotometer connected to a thermostatically controlled RM6 Lauda water bath over the range 300-900 nm in 1 cm quartz cuvettes. Gas chromatography was carried out on a Hewlett Packard 6890 Series gas chromatograph with a 35 % phenyl-65% methyl-polysiloxane column (MDN-35 fused silica capillary column 30 m long with an i.d. of 0.25 mm and a 0.25 μm film thickness) and a Hewlett Packard 5973 mass selective FID detector, with helium as the carrier gas. EPR spectra were recorded on a Bruker EMX 10/12 spectrometer operating at 9.5 GHz with 100 kHz modulation. EI, ES and FAB MS (positive ionisation mode, 3-nitrobenzyl alcohol matrix) were recorded by the EPSRC National Mass Spectrometry Service (Swansea) and at the University of St Andrews. Cyclic voltammetry was performed using a PC-controlled EG & G PAR273A potentiostat, with a three electrode cell comprising a platinum disc working electrode (0.5 mm diameter), a platinum wire auxiliary electrode and an

Ag/Ag⁺/0.1 M [Bu₄N][PF₆]/0.01 M Ag[NO₃] reference electrode. Magnetic susceptibility measurements were performed on an MPMS–XL squid magnetometer (Quantum Design, San Diego).

Chapter One

Oxidation Catalysis by Transition Metal Complexes

1.1 Transition Metal Catalysed Oxidations

Enzymes exert a significant effect on fundamental biological cycles. Since the enzymes responsible for the recycling of carbon, sulfur, hydrogen, oxygen and nitrogen all involve transition metals, substantial efforts have been made to understand the mechanism of these processes. Moreover, metalloenzyme-based oxidation catalysts are essential for biological energy transformation and storage, as well as for the biosynthesis and metabolism of amino acids, hormones and other biomolecules.

Metal complexes also possess significant technological interest. Transition metal based catalysts are used industrially to produce millions of tonnes of oxygenated compounds annually, either homogeneous liquid-phase or, more recently, heterogeneous solid/liquid-phase processes. The major strength of homogeneous catalysis, which has led to its widespread use by the chemical industry, is the chemoselectivity, which originates from the ability to better control reaction conditions (temperature, mixing, nature of active catalytic species) in the liquid phase.

Although there have been major advances in the oxidation of saturated hydrocarbons with molecular dioxygen, the development of effective and selective methods for the catalytic functionalisation of hydrocarbons remains a major challenge. In particular, selective oxidation of alkanes with dioxygen to high value oxygenates (alcohols, ketones, carboxylic acids) is important from economical and environmental perspectives. Direct alkane oxidation with dioxygen (autoxidation) requires relatively harsh conditions and suffers from limited conversion and selectivity. The autoxidation of cyclohexane to

cyclohexanol (A) and cyclohexanone (K) (a mixture termed K/A oil, which is the feedstock for adipic acid and caprolactam for nylon synthesis), is carried out using cobalt naphthenate at 150 °C/10 atm.¹ The oxidation process is operated with 3-6 % conversion of cyclohexane to maintain higher selectivity (75–80 %) to the K/A oil. Unwanted overoxidation byproducts include dicarboxylic acids, which require neutralisation and separation. DuPont industrialised this process for producing adipic acid from K/A oil in the 1940's. Despite substantial efforts to develop a more efficient oxidation system with molecular dioxygen, the DuPont process is currently employed with little modification of the original conditions.

Several specialist reviews cover the classification of oxidation reactions^{2, 3}, the various families of oxidants and the importance of Fenton-like reactions in biological systems^{4, 5}. In particular, a recent Perspective article by Crabtree⁶ concerning alkane C-H activation and functionalisation and a review by Dunford⁷ on oxidation of iron(II)/(III) by hydrogen peroxide are highly recommended. This review covers only a small fraction of the available literature and therefore is not exhaustive. In this Chapter the role played by oxidation reactions in the chemicals industry will be examined. The categorisation of oxidation reactions will be discussed, for both metal-dioxygen species and organometallic complexes, according to their mechanism. Fenton chemistry and the Gif and GoAgg families of oxidants will be introduced. Finally the bleomycins, a group of glycopeptide derived antibiotics, and the topic of DNA footprinting, in which non-selective cleavage of DNA is conducted using iron-bleomycin complexes, will be discussed.

1.1.2 Industrial Applications of Oxidation by Metal Complexes

Millions of tonnes of oxygenated compounds are produced annually worldwide; they find application in all areas of the chemical and pharmaceutical industries¹. Some of the bulk oxygenated products obtained by metal catalysed oxidation reactions are shown in Table 1.1.

Table 1.1: Main industrial catalytic oxidation processes.¹

Product	Substrate	Oxygen	Main
Formaldehyde	Methanol	O ₂	Resins
Acetaldehyde	Ethene	O ₂	Acetic acid, n-butanol, 2-ethylhexanol
Acetic acid	Acetaldehyde Butane Naphthas	O ₂	Vinyl acetate cellulose, acetate, Acetic anhydride
Ethene oxide	Ethene	O ₂	Ethylene glycol, polyesters,
Propene oxide	Propene	Bu ^t OOH or PhCHMeOOH	Polyurethane, polypropylene glycol
Vinyl acetate	Ethene and acetic acid	O ₂	Polymers
Acrylic Acid	Propene	O ₂	Polymers
Cyclohexanol And cyclohexanone	Cyclohexane	O ₂	Adipic acid (caprolactam) → Nylon

The hydrocarbon feedstocks are generally oil-derived, the oxygenated products in the Table find their main application in the synthesis of polymers. In all of the processes shown transition metal catalysts are required, both homogeneous and heterogeneous methods are employed, at temperatures and pressures far beyond ambient conditions.

1.1.3 Catalytic Oxidations in the Manufacture of Fine Chemicals⁸

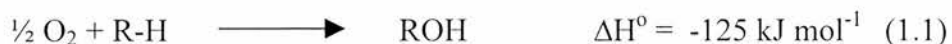
Economics and stringent environmental constraints have driven research into cheaper and more efficient catalytic oxidation methods to fine chemicals manufacture. Use of oxidants such as dichromate or permanganate in stoichiometric amounts is unfeasible, the focus is on catalytic processes generating small amounts of inorganic salt by-products. The simplest, cleanest and cheapest reagent for oxidation reactions is of course dioxygen, but there are difficulties involved with its direct reaction with organic molecules. Firstly, dioxygen has a triplet ground state, making its reaction with organic molecules spin forbidden. Secondly, the initial oxidation products are more easily oxidised than the original hydrocarbon substrate, as a result of activation of adjacent C-H bonds, making the isolation of partial oxidation products difficult. Finally, dioxygen displays little chemo- and regioselectivity.

Catalytic oxidations of organic molecules fall between the extremes of complete oxidation to carbon dioxide and water and the chemo-, regio- and enantioselectivity of partial oxygenations carried out by enzymes present in micro-organisms.

1.1.4 Alkane Oxidation

Selective conversion of *n*-alkanes to high value oxygenates (linear alcohols, aldehydes or carboxylic acids) in high yields under mild conditions is difficult to achieve due to the high activation energy of alkane C-H bonds, necessitating harsh conditions to activate the substrate and encouraging overoxidation (multiple oxygenation), with consequent loss of selectivity. Although alkane oxidation reactions are exothermic, suitable catalyst activation is still necessary due to their inherent slow rates. Sacrificial methods have been used to promote the reaction, such as the use of alkenes as hydrogen acceptors or photochemical means.

The insertion of electronegative elements into the C-H bond is an exothermic process, equation 1.1.



HO[•] or RO[•] radicals have been employed for exothermic hydrogen abstraction from the alkane, as the newly formed O-H bond is stronger than aliphatic C-H bonds (in the case of HO-H it is 497 kJ mol⁻¹).⁶ Selectivity is also a function of the C-H bond strengths of the organic molecule:



Hence the reactivity series is



Superacids can also abstract H⁺ from alkanes,⁹ selectivity being dictated by the relative stabilities of the resulting carbocations. Abstraction of *tert* C-H is favoured, leading to the same relative ordering seen for radical reactions.

1.2 Classifications of Metal Catalysed Oxidation Reactions

Metal catalysed oxidations can be divided into homolytic and heterolytic processes (Table 1.2).

Table 1.2: Characteristics of homolytic and heterolytic oxidations.¹

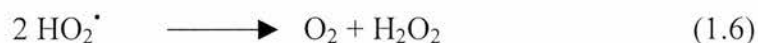
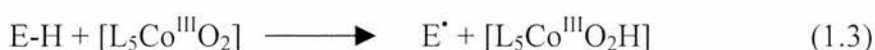
Homolytic Oxidations	Heterolytic Oxidations
<i>Characteristics:</i>	
Free-radical intermediates	No free-radical intermediates
Outer-sphere oxidation in bimolecular steps.	The reaction occurs in the coordination sphere of the metal
The substrate is generally not co-ordinated.	The substrate is generally activated by coordination.
Oxidations generally not very selective and not stereospecific	High selectivity and stereospecificity of the transformation
One-electron oxidation and reduction step of the metal	No change in the Oxidation State of the metal or two-electron steps
<i>Transition Metals commonly involved:</i>	
V ^V /V ^{IV} , Cr ^{VI} /Cr ^V , Mn ^{III} /Mn ^{II} , Fe ^{III} /Fe ^{II} , Co ^{III} /Co ^{II} , Cu ^{II} /Cu ^I	Ti ^V , V ^V , Cr ^{VI} , Mo ^{VI} , W ^{IV} , Mn ^{VII} , Ru ^{VII} , Os ^{VI-VIII} , Rh ^{III} /Rh ^I , Ir ^{III} /Ir ^I , Pd ^{II} /Pd ⁰ , Pt ^{II} /Pt ⁰
<i>Relevant Oxidations:</i>	
Non-stereoselective epoxidation of alkenes (V, Mn, Fe)	Stereoselective epoxidation of alkenes (Ti, V, Mo, W)
Hydroxylation of alkanes and arenes (V, Cr, Mn, Fe, Co, Cu)	Ketonisation of alkenes (Rh, Ir, Pd, Pt)

The homolytic or heterolytic character is governed principally by the nature of the metal, but also by the ligands, the availability of co-ordination sites, the substrate and the reaction conditions. Drago's classification of oxidation reactions by the role of the metal complex can be used to choose appropriate catalysts for selective transformations.²

1.2.1 Class I - Metal Bound Dioxygen

In this category the metal complex reversibly binds dioxygen diamagnetically, *e.g.* cobalt(II)-Schiff base complexes,¹⁰ which acquire dioxygen reversibly in solvents such as pyridine or dmf at low temperatures. When dioxygen binds to

cobalt(II) in an η^1 - fashion the terminal oxygen atom becomes basic and the radical reactivity of the oxygen atom is also enhanced since the dioxygen is essentially bound as a superoxide anion radical. The established reaction path for this class involves hydrogen atom abstraction to initiate the reaction, equations 1.2-1.6.

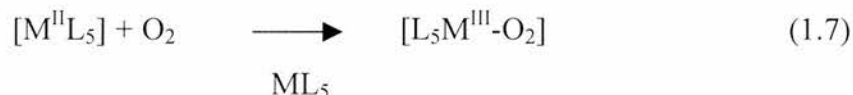


Where L is an unspecified ligand and E-H indicates oxidisable substrates with readily abstracted hydrogen atoms, *e.g.* substituted phenols. Once the hydrogen atom has been abstracted from the substrate by the metal-bound dioxygen (equation 1.3), the complex dissociates (equation 1.4) and regenerates the catalyst. In order for hydrogen atom abstraction to occur, it is essential that the E-H bond energy is weaker than the $[\text{L}_5\text{Co}^{\text{III}}\text{O}_2\text{-H}]$ bond energy. The fate of $[\text{L}_5\text{CoO}_2\text{E}]$ is detailed in Class IV.

1.2.2 Class II – Formation of a Metal Oxo Species *via* Dioxygen

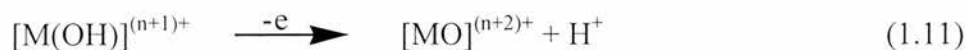
In this category a high-valent metal-oxo species forms by reaction of a low-valent metal complex with dioxygen. The metal-oxo species then reacts with the substrate, regenerating the metal species in its lower oxidation state. Formal oxidation state cycles of the metal are by definition two electron with $\text{M(II)} \leftrightarrow \text{M(IV)}$, $\text{M(III)} \leftrightarrow \text{M(V)}$ or $\text{M(IV)} \leftrightarrow \text{M(VI)}$ redox changes commonly involved. In Class II reactions, four electrons are used to reduce dioxygen to the

oxide level in the formation of the metal-oxo grouping. The formation of high-valent metal-oxo species from dioxygen can proceed *via* several paths, *e.g.* from M(II) complexes, equations 1.7-1.9.



The μ_2 -peroxo dinuclear complex decomposes to form the metal(IV)-oxo species. Examples include the conversion of $[Fe^{II}(TMP)]$ to $[Fe^{IV}(O)(TMP)L]$,¹¹ (TMP = *meso*-tetramesityl porphyrinate) and the disproportionation of $[Ru^{IV}(O)(TMP)]$ to $[Ru^{VI}(O)_2(TMP)]$ and $[Ru^{II}(TMP)]$.¹² Metal complexes having oxidation states of (III) and (IV) do not form stable dioxygen adducts, and in fact their interaction with dioxygen leads them to become M(V) and M(VI) oxo complexes.

Other possible pathways include unstable metal bound dioxygen or superoxide/peroxide species formed by metal-dioxygen electron transfer. Coordinated water may also be a source of high-valent oxo species, equations 1.10-1.11.

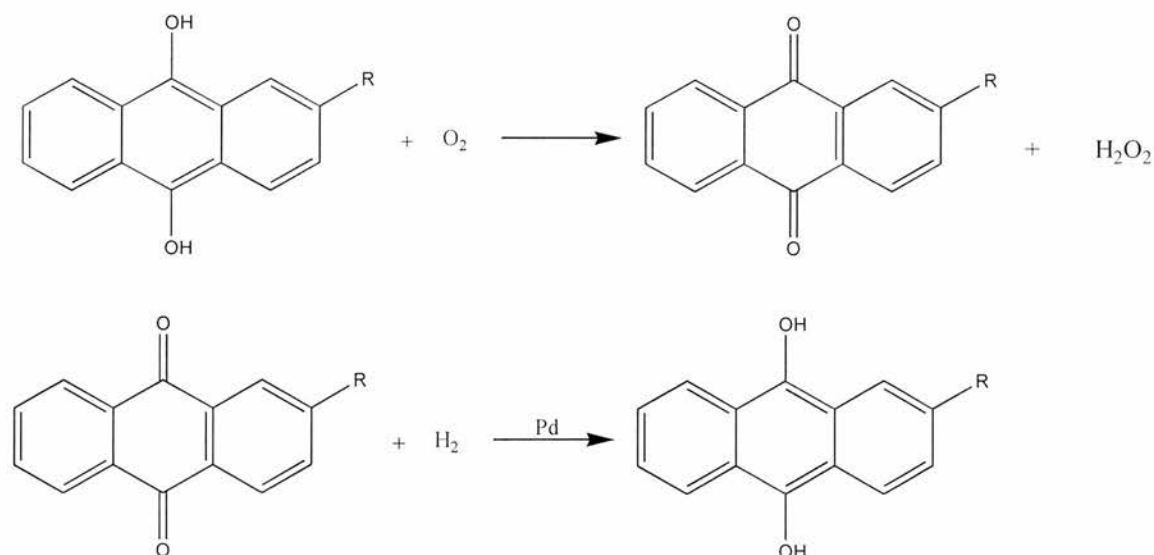


High-valent species are involved in such reactions as epoxidation of alkenes, oxidation of alcohols to aldehydes and alkane hydroxylation. Epoxidation proceeds *via* end-on approach of the M=O bond to a C=C bond, while oxidation of alcohols to aldehydes requires side-on attack of HO-CR₂-H to the M=O unit.

1.2.3 Class III - Metal Oxo *via* Peroxides

While similar to Class II, in this category dioxygen does not convert M^{n+} to $M^{(n+2)+}$. If stronger oxidants, *e.g.* hydrogen peroxide or alkyl peroxide are present, then oxidation occurs. In the presence of a sacrificial reducing agent dioxygen is converted to hydrogen peroxide or an alkyl peroxide. Formation of the O_2^{2-} state requires two oxidising equivalents, which leaves two equivalents (one oxygen atom) for substrate oxidation. These systems function as monooxygenases.

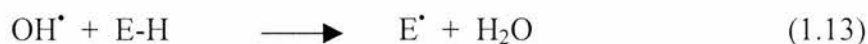
Reducing reagents which convert dioxygen into hydrogen peroxide include sodium borohydride, NADH (nicotinamide adenine dinucleotide) and substituted anthraquinol. The latter is used commercially in the catalytic production of hydrogen peroxide from dioxygen and dihydrogen, palladium metal being used catalytically to reduce the quinone back to the quinol, Scheme 1.1.



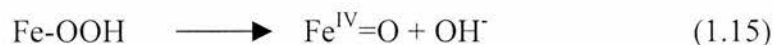
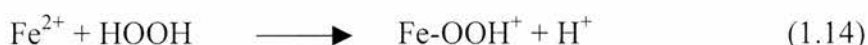
Scheme 1.1: Catalytic reduction of dioxygen to hydrogen peroxide using anthraquinol.

Peroxo complexes can also be formed by metal ions with oxidation states differing by two, *e.g.* ruthenium(I/III), cobalt(I/III). These dioxygen adducts react with water or acid to give hydrogen peroxide or M-OOH species.

Once formed a metal peroxide may react in several ways. Most first row transition metal ions in aqueous solution react with hydrogen peroxide giving HO[•], eventually forming water and dioxygen. When organic substrates E-H are present, HO[•] react with the substrate in a Fenton-type reaction. Equations 1.12, 1.13 depict the formation of the active species.

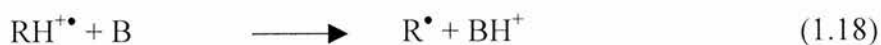


Hydrogen peroxide may also form high-valent metal-oxo species, such as Fe^{IV}=O from iron(II),¹³ equations 1.14, 1.15. Alternatively a binuclear μ₂-peroxo complex could form (equation 1.16), which subsequently decomposes to an M=O unit (equation 1.9).



1.2.4 Class IV – Metal-Peroxo Systems

In Class IV, metal-peroxo complexes are involved as reactive intermediates as opposed to high-valent metal-oxo complexes. Hydroperoxo (M-OOH) and alkylperoxo (M-OOR) complexes are eventually generated from ROOH, itself formed by the reactions in equations 1.17-1.20.



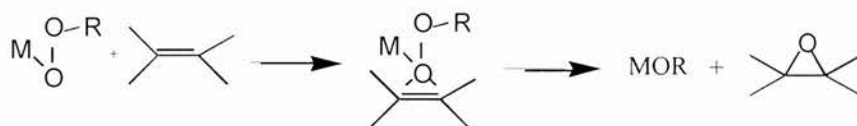
(B = solvent, substrate or base)



Subsequent reactions of R^{\bullet} lead to ROOH, M(II) being oxidised back to M(III) by dioxygen. Once formed, the metalloperoxo species may undergo one of three fates.

(i) *Nucleophilic attack on peroxo or alkylperoxo complexes*

Substrate attack occurs with high stereoselectivity on a coordinated peroxo or alkylperoxo ligand. Early transition metal catalysts with high oxidation states, *e.g.* molybdenum(VI), give *cis*-epoxides, Scheme 1.2.



Scheme 1.2: Nucleophilic attack by coordinated peroxo oxygen on an olefin.

The metal peroxo species is then regenerated, equation 1.21.



Propylene oxide is produced commercially *via* this route. Late transition metals, *e.g.* rhodium(III), generate aldehydes and ketones from alkenes; this transformation may take place with a sacrificial reducing agent such as triphenylphosphine, or using copper(II)/rhodium(III) chloride without reducing agent.¹⁴

(ii) *Metal-catalysed peroxide decomposition*

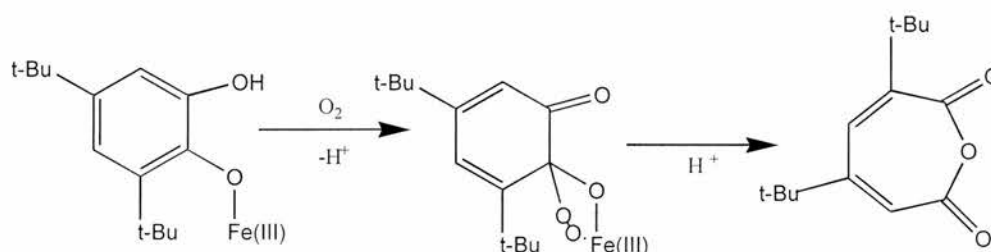
Alkylperoxides undergo decomposition according to the Haber-Weiss mechanism, induced by metal ions which undergo one-electron redox processes *e.g.* cobalt(II)/(III). The decomposition process results in alcohols and ketones from alkyl hydroperoxides. Homogeneous catalytic oxidation of cyclohexane

(Section 1.1) can be initiated at lower temperatures with a cobalt(II) catalyst.¹⁵ Relative rates of substrate oxidation are proportional to bond strength:



(iii) *Other reactions of metal peroxo intermediates*

An example of a catalyst outside the above subcategories is catecholase, an iron containing enzyme which cleaves catechol into muconic acid *via* the cyclic anhydride, Scheme 1.3.



Scheme 1.3: Catecholase induced oxidation of 3,5-di-^tbutylcatechol.

The mechanism involves dioxygen attack on a monodentate catechol bound to iron(III). Formation of a peroxo-quinone complex precedes ring expansion to the *cis,cis* muconic acid anhydride.

1.2.5 Class V – Metal-Centred Oxidising Agents

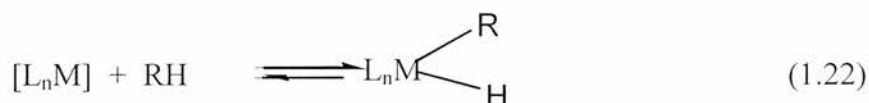
This classification includes the Wacker process in which nucleophilic attack by water on $[\text{PdCl}_2(\text{OH}_2)(\eta^2\text{-CH}_2=\text{CH}_2)]$, rearrangement of the σ -bonded complex $[\text{PdCl}_2(\text{OH}_2)(\text{CH}_2\text{CH}_2\text{OH})]$ to $[\text{Pd}(\text{H})(\text{H}_2\text{O})\text{Cl}(\text{CH}_2=\text{CHOH})]$ followed by β -hydride elimination from the intermediate hydroxyethyl complex, generates acetaldehyde. Palladium(II) is regenerated from palladium(0) *via* oxidation with dioxygen using copper(II) chloride.¹⁶ This reaction is assigned to Class V because the palladium performs the oxidation and the dioxygen functions to regenerate the initial high oxidation state of copper.

1.3 Homogeneous Alkane Activation Systems

An organometallic approach to alkane functionalisation involves oxidative addition, where a complex $[L_nM]$ attacks the least hindered terminal methyl group, causing C-H bond rupture and M-C bond formation, producing linear functionalised alkanes, as opposed to branched species which result from radical reactions. Typically M is a second or third row transition metal, L can be cyclopentadienyl, phosphine or carbon monoxide. The complexes are generally diamagnetic and undergo two-electron chemistry. An inherent disadvantage is that organometallic species are often destroyed by strong oxidants, restricting the generality of this approach. Homogeneous activation of alkanes using various catalysts is described below.

1.3.1 Activation by Platinum(II) Complexes

An approach to C-H bond activation proposed by Shilov¹⁷ invoked oxidative addition of an alkane to a coordinatively unsaturated transition metal complex, equation 1.22.



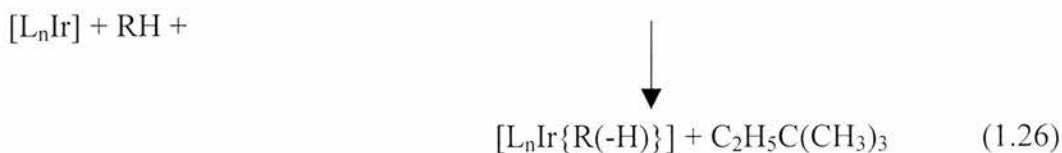
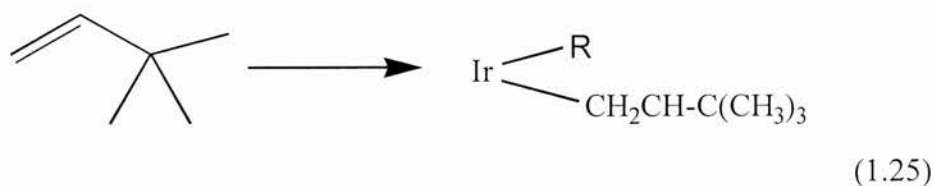
Garnett and Hodges¹⁸ provided initial evidence for this equilibrium, demonstrating that $[PtCl_4]^{2-}$ catalysed H-D exchange of aromatic hydrocarbons and their side chains (*e.g.* hydrogen atoms of the methyl group in ethylbenzene) in aqueous CH_3COOD .¹⁸ It has been implied that a prerequisite of C-H bond activation is the formation of platinum(III) π -complexes, suggesting the necessity of aromatic rings, although an opposing argument¹⁷ postulated direct attack of platinum(II) at the C-H bond. Shilov subsequently showed¹⁷ that methane and ethane underwent H-D exchange in the presence of $[PtCl_4]^{2-}$; the use of other metals with chloride, or other ligands with platinum(II), lead to a decrease in the reaction rate or complete cessation.

It is now accepted that the mechanism proceeds *via* alkyl platinum derivatives and several examples exist.¹⁷ Platinum(IV)-platinum(II) mixtures can oxidise alkanes to chlorides and alcohols, *e.g.* for methane, equations 1.23, 1.24.



The systems are not catalytic as written; by using dioxygen and an electron transfer agent [*e.g.* copper(II) chloride] the system can become catalytic, however secondary reactions limit turnover numbers. Parallel studies by Webster and Hodges^{18a}, and Rodakov^{18b} reached similar conclusions. Chemical and NMR spectroscopic studies of the oxidation of methane, supported by kinetic measurements, provided evidence for an alkylplatinum(IV) intermediate $[(\text{CH}_3)\text{PtCl}_5]^{2-}$.

In the early 1980's it was discovered that alkanes underwent oxidative addition with iridium(I) to form alkyl hydrides (equations 1.25, 1.26),¹⁹ *via* photochemical elimination of dihydrogen from $[\text{L}_n\text{Ir}(\text{H}_2)]$ to leave a coordinatively unsaturated species $[\text{L}_n\text{Ir}]$, which can react with alkanes.



R(-H) = dehydrogenated RH

RH = cyclopentene, [2.2.2]bicyclooctene, cyclohexene.

$[\text{L}_n\text{Ir}] = [\text{Ir}(\text{acetone})_2(\text{PPh}_3)_2]^+$ or $[(\eta^5\text{-C}_5\text{H}_5)\text{Ir}(\text{PMe}_3)]$

1.3.2 Hydrides and Organometallics

Selective oxidation of methane, of the type carried out in Nature by bacterial enzymes such as methane monooxygenase, remains a considerable challenge for the chemist. The main obstacle in the search for methane activating reagents is the choice of suitable solvent; if a hydrocarbon is used then it usually is more reactive towards C-H activating species than methane. In 1969, H-D exchange between D₂ and methane was observed using [(Ph₃P)₃CoH₃] in benzene. In 1975, Grigoryan¹⁷ described the reaction of methane in heptane using a Ziegler-Natta catalyst. The superior reactivity of methane over other hydrocarbons was explained by steric factors, *i.e.* relative hindrance of alkyl groups on the metal complex intermediate.

1.3.3 Biological Monooxygenases and Dioxygenases

The bacterial iron-dependent soluble methane monooxygenase (sMMO) oxidises simple hydrocarbons (including methane) and halocarbons to *inter alia* alcohols, including methanol. Consequently methanotropic bacteria, which utilise this enzyme to metabolise carbon in the form of alkanes, have been used to remove chlorinated hydrocarbons from drinking water and oil from contaminated beaches. Functional mimics of sMMO could provide an economical source of methanol, new catalysts for water purification and cleanup of toxic wastes. To develop such catalysts requires a better understanding of the nature of the interaction between dioxygen and methane in biological systems. Oxidation of methane to methanol is fundamentally difficult to achieve selectively under mild conditions since methanol is easily overoxidised to higher oxygenates. To establish how MMO overcomes this problem to achieve high selectivity to the C-OH product would be of great value in the design of new catalysts.

When monooxygenases use dioxygen to oxidise an organic substrate, each C-H bond requires two equivalents of reductant, either in the form of 2H⁺ + 2e⁻ or two hydrogen atoms. In Nature they are derived from NADH or NADPH but *in vitro* mimics require a suitable agent to re-reduce the oxidised reductant, setting up a

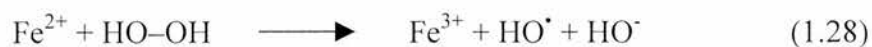
secondary catalytic pathway, a requirement which makes the system more complicated. In model systems a sacrificial reductant is often present, equation 1.27.



The core of MMO contain two iron atoms, which in its activated form comprises an $\text{Fe}^{\text{IV}}_2(\mu_2\text{-O})_2$ “diamond” metallacycle, which oxidises RH to ROH. In cytochrome P450, a monooxygenase enzyme which hydroxylates unactivated C-H bonds, the iron-porphyrin cofactor has an axial thiolate ligand. In model systems this is replaced with pyridine and other similar functionalities which tolerate oxidising conditions better. A vacant sixth co-ordination site enables dioxygen to bind to the iron(II) centre to give an iron(III) superoxide, which interacts with NADPH forming an iron(III)-hydroperoxy species. This cleaves heterolytically to an $\text{Fe}^{\text{V}}=\text{O}$ species, oxidising the substrate *via* C-H abstraction followed by attack of iron-bound HO^\bullet .

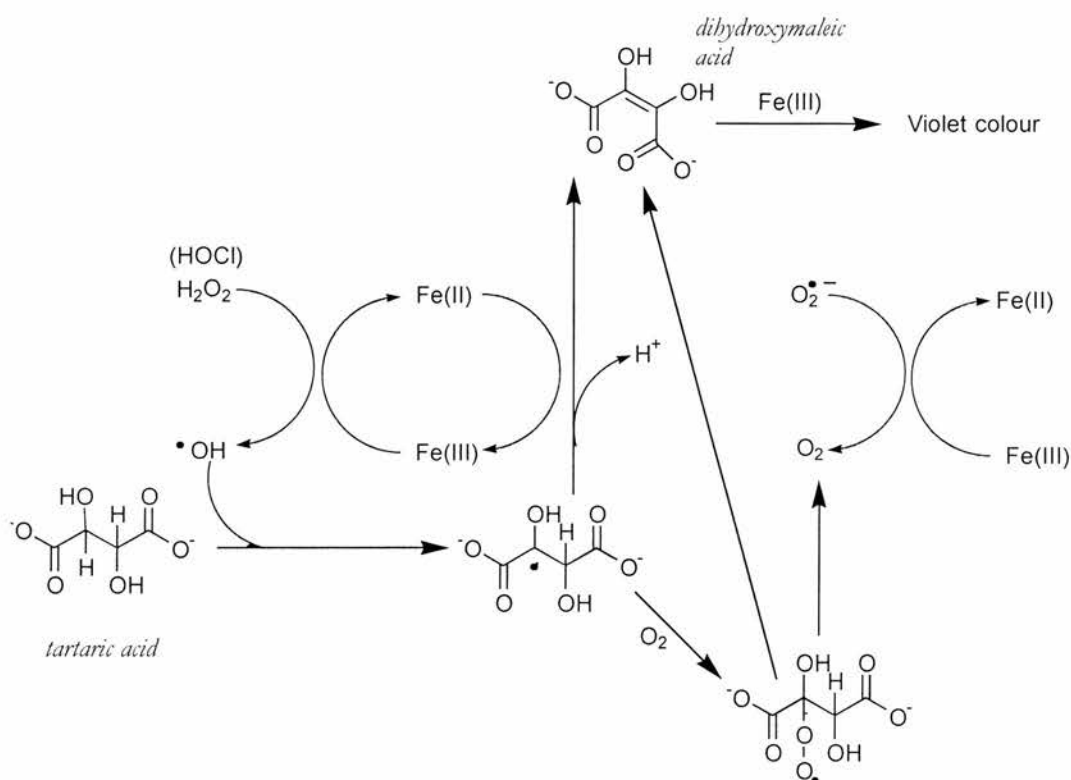
1.4 Fenton Chemistry

The most reactive oxygen-centred radical, HO^\bullet , is readily generated through a redox process known as the Fenton reaction, equation 1.28.²⁰



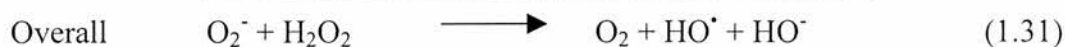
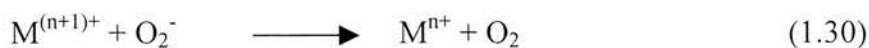
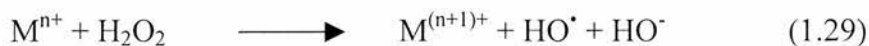
$$k_0 = 76 \text{ M}^{-1}\text{s}^{-1} \text{ (usually in aqueous media at pH } \leq 2 \text{ at } 30^\circ\text{C)}^4$$

Fenton’s initial experiment in 1876 was the reaction between iron(II) sulfate, hydrogen peroxide and tartaric acid. Scheme 1.4 shows the oxidation of tartaric acid initiated by HO^\bullet generated from iron(II) ions and hydrogen peroxide.



Scheme 1.4: Reaction intermediates in the oxidation of tartaric acid to dihydroxymaleic acid by iron(II) and hydrogen peroxide or hypochlorous acid.

Most redox-active metals capable of one electron changes *e.g.* iron, copper and titanium react in the lower valent form with hydrogen peroxide to generate OH[•],²¹ or with ROOH, producing RO[•]. For the reaction to cycle, M⁽ⁿ⁺¹⁾⁺ must be reduced again by a one electron donor, a particularly efficient reductant being superoxide, equations 1.29-1.31.



The overall reaction in equation 1.31 is termed Fenton Chemistry.¹⁹ *In vivo*, such reactions are carried out by iron and possibly also copper.

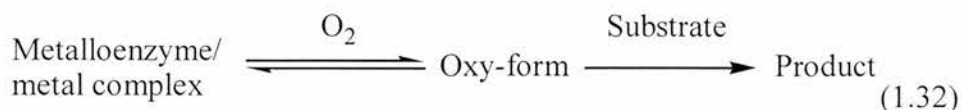
When R^\bullet is a primary or secondary alkyl radical, the chain terminates by dimerization (reaction 4). If dioxygen is present, either deliberately added or produced at relatively high concentrations of hydrogen peroxide, R^\bullet will afford ROO^\bullet , which may produce stable products through various termination reactions. Although rather inert with unactivated C–H bonds, ROO^\bullet may also be reduced to $ROOH$ and subsequently to RO^\bullet , which abstracts hydrogen from C–H bonds more selectively than HO^\bullet .

In Nature aerobic organisms reduce dioxygen cleanly to water *via* a series of coupled proton and electron transfer reactions catalysed by transition metals in order to synthesise ATP. However some of the dioxygen consumed is not reduced completely and results in the formation of superoxide, itself a poor oxidant. It is believed that the harmful effects of superoxide, such as tissue damage, are due to its conversion to the more reactive HO^\bullet .

1.5 Copper Complexes In Oxidation Processes

Copper(II) is integral to the active site of numerous electron transfer and oxygenase metalloproteins, which transport (*e.g.* hemocyanin for arthropods and molluscs) or transfer (*e.g.* tyrosinase, a monooxygenase) molecular dioxygen. These biosites often contain several copper ions in very close proximity to one another, *e.g.* ascorbate oxidase and laccase each have four copper atoms in the active site. Interest in copper bioinorganic chemistry has motivated the preparation of low molecular weight model complexes for copper enzymes, enabling accumulation of information about copper-dioxygen interactions and reactivity, allowing a better insight into the mechanism of dioxygen binding and activation at copper reaction sites and the development of new catalysts for selective oxidation under mild conditions. For example, a copper(II) phenoxyl radical complex reported by Weighardt *et al.*²² catalyses the oxidation of primary and secondary alcohols to aldehydes and ketones, representing a functional model of galactose oxidase.

The factors influencing the reversible binding and activation of dioxygen are of paramount importance, equation 1.32.



Dioxygen can adopt many coordination modes with copper,²³ e.g. η^1 - or η^2 -, terminal or bridging, which can be identified by Raman spectroscopy. The bonding and activation of dioxygen with copper(I) can be altered by modulating the ligand environment and the reaction conditions (concentration, solvent, temperature).

1.6 The Bleomycin Family of Anticancer Agents

The bleomycins (BLMs) are a family of glycopeptide derived antibiotics, discovered by Umezawa and co-workers²⁴ from *Streptomyces verticillus*, widely used for treatment of cancer (testicular, head, neck) and malignant lymphomas, whose therapeutic activity derives from their ability to bind and cleave DNA. DNA cleavage by BLMs requires dioxygen and a metal ion, with iron(II) being the most extensively studied,²⁵ although copper(II), cobalt(III),²⁶ zinc(II), lead(II)²⁷ and manganese(II)²⁸ have also been investigated. The general structure of bleomycins incorporate a DNA binding domain, a region which accommodates the metal ion, an oligopeptide linkage between these two subunits and a disaccharide unit.

The tertiary structure of BLM (Figure 1.1) is distinguished as three domains: the pyrimidine, β -aminoalanine and β -hydroxyimidazole moieties. These are involved in the formation of $[\text{Fe}^{\text{II}}\text{BLM}]$ containing a square pyramidal $[\text{FeN}_5]$ core, the nitrogen atoms which bind to iron denoted by (\bullet).

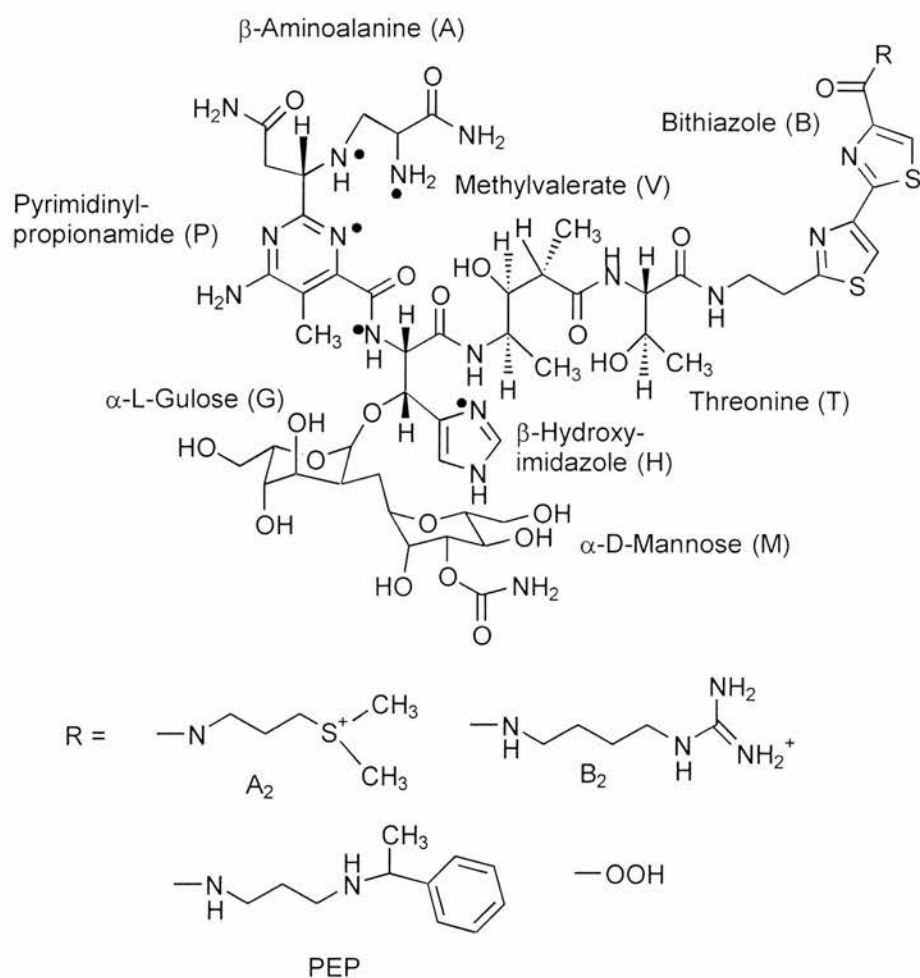
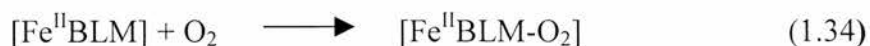
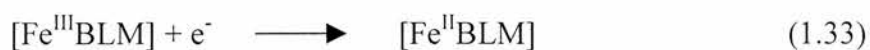


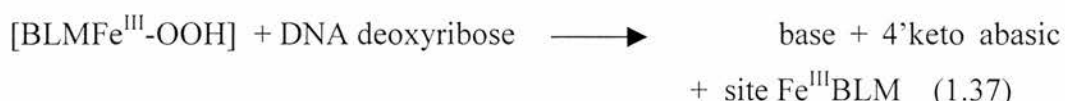
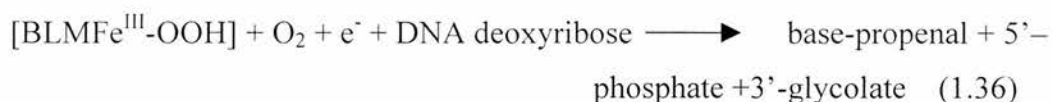
Figure 1.1: General structure of bleomycins.

The active DNA cleaving species is an octahedral hydroperoxy complex $[\text{BLMFe}^{\text{III}}\text{-OOH}]$ (“activated BLM”), accessible either from uptake of dioxygen by $[\text{Fe}^{\text{II}}\text{BLM}]$ or the reaction of $[\text{Fe}^{\text{III}}\text{BLM}]$ with hydrogen peroxide, equations 1.33-1.35.²⁹



Reviews have covered the mechanism of formation, mode of action and spectroscopic characterisation of activated BLM.^{25,27,30} Briefly the bithiazole unit of activated BLM is a DNA recognition element (*via* intercalation), which

increases the affinity of the ternary complex for DNA, as interaction of the activated bleomycin is the initial step. Scission involves C-H bond cleavage at the C4' position of the deoxyribose moieties and results in the production of base propenals, equations 1.36, 1.37.²⁹



There is no clear evidence that the $[\text{BLMFe}^{\text{III}}\text{-OOH}]$ species attacks directly the DNA, but this is considered very likely.²⁷ Also the chemical identity and fate of the residual oxidant have not been established. Simple chemical models of bleomycin have been designed,³¹ Figure 1.2.

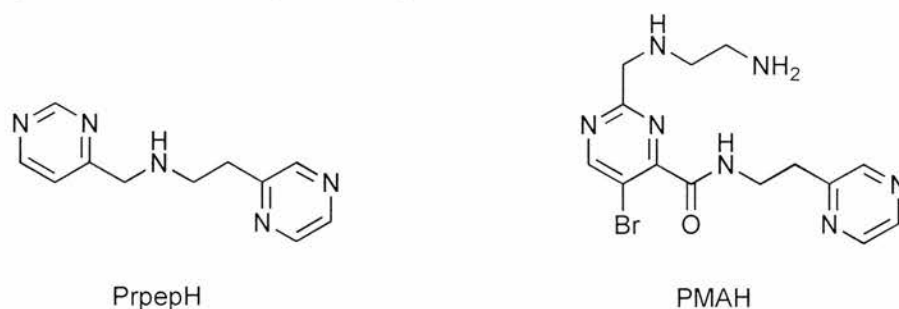


Figure 1.2: Simple chemical models of bleomycin.

1.7 DNA Footprinting

In recent times, research aimed at isolating and evaluating naturally occurring DNA cleaving agents and the design of model compounds which specifically recognise and cleave DNA has experienced a huge growth.³² Potential applications for such compounds range from developing chemotherapeutic agents to the creation of synthetic restriction enzymes.

The existence of metal-binding sites in biological materials means that if Fenton chemistry occurs, site specific binding in catalytic metals will result in site

specific damage.²⁰ Drugs such as bleomycin which bind to both DNA and iron can cause extensive DNA damage.²⁹ Iron(II)-hydrogen peroxide chemistry can also be used as a non-selective source of DNA damage in drug footprinting assays. Using site specific chelates, however, DNA footprinting and chemotherapy can both be achieved. DNA footprinting allows identification of the affinity of a protein to a selected sequence of DNA by identifying the protected regions of DNA. The regions which are protected by proteins are not cleaved, however the rest of the molecule is non-specifically cleaved. Detection is by DNA fragment separation according to size by electrophoresis.

Among the first iron chelates used for DNA footprinting were iron(II)-EDTA ($H_4EDTA = N,N,N',N'$ -ethylenediaminetetraacetic acid) and substituted EDTA derivatives. These chelates were used to produce HO^\bullet in aqueous medium *via* Fenton reactions which acted to cleave DNA non-specifically. Footprinting techniques are known to provide important information, for example see the work of Sigman *et al*²¹ and Nagaraja *et al*³³.

In the iron(II)-EDTA-hydrogen peroxide system it was observed that when HO^\bullet scavengers, *e.g.* glycerol, were present then the system was impaired.²¹ Secondly the flux of HO^\bullet can cause degradation of the culture medium present. Efforts were therefore made to produce reagents which do not utilise HO^\bullet and are therefore unaffected by the presence of radical scavengers. One example prepared by Ishikawa *et al*.³⁴ (Figure 1.4) in the presence of hydrogen peroxide cleaved DNA at micromolar concentrations.

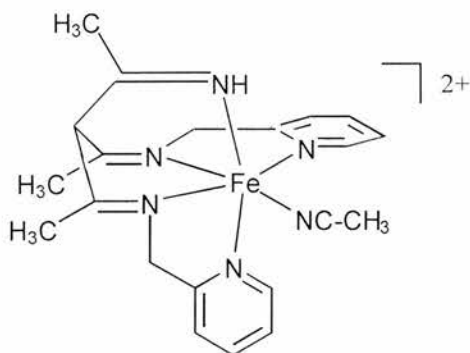


Figure 1.3: An iron(II)-imine complex which cleaves DNA in the presence of hydrogen peroxide.³⁴

This complex also oxidised cyclohexane to cyclohexanol and cyclohexanone in acetonitrile upon addition of fifty equivalents of hydrogen peroxide. EPR measurements supported the formation of a low spin iron(III)-hydroperoxy complex ($g = 2.16, 2.10$ and 1.98). However these g values may also be explained to polynuclear effects caused by high iron concentrations.

Ishikawa's study of DNA cleavage using iron(II) complexes of pentadentate ligands with fluorophenyl substituents found that the cleavage efficiency increased as the number of fluorine atoms increased,³⁵ which was attributed to the stabilisation of the intermediate iron(III)-hydroperoxy species by electron withdrawing effects. Liu³⁶ has shown that $[\text{Fe}_2(\mu_2\text{-O})(\text{DTPB})(\mu_2\text{-OAc})]$ [DTPB = 1,1,4,7,7-penta(2'-benzimidazol-2-ylmethyl)-triazasheptane] hydrolytically cleaved DNA even without hydrogen peroxide, with a rate enhancement factors of ten orders of magnitude against DNA.

A diiron(III) dihydroxy complex (Figure 1.4) has been used to cleave plasmid DNA, producing single and double strand breaks.³⁷ Interestingly, simple phosphate esters resisted hydrolysis under analogous conditions. The difference arose from the facilitation of hydrolytic cleavage by interaction of the ligand array with the DNA major groove, positioning the complex to attack the phosphodiester backbone.

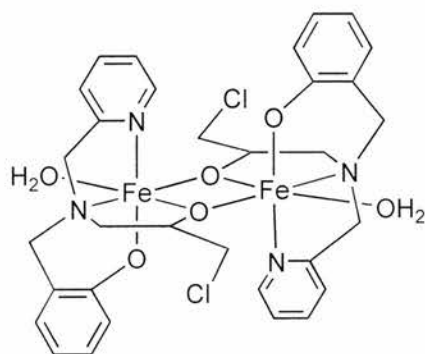


Figure 1.4: A diiron(III) complex which cleaves DNA but not phosphate esters.³⁷

Mercury(II), cadmium(II) and lead(II) porphyrin complexes can also cleave DNA,³⁸ showing that d^{10} metals can also play such a role.

1.3 The Gif Family of Oxidants

In 1980 Tabushi *et al.* published an article describing a dioxygen-dependent system for the oxidation of adamantane mediated by $[\{\text{Fe}(\text{salen})\}_2(\mu_2\text{-O})]$ [$\text{H}_2\text{salen} = N,N'$ -bis(salicylidene)ethanediamine] in the presence of 2-mercaptoethanol in pyridine.³⁹ The products were 1-adamantanol, 2-adamantanol and 2-adamantanone, with turnover numbers between one and four. Re-investigation by Barton showed this reaction to be far from reproducible. However, the addition of iron powder and acetic acid yielded better results. Barton's first system used dioxygen and iron powder in a 10:1 v:v pyridine-acetic acid mixture in the presence of hydrogen sulfide to catalyse oxygenation of adamantane.⁴⁰ From these origins the Gif family of systems⁴¹ was developed, their great practicality arising from their employment of simple reagents and, in certain cases, atmospheric dioxygen. The systems were named according to the geographical location of their discovery and study (Table 1.3). Subsequently the Gif^{IV} and GoAgg systems have proved the most viable for practical use and mechanistic study.⁴¹ Among the many reviews devoted to the area of Gif chemistry, recent contributions by Stavropoulos⁴² and Gozzo⁴ are highly recommended.

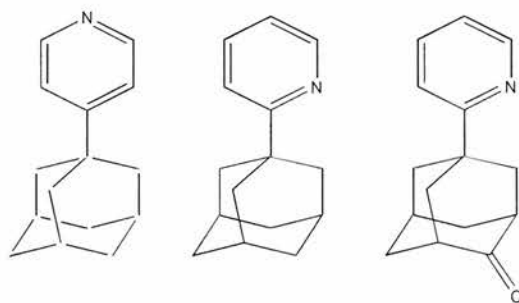
To achieve efficient Gif oxygenations both oxidising and reducing equivalents are necessary, either dioxygen combined with a reducing agent or *via* a reduced form of dioxygen. A heterogeneous mixture of iron(II), dioxygen, acetic acid as the proton source and zinc dust as a reducing agent (Gif^{IV}) supports the most effective oxygenation system in the former category, turnover numbers routinely exceeding 2000. The latter category is best represented by $\text{GoAgg}^{\text{III}}$ -type homogeneous combinations of iron(III) chloride-Hpic with hydrogen peroxide as the shunt agent. Hpic enhances the rate of Gif oxygenations fiftyfold over acetic acid.⁴³ The presence of a carboxylic acid source is necessary for hydrocarbon oxidation, otherwise solely disproportionation of hydrogen peroxide is observed.⁴⁴ Pyridine is decisive for obtaining good turnover numbers and the unusually high ketone/*sec*-alcohol ratios (~3-10) observed in Gif oxygenations, but its toxicity and potential corrosive properties makes the Gif family of

reactions non-viable for industrial scale oxidation processes. Although acetonitrile can be used as a solvent, a minimum amount of a coordinatively unhindered pyridine (>10 equivalents over catalyst) is essential for turnover.^{45, 46}

Table 1.3: The nomenclature of the Gif family of oxidants.⁴⁴

System	Catalyst	Electron source	Oxidant
Gif ^{III}	Fe(II)	Fe ⁰	O ₂
Gif ^{IV}	Fe(II)	Zn ⁰	O ₂
GO	Fe(II)	Hg/cathode	O ₂
GoAgg ^I	Fe(II)	KO ₂ / Ar	
GoAgg ^{II}	Fe(III)	H ₂ O ₂	
GoAgg ^{III}	Fe(III)/Hpic	H ₂ O ₂	
GoChAgg	Cu(II)	H ₂ O ₂	
Cu ⁰ /O ₂	Cu(I) ?	Cu ⁰	O ₂

Barton's initial experiments⁴⁰ using adamantane as substrate established that Gif systems oxidised selectively secondary, but not tertiary carbon atoms; it was also found⁴⁷ that pyridine coupled to adamantane at the tertiary position (Scheme 1.6).



Scheme 1.6: Coupling of pyridine to adamantane during Gif reactions.

Barton believed that Gif chemistry started with a ferrous salt and Hpic in pyridine-acetic acid, the presence of a chelating carboxylic acid enabling ketonisation (Gif chemistry) in preference to dioxygen formation (catalase reaction).⁴¹ Once all of the iron(II) had been oxidised to iron(III), Gif chemistry proceeded *via* [(pic)₂Fe^{III}-O-O-Fe^V(O)(pic)₂], which inserted an oxygen atom directly into the C-H bond of the substrate by a non-radical mechanism. This

proposition aroused controversy amongst many groups who disputed the existence of oxo intermediates⁴⁸ and argued that Barton's results were explicable by diffusively free oxygen- and carbon- centred radicals. Newcomb's⁴⁹ study highlighted important differences between the mechanism of a GoAgg^{III} reagent and the oxygenases P-450 and sMMO. By employing ultrafast cyclopropane radical probe substrates, Newcomb contended that the Gif system generated diffusively free substrate-centred radicals whereas the enzymatic processes generated transient (<100 fs) carbon-centred radicals, participating as a component of the transition state. Barton^{50,51} concluded that the long-lived probe radicals resulted due to the exceptional cleavage of a precursor Fe^V-R bond, similar to that encountered with the *tert* positions of adamantane. A report by Perkins⁵² implicated participation of *c*-C₆H₁₁[•] and HO[•] in GoAgg^{III} oxidation of cyclohexane, while an influential review by the same author⁵³ pinpointed shortcomings in Barton's mechanistic analysis. The Stavropoulos group has focussed on mainstream Gif systems and common substrates used by Barton to support a non-radical mechanism. They also studied whether free oxygen-centred radicals (HO[•], RO[•]) rather than metal-bound oxidants, were responsible for abstracting hydrogen atoms from alkanes.⁵⁴ While current opinion weighs heavily in favour of a free radical mechanism, both pathways will be described here.

1.8.1 The Mechanism of The Gif Reaction

1.8.1.1 Radical or Non-Radical?

Both radical^{53,54} and non-radical⁵⁵ pathways have been suggested for the mechanism of the Gif reaction. The apparent selectivity for the oxygenation of secondary bonds in Gif chemistry (*sec* > *tert* >> *prim*) and the moderate KIE values (~2 for ketone) were interpreted by Barton to signify a mechanism involving a high-valent Fe^V=O oxidant performing [2+2]-type concerted addition to C-H bonds of methylene groups in the substrate to give an Fe^V-C bond. The affinity for *sec*-C-H activation is a compromise between bond strength and steric

hindrance, while the KIE values echo the side-on C-H approach in the transition state. The organometallic species containing an $\text{Fe}^{\text{V}}\text{-C}$ bond is converted to ketone (major product) and alcohol (minor product) *via* dioxygen insertion and initial formation of an alkylhydroperoxide. Dehydration affords the ketone and regenerates the catalyst. For secondary C-H bonds, the major product is the ketone rather than the alcohol.

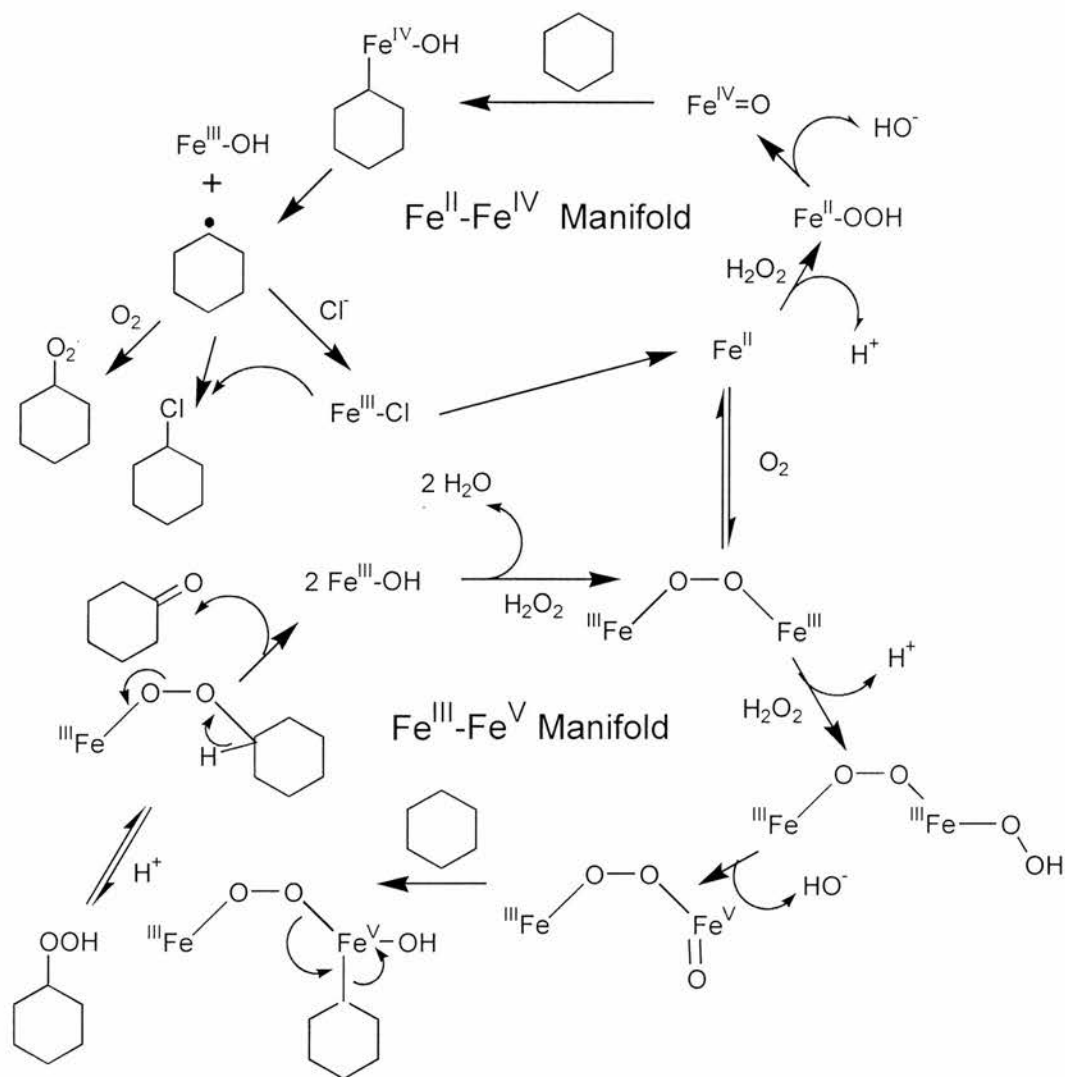


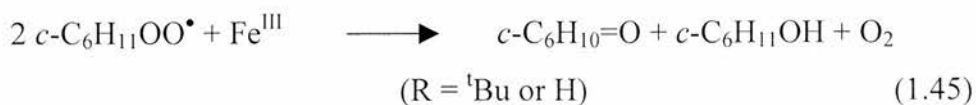
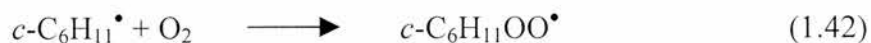
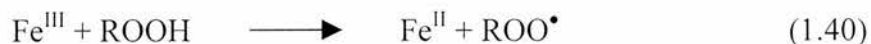
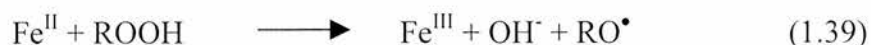
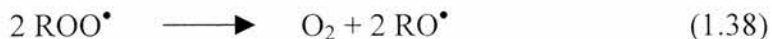
Figure 1.5: Two possible manifolds of Gif Chemistry: $\text{Fe}^{\text{III}}\text{-Fe}^{\text{V}}$, the non-radical forming manifold and $\text{Fe}^{\text{II}}\text{-Fe}^{\text{IV}}$, the radical forming manifold.⁴²

The oxygen content of ROOH in cyclodecane oxygenation experiments was shown by Perkins (confirmed by Barton for cyclohexane) to be derived from dioxygen. This result alone strongly suggests the possibility of radical interference ($\text{R}^\bullet + \text{O}_2 \rightarrow \text{ROO}^\bullet$), although further studies conducted by Barton to trap alkyl radicals allegedly excluded $\text{R}^\bullet/\text{ROO}^\bullet$ involvement. Barton emphasised

that iron(II) is activated by superoxide and that iron(III) is activated by nucleophilic displacement by hydrogen peroxide, affording the same iron(III)-hydroperoxy intermediate as exemplified in Figure 1.5.⁴²

Work conducted in the 1990's by the Barton⁵⁵ and Sawyer^{56,57} groups suggested that HO• was not involved in Gif chemistry in pyridine. Arguments to support this statement came from the coupling of carbon radicals to pyridine,²⁶ the selectivity for secondary attack²⁶, and the study of kinetic isotope effects²¹.

Perkins commented that Barton had deduced the Gif mechanism solely from the oxidation of adamantane.⁵² Perkins had earlier postulated that the catalysed decomposition of hydrogen peroxide would generate HO•, and catalyse the decomposition of intermediate alkyl hydroperoxides resulting in the production of RO• (both HO• and RO• abstract hydrogen from alkanes, continuing the cycle), equations 1.38-1.45. Stavropoulos⁵⁴ has provided further evidence in support of this mechanism.



Walling argued that in the GoAgg^{III} manifold, iron(III) systems should be capable of catalysing the production of HO[•] from hydrogen peroxide, a proposition widely accepted in a biological context. This is thought to occur *via* a slow reaction which generates iron(II) followed by a very rapid Fenton-type reaction (see below) in which the iron(II) is re-oxidised, again as described in equations 1.38-1.45.

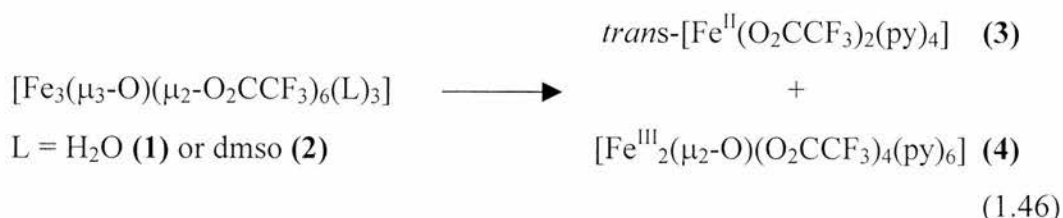
1.8.1.2. The Role of Pyridine

Pyridine is integral to Gif systems, hydrocarbon oxidation occurs with low efficiency and selectivity in its absence. Its influence extends further than its solvent properties; pyridine has a mechanistic role, stabilising oxygenated iron intermediates *via* coordination. However pyridine's role as a radical scavenger is deleterious to overall hydrocarbon oxidation. Hydroxylated pyridines and bipyridines are commonly observed in product profiles from Gif reactions, moreover protonated pyridine undergoes fast reactions with alkyl radicals to give 2- and 4-alkylpyridines. For adamantane the appearance preferentially of 1-adamantylpyridine products was interpreted to mean that (1-Ad)Fe species were less thermodynamically stable than (2-Ad)Fe species, although interception of these species by dioxygen will be seen to be a crucial factor explaining the selectivity to 2-adamantyl oxygenated products.

1.8.1.3 Iron Trifluoroacetate – Hydrogen Peroxide Systems

Dissociation of $[\text{Fe}_3(\mu_3\text{-O})(\mu_2\text{-O}_2\text{CCF}_3)_6(\text{L})_3]$, L = H₂O (**1**) or dmsO (**2**), in pyridine to give (**3**) and (**4**), (equation 1.46) provided evidence that both *tert*- and *sec*-C-H sites of adamantane could be activated via hydrogen atom abstraction to generate Ad[•] in pyridine-trifluoroacetic acid (10:1 v/v).⁵⁸

A sensitivity of the product distribution for adamantane (oxygenates versus pyridine coupled products) to partial pressure of dioxygen [$p(\text{O}_2)$] was also noted.



More importantly, *sec*-adamantylpyridines were observed for the first time in product profiles; their assumed absence from Gif product profiles had been integral to the argument in support of a predominantly non-radical mechanism⁴¹ for *sec*-C-H bond activation in adamantane oxidation. It is also noteworthy that both **(3)**-hydrogen peroxide [iron(II)] and **(4)**-hydrogen peroxide [iron(III)] systems yielded *sec*-adamantylpyridines, suggesting that any differentiation between the proposed two manifolds cannot automatically be made. However, in both cases the active oxidant is most likely generated through iron(II)-hydrogen peroxide chemistry, as moderately air-stable iron(II) sites can be easily formed by **(4)**-hydrogen peroxide combinations in pyridine-trifluoroacetic acid. Another notable trend in the product profile as $p(\text{O}_2)$ increases is that more oxidised hydrocarbons and less pyridine coupled products are formed, most predominantly at the *sec* position, while a marked increase in 3°/2° selectivity occurs with increasing $p(\text{O}_2)$. Stavropoulos commented that (i) the former observation suggested that pyridine and dioxygen competed to capture *tert* and *sec* Ad• radicals and (ii) the latter indicated participation of a more selective oxidant as $p(\text{O}_2)$ increased.

Minisci⁴⁷ has reported that the decrease in pyridine coupled products may be due to the reductive environment of the Gif^V solutions which hinders the rearomatisation of adamantylpyridinium radicals, dioxygen is allowed to compete effectively for capturing *sec*-adamantyl radicals. Stavropoulos re-investigated this system using **(3)** under the same conditions as Barton,⁴² in order to prevent the iron ions from reacting with the alkyl radicals and thus affecting the product profile when adamantane is oxidised under Gif conditions. Barton's findings of higher yields of 2-adamantanone over 1-adamantanol convinced him that secondary C-H bonds were more reactive than tertiary ones.⁵⁰ Further experiments by Barton at low $p(\text{O}_2)$ found that 2- and 4-(1-adamantyl)pyridines were detected in the product profile and the major product under ordinary

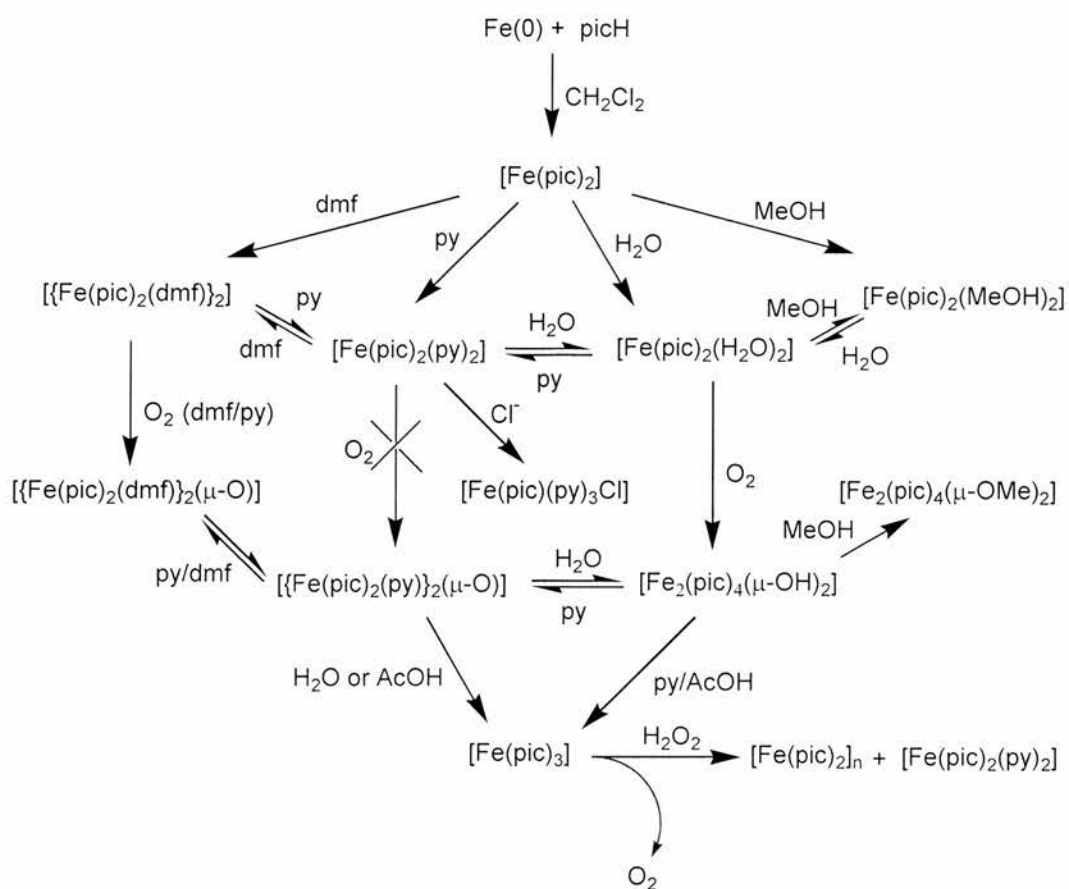
conditions, 2-adamantanone, was absent. The implication was that *tert*-adamantyl radicals were produced under Gif conditions.

In fact when the two isomeric adamantyl radicals were generated in pyridine-acetic acid by photolysis under the same $p(\text{O}_2)$, both afforded oxygenated and pyridine-coupled products in approximately equal ratios.⁵¹ The Gif results were interpreted as meaning that the difference between (1-Ad)Fe and (2-Ad)Fe bonds was their strength *i.e.* it was assumed that the (1-Ad)Fe bond was weaker and thought to undergo spontaneous fragmentation to *tert*-adamantyl radicals

1.8.1.4 The Importance of Hpic to GoAgg^{III} Systems

Iron(II,III) complexes of pic⁻ have been used to mediate Gif- and Fenton-type oxidation of hydrocarbons. Several iron(II) complexes are readily generated from iron powder and Hpic (Scheme 1.7). Studies by Stavropoulos⁵⁴ using iron(II) picolinate complexes under GoAgg^{III} conditions supported the radical pathway suggested by Perkins^{52,53} and others for the Gif mechanism.

Zinc's role in Gif^{dV} is to slowly scavenge dioxygen or rapidly to reduce iron(III) sites, thus minimising dioxygen generated from iron(III)-hydrogen peroxide interactions and keeping the redox cycle going, although under dinitrogen the oxidised hydrocarbon is not the preferential product. Another interesting observation was that the *tert*-/*sec*- selectivity (~ 4.6) in the presence of zinc was the highest obtained, suggesting that zinc may quench HO• more effectively than RO•. With [Fe₂(μ₂-OH)₂(pic)₄] the product profile contained an unusually high amount of 2-ol *versus* 2-one.⁵⁴ A similar reaction may account for -OH abstraction from iron(III)-OH moieties. Competition kinetics confirmed that the observed product profiles were dictated by partition of *tert*- and *sec*-adamantyl radicals between dioxygen (4 %) and protonated pyridine.²⁸ Studies carried out using TEMPO as a radical trap confirmed that carbon-centred radicals are generated under all conditions, irrespective of $p(\text{O}_2)$ and the presence of iron(II) or iron(III).



Scheme 1.7: Interconversions of iron-pic complexes.

1.8.1.5 The Work of Kyu-Wan Lee

Lee⁵⁹ studied the oxidation of (+)-car-3-ene (Figure 1.6) to achieve selective ketonisation under both Gif^{IV} and GoAgg^{II} conditions. His choice of substrate was made to test the mildness of Gif systems in the presence of the cyclopropane ring, which is susceptible to ring opening. Lee found that iron species with more electron-withdrawing ligands favoured increased reactivity. The selectivity pattern for the site of oxidation was found to be *sec* > *tert* ≥ *prim* under Gif conditions, whereas for a radical type reaction it would be expected to be *tert* > *sec* > *prim*.

Lee also found an optimum concentration of iron(II) above which the reaction yield dropped and confirmed the rate enhancing effect of adding Hpic to the reaction mixture. Although the findings of the paper are valid, the key premise

stated, that “Gif chemistry does not involve carbon radicals”, means that the results must be considered in a different light as a consequence.

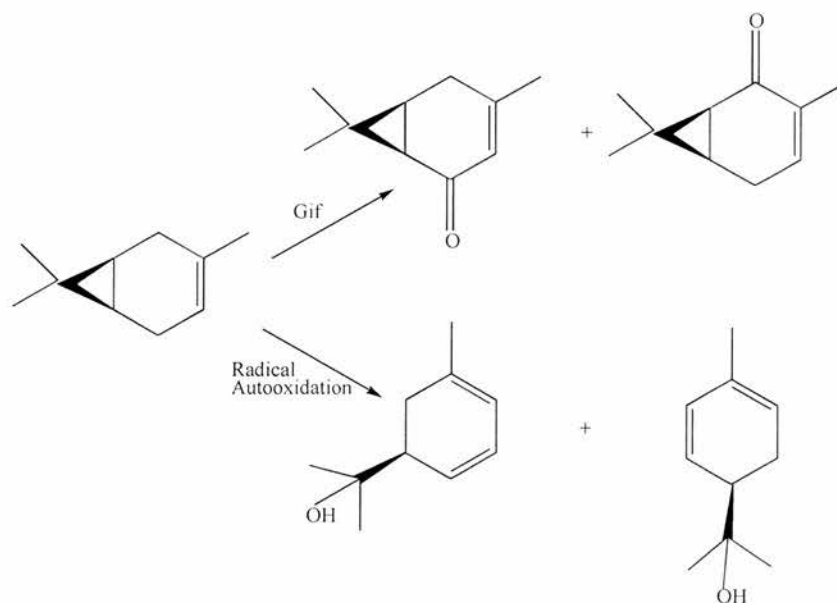


Figure 1.6: Selective oxidation of (+)-car-3-ene (upper path = Gif, lower path = radical autooxidation).

Lee’s investigation on the role of the iron precursor in Gif^{dV} and GoAgg^{II} manifolds towards cyclohexane oxygenation revealed that the anion (Z) influenced both the activity of the catalyst and the ketone-to-alcohol ratio.⁶⁰ When Z is electron withdrawing it destabilises the oxometal ($Z\text{-Fe=O}$) unit towards greater reactivity with the hydrocarbon, producing ketone (path **A**). If Z is more electron donating, then the oxometal species is stabilised and proceeds through a radical rebound mechanism to produce alcohol (path **B**). Lee proposed a tailored version of Barton’s mechanism (Figure 1.7).

Once more, their mechanistic analysis is flawed in the light of the now-accepted radical theory.

Lee reported⁶¹ oxidation of cyclohexane using a modified Gif system without pyridine as a solvent, using an iron-silica/palladium catalyst. Palladium catalysed the reaction between dihydrogen and dioxygen to give hydrogen peroxide *in situ* while iron catalysed the oxidation of alkane to alcohol. Lee later reported that when pyridine was used as a solvent very low yields of respective

products were obtained. The reaction was conducted in acetone-acetic acid and displayed high yields and a high selectivity for alcohol, the ketone apparently being formed *via* oxidation of the alcohol. All the evidence suggests that the mechanism is quite different from typical Gif chemistry.

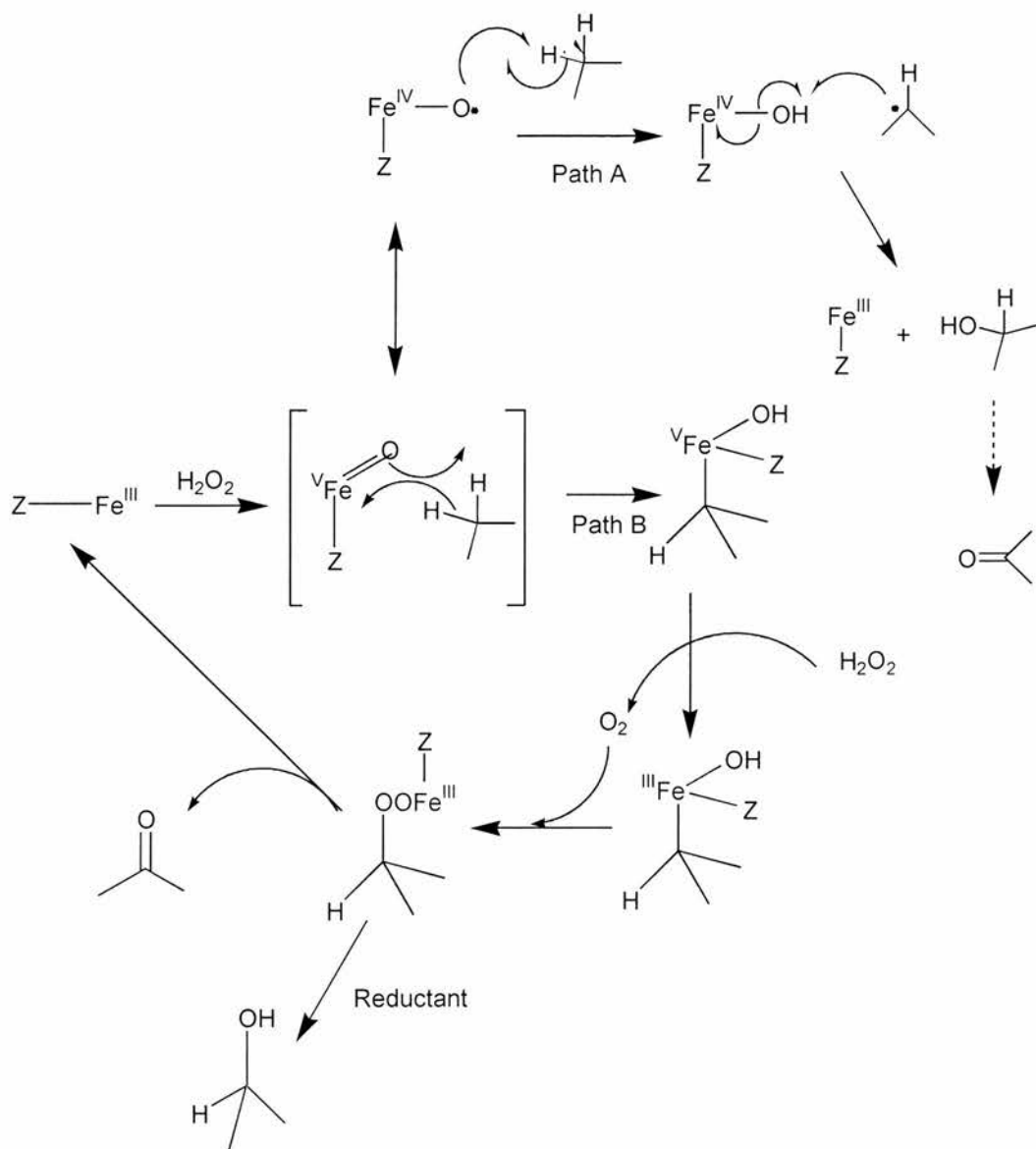


Figure 1.7: Lee's reaction scheme for Gif (GoAgg) chemistry.

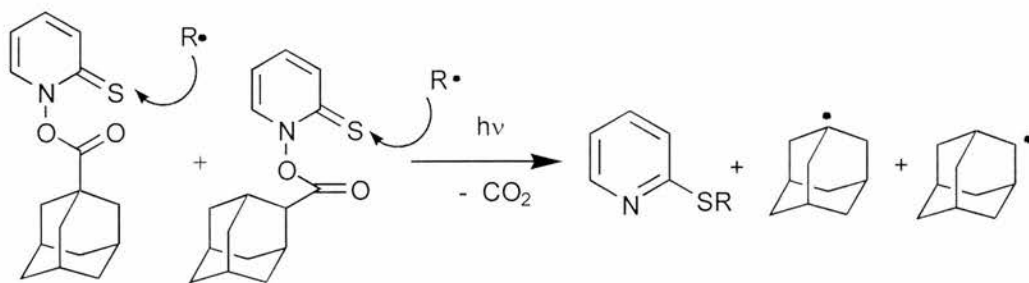
1.8.1.6 Reappraisal of Gif/*t*-BuOOH Systems.

In a re-examination of GoAgg^{IV} and GoAgg^V systems, Minisci⁶² recognised that these *t*-BuOOH-based reagents provided unambiguous evidence of *t*-BuO[•]/*t*-

BuOO• involvement. As a result of the hydrogen-bonded *t*-BuOOH to withstand hydrogen atom abstraction,^{48b} selectivities were dictated by the prevalence of *t*-BuO• over *t*-BuOO•, Minisci's mechanism for Gif/*t*-BuOOH systems is a Haber-Weiss-Walling radical chain. Ingold and Wayner⁶³ reached similar conclusions by employing GoAgg^V systems supported by diagnostic alkylhydroperoxides. Barton's re-evaluation⁵⁵ of the Gif/*t*-BuOOH systems concurred that *t*-BuO•/*t*-BuOO• radicals were generated *via* decomposition of *t*-BuOOH by iron(II)/(III). However Minisci's work with *t*-BuOOH-supported P-450 mimics^{48b} confirmed that employment of *t*-BuOOH introduced a significant *t*-BuO•/*t*-BuOO• radical component to the catalytic cycle. Therefore, *t*-BuOOH-based systems were not wholly reliable mechanistic probes for reagents supported by hydrogen peroxide or dioxygen.

1.8.1.7 Radical Trapping Experiments

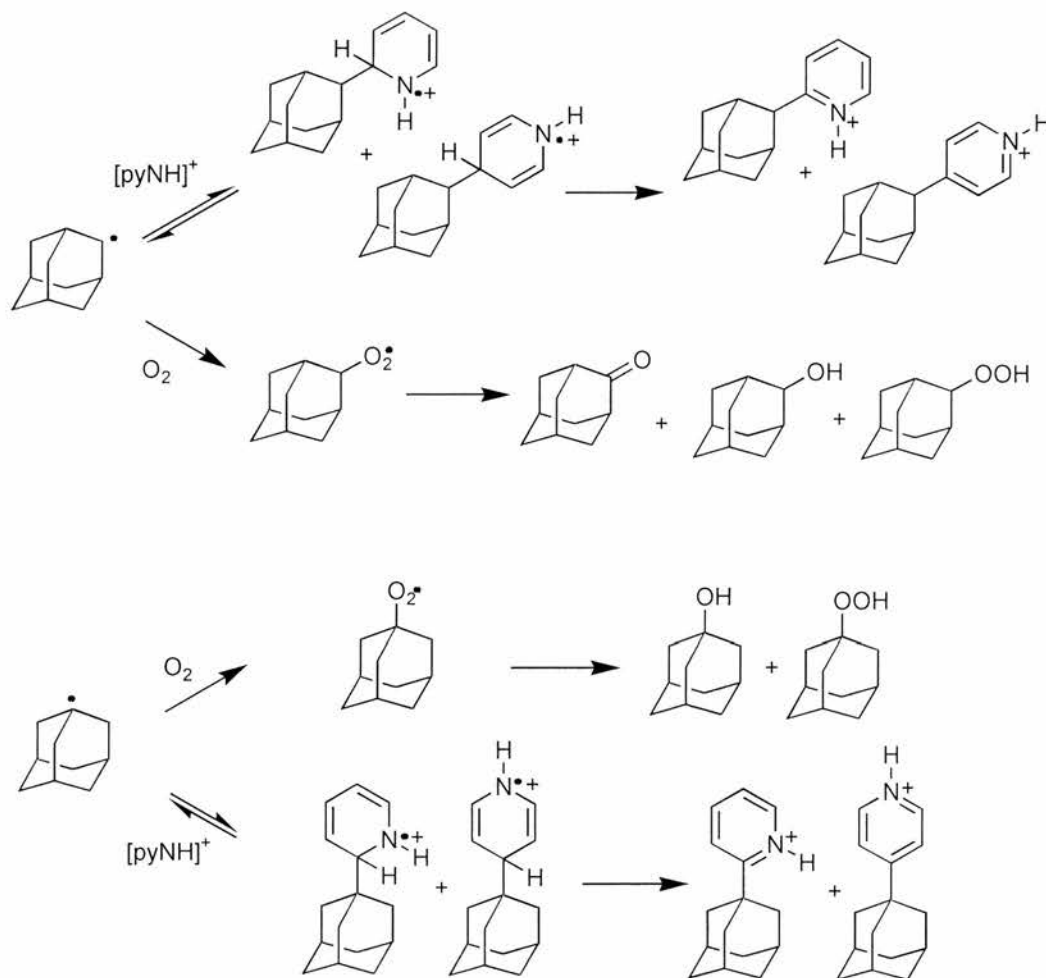
Barton's argument for a non-radical mechanism for the activation of *sec*-C-H positions of alkanes was based on experiments using genuine tertiary and secondary adamantyl radicals⁵¹ generated photolytically (Scheme 1.8) in pyridine-acetic acid under 4 % dioxygen, which react with pyridinium, dioxygen and the 2-pyridylthiyl moiety of the PTOC ester.



Scheme 1.8: Photolysis of thione esters to generate *sec*- and *tert*-adamantyl radicals.

Although oxygenated products were formed at *sec*- and *tert*- positions, the rate constant for the *reversible* addition of the highly nucleophilic *tert*-adamantyl

radicals to protonated pyridine was evaluated⁴⁷ to be two orders of magnitude larger than for *sec*-adamantyl radicals (Scheme 1.9). The adamantylpyridinium radicals re-aromatised to adamantylpyridines due to their highly reducing nature. Barton evaluated the ratio of oxygenated products *versus* pyridine-coupled *tert*-adamantyl radicals as 0.74 and 4.3 for the *sec*-adamantyl radicals.



Scheme 1.9: Competition between dioxygen trapping and coupling to pyridinium cations by adamantyl radicals.

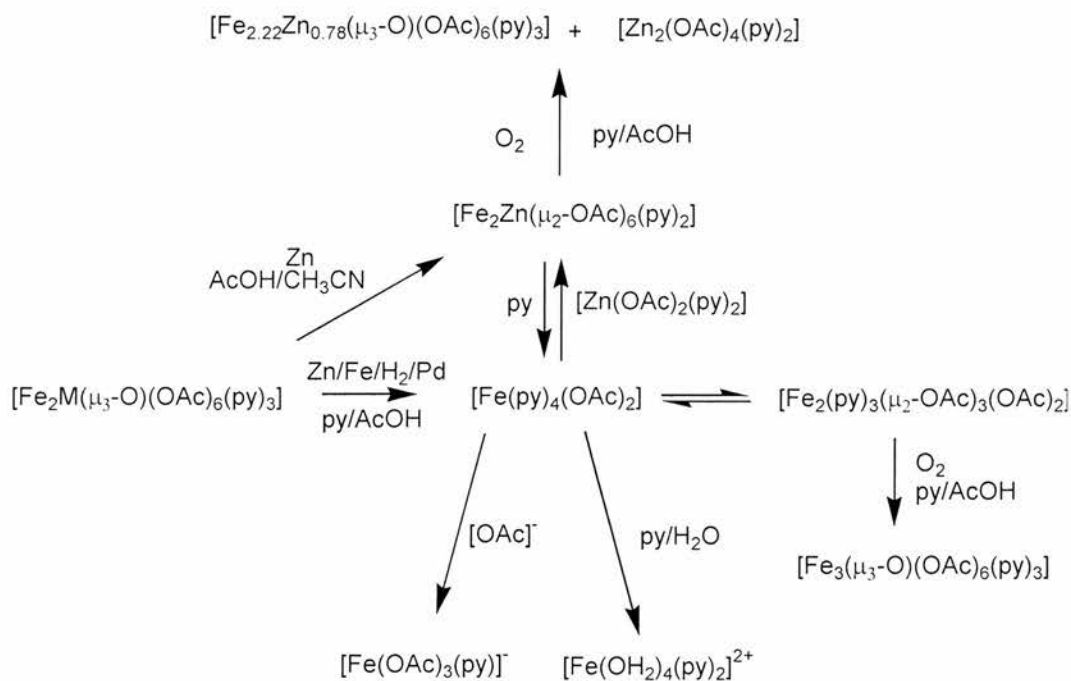
For the Gif^{IV} systems, again with 4 % dioxygen the oxidation of adamantane gave ratios of 0.03 and 94 for the *tert*- and *sec*- positions respectively. The prevalence of *tert*-adamantylpyridines in the Gif experiment strongly supported radical activation for the *tert*-C-H position, and the inconsistency of values by comparison to the control experiment was ascribed to preferential coupling of

tert-adamantyl radicals to *metal-bound* pyridine.⁵¹ Conversely the miniscule amounts of *sec*-adamantylpyridines observed in the Gif oxidation *versus* the control experiment were interpreted as the operation of a non-radical mechanism for the *sec* position. Stavropoulos re-investigated this system using **(3)** under Barton's conditions,⁵⁸ in order to prevent the iron ions from reacting with the alkyl radicals and thus affecting the product profile of the competition experiment. The ratio of oxo- *versus* pyridine-trapped adamantyl products was found to be 0.03 for the tertiary and 5.4 for the secondary position. The Gif reaction [(**3**)-hydrogen peroxide] under comparable conditions provided parallel values of 0.02 and 3.7, which agreed well and highlighted that the entire product profile of adamantane oxidation was dependent on the partitioning of Ad[•] between dioxygen and pyridinium.

The highly specific addition reaction of HO[•] radicals to dmsO was employed, along with the competitive hydrogen atom abstraction from ethanol, to investigate whether the competition kinetics support HO[•] radical involvement. The analysis was accomplished by trapping R[•] with pyridine/pyridinium. A constant stream of argon was applied to avoid capture of RO[•] by dioxygen. The diffusion-controlled oxidation of α -hydroxyethyl radicals to acetaldehyde by iron(III) can interfere, but the low iron concentrations and the preponderance of TFA-stabilized iron(II) sites minimised the importance of this reaction. In the presence of dmsO, all possible methylpyridines were observed, resulting from the addition of CH₃[•] to pyridine/pyridinium, traces of methylated bipyridines were also observed (GC-MS). Upon addition of increasing amounts of ethanol, both 1- and 2-hydroxyethylpyridines were obtained in increasing relative amounts *versus* those of methylpyridines, denoting competition between ethanol and dmsO. An average $k_{\text{ethanol}}/k_{\text{dmsO}}$ value of 0.32(4), extracted from the ratio of methylpyridines over hydroxyethylpyridines and the initial concentrations of dmsO and ethanol, is consistent with the expected ratio of rate constants ($k_{\text{ethanol}}/k_{\text{dmsO}} = 0.29$) for radiolytic HO[•] attack on ethanol/dmsO.

1.9 Gif-Dioxygen-Zinc Systems Using Iron and Ruthenium Acetate Reagents.

These systems were initially analysed by Barton,⁴⁴ who claimed that they were structurally and functionally related to the activity of the diiron site of sMMO.



Scheme 1.10 Stoichiometric reductions of Gif^{IV} catalyst precursors.

Analysis by Stavropoulos⁶⁴ found that the reduction of $[\text{Fe}_3(\mu_3\text{-O})(\mu_2\text{-O}_2\text{CCH}_3)_6(\text{py})_3]$ generated *trans*- $[\text{Fe}(\text{O}_2\text{CCH}_3)_2(\text{py})_4]$ and $[\text{Fe}_2(\mu_2\text{-O}_2\text{CCH}_3)_4(\text{py})_3]_n$ (Scheme 1.10). The latter species shows structural analogies, albeit divergent electromagnetic properties, to the diferrous site (Hred) of sMMO.⁶⁵

Despite these structural analogies, the *tert*-/*sec*- selectivities and KIE values obtained in Gif^{IV} oxidations seem to suggest a more selective oxidant than the presumed high-valent, iron-oxo units operating in oxygenations by sMMO or P-450. In retrospect, this is only true inasmuch as the role of the more selective substrate-centered RO[•] is highlighted due to the dioxygen dependence of the Gif^{IV} systems. As noted above, zinc may have a similar effect by preferentially quenching HO[•] rather than RO[•].

Those selected product profiles which seemed to diminish the importance of HO• need eventually to be reconciled with the action of oxygen-centred radicals. A frequently cited⁶⁶ anomaly is the alleged inferiority of *sec*-alcohols as substrates by comparison to the parent alkanes. Based on *normalised* data,⁶⁷ competition for the oxidation of 2-ol/ane by Gif/*t*-BuOOH and Gif/hydrogen peroxide systems favours the alcohol in all cases. The 2-ol/ane ratio is higher by a factor of 4-5 for Gif/*t*-BuOOH systems than that for Gif/hydrogen peroxide oxidations. This important observation was interpreted by Barton⁶⁷ as confirming the difference between *t*-BuO• radical chemistry (Gif/*t*-BuOOH) and non-radical oxidations (Gif/hydrogen peroxide). However, it is also consistent with the difference in reactivity/selectivity between *t*-BuO• and HO•.

A comparative study of Gif^{dV} type solutions, based on [M₃(μ₃-O)(μ₂-O₂CCH₃)₆(py)₃], M = iron(III) or ruthenium(III),⁶⁸ revealed a close relationship between *in situ* generation of the reduced [M^{II}(O₂CCH₃)₂(py)₄] and ketone formation. Using cyclic voltammetry, ¹H NMR and UV-vis spectroscopies it was found that cyclohexane oxygenation by ruthenium_{cat}/dioxygen/zinc produced cyclohexanol much earlier during the reaction than in the iron-based system, while generation of cyclohexanone became more prominent at later stages, in strict correspondence to the slower rates observed for the assembly of the ruthenium(II) *versus* the iron(II) sites. These results stress the importance of M(II)/ROOH systems in the decomposition of the intermediate *sec*-alkylhydroperoxide mainly to ketone. The bulk of alcohol was formed *via* the facile reduction of ROOH by zinc dust. Therefore, the one/2-ol ratio is dictated by competition between M(II) and zinc toward decomposition of ROOH.

1.10 New Vistas in Hydrocarbon Oxidation using Gif Techniques

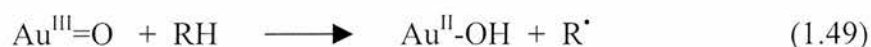
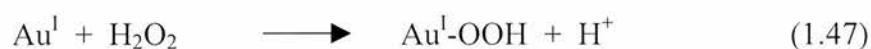
Recent publications give tantalising glimpses of new directions in hydrocarbon oxidation.

1.10.1 Applications of Ultrasound

The well-known rate enhancements observed upon application of ultrasound (sonication) to chemical reactions has been applied to Gif systems. Cyclohexane was oxidised under GoAgg^{II} conditions [iron(III) chloride-pyridine-hydrogen peroxide] to cyclohexanol and cyclohexanone under 0.5 h of sonication in higher yields than after 24 h in the absence of ultrasound.⁶⁹ However the greater reactivity of cyclohexane compared with cyclooctane was taken to support Barton's non-radical mechanism, which was further espoused by the non-acceleration of oxidation of cyclohexane upon application of ultrasound with *t*-BuOOH as oxidant. This set of observations merits greater research, as the conflicting results with regards to mechanistics cannot be readily explained.

1.10.2 Use of Gold Catalysts

In a rare study of the catalytic behaviour of one of the noblest metals, both gold(I) and gold(III) complexes were found to catalyse the oxygenation of cyclic hydrocarbons. Shul'pin showed that cyclooctane was oxidised by hydrogen peroxide in the presence of sodium tetrachloroaurate(III) to cyclooctyl hydroperoxide, cyclooctane and cyclooctanone, the total turnover number being 520 after 144 h.⁷⁰ Gold(I) triphenylphosphine chloride performed similarly. In both instances the major product was the alkyl hydroperoxide, consequently the following cycle was proposed by the authors, equations 1.47-1.51.



1.10.3 Biologically Relevant Substrates

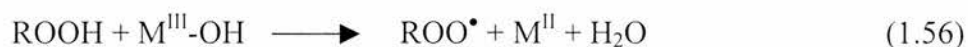
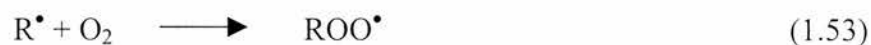
Kotani reported the [Fe(pic)₃]-hydrogen peroxide-acetonitrile system as an alternative to GoAgg^{III} and as a simple model for monooxygenase.⁷¹ The triterpenoid methyl-3-*O*-acetyl oleanolate was oxidised stereoselectively at the C-11 position to the alcohol (19.2 %) at room temperature after 3 h, with smaller quantities of ketones (< 10 %), while 3 β ,28-di-*O*-acetylbatulin was oxidised to an epimeric mixture of isomeric aldehydes *via* an intermediate epoxide. The same oxidant system hydroxylated cholesteryl acetate primarily at the C-7 position.⁷² The active species in the oxygenation of these substrates was proposed to be a mixed iron(III)-iron(V) oxo complex; the iron(III) centre was anchored by the olefin of the substrate while the Fe=O bond abstracted a vinylic hydrogen atom and formed a C-O bond. Subsequent rearrangement and elimination of iron gave the oxygenated products. While this mechanism is, of course, incorrect, a radical based scheme awaits proposal.

1.11 Zeolite-Mediated Alkane Oxidation

A major shortcoming of Gif Chemistry is its inability to oxidise regioselectively linear alkanes. Hydrocarbons oxidised at the terminal (α or 1-) position are important feedstocks for the chemical and pharmaceutical industries. Nevertheless the selective oxidation of alkanes at their terminal methyl groups remains a challenge in catalysis research. The ability of enzymes to induce selective oxidations may well be due to the steric effects within the enzyme active site which places the terminal position in close proximity.

Pure inorganic catalysts enabling C-1 oxidation of *n*-alkanes with high selectivity using dioxygen have been produced.⁷³ These catalysts belong to the group of zeolite-like crystalline and microporous aluminophosphates, in which manganese and cobalt dopant ions are introduced as redox centres into the zeolite framework. Fine-tuning of the pore diameter allows the terminal carbon atom of the *n*-alkane to approach the catalytically active site where it becomes oxidised at

the end of the hydrocarbon chain to give alcohol, aldehyde or carboxylic acid products. The oxidation mechanism is believed to involve radical intermediates, equations 1.52-1.57.



A limitation of this type of catalyst is that only alkanes of certain chain length can be oxidised as a result of restricted space in the zeolite channels and the long-term stability of the catalyst. It is assumed that catalyst deactivation occurs as a result of metal ions leaching into the solution and polar reaction products blocking the catalytically active sites. A recent review by Thomas⁷⁴ detailing his investigations into molecular sieve catalysts for alkane oxygenation provides a good overview for the interested reader.

One recently reported heterogeneous catalyst for cyclohexane oxygenation was prepared by ion exchange of montmorillonite clay by an aqueous solution of iron(III) nitrate.⁷⁵ The key feature of the catalyst was the presence of Fe-O-Fe units, demonstrated by EXAFS spectroscopy. Liquid phase oxygenation of cyclohexane with hydrogen peroxide afforded cyclohexyl hydroperoxide as the major product, with a turnover number of 23,200 after 60 h at 40 °C.

1.12 Summary and Conclusions

Oxidation processes are intrinsic to the biochemistry of life. Biochemical oxidations are almost invariably catalysed by metalloproteins, certain metals (iron, cobalt, copper) being essential in this regard. Within the chemical industry, catalytic oxidation of saturated and unsaturated hydrocarbon substrates provides the raw chemical feedstocks for a multitude of applications, from polymer synthesis to drug manufacture. While alkanes are difficult to oxidise regioselectively without overoxidation, the Gif and GoAgg oxidant families can provide limited functionalisation of these inert but valuable substrates. In both classes of catalysts, elemental iron or iron salts and pyridine are integral to their performance. Substantial controversy has surrounded the precise mechanisms by which Gif and GoAgg systems operate, since their introduction by Barton some twenty years ago. The body of evidence currently favours a free radical mechanism instead of one based on high-valent metal-oxo intermediates as initially proposed. The necessity of pyridine as a solvent has barred their application to anything larger than laboratory scale reactions. The development of pyridine-free systems retaining catalytic activity and selectivity remains a challenging goal, one which is addressed by the work conducted during this thesis. An outline of the research presented in this thesis is as follows.

(i) An examination of the kinetics of the GoAgg^{III} reaction between $[\text{Fe}(\text{pic})_3]$ in pyridine with hydrogen peroxide, both in the presence and absence of cyclohexane, has been conducted by UV-vis and EPR spectroscopies with the aim of establishing the nature and time of generation of the active oxygenating species, the iron species formed and the role of oxygen-centred radicals.

(ii) Chapter Three outlines the synthesis and coordination chemistry to iron of polydentate ligands containing 2-pyridyl groups. One class of ligands, the pyridine dicarboxamides, have received particular attention owing to their ability to stabilise bi-, tri-, and in one instance tetranuclear copper(II) species (Chapter Four).

(iii) A study of the catalytic efficiency towards oxygenation of cyclohexane by iron(II,III) complexes bearing multidentate nitrogen and oxygen donor ligands under G_{if}^{IV} conditions (dioxygen/zinc/pyridine-acetic acid) has been investigated.

(iv) Preliminary results of investigations into the coordination chemistry of polyaza macrocyclic ligands with iron are given in Chapter Six.

1.13 References

1. *Encyclopaedia of Inorganic Chemistry*, volume 6, Ed. R.B. King, Wiley, 1994.
2. R. S. Drago, *Coord. Chem. Rev.*, 1992, **117**, 185.
3. H. Mimoun, *Comp. Coord. Chem.*, 1987, **6**, 317.
4. F. Gozzo, *J. Mol. Catal.(A)*, 2001, **171**, 1.
5. M. Fontecave and J. L. Pierre, *Bull. Chim. Soc. Fr.*, 1993, **130**, 77.
6. R. H. Crabtree, *J. Chem. Soc., Dalton Trans.*, 2001, 2437.
7. H. B. Dunford, *Coord. Chem. Rev.*, 2002, in press.
8. R.A. Sheldon, *New Developments in Selective Oxidations*, 1990, 1.
9. G. A. Olah and A. Molnar, *Hydrocarbon Chemistry*, Wiley, New York, 1995.
10. F. A. Cotton and G. Wilkinson, *Advanced Inorganic Chemistry*, 5th Edition, John Wiley, New York, 1988, p 737.
11. A. L. Balch, Y. W. Chan, R. S. Cheng, G. N. Lamar, B. Latos, L. Grazynski and M. W. Denner, *J. Am. Chem. Soc.*, 1984, **106**, 7779 and references within.
12. J. T. Groves and R. Quinn, *J. Am. Chem. Soc.*, 1985, **107**, 5790.
13. J. T. Groves and M. V. D. Puy, *J. Am. Chem. Soc.*, 1976, **98**, 5290.
14. R. S. Drago, A. Zuzich and E. D. Nyberg, *J. Am. Chem. Soc.*, 1985, **107**, 2898.
15. A. S. Goldstein and R. S. Drago, *Inorg. Chem.*, 1991, **30**, 4506.
16. J. E. Backvall, B. Akermark and S. O. Ljungren, *J. Am. Chem. Soc.*, 1979, **101**, 2411.
17. A. E. Shilov in *Activation and Functionalisation of Alkanes*, Ed. C. Hill, John Wiley, New York, p.1
18. (a) R. J. Hodges and J. L. Garnett, *J. Phys. Chem.*, 1986, **72**, 1673. (b) V. P. Tretyakov, E. S. Rudakov, A. V. Moravsky and A. E. Shilov, *Nouv. J. Chem.*, 1983, **7**, 729. (c) D. Webster, *Adv. Organomet. Chem.*, 1977, **15**, 147.
19. R. H. Crabtree, S. M. Miheicic and J. M. Quirk, *J. Am. Chem. Soc.*, 1979, **101**, 7738.
20. P. Wardman and L. P. Candeias, *Radiat. Res.*, 1996, **145**, 523.

- 21 D. S. Sigman, A. Mazumder and D. M. Perrin, *Chem. Rev.*, 1993, **93**, 2295.
- 22 P. Chaudhuri, M. Hess, J. Muller, K. Hildenbrand, E. Bill, T. Weyhermuller and K. Wieghardt, *J. Am. Chem. Soc.*, 1999, **121**, 9599.
- 23 S. Schindler, *Eur. J. Inorg. Chem.*, 2000, 2311.
- 24 H. Umezawa, K. Maeda, T. Takeuchi and Y. Okami, *J. Antibiot. Ser. A*, 1966, **19**, 200.
- 25 G. Pratviel, J. Bernadou and B. Meunier, *Angew. Chem., Int. Ed. Engl.*, 1995, **34**, 746.
- 26 Y. Nishida, M. Kumita and S. Nishino, *Inorg. Chem. Commun.*, 1999, **2**, 156.
- 27 J. Stubbe and J. W. Kazarich, *Chem. Rev.*, 1987, **87**, 1107.
- 28 T. Suzuki, J. Kuwaraha, M. Goto and Y. Sugiura, *Biochim. Biophys. Acta*, 1984, **824**, 330.
- 29 W. Li, W. E. Antholine and D. H. Petering, *J. Inorg. Biochem.*, 2002, **90**, 8.
- 30 S. M. Hecht, *Acc. Chem. Res.*, 1986, **19**, 383.
- 31 (a) R. J. Guajardo, S. E. Hudson, S. J. Brown and P. K. Mascharak, *J. Am. Chem. Soc.*, 1993, **115**, 7971. (b) P. Mialane, A. Nivorojkine, G. Pratviel, L. Azema, M. Slany, F. Godde, A. Simaan, F. Banse, T. K. Grisel, G. Bouchoux, J. Sainton, O. Horner, J. Guilhem, L. Tchertanova, B. Meunier and J.-J. Girerd, *Inorg. Chem.*, 1999, **38**, 1085. (c) I. Bernel, I. M. Jensen, K. B. Jensen, C. J. M^cKenzie, H. Toftlund and J. P. Tuchagues, *J. Chem. Soc., Dalton Trans.*, 1995, 3667. (d) M. Lubben, A. Meetsma, E. C. Wilkinson, B. Feringa and L. Que, Jr., *Angew. Chem. Int. Ed. Engl.*, 1995, **34**, 1512. (e) C. Nguyen, R. J. Guajardo and P. K. Mascharak, *Inorg. Chem.*, 1996, **35**, 6273. (f) M. E. de Vries, R. J. La Cois, G. Roelfes, H. Kooijman, A. L. Spek, R. Hage and B. L. Feringa, *Chem. Commun.*, 1997, 1549.
- 32 M. Searcey, S. M^cClean, B. Madden and L. P. G. Wakelin, *J. Chem. Soc., Perkin Trans. 2*, 1997, 523.
- 33 S. Basak and V. Nagaraja, *Nucleic Acids Res.*, 2001, **29**, e105.
- 34 Y. Ishikawa, Y. Morishita, T. Yamamoto, H. Kurosaki, M. Goto, H. Matsuo and M. Sugiyama, *Chem. Lett.*, 1998, 39.

- 35 H. Kurodaki, A. Maruyama, H. Koike, N. Kuroda, Y. Ishikawa and M. Goto, *Bioorg. Med. Chem. Lett.*, 2002, **12**, 201.
- 36 C. Liu, S. Yu, D. Li, Z. Liao, X. Sun and H. Xu, *Inorg. Chem.*, 2002, **41**, 913.
- 37 A. Neves, H. Terenzi, R. Horner, A. Horn, B. Szpoganicz and J. Sugai, *Inorg. Chem. Commun.*, 2001, **4**, 388.
- 38 E. Nyarko and M. Tabata, *J. Porphyrins Phthalocyanins*, 2001, **5**, 873.
- 39 T. Tabushi, *Tetrahedron Lett.*, 1980, **21**, 2565.
- 40 D. H. R. Barton, M. J. Gastiger and W. B. Motherwell, *J. Chem. Soc., Chem Commun.*, 1983, 731.
- 41 D. H. R. Barton, S. D. Beviere, W. Chavasiri, E. Csuhai, D. Doller and W.G. Liu, *J. Am. Chem. Soc.*, 1992, **114**, 2147.
- 42 P. Stavropoulos, R. Celenligil-Cetin and A. E. Tapper, *Acc. Chem. Res.*, 2001, **34**, 745.
- 43 E. About-Jaudet, D. H. R. Barton, E. Csuhai and N. Ozbalik, *Tetrahedron Lett.*, 1990, **31**, 1657.
- 44 D. H. R. Barton, B. H. Lu, D. K. Taylor and R. U. R. Whal, *J. Chem. Soc., Perkin Trans. 2*, 1996, 1032.
- 45 U. Schuchardt, W. A. Carvalho and E. V. Spinace, *Synlett*, 1993, 713.
- 46 D. H. R. Barton, S. D. Beviere and D. R. Hill, *Tetrahedron*, 1994, **50**, 2665.
- 47 F. Recupero, A. Bravo, H. R. Bjorsvik, F. Fontana, F. Minisci and M. Piredda, *J. Chem. Soc., Perkin Trans. 2*, 1997, 2399.
- 48 (a) F. Minisci, F. Fontana, S. Araneo and F. Recupero, *Tetrahedron Lett.*, 1994, **35**, 3759. (b) F. Minisci, F. Fontana, S. Araneo and F. Recupero, S. Banfi and S. Quici, *J. Am. Chem. Soc.*, 1995, **117**, 226.
- 49 M. Newcomb, P.A. Simakov and S.-U. Park, *Tetrahedron Lett.*, 1996, **37**, 819.
- 50 D. H. R. Barton, *Tetrahedron*, 1998, **54**, 5805.
- 51 D. H. R. Barton, F. Halley, N. Azbalik, M. Schmitt, E. Young and G. Balavoine, *J. Am. Chem. Soc.*, 1989, **111**, 7144.
- 52 C. Knight and M. J. Perkins, *J. Chem. Soc., Chem Commun.*, 1991, 925.
- 53 M. J. Perkins, *Chem. Soc. Rev.*, 1996, 229.

- 54 S. Kiani, A. Tapper, R. J. Staples and P. Stavropoulos, *J. Am. Chem. Soc.*, 2000, **122**, 7503.
- 55 D. H. R. Barton, *Chem. Soc. Rev.*, 1996, 237.
- 56 D. T. Sawyer, C. Khan, A. Llobet and C. Redman, *J. Am. Chem. Soc.*, 1993, **115**, 5817.
- 57 J. P. Hague, A. Hobet and D. T. Sawyer, *Bioorg. Med. Chem.*, 1995, **3**, 1383.
- 58 A. E. Tapper, J. R. Long and P. Stavropoulos, *Angew. Chem., Int. Ed. Engl.*, 2000, **39**, 2343.
- 59 K. W. Lee, S. B. Kim, S. B. Kim, D. H. R. Barton and D. Doller, *Bull. Korean Chem. Soc.*, 1991, **12**, 459.
- 60 S. B. Kim, K. W. Lee, Y. J. Kim and S. I. Hong, *Bull. Korean Chem. Soc.*, 1994, **15**, 424.
- 61 S. B. Kim, K. W. Jun, S. B. Kim and K. W. Lee, *Chem. Lett.*, 1995, 535.
- 62 F. Minisci, F. Fontana, S. Araneo, F. Recupero and L. Zhao, *Synlett*, 1996, 119.
- 63 D. W. Snelgrove, P. A. MacFaul, K. U. Ingold and D. D. M. Wayne, *Tetrahedron Lett.*, 1996, **37**, 823.
- 64 B. Singh, J. R. Long, F. Fabrizi de Biani, D. Gatteschi and P. Stavropoulos, *J. Am. Chem. Soc.*, 1997, **119**, 7030.
- 65 A. C. Rosenzweig, P. Nordlund, P. M. Takahara, C. A. Frederick and S. J. Lippard, *Chem. Biol.*, 1995, **2**, 409.
- 66 S. Rahhal and H. W. Richter, *J. Am. Chem. Soc.*, 1988, **110**, 3126.
- 67 D. H. R. Barton, S. D. Beviere, W. Chavasiri, D. Doller, W. G. Liu and J. H. Riebenspies, *New. J. Chem.*, 1992, **16**, 1019.
- 68 S. B. Marr, R. O. Carvel, D. T. Richens, H. J. Lee, M. Lane and P. Stavropoulos, *Inorg. Chem.*, 2000, **39**, 4630.
- 69 R. Duriska and S. Toma, *Chem. Pap.*, 2001, **55**, 308.
- 70 G. B. Shul'pin, A. E. Shilov and G. Suss-Fink, *Tetrahedron. Lett.*, 2001, **42**, 7253.
- 71 I. Okamoto, T. Takeya, Y. Kogawa and E. Kotani, *Chem. Pharm. Bull.*, 2000, **48**, 120.
- 72 T. Takeya, H. Egawa, N. Inoue, A. Miyamoto, T. Chuma and E. Kotani, *Chem. Pharm. Bull.*, 1999, **47**, 64.

- 73 M. Hartmann and S. Ernst, *Angew. Chem., Int. Ed. Engl.*, 2000, **39**, 39.
- 74 J. M. Thomas, R. Raja, G. Sankar and R. G. Bell, *Acc. Chem. Res.*, 2001, **34**, 191.
- 75 K. Ebitani, M. Ide, T. Mitsudome, T. Mizugaki and K. Kaneda, *Chem. Commun.*, 2002, 690.

Chapter Two

Kinetic and EPR Spectroscopic Study of the Reaction of Hydrogen Peroxide in Pyridine with Iron Picolinate Complexes

2.1 Introduction

As described in Chapter One, there is firm evidence that both GoAgg and Gif systems undergo the same general mechanism. The GoAgg system, unlike the Gif^V system, is fully homogeneous, using hydrogen peroxide as the oxygen source. There are some differences between the systems. For example, the GoAgg^{III} system doesn't require acetic acid, picolinic acid (Hpic) is used as a replacement. Moreover, the addition of Hpic has been shown in previous studies to speed up the formation of oxygenated products whilst maintaining typical Gif reactivity (*e.g.* preferential ketone formation during oxidation of cyclic hydrocarbons). As a consequence numerous mechanistic conclusions have been made¹⁻³ and the following observations are noteworthy:

- (i) The presence of Hpic reduces the requirement for pyridine in the system and additionally a higher conversion rate is observed.
- (ii) An excess of Hpic is not required. The ideal ratio for efficient ketonisation has been established as iron(III):Hpic:hydrogen peroxide = 1:4:4.
- (iii) With two equivalents of Hpic (to iron salt) almost all production of *in situ* dioxygen is suppressed, *i.e.* Hpic effectively suppresses catalase activity.
- (iv) No alcohol formation is observed.
- (v) It was found that carboxylic acid ligands containing an N-heterocyclic component were most effective when coordinated to an iron(III) centre.

It has been proposed that under $\text{GoAgg}^{\text{III}}$ conditions an intermediate μ_2 -peroxy bridged diiron(III) complex is formed. This assumption is made based upon the results from experiments where the iron(II)-Hpic-hydrogen peroxide and iron(III)-Hpic-hydrogen peroxide systems were run in the presence and absence of dioxygen.

This Chapter describes the synthesis of some simple iron-pic complexes and their reactivity under $\text{GoAgg}^{\text{III}}$ conditions. In particular the kinetics of the reactions of $[\text{Fe}(\text{pic})_3]$ and $[\text{Fe}(\text{pic})_2(\text{H}_2\text{O})_2]$ with hydrogen peroxide in pyridine have been examined, which have been monitored by UV-visible spectroscopy and supported by NMR experiments. The reaction of $[\text{Fe}(\text{pic})_3]$ with hydrogen peroxide under $\text{GoAgg}^{\text{III}}$ conditions yields a purple high-spin iron(III) species which has been characterised by EPR spectroscopy.

2.2 Picolinate Complexes of Iron(II,III)

Stavropoulos generated $[\text{Fe}(\text{pic})_2]_n$ and $[\text{Fe}(\text{pic})_2(\text{py})_2]$ from metallic iron and Hpic in dichloromethane or pyridine respectively, and demonstrated their versatility for the synthesis of mixed ligand iron(II,III)-picolinate complexes (Scheme 1.7).⁴ As part of this study, the synthesis of mixed ligand iron(II) complexes containing both pic^- and 2,2'-bipyridine (2,2'-bipy) by treating iron(II) salts with solutions containing varying amounts of Hpic and 2,2'-bipy was attempted. However in all cases the only identifiable product was $[\text{Fe}(2,2'\text{-bipy})_3]^{2+}$ (UV-visible evidence), owing to its marked stability as a result of the low spin t_{2g}^6 configuration.

2.2.1 Iron(III) Tris(Picolinate)

$[\text{Fe}(\text{pic})_3]$ was prepared by reacting Hpic and iron(III) nitrate nonahydrate in a 3:1 molar ratio in methanol under aerobic conditions. X-Ray crystallography on single crystals grown from methanol under dinitrogen in the dark confirmed that

each pic⁻ anion coordinates to the iron centre *via* the pyridyl nitrogen and one carboxylate oxygen atom to form an octahedral tris(chelate) complex with a meridional [FeN₃O₃] geometry (Figure 2.1). The crystallographic data reported for [Fe(pic)₃].H₂O and [Fe(pic)₃].0.5py, crystallised from water⁵ and pyridine⁴ respectively, differed from our data as far as the cell dimensions, space group and β angle were concerned. The structural parameters are largely similar, a notable exception being the *trans*- O(8)-Fe(1)-O(28) angle [160.29(10)^o], *c.f.* 170.6(2)^o for the monohydrate,⁵ 165.95(15)^o for the pyridine solvate,⁴ which may arise from crystal packing effects due to the co-crystallised molecule of solvent. The *cis*- and *trans*- angles at Fe(1) lie in the ranges 78.16(1)–101.04(10)^o and 160.29(10)–165.58(10)^o, the (N-Fe-O)_{chelate} bite angles being *ca.* 78^o.

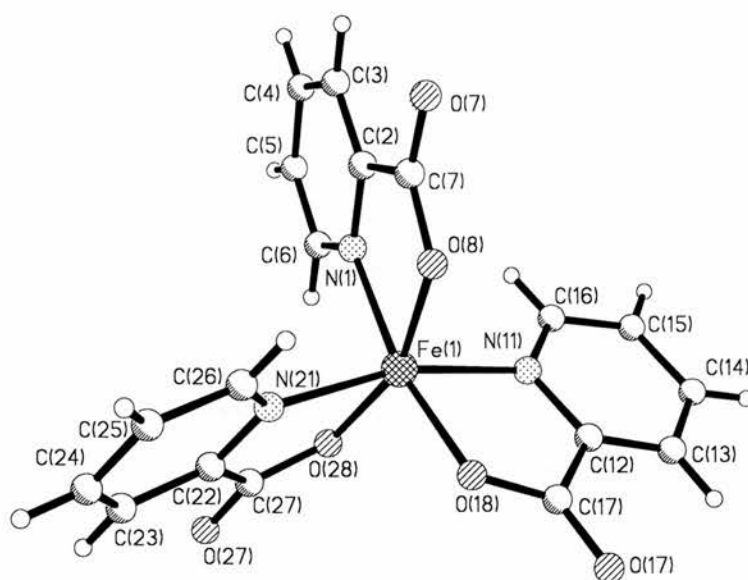


Figure 2.1: Molecular structure of [Fe(pic)₃].

Crystals of [Fe(pic)₃] turn from light green to yellow over a few days under ambient conditions unless stored in the dark, where they remain light green in colour indefinitely. It has been reported that [Fe(pic)₂(H₂O)₂], which is red, undergoes aerial oxidation in hot ethanol to give a yellow diiron(III) complex [Fe₂(μ₂-OH)₂(pic)₄];⁵ however no bands attributable to uncoordinated Hpic appeared in the IR spectrum of the yellow solid from [Fe(pic)₃], suggesting that

an Hpic ligand was not displaced from the metal during the yellowing process. Elemental analysis corresponded to a trihydrate, while in the IR spectrum a broad ν_{OH} band at 3222 cm^{-1} appeared, which was absent in the spectrum of $[\text{Fe}(\text{pic})_3]$.

Table 2.1: Selected bond lengths (\AA) and angles ($^\circ$) for $[\text{Fe}(\text{pic})_3]$, $[\text{Fe}(\text{pic})_3]\cdot 0.5\text{py}$ and $[\text{Fe}(\text{pic})_3]\cdot \text{H}_2\text{O}$ (esd's in parentheses).^{4,5}

	$[\text{Fe}(\text{pic})_3]$	$[\text{Fe}(\text{pic})_3]\cdot \text{H}_2\text{O}$	$[\text{Fe}(\text{pic})_3]\cdot 0.5\text{py}$
Fe(1)-O(18)	1.944(2)	1.970(3)	1.948(4)
Fe(1)-O(8)	1.952(2)	1.957(4)	1.972(4)
Fe(1)-O(28)	1.975(2)	1.977(4)	1.971(4)
Fe(1)-N(21)	2.118(3)	2.109(4)	2.126(4)
Fe(1)-N(1)	2.132(2)	2.148(4)	2.150(5)
Fe(1)-N(11)	2.155(3)	2.136(4)	2.128(4)
O(18)-Fe(1)-O(8)	96.81(10)	90.9(2)	94.07(19)
O(18)-Fe(1)-O(28)	98.82(10)	98.3(2)	97.95(17)
O(8)-Fe(1)-O(28)	160.29(10)	170.6(2)	165.95(15)
O(18)-Fe(1)-N(21)	89.45(10)	90.8(2)	95.36(17)
O(8)-Fe(1)-N(21)	90.10(10)	100.9(2)	92.63(17)
O(28)-Fe(1)-N(21)	78.16(10)	78.8(2)	79.07(16)
O(18)-Fe(1)-N(1)	168.44(10)	169.0(2)	168.89(16)
O(8)-Fe(1)-N(1)	78.50(10)	78.3(3)	78.24(16)
O(28)-Fe(1)-N(1)	88.18(10)	92.3(2)	90.79(17)
N(21)-Fe(1)-N(1)	101.04(10)	93.7(2)	93.01(16)
O(18)-Fe(1)-N(11)	78.61(11)	79.3(2)	79.76(15)
O(8)-Fe(1)-N(11)	99.25(10)	90.7(2)	94.76(17)
O(28)-Fe(1)-N(11)	95.54(10)	91.1(2)	94.51(17)
N(21)-Fe(1)-N(11)	165.58(10)	164.9(2)	171.41(15)
N(1)-Fe(1)-N(11)	91.62(10)	97.9(2)	92.78(17)

2.2.2 Synthesis of [pyH][Fe(pic)₂Cl₂]

The passage of a slow stream of dichlorine gas over a dichloromethane solution of [Fe(pic)₂(py)₂] under dinitrogen produced a yellow solution at room temperature over 2 h. Evaporation of the solvent followed by extraction of the crude product into acetonitrile (aerobic conditions) and diffusion of diethyl ether vapour into the solution gave yellow crystals, determined crystallographically to be [pyH][Fe(pic)₂Cl₂] (Figure 2.2). This complex has also been isolated by Barton as the [py₂H]⁺ salt from the reaction between iron(III) chloride hexahydrate and Hpic in a pyridine-cyclohexane-acetic acid solvent system.⁶ This synthesis, both in our hands and others,⁷ was irreproducible, with the almost instantaneous formation of a yellow precipitate (ν_{COO} 1660, 1334 cm⁻¹ indicating coordinated pic) whose microanalysis values did not correspond to the expected data, whereas the original report described formation of yellow crystals over one week (no IR data were reported). Barton had proposed that [Fe(pic)₂Cl₂]⁻ was formed in GoAgg^{III} systems from iron(III) chloride prior to addition of hydrogen peroxide, however its inaccessibility by the published procedure has prohibited further investigations into its chemistry. Chlorination of [Fe(pic)₂(py)₂] provides a simple and efficient route to [Fe(pic)₂Cl₂]⁻ in good yield, facilitating its wider study and usage.

Our structural determination and that of Barton's differ in several respects. Our cation is [pyH]⁺, not [py₂H]⁺, also we have found two crystallographically independent molecules (labelled molecules I and II) of [pyH][Fe(pic)₂Cl₂] in the unit cell, differing in the geometries of the anions. For the second independent molecule the iron atom is labelled Fe(2), with all of the other atomic labels being thirty higher in value than in molecule I; thus O(8) in the first independent molecule is O(38) in the second. In molecule I the [Fe(pic)₂Cl₂]⁻ anion has a *cis, cis, trans*- geometry of nitrogen, chlorine and oxygen donor atoms at Fe(1), in agreement with Barton's structure. In molecule II the chloride ligands retain their *cis* disposition but the oxygen atoms are *cis*- to one another. The structural parameters for the anion in [pyH][Fe(pic)₂Cl₂] [Fe-Cl 2.2814(14)-2.3129(14), Fe-O 1.969(3)-2.048(3), Fe-N 2.172(4)-2.216(4) Å] are similar to those in

[py₂H][Fe(pic)₂Cl₂] [2.308(1), 1.996(2) and 2.199(3) Å].⁶ The *cis*- angles at iron [75.92(14)-102.13(9)^o, 76.05(15)-100.77(11)^o in molecules I, II] resemble [Fe(pic)₃] [78.16(10)-101.04(10)^o], the *trans*- angles being 163.70(12)-166.43(11)^o [156.86(14)-173.16(11)^o for molecule II].

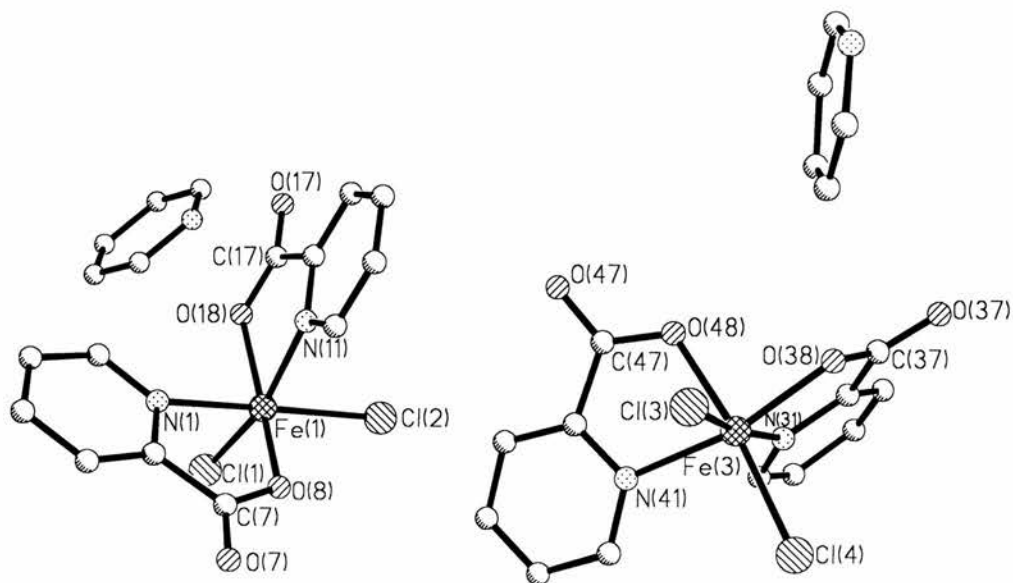


Figure 2.2: Molecular structure of [pyH][Fe(pic)₂Cl₂] (hydrogen atoms omitted for clarity).

Table 2.2: Selected bond lengths (Å) and angles (°) for [pyH][Fe(pic)₂Cl₂] (esd's in parentheses).

Molecule I			
Fe(1)-O(8)	1.991(3)	Fe(1)-O(18)	2.017(3)
Fe(1)-N(1)	2.189(4)	Fe(1)-N(11)	2.198(4)
Fe(1)-Cl(1)	2.2878(14)	Fe(1)-Cl(2)	2.3129(14)
O(7)-C(7)	1.228(6)	C(7)-O(8)	1.303(5)
O(8)-Fe(1)-O(18)	163.70(12)	O(8)-Fe(1)-N(1)	77.50(14)
O(18)-Fe(1)-N(1)	92.33(14)	O(8)-Fe(1)-N(11)	90.30(14)
O(18)-Fe(1)-N(11)	75.92(14)	N(1)-Fe(1)-N(11)	84.58(13)
O(8)-Fe(1)-Cl(1)	102.13(9)	O(18)-Fe(1)-Cl(1)	90.83(9)
N(1)-Fe(1)-Cl(1)	92.15(10)	N(11)-Fe(1)-Cl(1)	166.17(12)
O(8)-Fe(1)-Cl(2)	92.09(10)	O(18)-Fe(1)-Cl(2)	95.75(10)
N(1)-Fe(1)-Cl(2)	166.43(11)	N(11)-Fe(1)-Cl(2)	86.83(11)
Cl(1)-Fe(1)-Cl(2)	98.60(5)	O(7)-C(7)-O(8)	124.7(5)

Molecule II			
Fe(3)-O(38)	1.969(3)	Fe(3)-O(48)	2.048(3)
Fe(3)-N(41)	2.172(4)	Fe(3)-N(31)	2.216(4)
Fe(3)-Cl(3)	2.2814(14)	Fe(3)-Cl(4)	2.2926(15)
O(17)-C(17)	1.239(6)	C(17)-O(18)	1.269(5)
O(38)-Fe(3)-O(48)	86.83(14)	O(38)-Fe(3)-N(41)	156.86(14)
O(48)-Fe(3)-N(41)	76.05(15)	O(38)-Fe(3)-N(31)	77.04(14)
O(48)-Fe(3)-N(31)	86.88(14)	N(41)-Fe(3)-N(31)	86.46(14)
O(38)-Fe(3)-Cl(3)	96.91(10)	O(48)-Fe(3)-Cl(3)	89.62(10)
N(41)-Fe(3)-Cl(3)	98.40(10)	N(31)-Fe(3)-Cl(3)	173.16(11)
O(38)-Fe(3)-Cl(4)	100.77(11)	O(48)-Fe(3)-Cl(4)	169.50(10)
N(41)-Fe(3)-Cl(4)	94.61(12)	N(31)-Fe(3)-Cl(4)	87.77(11)
Cl(3)-Fe(3)-Cl(4)	96.59(5)	O(17)-C(17)-O(18)	126.2(5)

Although it is curious that two isomers of $[\text{Fe}(\text{pic})_2\text{Cl}_2]^-$ are generated by chlorination of $[\text{Fe}(\text{pic})_2(\text{py})_2]$ whereas one was available from iron(III) chloride hexahydrate, it is equally notable that no other isomers (e.g. *trans*-chloride ligands) co-crystallise. In the product from chlorination, this may reflect the existence of more than one structural isomer of $[\text{Fe}(\text{pic})_2(\text{py})_2]$, a molecule which has hitherto eluded crystallographic characterisation. It should be noted that both $[\text{Fe}(\text{pic})_2(\text{MeOH})_2]$ and $[\text{Fe}(\text{pic})_2(\text{H}_2\text{O})_2]$ are centrosymmetric,^{4,5} *i.e.* with a *trans,trans,trans*-configuration of nitrogen, carboxylate oxygen and OH donors at iron. $[\text{pyH}][\text{Fe}(\text{pic})_2(\text{py})_2]$ is soluble in acetonitrile and dichloromethane, although the deposition of an unidentified red material when acetonitrile solutions of the complex are left exposed to air for several days hints at some sensitivity to aerobic conditions. While $[\text{Fe}(\text{pic})_2\text{Cl}_2]^-$ is expected to be a good synthon for mixed ligand complexes following metathetical exchange of the chloro ligands, time constraints prevented further investigations in this direction.

2.2.3 Crystal Structure of $[\text{Fe}_2(\mu_2\text{-OMe})_2(\text{pic})_4]$

The μ_2 -methoxy bridged diiron(III) complex $[\text{Fe}_2(\mu_2\text{-OMe})_2(\text{pic})_4]$ was prepared and crystallised directly from the reaction of $[\text{Fe}(\text{pic})_2(\text{py})_2]$ with methanol in air, and its structure determined by X-ray crystallography (Figure 2.3). Stavropoulos⁴ has also reported this complex although several differences exist between their preparation and ours. Stavropoulos isolated yellow-green crystals of the complex by dissolving $[\text{Fe}_2(\mu_2\text{-OH})_2(\text{pic})_4]$ in methanol and slowly crystallising at room temperature, whereas our material is yellow-orange in colour. In the structure obtained by Stavropoulos the pic⁻ ligands have a *trans*- geometry of the nitrogen donors with the Fe-O_{pic} bonds *trans*- to the μ_2 -methoxy bridges. In our structure at Fe(2) the nitrogen atoms N(21) and N(31) are in a *trans*- configuration whereas at Fe(1) it is the oxygen atoms O(8) and O(18) which have a *trans*- orientation. Overall our complex possesses a pseudo C₂ symmetry axis through the Fe(1)...Fe(2) vector whereas Stavropoulos' complex is centrosymmetric. The bond lengths and angles in our structural determination must be treated with some caution in view of the high *R* factor (14.3 %). The Fe-O_{pic} and Fe-O_{methoxy} lengths are in the range 1.918(7)-2.044(6) Å, exceptionally Fe(2)-O(38) is 2.3621(16) Å, *c.f.* 1.9681(18)-1.9830(15) Å for Stavropoulos' isomer. The Fe-N lengths are 2.090(8)-2.148(7) Å, with the shorter values for nitrogen *trans*- to methoxy, *c.f.* 2.162(2)-2.172(2) Å for the centrosymmetric complex. Within the $\text{Fe}_2(\mu_2\text{-OMe})_2$ metallacycle, the O(9)-Fe-O(10) [78.0(3)^o for Fe(1), 76.0(2)^o for Fe(2)] and Fe(1)-O-Fe(2) [102.5(2)^o for O(9), 103.4(3)^o for O(10)] angles agree with literature values [75.73(11)^o and 76.43(11)^o, 103.57(11)^o and 104.27(11)^o]. The iron centres have a distorted octahedral geometry with *trans*-O(8)-Fe(1)-O(18) and N(21)-Fe(2)-N(31) angles of 163.9(3)^o and 162.3(3)^o. The (N-Fe-O)_{chelate} bite angles are *ca.* 78^o for the N(1), N(11) and N(21) chelates but 81.7(2)^o for the N(31) chelate.

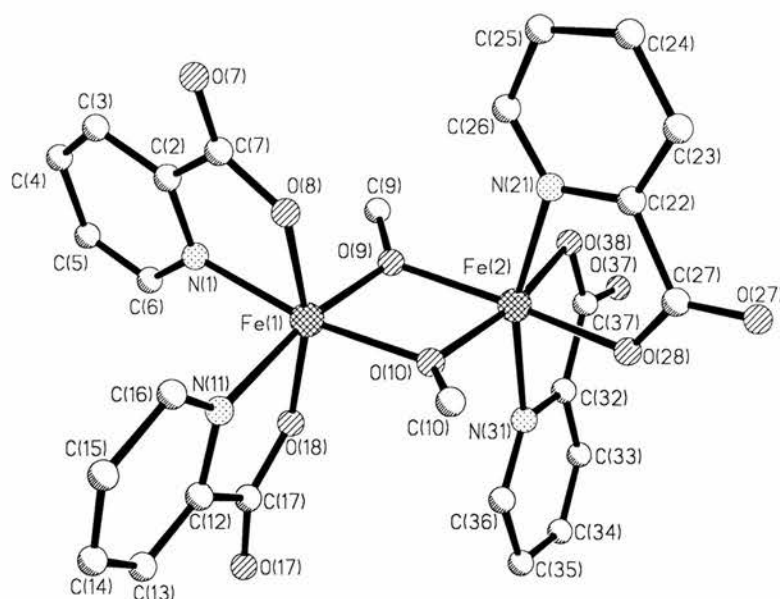


Figure 2.3: Molecular structure of $[\text{Fe}_2(\mu_2\text{-OMe})_2(\text{pic})_4]$ (C-H bonds omitted for clarity).

Table 2.3: Selected bond lengths (Å) and angles ($^\circ$) for $[\text{Fe}_2(\mu_2\text{-OMe})_2(\text{pic})_4]$ (esd's in parentheses).

Fe(1)-O(9)	1.927(6)	Fe(1)-O(18)	1.977(6)
Fe(1)-O(8)	1.993(6)	Fe(1)-O(10)	1.989(7)
Fe(1)-N(1)	2.090(8)	Fe(1)-N(11)	2.115(8)
Fe(2)-O(28)	1.918(7)	Fe(2)-O(10)	1.959(6)
Fe(2)-O(9)	2.044(6)	Fe(2)-N(21)	2.143(7)
Fe(2)-N(31)	2.148(7)	Fe(2)-O(38)	2.3621(16)
O(9)-Fe(1)-O(18)	93.1(3)	O(9)-Fe(1)-O(8)	98.9(3)
O(18)-Fe(1)-O(8)	163.9(3)	O(9)-Fe(1)-O(10)	78.0(3)
O(18)-Fe(1)-O(10)	94.5(3)	O(8)-Fe(1)-O(10)	98.4(3)
O(9)-Fe(1)-N(1)	93.7(3)	O(18)-Fe(1)-N(1)	90.5(3)
O(8)-Fe(1)-N(1)	78.2(3)	O(10)-Fe(1)-N(1)	170.6(3)
O(9)-Fe(1)-N(11)	169.9(3)	O(18)-Fe(1)-N(11)	78.2(3)
O(8)-Fe(1)-N(11)	90.6(2)	O(10)-Fe(1)-N(11)	97.3(3)
N(1)-Fe(1)-N(11)	91.5(3)	O(28)-Fe(2)-O(10)	93.0(3)

O(28)-Fe(2)-O(9)	167.8(3)	O(10)-Fe(2)-O(9)	76.0(2)
O(28)-Fe(2)-N(21)	78.3(3)	O(10)-Fe(2)-N(21)	94.1(3)
O(9)-Fe(2)-N(21)	96.9(3)	O(28)-Fe(2)-N(31)	86.1(3)
O(10)-Fe(2)-N(31)	94.9(3)	O(9)-Fe(2)-N(31)	100.0(3)
N(21)-Fe(2)-N(31)	162.3(3)	O(28)-Fe(2)-O(38)	102.2(2)
O(10)-Fe(2)-O(38)	164.02(19)	O(9)-Fe(2)-O(38)	89.15(17)
N(21)-Fe(2)-O(38)	93.5(2)	N(31)-Fe(2)-O(38)	81.7(2)
Fe(1)-O(9)-Fe(2)	102.5(2)	Fe(2)-O(10)-Fe(1)	103.4(3)

We were unable to prepare the analogous μ_2 -ethoxy diiron(III) complex $[\text{Fe}_2(\mu_2\text{-OEt})_2(\text{pic})_4]$ from ethanol under similar conditions. The difference in behaviour between the two alcohols may arise from the greater nucleophilic character of methanol compared to ethanol.

2.2.4 Summary and Conclusions

The chlorination of $[\text{Fe}(\text{pic})_2(\text{py})_2]$ provides a facile route to $[\text{Fe}(\text{pic})_2\text{Cl}_2]^-$, which hitherto has been difficult to synthesise. A new generation of mixed ligand complexes should be readily accessible from these two materials, enabling further investigations into both mechanistic details and Gif oxygenation activities of iron-picolinate complexes. The isolation of $[\text{Fe}_2(\mu_2\text{-OMe})_2(\text{pic})_4]$ from $[\text{Fe}(\text{pic})_2(\text{py})_2]$ suggests that reactions with mildly acidic substrates such as thiols or amines may lead to thiolate or amide complexes.

2.2.5 Experimental Section

General experimental conditions and instrumentation details are as described previously. $[\text{Fe}(\text{pic})_2]_n$, $[\text{Fe}(\text{pic})_3]$, $[\text{Fe}(\text{pic})_2(\text{py})_2]$ and $[\text{Fe}(\text{pic})_2(\text{H}_2\text{O})_2]$ were prepared by literature methods.⁴

$[\text{Fe}(\text{pic})_2]_n$: Iron powder (0.16 g, 2.86 mmol) and Hpic (0.66 g, 5.4 mmol) were stirred in dichloromethane (50 cm³) for four days under argon. The red solution

was filtered under argon to remove excess iron, addition of diethyl ether to the filtrate precipitated $[\text{Fe}(\text{pic})_2]_n$ as a red powder. Yield 0.55 g (65 %). Found (calc. for $\text{C}_{12}\text{H}_8\text{FeN}_2\text{O}_4$): C 49.64 (48.04), H 3.03 (2.69), N 9.69 (9.34) %.

[Fe(pic)₃]: Under aerobic conditions, Hpic (0.92 g, 7.41 mmol) was added to iron(III) nitrate nonahydrate (1.0 g, 2.48 mmol) in methanol (50 cm³), giving a pale green solution. The product was precipitated as a pale green powder by addition of diethyl ether (200 cm³). The complex was stored in the dark. Yield 0.72 g (68 %). Crystals suitable for X-ray analysis were grown from methanol under a dinitrogen atmosphere in the dark. Found (calc. for $\text{C}_{18}\text{H}_{12}\text{FeN}_3\text{O}_6$): C 51.18 (50.85), H 2.80 (2.86), N 9.82 (9.95) %. Selected IR bands (cm⁻¹): 1678s, 1327s (ν_{COO}).

In light, solid $[\text{Fe}(\text{pic})_3]$ turns yellow over 48 h. Microanalysis is in reasonable agreement for a trihydrate. Found (calc. for $\text{C}_{18}\text{H}_{12}\text{FeN}_3\text{O}_6 \cdot 3\text{H}_2\text{O}$): C 44.96 (45.40), H 2.57 (3.81), N 8.64 (8.84) %. Selected IR bands (cm⁻¹): 3222m,br (ν_{OH}), 1677s, 1340s (ν_{COO}).

[Fe(pic)₂(py)₂]: Iron powder (0.56 g, 10 mmol) and Hpic (2.6 g, 20 mmol) were suspended in pyridine (50 cm³) and heated at 110 °C for 1 h under argon. Unreacted iron powder was filtered off anaerobically and diethyl ether (100 cm³) was added to precipitate $[\text{Fe}(\text{pic})_2(\text{py})_2]$ as a red solid, which was collected by filtration under argon. Yield 3.44 g (75 %). Found (calc. for $\text{C}_{22}\text{H}_{18}\text{FeN}_4\text{O}_4$): C 59.38 (57.66), H 3.92 (3.96), N 12.62 (12.22) %. Selected IR bands (cm⁻¹): 1645s, 1348m (ν_{COO}).

[Fe₂(μ_2 -OMe)₂(pic)₄]: A solution of iron(II) bis(picolate) bis(pyridine) (150 mg, 0.33 mmol) was dissolved in methanol (10 cm³), giving an orange solution. Diethyl ether was added until the onset of cloudiness and the solution was cooled to -20 °C overnight, giving orange crystals. Yield 0.51 g (70 %). Found (calc. for $\text{C}_{26}\text{H}_{22}\text{FeN}_4\text{O}_{10} \cdot 2\text{H}_2\text{O}$): C 44.72 (44.73), H 3.41 (3.75), N 7.85 (8.02) %. Selected IR bands (cm⁻¹): 1674s, 1336s (ν_{COO}).

[Fe(pic)₂(H₂O)₂]: Hpic (1.24 g, 10.0 mmol) was added to iron(II) chloride tetrahydrate (1.0 g, 5.0 mmol) in methanol (20 cm³) and the solution stirred for 0.5 h. Addition of diethyl ether (100 cm³) precipitated the product as a brick red solid. Yield 1.39 g (72 %). Found (calc. for C₁₂H₁₂FeN₂O₆): C 42.84 (42.88), H 3.28 (3.60), N 8.20 (8.33) %. Selected IR bands (cm⁻¹): 3413m (ν_{OH}), 1717m (δ_{OH}), 1631s, 1346m (ν_{COO}).

[pyH][Fe(pic)₂Cl₂]: Dichlorine gas was passed slowly (approximately one bubble per second) over a solution of iron(II) bis(picolate) bis(pyridine) (1.00 g, 2.18 mmol) in dichloromethane (40 cm³) until the solution changed colour from red to yellow (*ca.* 2 h). The solvent was removed *in vacuo*, the yellow residue was extracted into acetonitrile (20 cm³), addition of diethyl ether (50 cm³) gave a yellow solid. Yield 0.54 g (55 %). Crystals suitable for X-ray analysis were grown by vapour diffusion of diethyl ether into an acetonitrile solution of the complex. Found (calc. for C₁₇H₁₄Cl₂FeN₃O₄): C 45.19 (45.27), H 3.13 (2.96), N 8.70 (9.31) %. Selected IR bands (cm⁻¹): 2856m,br (ν_{NH}), 1671s, 1334s (ν_{COO}). ES MS: The sample was only weakly ionised in ES negative ionisation mode, no peaks could be assigned with certainty.

2.3 Kinetic Studies of Iron(II,III)-Hydrogen Peroxide Systems

In this Section we describe time-dependent (kinetic) investigations of the reactions of $[\text{Fe}(\text{pic})_3]$ and $[\text{Fe}(\text{pic})_2(\text{H}_2\text{O})_2]$ under GoAgg conditions with hydrogen peroxide in pyridine using UV-visible spectrophotometry. These reactions have been followed at two wavelengths (430 and 520 nm) over time periods ranging from a few minutes to several hours. A number of kinetically stable intermediates have been detected and their relevance to the processes involved in the assembly of the active GoAgg (Gif) catalyst has been monitored by carrying out the kinetics in the presence and absence of cyclohexane and by comparing with the time of appearance of the oxygenated products (cyclohexanone and cyclohexanol) from previous studies.

2.3.1 Experimental Section

A stock solution of $[\text{Fe}(\text{pic})_3]$ was prepared by dissolution of the pale green-yellow solid in pyridine to give an initial concentration of $5 \times 10^{-3} \text{ mol dm}^{-3}$, which was diluted a further tenfold with pyridine ($5 \times 10^{-4} \text{ mol dm}^{-3}$). Solutions were freshly prepared and stored in the dark for not longer than three days. After this time solutions became darker in colour due to further (as yet unidentified) reactions with pyridine and/or water. Aqueous solutions of 30 % w/w hydrogen peroxide were standardised by titration with cerium(III) sulfate or potassium permanganate solutions as described in Vogel.⁸ The concentration was found to be 9.46 mol dm^{-3} . Using a Shimadzu W-2101 PC UV-vis scanning spectrophotometer and a thermostatically controlled Lauda RM6 water bath we measured the absorbance of a 3.0 cm^3 aliquot of $[\text{Fe}(\text{pic})_3]$ solution over the range 300-900 nm with varying concentrations of hydrogen peroxide in 1 cm path length quartz cuvettes. The kinetics carried out under pseudo first order conditions with > 40 fold excess of hydrogen peroxide ($0.016\text{-}0.124 \text{ mol dm}^{-3}$) over $[\text{Fe}(\text{pic})_3]$ ($5 \times 10^{-4} \text{ mol dm}^{-3}$), were studied by conventional means and initiated by the injection of 5-40 μl aliquots of the hydrogen peroxide solution into the $[\text{Fe}(\text{pic})_3]$ solution placed in the thermostatted cuvettes.

The reaction of $[\text{Fe}(\text{pic})_3]$ ($5 \times 10^{-4} \text{ mol dm}^{-3}$) with a 165 fold excess of hydrogen peroxide was initially monitored at 5°C in order to obtain time-resolved scanned spectra between 300 and 900 nm using two minute time intervals. A typical overlay plot is shown in Figure 2.4. The initially yellow solution of $[\text{Fe}(\text{pic})_3]$ in pyridine rapidly became a dark brownish-purple colour characterised by a peak at *ca* 530 nm. After twelve minutes a second process was evident, characterised by an isosbestic point at 520 nm. Thereafter a further rise in absorbance over the entire wavelength range characterised much slower changes resulting in a deep yellow-brown final solution after 12 hrs. At room temperature the slower changes were accompanied by the evolution of dioxygen. For the detailed kinetic study, two fixed wavelengths were chosen for monitoring, 430 nm (away from the isosbestic point) and 520 nm. A preliminary investigation revealed that the rapid initial changes surrounding the isosbestic point could be followed at 20°C using time intervals of two seconds.

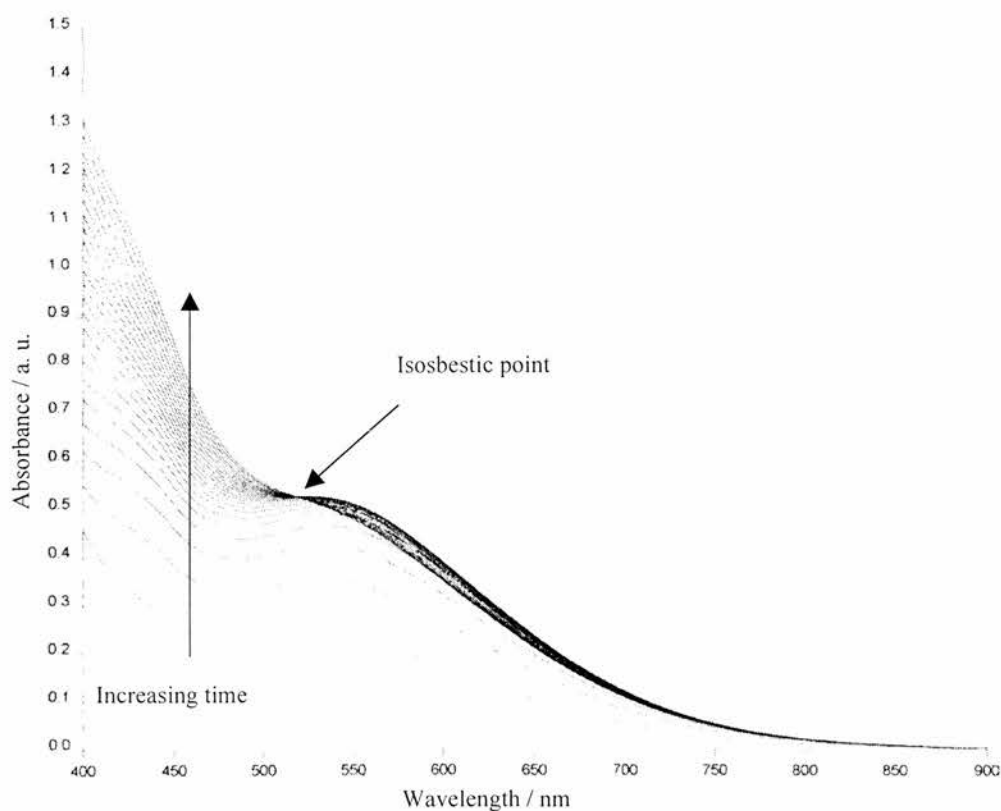


Figure 2.4: Time resolved spectra ($\Delta t = 2 \text{ mins}$) for reaction of $[\text{Fe}(\text{pic})_3]$ ($5 \times 10^{-4} \text{ mol dm}^{-3}$) with 165 fold excess hydrogen peroxide in pyridine at 5°C .

At each of the two wavelengths used the early stages of the absorbance vs time plots exhibited first order behaviour and could be fitted to either one or two successive exponentials using a non-linear least squares fitting procedure provided by the Grafit Software program⁹, which uses the standard Marquardt algorithm. For the fit to a single exponential, the simple first order equation 2.1 was employed,

$$A_t = A[1-\exp(-kt)] + A_0 \quad (2.1)$$

where A_t is the absorbance at time t , A and k represent respectively the extent of absorbance change and rate constant for the single stage and A_0 is the absorbance at $t = 0$. For the fit to two exponentials equation 2.2 was employed

$$A_t = A_1[1-\exp(-k_1t)] + A_2[1-\exp(-k_2t)] + A_0 \quad (2.2)$$

where A_1 and A_2 represent the extent of absorbance change for the first and second stages respectively, and k_1 and k_2 are the successive first order rate constants. Since the end of the second stage is not fully defined due to subsequent reactions, evaluation of the parameters in equation 2.2 was achieved by first fixing values for A_1 and k_1 based on data gathered at 520 nm wherein only the first stage contributes and letting the programme calculate values for A_2 , k_2 and A_0 representing the best fit to the data (lowest value of χ^2). The fixed values of A_1 and k_1 were then each varied in succession until χ^2 was further minimised. Values of A_1 , k_1 , A_2 , k_2 and A_0 were then tabulated as a function of the hydrogen peroxide concentration present.

[Fe(pic)₂(H₂O)₂] was also studied as added iron complex under the same conditions *i.e.* [Fe] = 5 x 10⁻⁴ mol dm⁻³, [H₂O₂] = 0.016–0.124 mol dm⁻³, T = 10 °C in pyridine. Initial experiments showed a change in colour from a red/ orange coloured solution [Fe(pic)₂(py)₂] to a pale yellow iron(III) solution when hydrogen peroxide was added to the iron(II) aqua complex dissolved in pyridine, with the formation of a purple colour only becoming apparent after *ca.* a few minutes. Here the colour changes may be attributed to the formation of iron(III)

as a result of Fenton chemistry. The subsequent purple species appeared analogous to that obtained when using $[\text{Fe}(\text{pic})_3]$ but here the isosbestic point was not fixed. The general trend was found to be with increased concentration of hydrogen peroxide the isosbestic point experiences a bathochromic shift. This is assumed to arise from multiple reaction pathways leading to several products, each with its own characteristic λ_{max} and half-life.

The same “shifting isosbestic point” phenomenon also occurred with $[\text{Fe}_2(\mu_2\text{-OMe})_2(\text{pic})_4]$, where $[\text{Fe}] = 5 \times 10^{-4} \text{ mol dm}^{-3}$, $[\text{H}_2\text{O}_2] = 0.032$ and $0.064 \text{ mol dm}^{-3}$ and $T = 10 \text{ }^\circ\text{C}$. Due to time constraints these iron(II,III)-picolinate systems were not studied further in this work.

2.3.2 Results and Discussion

The Reaction of $[\text{Fe}(\text{pic})_3]$ with Hydrogen Peroxide

Kinetics were carried out on the $[\text{Fe}(\text{pic})_3]$ reaction with varying concentrations of hydrogen peroxide in the presence (or absence) of 0.5 equivalents of cyclohexane/hydrogen peroxide, at 520 nm over a period of thirty mins at $20 \text{ }^\circ\text{C}$ and over longer periods (hours). The absorbance vs. time plots as a function of hydrogen peroxide concentration at the isosbestic point (520 nm) over a 10 min period are shown in Figure 2.5. There is a delay of approximately five seconds between the addition of hydrogen peroxide and commencement of the spectroscopic measurement. The effect on the absorbance at $t = 0$ is most pronounced at higher concentrations, however the intercept on the absorbance axis is not critical to the determination of the pseudo first-order rate constant.

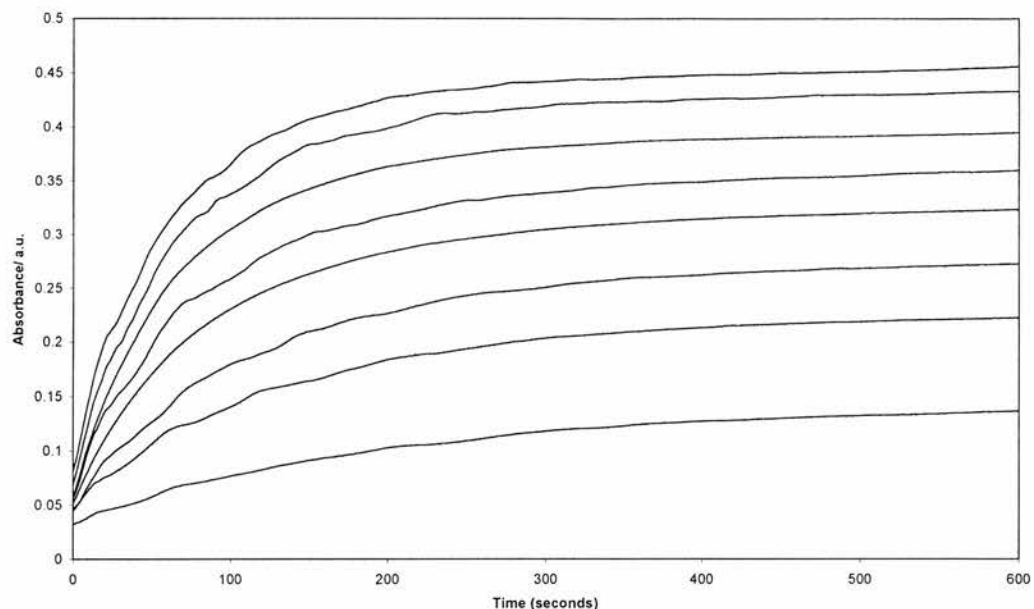


Figure 2.5: Absorbance vs time trace at 520 nm, $[\text{Fe}] = 5 \times 10^{-4} \text{ mol dm}^{-3}$, $[\text{H}_2\text{O}_2] = 0.016 - 0.124 \text{ mol dm}^{-3}$, $T = 20 \text{ }^\circ\text{C}$.

Figure 2.6 shows the absorbance vs time traces at 520 nm when 0.5 equivalents of cyclohexane with respect to $[\text{H}_2\text{O}_2]$ was added. Again we see very similar trends at this stage as when the cyclohexane is absent, *i.e.* the absorbance changes with time are largely unaffected by the addition of the hydrocarbon.

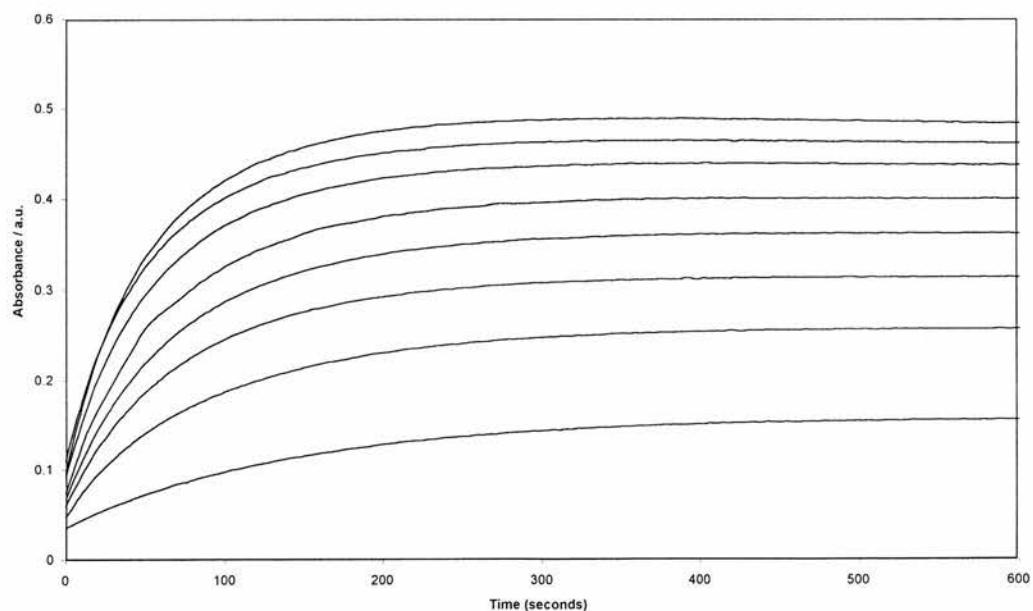


Figure 2.6: Absorbance vs time trace at 520 nm with cyclohexane ($0.006 - 0.062 \text{ mol dm}^{-3}$) added: $[\text{Fe}] = 5 \times 10^{-4} \text{ mol dm}^{-3}$, $[\text{H}_2\text{O}_2] = 0.016 - 0.124 \text{ mol dm}^{-3}$, $T = 20 \text{ }^\circ\text{C}$.

The curves in Figures 2.5 and 2.6 have first-order kinetic profiles over the first ten minutes, from which the pseudo first-order rate constant (k_{obs}) for the formation of the initial iron(III) product can be calculated.

The absorbance rise at 520 nm (isosbestic point) for runs both with and without the addition of cyclohexane were fitted to the single exponential function (equation 2.1) allowing values of k_{obs} to be obtained as a function of $[\text{H}_2\text{O}_2]$. The data are collected in Table 2.4 and plotted in Figure 2.7. The extent of absorbance change also increases with $[\text{H}_2\text{O}_2]$ with evidence of saturation in the A_∞ value at higher $[\text{H}_2\text{O}_2]$. Taken together, these findings suggest a first order reversible equilibration reaction with the slope of Figure 2.7 characterising the forward reaction rate constant k_1 and the intercept, the back reaction rate constant, k_{-1} , equations 2.3 and 2.4.



$$k_{\text{obs}} = k_1[\text{H}_2\text{O}_2] + k_{-1} \quad (2.4)$$

Values of k_1 and k_{-1} in the presence and absence of cyclohexane are listed in Table 2.5. It is concluded that there is little or no significant effect of adding the substrate during this stage of the reaction.

Table 2.4: Kinetic data for [Fe(pic)₃]-hydrogen peroxide system at 520 nm.^a

[H ₂ O ₂] (mol dm ⁻³)	k _{1obs} (avg)/ s ⁻¹	A _∞	k _{1obs} (avg) / s ⁻¹ (+ c-C ₆ H ₁₂)	A _∞ (+ c-C ₆ H ₁₂)
0.016	0.00465	0.1356	0.00560	0.1509
0.031	0.00670	0.2226	0.00835	0.24465
0.047	0.00830	0.2746	0.01030	0.3037
0.063	0.00990	0.3231	0.01095	0.3533
0.078	0.01090	0.3585	0.01205	0.49145
0.094	0.01255	0.3968	0.01295	0.43415
0.109	0.01345	0.43075	0.01420	0.458
0.124	0.01545	0.44975	0.01515	0.4799

^a [Fe(pic)₃] = 5 × 10⁻⁴ mol dm⁻³, T = 20 °C. All points are averaged over two runs

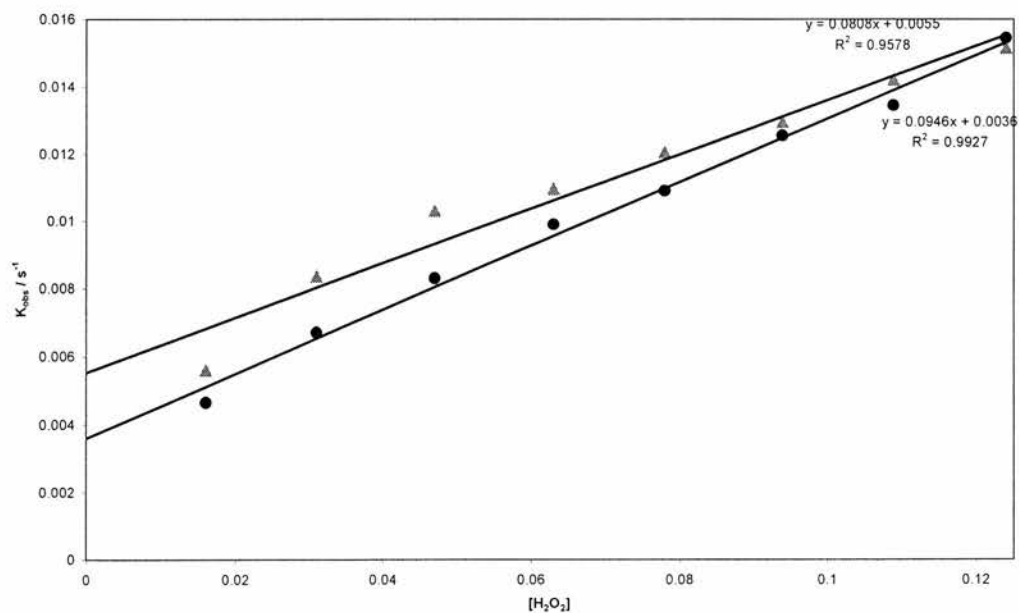


Figure 2.7: Plot of k_{obs} vs [H₂O₂] for [Fe(pic)₃]-hydrogen peroxide system at 520 nm in the presence and absence of cyclohexane (triangles represent data with cyclohexane added, filled circles are data without cyclohexane).

Table 2.5: Values of k_1 and k_{-1} for $[\text{Fe}(\text{pic})_3]$ -hydrogen peroxide system at 520 nm.

Constant		(+ <i>c</i> -C ₆ H ₁₂)
k_1 (dm ³ mol ⁻¹ s ⁻¹)	0.0946	(0.0808)
k_{-1} (s ⁻¹)	0.0036	(0.0055)

During retention of the isosbestic point at 520 nm, a second process is seen which results in fading of the absorption maximum at 530 nm for the first intermediate to give a shoulder at *ca.* 500 nm and a general increase in the absorbance below 520 nm. It was decided to monitor the reaction at 430 nm in order to obtain data characterising this second process.

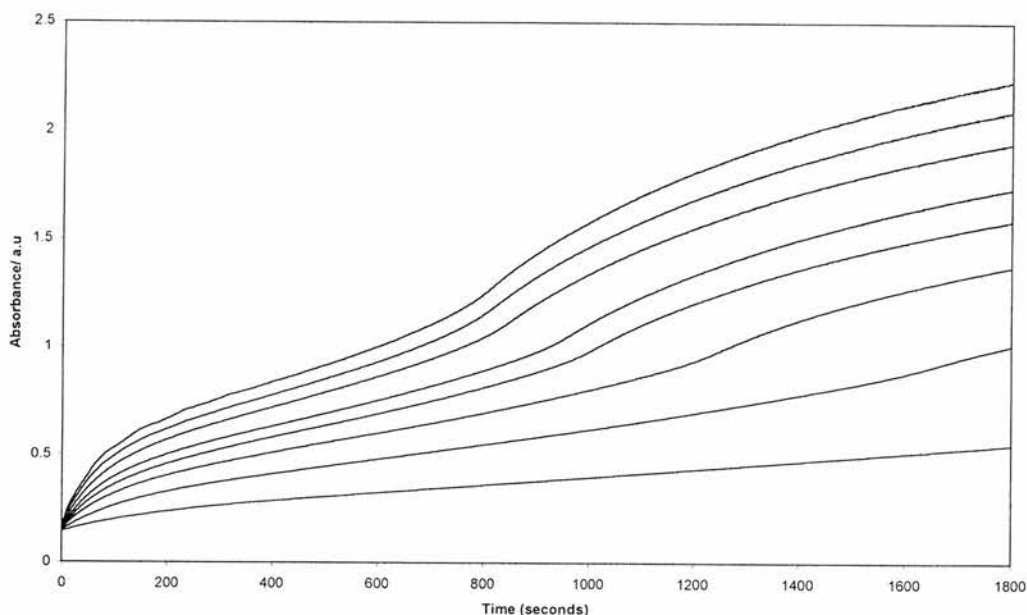


Figure 2.8: Absorbance vs. time trace for $[\text{Fe}] = 5 \times 10^{-4} \text{ mol dm}^{-3}$, $[\text{H}_2\text{O}_2] = 0.016 - 0.124 \text{ mol dm}^{-3}$, $T = 20 \text{ }^\circ\text{C}$ at 430 nm.

Figure 2.8 shows absorbance at 430 nm plotted as a function of time (secs) over the first 30 mins of the reaction for $[\text{H}_2\text{O}_2] = 0.016\text{--}0.124 \text{ mol dm}^{-3}$. Each run shows evidence of a complex series of stages. An initial relatively rapid rise over the first 1-2 mins is followed by a slower rise over the next 10 mins. Thereafter the behaviour becomes somewhat more complex. It was found that the initial two stages could be fitted successfully to two successive exponentials

using equation 2.2. The first stage was shown by the iterative treatment described above to correspond to the same process resulting in the formation and retention of the isosbestic point at 520 nm. This evidence of a first order equilibration was found to depend linearly on $[\text{H}_2\text{O}_2]$. The slower second process, however, was shown to be independent of $[\text{H}_2\text{O}_2]$. For both processes the extent of absorbance change (A_∞ value) increased with $[\text{H}_2\text{O}_2]$ but showing evidence of saturation at higher $[\text{H}_2\text{O}_2]$. These are the classic hallmarks of equilibration processes. Rate constants ($k_{\text{obs}}/\text{s}^{-1}$) obtained at 430 nm as a function of $[\text{H}_2\text{O}_2]$ are listed in Table 2.5 and plotted in Figure 2.9. Figure 2.9 illustrates the independence of the second process on $[\text{H}_2\text{O}_2]$. Thus it can be concluded that the isosbestic point involves a further reaction taking place once initial reaction with hydrogen peroxide is complete. Values for k_1 and k_{-1} (for the first stage) and k_2 (for the second stage) for the data obtained at 430 nm are listed in Table 2.6.

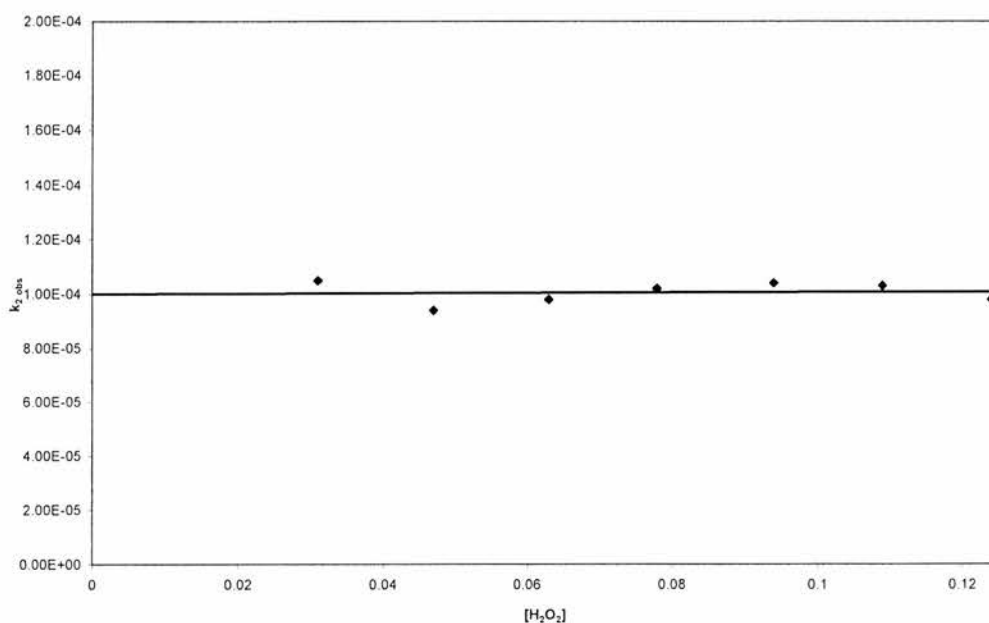


Figure 2.9: Plot of $k_{2(\text{obs})}$ vs $[\text{H}_2\text{O}_2]$ for $[\text{Fe}] = 5 \times 10^{-4} \text{ mol dm}^{-3}$, $[\text{H}_2\text{O}_2] = 0.016 - 0.124 \text{ mol dm}^{-3}$, $T = 20 \text{ }^\circ\text{C}$ at 430 nm

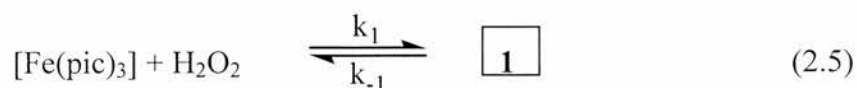
Table 2.6: Kinetic data at 430 nm for the reaction of [Fe(pic)₃] (5 × 10⁻⁴ mol dm⁻³) with excess hydrogen peroxide in pyridine at 20 °C

[H ₂ O ₂]/ mol dm ⁻³	k _{1(obs)} /s ⁻¹	A _∞	k _{2(obs)} /s ⁻¹	A _∞	χ ²
0.016	5.4 × 10 ⁻³	0.23	-	-	-
0.031	7.2 × 10 ⁻³	0.31	1.05 × 10 ⁻⁴	2.70	9.24 × 10 ⁻⁷
0.047	8.8 × 10 ⁻³	0.36	9.75 × 10 ⁻⁵	4.34	6.21 × 10 ⁻⁶
0.063	11.2 × 10 ⁻³	0.38	9.75 × 10 ⁻⁵	5.39	4.33 × 10 ⁻⁶
0.078	13.0 × 10 ⁻³	0.41	1.02 × 10 ⁻⁴	5.73	2.83 × 10 ⁻⁶
0.094	13.9 × 10 ⁻³	0.46	1.04 × 10 ⁻⁴	6.67	1.13 × 10 ⁻⁶
0.109	14.7 × 10 ⁻³	0.50	1.03 × 10 ⁻⁴	6.94	4.64 × 10 ⁻⁶
0.124	15.7 × 10 ⁻³	0.53	9.77 × 10 ⁻⁵	8.15	9.14 × 10 ⁻⁶

Table 2.7: Kinetic data for the reaction of [Fe(pic)₃] (5 × 10⁻⁴ mol dm⁻³) with excess hydrogen peroxide in pyridine at 20 °C followed at 430 nm

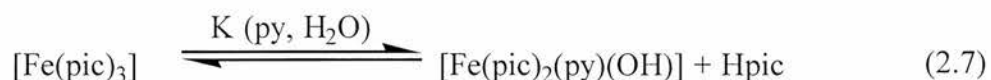
Constant	Value
k ₁	(9.74 ± 0.66) × 10 ⁻² dm ³ mol ⁻¹ s ⁻¹
k ₋₁	(4.39 ± 0.52) × 10 ⁻³ s ⁻¹
k ₂	(1.001 ± 0.054) × 10 ⁻⁴ s ⁻¹

The kinetic data presented above are consistent with the reaction scheme in equations 2.5 and 2.6.



In order to test further the process that may be involved in the formation of **1** and its subsequent reaction to give **2**, runs were also conducted in the presence of a tenfold excess of Hpic. If loss of pic⁻ was a process taking place prior to the rate determining formation of **1** a decrease in the observed reaction rate constant k₁

would be expected at each concentration of hydrogen peroxide. The results of this study are shown in Figure 2.10. There is clear evidence that the initial stage of reaction is now much slower with the rate of the second stage largely unaffected. This result suggests that the first stage of reaction is accompanied by the reversible loss of pic⁻ prior to the rate determining step with hydrogen peroxide. A possible scheme is outlined in equations 2.7 and 2.8 .



$$\text{Rate} = k_{\text{obs}}[\text{Fe}]_{\text{T}} \quad (2.9)$$

If all of the subsequent reactions go *via* the iron(III) bis(picolate) complex then expression 2.10 for k_{obs} is relevant:

$$k_{\text{obs}} = \left(\frac{k_1 K [\text{H}_2\text{O}_2]}{[\text{Hpic}] + K} \right) + k_{-1} \quad (2.10)$$

A full explanation of the derivations of the above equations is given in Appendix Two.

The observation that increasing [Hpic] decreases k_{obs} for each concentration of hydrogen peroxide studied suggests that, qualitatively, K is smaller or within an order of magnitude to [Hpic]. Further evidence of a reaction of $[\text{Fe}(\text{pic})_3]$ with pyridine- H_2O prior to reduction with hydrogen peroxide comes from studies of the electronic spectrum of $[\text{Fe}(\text{pic})_3]$ in various solvents. Freshly prepared crystals of $[\text{Fe}(\text{pic})_3]$ are pale green in the solid state and dissolve in methanol to give a bright green coloured solution. In pyridine, however, the crystals dissolve to give a distinctly yellow solution, the intensity of which becomes weaker in the presence of a tenfold excess of Hpic (see value of absorbance at $t = 0$ in Figure 2.10 compared to Figure 2.6). It is thus concluded that a pyridine solvated

iron(III)-bis(picolinato) complex is probably formed by rapid pyridine and/or water (HO^-) solvation and is a strong candidate for the species that reacts with hydrogen peroxide to give **1**. The involvement of pyridine in this reaction is noted given its importance to the overall Gif oxygenating reactivity. In order to establish whether the Hpic effect was a generalised acid effect, runs were also conducted in the presence of a tenfold excess of *p*-toluenesulfonic acid. A similar retardation effect was seen although here a completely different absorbance–time profile was observed. Here the retardation effect could reflect protonation of the pyridine and suppression of its ability to displace Hpic in the initial step. As the rate constants for the second stage of the reaction were found to be independent of $[\text{H}_2\text{O}_2]$ and $[\text{Hpic}]$ when added from the start. This implies a simple conversion from one bis(picolinate) iron complex **1** to another **2**. The saturation seen in the A_∞ values as $[\text{H}_2\text{O}_2]$ increases (Table 2.5) indicates that this reaction, as with the first stage, is reversible. The A_∞ values for the second stage have, however, only been estimated since after periods of 10-30 mins depending on $[\text{H}_2\text{O}_2]$, further complex reactions occur, the onset of which is dependent on $[\text{H}_2\text{O}_2]$.

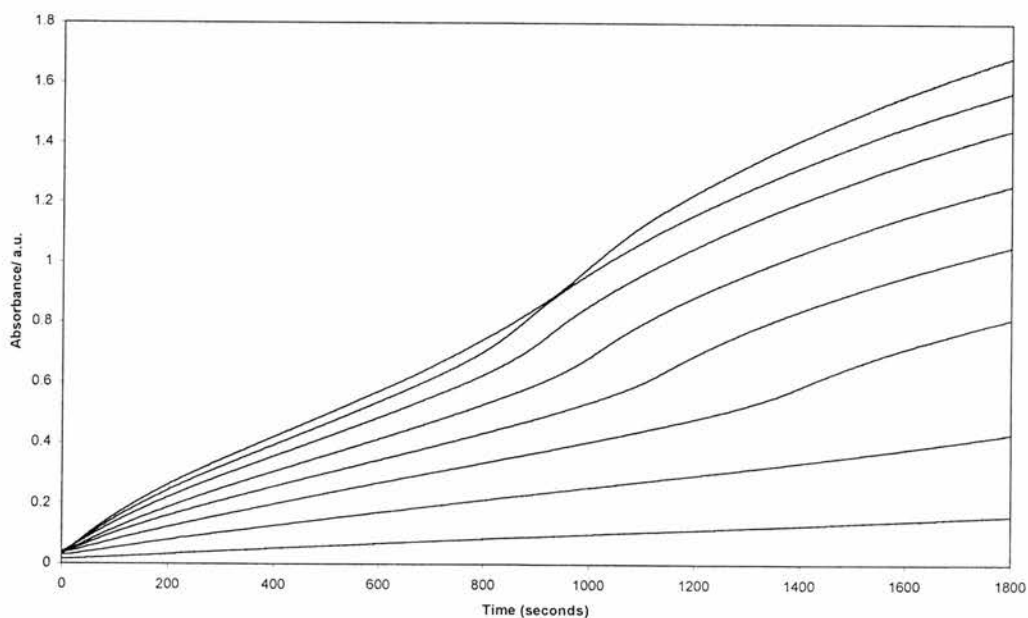


Figure 2.10: Absorbance vs. time trace for $[\text{Fe}] = 5 \times 10^{-4} \text{ mol dm}^{-3}$, $[\text{H}_2\text{O}_2] = 0.016 - 0.124 \text{ mol dm}^{-3}$, $T = 20 \text{ }^\circ\text{C}$ at 430 nm, with the addition of a tenfold molar excess of Hpic over $[\text{Fe}]$.

It was also found that when the reaction time exceeds *ca.* 30 mins a complex series of reactions was occurring, that encompasses the synthesis and recycling of the active Gif oxygenating catalyst. Studies over a longer time frame (10-12 hrs) showed that a second chemical process occurred during this period. This is illustrated in Figure 2.11, for $[\text{H}_2\text{O}_2] = 0.042$ and $0.126 \text{ mol dm}^{-3}$ respectively, with cyclohexane present and absent. It was found that at all concentrations of hydrogen peroxide studied the addition of cyclohexane caused a marked decrease in the overall absorbance over these time periods. The same general trend noted above, of a reduction in rate upon cyclohexane addition, was apparent at all concentrations of hydrogen peroxide. After approximately 6 hrs the curves for the $0.042 \text{ mol dm}^{-3}$ runs cross over the traces for the $0.126 \text{ mol dm}^{-3}$ aliquots, which reach a plateau after 3-4 hrs, leading to higher absorbances for the former. At higher concentrations of hydrogen peroxide the precipitation of an iron hydroxy species may interfere with the course of the reaction, an effect not apparent at the lower concentrations. Indeed, for the $0.042 \text{ mol dm}^{-3}$ solutions, the absorbance continues to rise steadily even after 10 hrs possibly due to further reactions of the better solubilised iron species.

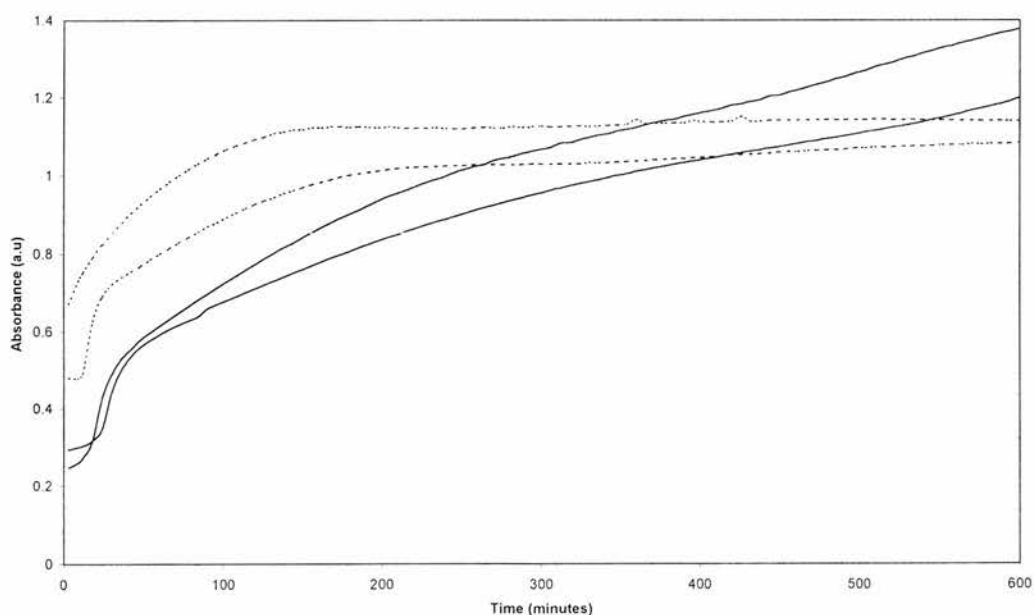
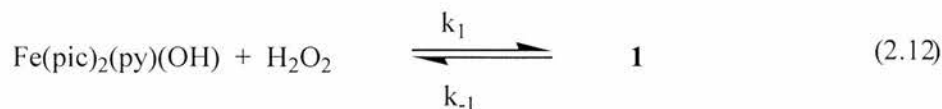
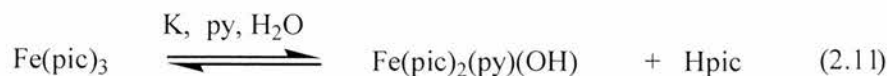


Figure 2.11: Absorbance vs time trace for $[\text{Fe}(\text{pic})_3]$ with $[\text{H}_2\text{O}_2] = 0.042$ and $0.126 \text{ mol dm}^{-3}$, $T = 20 \text{ }^\circ\text{C}$, 520 nm . Dotted line = $0.126 \text{ mol dm}^{-3}$, full line = $0.042 \text{ mol dm}^{-3}$. Within each pair of curves the lower line represents the rates when cyclohexane is added.

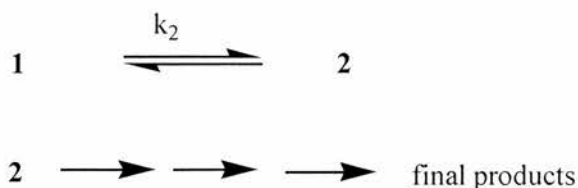
The following overall scheme summarises the reaction of $[\text{Fe}(\text{pic})_3]$ with hydrogen peroxide in pyridine solvent:



$$\text{Rate} = k_{\text{obs}} [\text{Fe}]_{\text{T}}$$

$$[\text{Fe}]_{\text{T}} = [\text{Fe}(\text{pic})_3] + [\text{Fe}(\text{pic})_2(\text{py})(\text{OH})]$$

$$k_{\text{obs}} = \frac{k_1 K [\text{H}_2\text{O}_2]}{K + [\text{Hpic}]} + k_{-1} \quad (2.13)$$



2.3.3 $^{13}\text{C}\{^1\text{H}\}$ NMR Investigations

Barton made an attempt to elucidate the ligand environment of iron(III)-complexes with chelating carboxylic acids (quinaldic acid, isoquinoline-1-carboxylic acid, Hpic and 2-hydroxypyridine) in pyridine solvent using quantitative $^{13}\text{C}\{^1\text{H}\}$ NMR spectroscopy.¹⁰ In his experiments, the performed iron(III) complexes were treated with excess oxalic acid to displace the carboxylate ligands from the iron centre. By comparison of signal intensities relative to precisely known quantities of hexachloroethane as an internal calibrant, Barton was able to estimate how many ligands were displaced. In the instance of $[\text{Fe}(\text{pic})_3]$, upon addition of oxalic acid all three of the pic^- ligands were displaced. A similar approach was used to try to quantify the number of pic^- ligands which are displaced upon addition of hydrogen peroxide solution.

Following Barton's conditions, $[\text{Fe}(\text{pic})_3]$ (0.055 mmol) and hexachloroethane (0.1 mmol) were dissolved in 1:2 v/v d_5 -pyridine/pyridine (1.5 cm^3). The $^{13}\text{C}\{^1\text{H}\}$ NMR spectrum showed resonances due solely to solvent and hexachloroethane. Hydrogen peroxide (5 μl) was added to the NMR solution, which caused the yellow solution to change instantly to purple. The $^{13}\text{C}\{^1\text{H}\}$ NMR spectrum was re-recorded immediately to establish whether any free Hpic ligand signals had appeared. However, the solution dynamics prevented a suitable lock signal being obtained, so the resulting spectrum showed broad resonances from which little useful information could be surmised. Repetition of the experiment using neat d_5 -pyridine failed to improve signal resolution. The simplicity of this technique for determining the progress of the GoAgg type reaction suggests that much useful information is available, however further consideration of conditions is required.

2.4 EPR Analysis of the $[\text{Fe}(\text{pic})_3]$ -Hydrogen Peroxide System

In order to probe further the nature of the iron species in intermediates **1** and **2** of equations 2.5, 2.6 the reaction was followed by EPR at 110 K on rapidly frozen glasses after 2 min time intervals following the addition of hydrogen peroxide to $[\text{Fe}(\text{pic})_3]$ in pyridine.

Under all conditions, the iron(III) complexes present in these solutions are paramagnetic and therefore no meaningful NMR spectroscopic characterisation is feasible. Also, the very low concentrations used prohibit the use of Raman spectroscopy to investigate the possible intermediates. However, EPR spectroscopy is ideal for the study of short-lived paramagnetic species.¹¹⁻¹⁵ In 1996 Talsi described EPR and ^1H NMR spectroscopic characterisation of the iron(III) complex formed in the $\text{K}[\text{Fe}^{\text{II}}(\text{pic})_3]$ -pyridine-acetic acid system upon addition of hydrogen peroxide.¹⁶ The mononuclear hydroxo complex $[\text{Fe}(\text{pic})_2(\text{OH})(\text{py})]$ was presumed formed when an equimolar quantity of hydrogen peroxide was added to a 2:1 v:v pyridine-acetic acid solution of $\text{K}[\text{Fe}(\text{pic})_3]$, while the addition of a large excess of hydrogen peroxide led to the

formation of an unstable high-spin iron(III)-peroxo complex, whose formulation was suggested to be $[\text{Fe}(\text{pic})_2(\text{OOH})(\text{py})]$.

However the $[\text{Fe}(\text{pic})_3]$ -hydrogen peroxide system has yet to be examined by this technique. An EPR spectroscopic study of this system to complement the UV-vis measurements was therefore undertaken. Only a qualitative analysis was possible in the time available.

In an attempt to reproduce the conditions used in the UV-vis spectroscopic study, 3.0 cm^3 of a $5 \times 10^{-4} \text{ mol dm}^{-3}$ solution of $[\text{Fe}(\text{pic})_3]$ in pyridine was used as a stock solution. Approximately 0.3 cm^3 of this solution was transferred to an EPR tube and the tube was dipped into a test tube containing 5:1 v/v isopentane-methylcyclohexane, which was itself immersed in a Dewar of liquid nitrogen. This rapid freezing technique allows better resolution spectra of the frozen glasses to be obtained compared to when solely liquid nitrogen is used for cooling. The frozen solution of $[\text{Fe}(\text{pic})_3]$ was transferred to the EPR spectrometer whose cavity was maintained at 110 K. The X-band EPR spectrum of the frozen glass showed a signal at $g = 4.41$ [Figure 2.12(a)], indicating a high spin ($S = 5/2$) iron(III) complex in a rhombic environment. The overall complexity of the spectrum may indicate the presence of several contributing high-spin iron(III) species conceivably arising from reactions of $[\text{Fe}(\text{pic})_3]$ with pyridine or water involving reversible loss of pic^- , consistent with the reaction of equation 2.7.

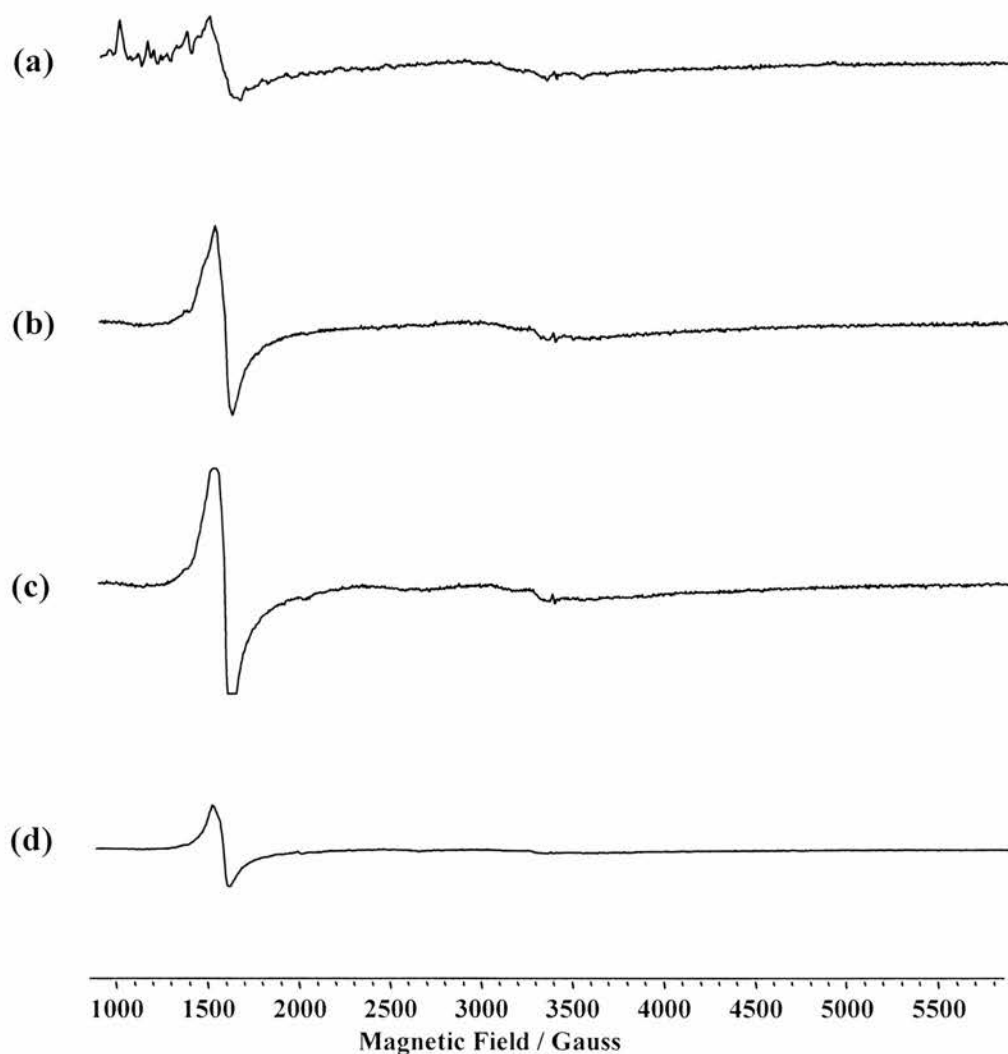


Figure 2.12: EPR spectra at 110 K for (a) 5×10^{-4} mol dm⁻³ solution of [Fe(pic)₃] in pyridine. (b) Solution (a) with 170-fold excess of hydrogen peroxide after 2 mins (purple species). (c) Solution (b) warmed for a further 2 mins and then refrozen. (d) Solution (c) warmed for a further 2 mins and then refrozen.

Attempts to quantify signal intensities by double integration of the spectrum did not give accurate values, as the baselines of the spectra were insufficiently flat. A small feature in the $g = 2$ region is apparent in all of the spectra, which may be due to a polynuclear iron(III) species.

The tube was then removed from the spectrometer, allowed to thaw completely and the tube contents combined with the stock solution. An aliquot of hydrogen peroxide (20 μ l, *ca.* 170-fold excess over iron) was added to the [Fe(pic)₃] solution, giving a transient purple colour almost immediately. After 1 min a

small quantity of the purple solution was quickly transferred into a clean EPR tube, frozen as before and its EPR spectrum recorded [Figure 2.12(b)]. A single isotropic high-spin $g = 4.4$ signal appeared, whose sharpness and intensity may result from an increase in molecular symmetry in the oxidised complex compared to $[\text{Fe}(\text{pic})_3]$ as well as the preference of only a single contributing species. The sample was again removed from the spectrometer, thawed for *ca.* 2 mins and then refrozen. A spectrum was recorded again [Figure 2.12(c)] and showed little change compared to (b) apart from a further increase in intensity of the $g = 4.4$ signal. The appearance of the isotropic signal exactly matches the timescale of the appearance of **1** with λ_{max} at 530 nm shown by UV-visible spectroscopy. Once again the sample was removed from the spectrometer, thawed for *ca.* 2 mins, refrozen and the spectrum recorded again [Figure 2.12(d)]. The spectrum had a noticeably smaller $g = 4.4$ signal compared to (c), believed to be due to further reactions of **1** giving an EPR-silent species **2**.

Further clues to the nature of **2** (and hence **1**) came from an EPR study of the corresponding reaction of $[\text{Fe}(\text{pic})_3]$ in pyridine with *t*-BuOOH. *t*-BuOOH can replace hydrogen peroxide in Gif (GoAgg)-type reactions and preserve the basic reactivity profile. Studies of the $[\text{Fe}(\text{pic})_3]$ -*t*-BuOOH reaction under analogous conditions to the hydrogen peroxide experiment were also conducted, *i.e.* with a 170-fold excess of hydroperoxide over $[\text{Fe}]$.

The EPR spectrum resulting after 2 mins of reaction of $[\text{Fe}(\text{pic})_3]$ with *t*-BuOOH is shown in Figure 2.13(b). The presence of *t*-BuOO \cdot is clearly apparent in these solutions from the sharp $g = 2$ signal, a feature consistent with homolytic cleavage of an initially formed iron(III)-butylperoxyl complex, probably $[\text{Fe}(\text{pic})_2(\text{py})(\text{OOBu-}t)]$, resulting in formation of a high spin iron(II) complex **2** (EPR silent), which from independent study is speculated to be $[\text{Fe}(\text{pic})_2(\text{py})_2]$. Since the *t*-BuOOH reaction gave a similar purple species to that with hydrogen peroxide it is concluded, by extrapolation, that in the latter reactions the purple intermediate **1** is a high-spin iron(III) hydroperoxy complex $[\text{Fe}(\text{pic})_2(\text{py})(\text{OOH})]$ and **2** is $[\text{Fe}(\text{pic})_2(\text{py})_2]$ along with HOO \cdot ; this radical species, unlike *t*-BuOO \cdot , having a short half-life in these solutions and rapidly disproportionating to

hydrogen peroxide and dioxygen. Indeed the evolution of dioxygen is a feature of these solutions as they are allowed to warm to room temperature.

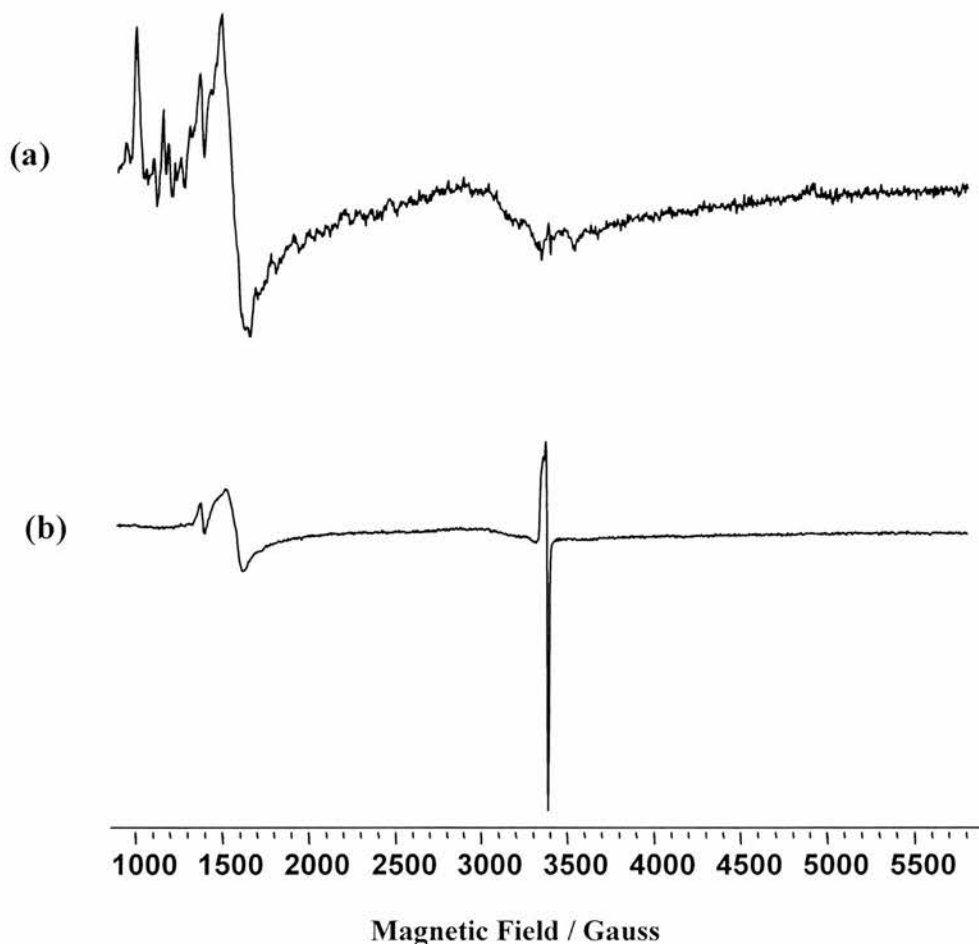


Figure 2.13: EPR spectra at 110 K for (a) 5×10^{-4} mol dm⁻³ solution of [Fe(pic)₃] in pyridine. (b) Solution (a) with 170-fold excess of *t*-BuOOH after 2 mins (purple species).

2.5 Summary and Conclusions

Using high spin [Fe(pic)₃] with hydrogen peroxide in pyridine, EPR and UV-vis spectroscopic evidence are presented for the rapid ($t_{1/2} \sim 1$ min at 293 K) formation of a high spin purple iron(III)-hydroperoxy species [Fe(pic)₂(py)OOH] ($\lambda_{\max} \sim 530$ nm, $\epsilon \sim 1,000$ dm³ mol⁻¹ cm⁻¹) in the early stages of assembly of a well known iron-based Gif (GoAgg) oxygenating system. Formation of the purple

species is reversible while an isosbestic point at 520 nm characterises a further equilibration to give a related species believed to be due to pyridine solvation.

The EPR spectrum of $[\text{Fe}(\text{pic})_3]$ in pyridine contains a complex signal which is consistent with equilibration mixtures of tris- and bis(picolinato) pyridine solvated iron(III) species as detected in the kinetic studies of the reaction with hydrogen peroxide. The production of a more intense isotropic high spin iron(III) signal on reaction with hydrogen peroxide reflects the presence of only one contributing species **1**, while the decrease in intensity with time reflects conversion of **1** to **2** [iron(II)] which is EPR silent.

The formation of iron(II) species in these solutions prior to any detectable influence of added cyclohexane substrate corroborates the recent work of Stavropoulos and co-workers⁴ that Fenton/ Haber-Weiss reactions involving the formation of OH radicals from iron(II)/ hydrogen peroxide chemistry is central to the mechanism of oxygenation by these and other Gif-type systems.

Although we believe that the $[\text{Fe}(\text{pic})_3]$ system reacts reversibly with hydrogen peroxide, it has been shown that hydrogen peroxide reacts irreversibly with dinuclear and tetranuclear iron complexes. It has been shown that these complexes have a high affinity toward hydrogen peroxide and have been studied using multielement NMR and resonance Raman spectroscopy.

In the case with $[\text{Fe}(\text{pic})_2(\text{H}_2\text{O})_2]$ under the same conditions as the $[\text{Fe}(\text{pic})_3]$ complex, a steady isosbestic point is not observed at all concentrations of hydrogen peroxide. It is tentatively concluded that multiple reaction pathways giving rise to several products, each with its own characteristic λ_{max} and half-life are responsible for this shift. Thereafter it is assumed that the iron(III)-hydroperoxy species which are formed exhibit similar chemistry to the $[\text{Fe}(\text{pic})_3]$ system, but this can only be verified by further experiments.

2.6 Further Work

Two different chemical processes take place upon addition of hydrogen peroxide to a dilute solution of $[\text{Fe}(\text{pic})_3]$ in pyridine, one which takes place over a few minutes while the second takes hours to reach completion. We can merely speculate about the nature of the intermediates formed during these processes, and only isolation of these species will enable full characterisation to be made. In conjunction with the UV-vis spectroscopic studies in a range of solvents, further EPR investigations of the $[\text{Fe}(\text{pic})_3]$ -hydrogen peroxide system in other media are necessary, to see if pyridine has a unique influence on the behaviour of the tris(picolate) complex. Also, a GC analysis of product profiles would ensure a correct determination of whether any oxygenated compounds are formed during the first thirty minutes following addition of hydrogen peroxide to $[\text{Fe}(\text{pic})_3]$ in pyridine when cyclohexane is present.

2.7 References

- 1 D. H. R. Barton, B. Hu, R. Wahl and D. K. Taylor, *New J. Chem.*, 1996, **20**, 121,
- 2 D. H. R. Barton, B. Hu, D. K. Taylor and R. U. R. Wahl, *Tetrahedron Lett.*, 1996, 1031,
- 3 D. H. R. Barton, B. Hu, D. K. Taylor and R. U. R. Wahl, *J. Chem. Soc., Perkin Trans. 2*, 1996, 1031
- 4 S. Kiani, A. Tapper, R. J. Staples and P. Stavropoulos, *J. Am. Chem. Soc.*, 2000, **120**, 7503.
- 5 S. G. Shova, N. V. Brashovyanu, K. I. Turte and M. D. Mazus, *Russ. J. Coord. Chem.*, 1996, **22**, 438.
- 6 D. H. R. Barton, S. D. Beviere, W. Chavisiri, D. Doller, G. Liu and J. H. Riebenspies, *New J. Chem.*, 1992, **16**, 1019.
- 7 P. Stavropoulos, personal communication.
- 8 Vogel's Textbook of Quantitative Inorganic Analysis, fourth edition, Longman London and New York, 1978
- 9 GRAFIT[®] is a trademark of Erithacus Software, Leatherhead, Surrey, UK. The package uses a standard Marquardt algorithm for non-linear least squares fitting.
- 10 D. H. R. Barton, B. Hu, R. U. R. Wahl and D. K. Taylor, *New J. Chem.*, 1996, **20**, 121.
- 11 G. Roelfes, M. Lubben, K. Chen, R. Y. N. Ho, A. Meetsma, S. Gemselberger, R. M. Hermant, R. Hage, S. K. Mandal, V. G. Young Jr, Y. Zang, H. Kooijman, A. L. Spek, L. Que Jr. and B. L. Feringa, *Inorg. Chem.*, 1999, **38**, 1929.
- 12 A. Wada, S. Ogo, S. Nagamoto, T. Kitagawa, Y. Watanabe, K. Jitsukawa and H. Masuda, *Inorg. Chem.*, 2002, **41**, 616.
- 13 Y. Ishikawa, Y. Morishita, T. Yamamoto, H. Kurosaki, M. Goto, H. Matsuo and M. Sugiyama, *Chem. Lett.*, 1998, 39.
- 14 M. Rivera, G. A. Caignan, A. V. Astashkin, A. M. Raisimring, T. K. Shokhireva and F. A. Walker, *J. Am. Chem. Soc.*, 2002, **124**, 6077.
- 15 A. P. Sobolev, D. E. Babushkin and E. P. Talsi, *J. Mol. Catal.(A)*, 2000, **159**, 233.
- 16 A. P. Sobolev, D. E. Babushkin, A. A. Shubin and E. P. Talsi, *J. Mol. Catal. A*, 1996, **112**, 253.

Chapter Three

Iron Complexes Containing Multidentate Nitrogen Donor Ligands

3.1 Introduction

Chapter One outlined the Gif family of oxidants and their necessary components for the oxidation of saturated cyclic hydrocarbons – metallic iron or an iron salt, pyridine, an oxidant and a reductant. Commercial viability necessitates that Gif systems use solvents other than pyridine; however pyridine cannot be wholly removed from the system as it may be functioning as a replaceable ligand on the iron, a buffer or as a trap for tertiary radicals. If pyridine acts solely as a ligand then by incorporating the pyridyl group into a chelate ligand on the metal centre it may be possible to adapt the Gif system to work in more benign solvents. Reference to the studies on activated BLM suggested that possible targets might be iron(II,III) complexes of pyridyl-containing pentadentate ligands, having one vacant site for inner sphere reaction with dioxygen or hydrogen peroxide. Iron-picolinate complexes have high (Gif) oxygenating activity only when free pyridine is present, a dependency which requires assessment with other iron chelate complexes having 2-pyridyl co-ordinating substituents. The ultimate aim is to design a highly active system which does not require pyridine.

This Chapter describes the synthesis and coordination chemistry of multidentate nitrogen donor ligands containing a 2-pyridyl ring, an imine or a carboxamide group, ensuring substantial differences in the basicities of the nitrogen donors. Iron complexes containing these ligands were synthesised in order to investigate their activity towards oxygenation of cyclohexane both in pyridine-acetic acid (Gif conditions) and acetonitrile. Dipic²⁻ and quin⁻ complexes of iron(II,III) were also examined.

3.2 Pyridine Dicarboxamide Ligands

3.2.1 Synthesis of Pyridine Dicarboxamide Ligands

The carboxamide [-C(O)NH-] group, ubiquitous throughout Nature in the primary structure of proteins, is an important ligand construction unit for coordination chemists. One burgeoning class of multidentate ligands containing this linkage are pyridine carboxamides, which are available from condensation reactions between amines and carboxylic acids containing pyridyl groups, promoted by coupling agents such as 1,1'-carbonyldiimidazole, diphenoxyphosphoryl azide or triphenylphosphite.¹⁻⁵ Upon deprotonation of the carboxamide nitrogen atom, this centre and the pyridyl ring(s) chelate to the metal centre. Pyridine carboxamide ligands have found use in asymmetric catalysis,^{2,6} in molecular receptors,^{7,8} for dendrimer synthesis⁹ and platinum(II) complexes with antitumour properties.⁴

We have synthesised several new polydentate pyridine dicarboxamide ligands from H₂dipic, pyridine-2,6-dicarbonyl dichloride or 2,6-diaminopyridine (Figure 3.1). Compounds H₂L¹⁻³ are generated from reactions of H₂dipic with 2-aminothiazole, 2-amino-5-chloropyridine or 2-amino-4-methylpyridine respectively in the presence of triphenylphosphite. When 2-aminopyrimidine is used under analogous conditions the diester *O,O'*-diphenylpyridine-2,6-dicarboxylate is isolated rather than the desired dicarboxamide H₂L⁴, phenoxide presumably originating from triphenylphosphite. To overcome this problem H₂L⁴ was synthesised from pyridine-2,6-dicarbonyl dichloride and 2-aminopyrimidine with triethylamine as hydrogen chloride acceptor; similarly, H₂L⁵ was prepared using 2-(aminomethyl)naphthalene. Treatment of 2,6-diaminopyridine with pyrazine-2-carboxylic acid or Hp₂ic lead to H₂L⁶ and H₂L⁷ respectively, the reaction between 1,3-phenylenediamine with two equivalents of Hp₂ic generated 1,3-bis(pyridine-2-carboxamido)benzene H₂L⁸, triphenylphosphite being the activating agent for these condensations.

Compound H₂L⁷ is regioisomeric with *N,N'*-bis(2-pyridyl)pyridine-2,6-dicarboxamide (H₂L⁹),¹⁰ H₂L⁸ and its 1,2 regioisomer are known.^{11,12} The thiazole (H₂L¹), pyrimidine (H₂L⁴) and pyrazine (H₂L⁶) derivatised molecules

add further chemical and structural diversity to the existing pyridine dicarboxamide ligands in the literature. In particular H_2L^1 would be anticipated to have substantial differences in its coordination chemistry compared with its counterparts with 2-pyridyl groups.

Compounds H_2L^{1-8} are air- and moisture-stable solids available in 40-88 % isolated yields, with slight to moderate solubilities in chloroform and thf but they are insoluble in methanol and diethyl ether. Microanalysis revealed that several of the compounds crystallised as hydrates upon recrystallisation from wet solvents. 1H NMR, IR and EI MS were consistent with their structures. In their IR spectra, ν_{NH} and ν_{CO} bands appeared between 3351-3242 cm^{-1} and 1718-1656 cm^{-1} respectively, in their 1H NMR spectra the *NH* resonance was a broad singlet in the region δ 10-12, with the exception of H_2L^5 , for which the resonance was obscured by the aromatic protons.

3.2.2 X-Ray Crystallographic Analysis of Pyridine Dicarboxamide Ligands

Despite our best efforts using solvent or vapour diffusion methods it proved impossible to grow X-ray quality crystals of the dipic or 2,6-diaminopyridine derived ligands H_2L^{1-7} . For comparative purposes we obtained the crystal structures of *N,N'*-bis(2-pyridyl)pyridine-2,6-dicarboxamide monohydrate ($H_2L^9 \cdot H_2O$), *N,N'*-bis[2-(2-pyridyl)methyl]pyridine-2,6-dicarboxamide (H_2L^{10}) and *N,N'*-bis[2-(2-pyridyl)ethyl]pyridine-2,6-dicarboxamide monohydrate ($H_2L^{11} \cdot H_2O$), whose syntheses have been reported in the literature.^{13,14} Selected interatomic distances and bond angles are given in Table 3.1, hydrogen bonding parameters appear in Table 3.2.

The molecular framework of H_2L^9 is essentially planar, with the C(8)-O(8) and C(15)-O(15) vectors oriented outwards from the central pocket of H_2L^9 in which the water molecule resides (Figure 3.2). An extensive array of hydrogen bonding interactions exists between H(30A) and H(30B) of the water of crystallisation

with N(1) and N(18) of the terminal pyridyl rings, O(30) with H(7N) and H(16N) and also between H(7N) and N(10) [H...A 2.02-2.40(14) Å, D...A 2.666(10)-3.260(9) Å, where hydrogen bonds are represented by D-H...A].

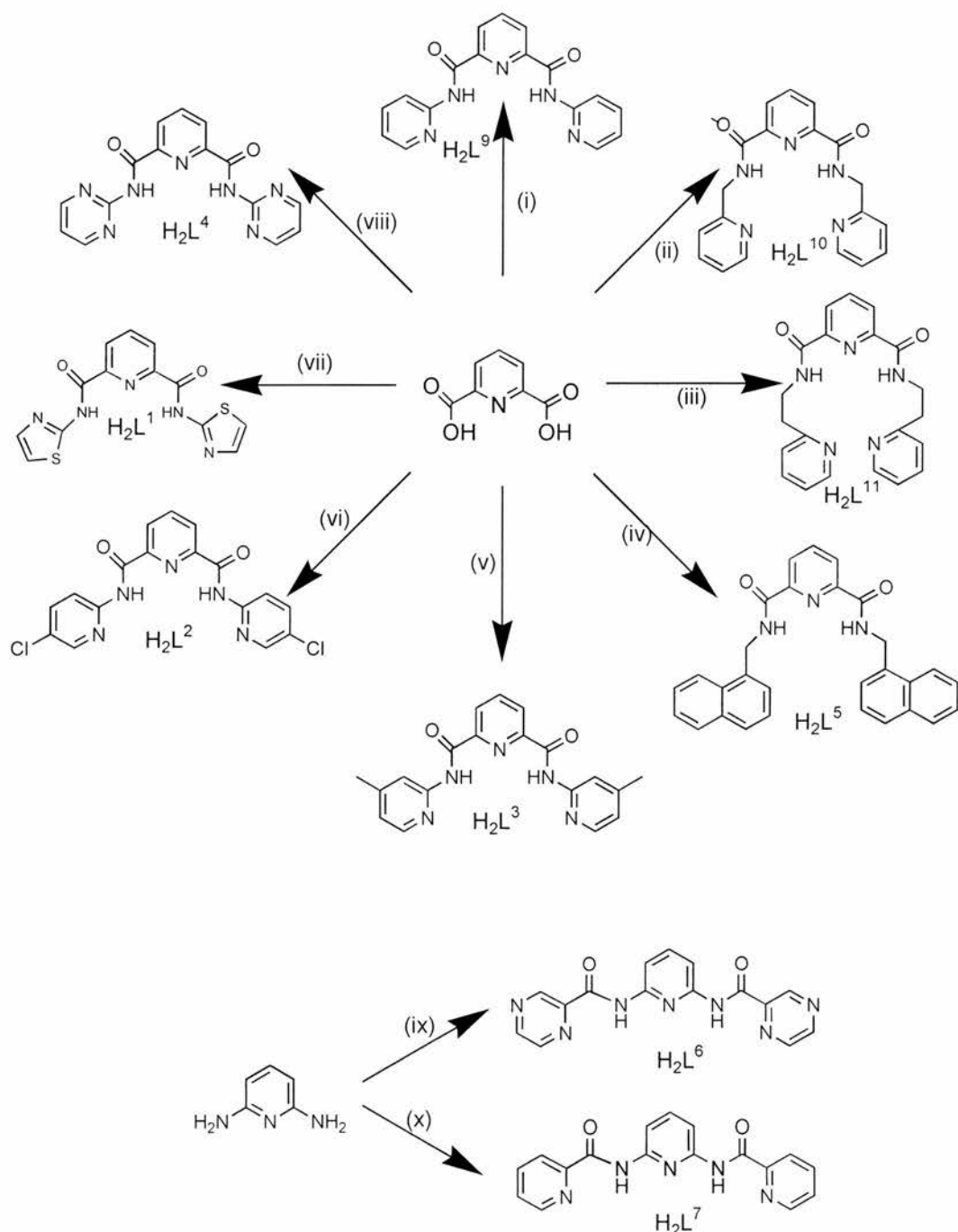


Figure 3.1: Reaction of H_2dipic or pyridine-2,6-dicarbonyl dichloride with: (i) 2-aminopyridine, (ii) 2-(aminomethyl)pyridine, (iii) 2-(aminoethyl)pyridine, (iv) 2-(aminomethyl)naphthalene, (v) 2-amino-4-methylpyridine, (vi) 2-amino-5-chloropyridine, (vii) 2-aminothiazole, (viii) 2-aminopyrimidine, (ix) 2-pyrazinecarboxylic acid and (x) Hpic.

In contrast to $\text{H}_2\text{L}^9\cdot\text{H}_2\text{O}$, H_2L^{10} crystallises as dimer pairs of molecules crosslinked by four-membered hydrogen bonded rings involving pyridyl nitrogen atoms and NH groups (Figure 3.3). H(8N) and H(17N) form intramolecular hydrogen bonds to N(11) and to N(20A) from the second molecule in the dimer, with N(20) hydrogen bonding reciprocally with the amide protons of the second molecule [H...A 2.218(10)-2.459(9) Å, D...A 2.6899(16)-3.3346(17) Å]. N(1) and N(1A) are uninvolved in interactions with amide protons either within the dimer or to adjacent molecules.

$\text{H}_2\text{L}^{11}\cdot\text{H}_2\text{O}$ combines structural motifs from $\text{H}_2\text{L}^9\cdot\text{H}_2\text{O}$ and H_2L^{10} (Figure 3.4). Two H_2L^{11} molecules adopt a head-to-tail arrangement with H(9N), H(18N) and N(22) hydrogen bonding with one water molecule while N(1) hydrogen bonds to a second water molecule [H...A 1.969(15)-2.328(10) Å, D...A 2.902(3)-3.275(4) Å]. The arms of H_2L^{11} hydrogen bond independently of one another, the dimeric structure being maintained solely by the water molecules, as there are no other intra-dimer interactions.

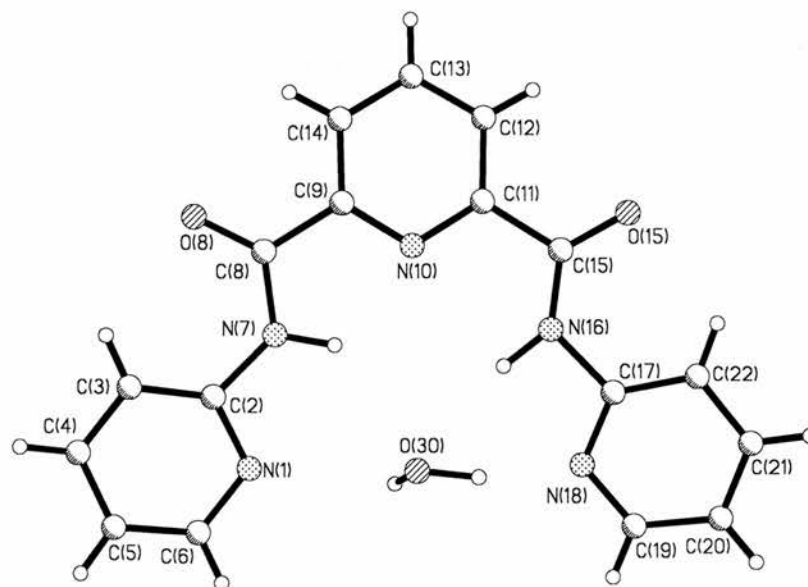


Figure 3.2: Molecular structure of $\text{H}_2\text{L}^9\cdot\text{H}_2\text{O}$.

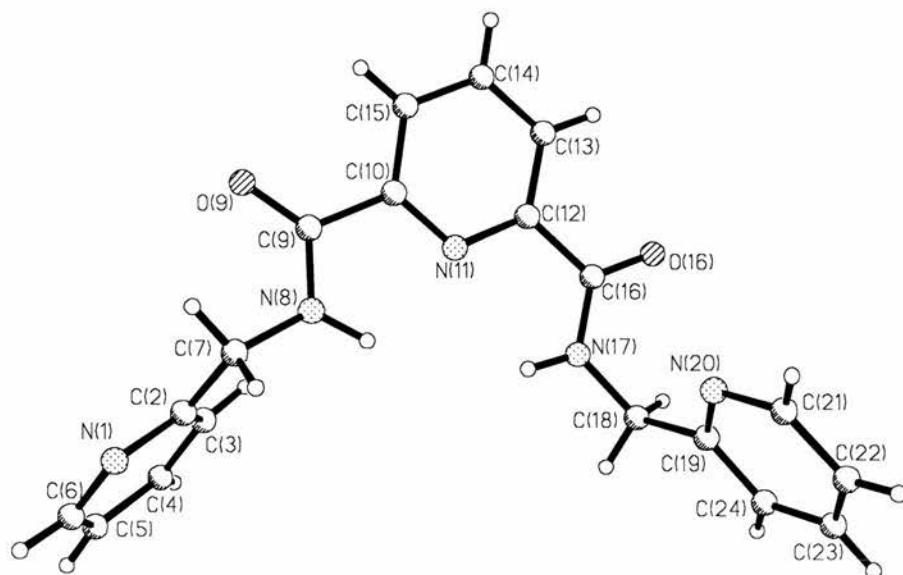


Figure 3.3(a): Molecular structure of H_2L^{10}

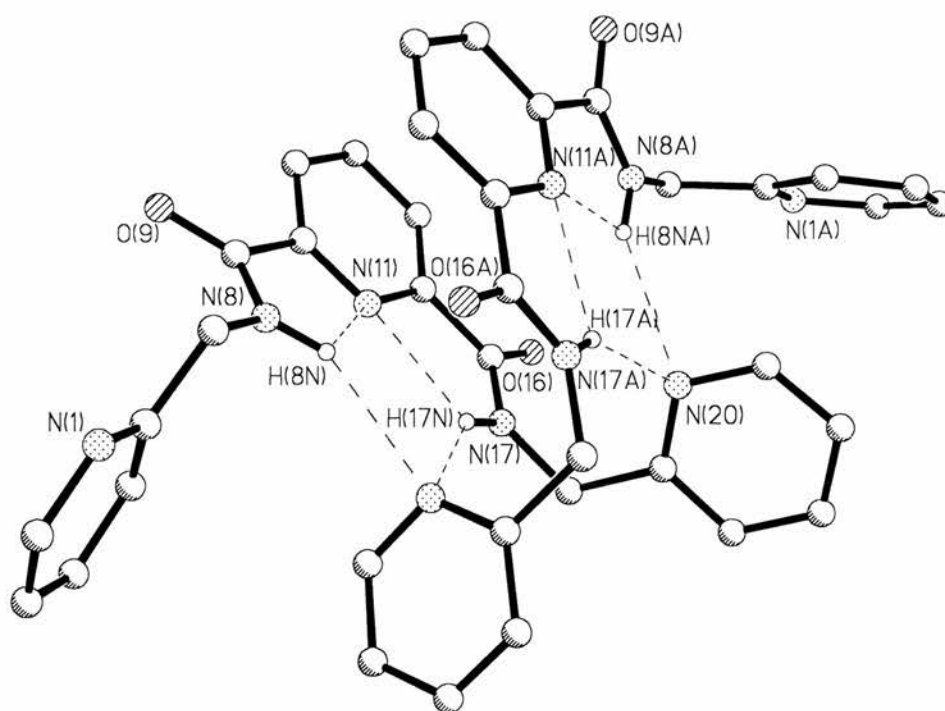


Figure 3.3 (b): Hydrogen-bonded dimer formation in H_2L^{10} .

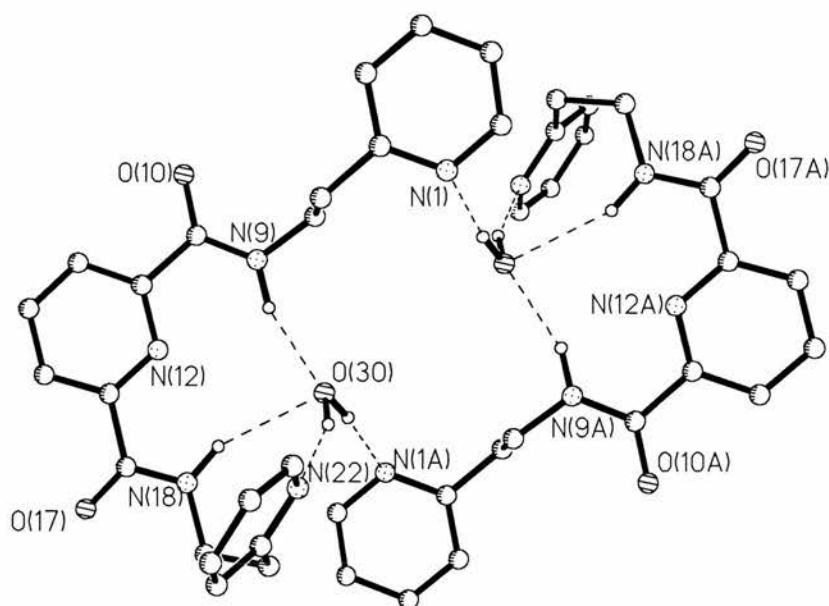


Figure 3.4: Molecular structure of $\text{H}_2\text{L}^{11} \cdot \text{H}_2\text{O}$ (C-H bonds omitted for clarity).

Table 3.1: Selected bond lengths (Å) and angles ($^\circ$) for $\text{H}_2\text{L}^9 \cdot \text{H}_2\text{O}$, H_2L^{10} and $\text{H}_2\text{L}^{11} \cdot \text{H}_2\text{O}$ (esd's in parentheses).

$\text{H}_2\text{L}^9 \cdot \text{H}_2\text{O}$			
C(2)-N(7)	1.426(10)	C(15)-O(15)	1.246(9)
N(7)-C(8)	1.376(10)	C(15)-N(16)	1.317(12)
C(8)-O(8)	1.247(8)	N(16)-C(17)	1.449(11)
C(8)-N(7)-C(2)	128.1(7)	O(8)-N(8)-C(7)	124.2(7)
O(8)-C(8)-C(9)	121.2(8)	N(7)-C(8)-C(9)	114.6(7)
O(15)-C(15)-N(10)	125.4(9)	N(16)-C(15)-C(11)	115.2(9)
O(15)-C(15)-C(11)	119.4(9)	C(15)-N(16)-C(17)	129.2(8)
H_2L^{10}			
C(7)-N(8)	1.4516(18)	N(8)-C(9)	1.3354(19)
C(9)-O(9)	1.2294(18)	C(16)-O(16)	1.2315(17)
C(16)-N(17)	1.3288(18)	N(17)-C(18)	1.4462(19)
C(9)-N(8)-C(7)	121.83(12)	O(9)-C(9)-N(8)	124.09(14)
N(8)-C(9)-O(10)	115.17(12)	O(9)-C(9)-C(10)	120.69(14)
O(16)-C(16)-N(17)	123.71(14)	O(16)-C(16)-C(12)	120.85(13)
N(17)-C(16)-C(12)	115.44(12)	C(16)-N(17)-C(18)	122.26(13)

H ₂ L ¹¹ .H ₂ O			
C(8)-N(9)	1.452(3)	N(9)-C(10)	1.332(3)
C(10)-O(10)	1.238(3)	C(17)-O(17)	1.226(3)
C(17)-N(18)	1.338(3)	N(18)-C(19)	1.456(3)
C(10)-N(9)-C(8)	121.90(19)	O(10)-C(10)-N(9)	123.2(2)
O(10)-C(10)-C(11)	120.0(2)	N(9)-C(10)-C(11)	116.86(18)
O(17)-C(17)-N(18)	122.49(19)	O(17)-C(17)-C(13)	121.20(18)
N(18)-C(17)-C(13)	116.23(19)	C(17)-N(18)-C(19)	119.46(19)

Table 3.2: Hydrogen bonding distances (Å) and angles (°) for H₂L⁹.H₂O, H₂L¹⁰ and H₂L¹¹.H₂O (esd's in parentheses). The hydrogen bond donor atoms are denoted as *D* and the acceptors as *A*.

	<i>D</i> -H	H... <i>A</i>	<i>D</i> ... <i>A</i>	<i>D</i> -H... <i>A</i>
H ₂ L ⁹ .H ₂ O				
N(7)-H(7N)...N(10)	0.984(17)	2.35(16)	2.666(10)	98(11)
N(7)-H(7N)...O(30)	0.984(17)	2.40(14)	3.252(7)	145(16)
N(16)-H(16N)...O(30)	0.9801(11)	2.34(2)	3.260(9)	156(5)
O(30)-H(30A)...N(1)	0.98	2.34	2.909(7)	116.4
O(30)-H(30B)...N(18)	0.98	2.02	2.954(7)	158.5
H ₂ L ¹⁰				
N(8)-H(8N)...N(11)	0.969(5)	2.296(15)	2.7184(16)	105.4(10)
N(17)-H(17N)...N(11)	0.970(5)	2.273(16)	2.6899(16)	104.8(11)
N(8)-H(8N)...N(20#)	0.969(5)	2.459(9)	3.3346(17)	150.1(12)
N(17)-H(17N)...N(20#)	0.970(5)	2.218(10)	3.0744(18)	146.6(13)
H ₂ L ¹¹ .H ₂ O				
N(9)-H(9N)...O(30)	0.979(5)	2.082(15)	2.961(3)	148(2)
N(18)-H(18N)...O(30)	0.977(5)	2.328(10)	3.275(4)	163(2)
O(30)-H(30B)...N(22)	0.979(5)	1.969(15)	2.902(3)	159(3)
O(30)-H(30A)...N(1#)	0.981(5)	2.166(14)	3.120(3)	164(4)

^a For H₂L¹⁰ and H₂L¹¹.H₂O ' # ' denotes atom from second molecule in dimer.

In H_2L^{9-11} the carbonyl groups do not hydrogen bond with amine protons or water molecules. The C-N_{amide} and C=O distances [1.317(12)-1.376(10), 1.226(3)-1.247(8) Å] concur with 1,2-bis(pyridine-2-carboxamido)benzene and 1,2-bis(pyridine-2-carboxamido)cyclohexane [1.321(2)-1.343(3), 1.222(3)-1.229(3) Å].¹ *N,N'*-dimethylpyridine-2,6-dicarboxamide and pyridine-2,6-dicarboxamide form hydrogen bonding networks in the solid state both intra- and intermolecularly, which high temperature ¹H NMR spectroscopy shows are retained in dmsO solution up to 150°C.¹⁵ Notably, despite their crystallisation from strongly hydrogen bonding media (water, dmsO, ethanol) no solvent inclusion occurred in either structure, a testament to the strength of the hydrogen bonding in these molecules. Thus the hydrate formation in the structures of H_2L^9 , H_2L^{11} and several of the pyridine dicarboxamide ligands H_2L^{1-8} is unexpected.

3.3 Pyridyl Containing Polydentate Ligands

N,N'-Bis(2-picolyl)amine, L^{12} , was synthesised by reduction of the Schiff base generated from the condensation reaction between pyridine-2-carboxaldehyde and 2-(aminomethyl)pyridine using sodium borohydride.¹⁶ Reduction was confirmed by the disappearance of the imine proton resonance from the ¹H NMR spectrum of the Schiff base and the appearance of an NH peak at δ 2.57 for L^{12} .

The terpyridyl ligand, 4'-(4-pyridyl)-2,2':6',2''-terpyridine (hereafter 'pyterpy') was prepared by the condensation of 2-acetylpyridine with pyridine-4-carboxaldehyde followed by ring closure of the intermediate dicarbonyl compound with ammonium acetate in glacial acetic acid.¹⁷ ¹H NMR and IR spectral data were in accord with the literature values.

The diimines L^{13} and L^{14} were available by dehydrative condensation reactions of 1,2-diaminoethane with pyridine-2-carboxaldehyde or 2-acetylpyridine respectively in ethanol,¹⁸ while the tripodal ligand *N,N',N''*-tris-2-(pyridine-2-carboxaldimino)ethylamine L^{15} was derived from tris(2-aminoethyl)amine and pyridine 2-carboxaldehyde (Figure 3.5).¹⁹ Spectroscopic data corroborated

Schiff base formation, with $\delta(\text{CH}=\text{N})$ 8.52 and 8.36 for L^{14} and L^{15} in their ^1H NMR, with $\nu_{\text{C}=\text{N}}$ bands at 1647 (L^{13}), 1631 (L^{14}) and 1648 cm^{-1} (L^{15}) in their IR spectra.

3-[Bis(2-pyridylmethyl)amino]propanoic acid (hereafter 'bppH') was prepared from the reaction between *N,N'*-bis(picolyl)amine and 3-bromopropanoic acid with triethylamine as the hydrogen bromide acceptor.^{20,21} BppH offers both pyridyl and carboxylic acid functional groups in one ligand; in $[\text{VO}(\text{O}_2)(\text{bppH})][\text{ClO}_4]$ and $[\{\text{Fe}(\text{bpp})(\text{H}_2\text{O})\}_2(\mu_2\text{-O})][\text{ClO}_4]_2$ the polydentate ligand coordinates to the metal centre through all of the nitrogen atoms and one of the carboxyl oxygens in a tetradentate fashion.

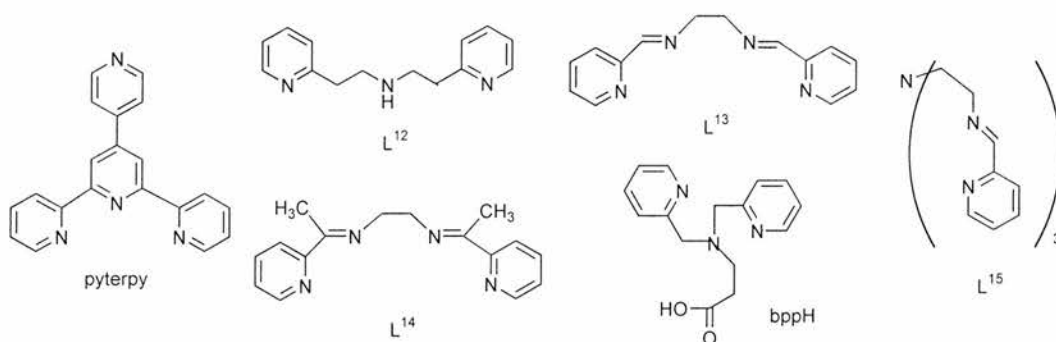


Figure 3.5: Structures of L^{12-15} , bppH and pyterpy.

3.4 Synthesis of Iron Complexes

Iron is the metal of choice for Gif chemistry. Preformed metal complexes are not generally used, however if pyridine is to be removed from the system altogether then ligands containing pyridyl functionalities may represent a suitable compromise solution. Additionally, the presence of a carboxylic acid group may also be beneficial, as it is well known that Hpic dramatically enhances the rate of Gif oxygenations.

Iron(III) complexes of pyridine dicarboxamide ligands were prepared using $[\text{Fe}(\text{dmf})_6][\text{ClO}_4]_3$, which was generated by dissolving iron(III) perchlorate hexahydrate in dmf, followed by several successive cycles of evaporation and addition of fresh solvent. Dipic^{2-} and quin^- complexes were prepared from

metallic iron and the respective carboxylic acid in pyridine. For imine and polypyridyl ligands, iron(II) perchlorate hexahydrate, iron(II) chloride tetrahydrate or iron(III) perchlorate hexahydrate were used. Except when using metallic iron, complexation reactions were generally rapid (instantaneous to a few minutes), evidenced visually by the change in colour of the iron solution upon addition of ligand. Characterisation was performed using IR and mass spectrometries, elemental analysis and, in certain instances, X-ray crystallography.

3.4.1 Reaction of Elemental Iron with H₂dipic in Pyridine

Although Hpic is integral to the GoAgg^{III} oxidant system, H₂dipic has not been studied in this capacity, despite its obvious resemblance to Hpic. The dipic²⁻ dianion functions as an *N,O,O'*-tridentate ligand at manganese(II), cobalt(II,III) and iron(II),²²⁻²⁷ giving two fused five membered *N,O* chelate rings at the metal; notably [Mn(dipic)(bipy)₂] and [Fe₂(dipic)₂(OH₂)₆] are heptacoordinate complexes.^{22,24} The crystal structures of [Ph₄As][Fe(dipic)₂] and [H₅O₂][Fe(dipic)₂] confirmed meridional *N,O,O'*-tridentate coordination of dipic²⁻ to iron, with the *trans* N-Fe-N axis being *ca.* 172°.^{28,29} In all cases to date, iron complexes have been prepared from iron salts, no reports exist where metallic iron has been reacted with H₂dipic under similar conditions to those employed for synthesising [Fe(pic)₂]_n. We have found that the iron-H₂dipic-pyridine system generates some highly unusual complexes.

Refluxing a mixture of H₂dipic and iron powder (molar ratio 2:1) in pyridine for 5 hrs under an argon atmosphere produced a deep red solution from which unreacted metallic iron was removed by filtration whilst hot using a filter frit. Upon cooling the filtrate to -20 °C for 24 hrs a red crystalline solid deposited. Its molecular structure was determined crystallographically to be [pyH][Fe(dipic)(Hdipic)(py)₂].3py (Figure 3.6) in which one dipic²⁻ dianion is coordinated to Fe(1) *via* N(1), O(7) and O(8) with Hdipic⁻ bound *via the* oxygen atoms O(16) and O(17) of one carboxylate group to give a four membered metallacycle.

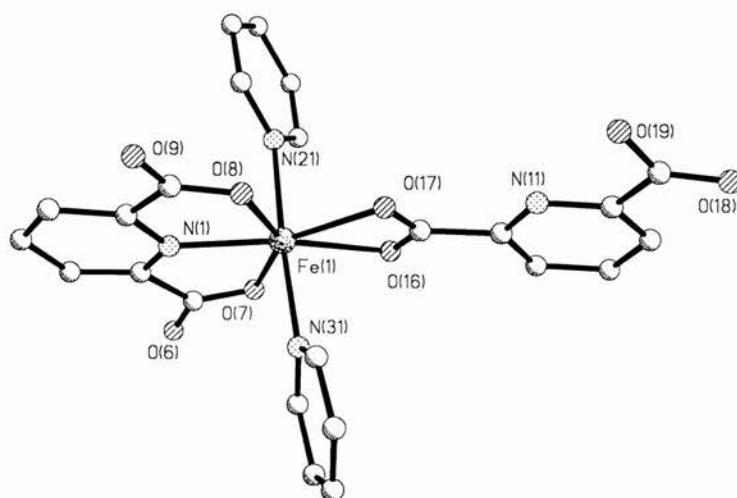


Figure 3.6: Molecular structure of the anion in $[\text{pyH}][\text{Fe}(\text{dipic})(\text{Hdipic})(\text{py})_2].3\text{py}$ (C-H bonds, cation and pyridine solvate molecules omitted for clarity).

Table 3.3: Selected bond lengths (Å) and angles ($^\circ$) for $[\text{pyH}][\text{Fe}(\text{dipic})(\text{Hdipic})(\text{py})_2].3\text{py}$ (esd's in parentheses).

Fe(1)-N(1)	2.132(2)	Fe(1)-O(7)	2.1615(19)
Fe(1)-O(8)	2.2091(19)	Fe(1)-N(31)	2.218(2)
Fe(1)-N(21)	2.234(2)	Fe(1)-O(17)	2.246(2)
Fe(1)-O(16)	2.2900(19)		
N(1)-Fe(1)-O(7)	73.51(8)	N(1)-Fe(1)-O(8)	72.35(8)
O(7)-Fe(1)-O(8)	145.73(7)	N(1)-Fe(1)-N(31)	95.14(8)
O(7)-Fe(1)-N(31)	90.15(8)	O(8)-Fe(1)-N(31)	90.00(8)
N(1)-Fe(1)-N(21)	88.22(8)	O(7)-Fe(1)-N(21)	90.05(8)
O(8)-Fe(1)-N(21)	91.77(8)	N(31)-Fe(1)-N(21)	176.55(9)
N(1)-Fe(1)-O(17)	147.06(8)	O(7)-Fe(1)-O(17)	139.38(7)
O(8)-Fe(1)-O(17)	74.71(7)	N(31)-Fe(1)-O(17)	84.91(8)
N(21)-Fe(1)-O(17)	92.70(8)	N(1)-Fe(1)-O(16)	154.77(8)
O(7)-Fe(1)-O(16)	81.55(7)	O(8)-Fe(1)-O(16)	132.71(7)
N(31)-Fe(1)-O(16)	88.52(8)	N(21)-Fe(1)-O(16)	88.10(8)
O(17)-Fe(1)-O(16)	58.08(7)		

The nitrogen atom N(11) and the oxygen atoms O(18) and O(19) of the pendant carboxylic acid group of the Hdipic⁻ ligand orient away from Fe(1). Fe(1) has a pentagonal bipyramidal geometry, the equatorial [NO₄] donor atoms being supplied by dipic ligands with two axial pyridines bound through N(21) and N(31) completing the coordination sphere. By analogy with the iron(0)-Hpic reaction, and also considering the rigorous exclusion of dioxygen from the reaction we have assigned a +2 oxidation state for iron. Microanalysis suggested that the pyridine solvate molecules were rapidly lost upon removal from the mother liquor as the elemental analysis determined after a sample had been left open to air for several days corresponded to [pyH][Fe(dipic)(Hdipic)(py)₂]. This is corroborated by thermogravimetric analysis of a sample of the material. At 118 °C a five mg sample lost 27.8 % of its mass, *c.f.* for [pyH][Fe(dipic)(Hdipic)(py)₂].3py the pyridine solvate constitutes 27.5 % of the mass of the sample. The FAB⁺ MS contained a peak at *m/z* 388 for [Fe(dipic)]⁺, no peaks at higher *m/z* ratios could be assigned.

Upon sonication of a solution of [pyH][Fe(dipic)(Hdipic)(py)₂] in wet pyridine under aerobic conditions a colourless solid (either H₂dipic or its pyridinium salt) settled and was removed by filtration. Upon exposure to air overnight the filtrate deposited deep red crystals of the μ₂-oxo bridged diiron(III) complex [{Fe(dipic)(py)₂}₂(μ₂-O)].2py.H₂O (Figure 3.7), in which dipic²⁻ is tridentate at Fe(1) *via* N(7), O(11) and O(11B) with N(7) *trans* to the μ₂-oxo linkage O(1). The octahedral coordination at Fe(1) is completed by two mutually *trans* pyridine ligands, bound through N(1) and N(1B). The complex is centrosymmetric, with molecules of pyridine and water co-crystallised.

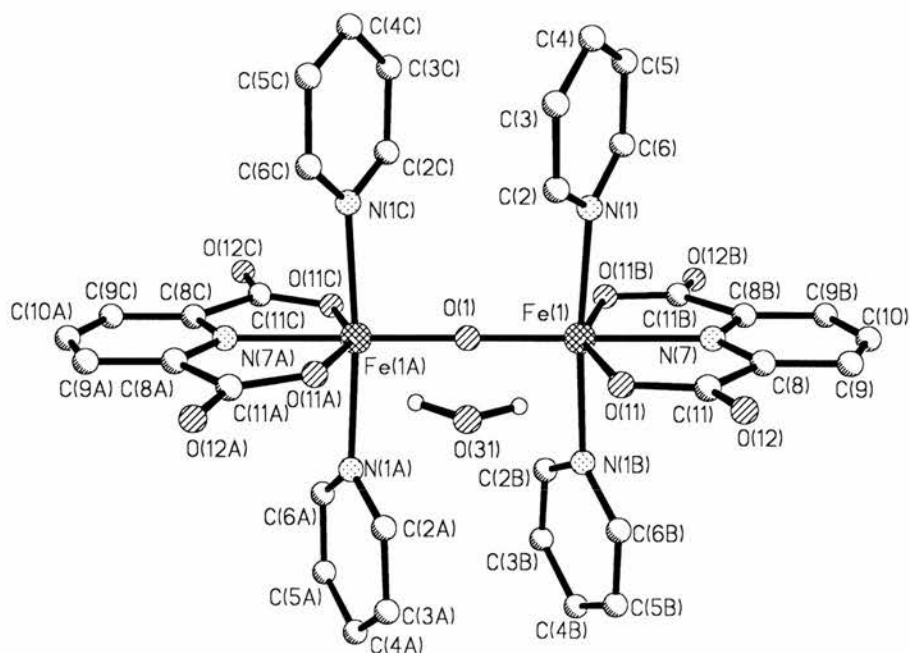


Figure 3.7: Molecular structure of $[\{\text{Fe}(\text{dipic})(\text{py})_2\}_2(\mu_2\text{-O})].2\text{py}.\text{H}_2\text{O}$ (C-H bonds and pyridine solvate omitted for clarity).

Table 3.4: Selected bond lengths (Å) and angles ($^\circ$) for $[\{\text{Fe}(\text{dipic})(\text{py})_2\}_2(\mu_2\text{-O})].2\text{py}.\text{H}_2\text{O}$ (esd's in parentheses).

Fe(1)-O(1)	1.7808(9)	Fe(1)-O(11)	2.048(8)
Fe(1)-O(11B)	2.048(4)	Fe(1)-N(7)	2.106(6)
Fe(1)-N(1B)	2.216(5)	Fe(1)-N(1)	2.216(5)
O(1)-Fe(1B)	1.7808(9)		
O(10)-Fe(1)-O(11)	104.71(10)	O(1)-Fe(1)-O(11B)	104.71(10)
O(11)-Fe(1)-O(11B)	150.6(2)	O(1)-Fe(1)-N(7)	180.0
O(11)-Fe(1)-N(7)	75.29(10)	O(11B)-Fe(1)-N(7)	75.29(10)
O(1)-Fe(1)-N(1B)	92.51(11)	O(11)-Fe(1)-N(1B)	91.01(14)
O(11B)-Fe(1)-N(1B)	87.72(14)	N(7)-Fe(1)-N(1B)	87.49(11)
O(1)-Fe(1)-N(1)	92.51(11)	O(11)-Fe(1)-N(1)	87.72(14)
O(11B)-Fe(1)-N(1)	91.01(14)	N(7)-Fe(1)-N(1)	87.49(11)
N(1B)-Fe(1)-N(1)	175.0(2)	Fe(1)-O(1)-Fe(1A)	180.0

The structure of the complex is symmetry generated hence the Fe(1)-O(1)-Fe(1A) axis is exactly 180°. Tridentate chelation of the (dipic)²⁻ anion distorts the geometry at Fe(1), the *trans* O(11)-Fe(1)-O(11B) angle is 150.6(2)°, with *cis* O(1)-Fe(1)-O(11) 104.71(10)°. The Fe(1)-O(1) distance [1.7809(4) Å] is substantially shorter than Fe(1)-O(11) [2.048(4) Å] indicating significant π -bonding within the Fe-oxo linkage. The *trans* influence of O(1) lengthens Fe(1)-N(7) [2.106(6) Å] compared with [cation][Fe(dipic)₂], cation = [H₅O₂]⁺ [2.053(2), 2.067(2) Å] or [Ph₄As]⁺ [2.037(3), 2.076(3) Å].^{28,29} The Fe(1)-O(11) length [2.048(4) Å] is only marginally longer than in the homoleptic complexes [2.001(2)-2.035(2) Å],^{28,29} with the Fe(1)-N(1) distance unchanged from [pyH][Fe(dipic)(Hdipic)(py)₂] [2.218(2), 2.234(2) Å]. The *cis* (N-Fe-O)_{chelate} bite angle is 75.29(10)°. There is a hydrogen bonding interaction between one of the hydrogen atoms H(31) from the solvate water molecule and O(11) [H(31)...O(11) 1.893(9) Å].

Crystalline [{Fe(dipic)(py)₂}₂(μ_2 -O)].2py.H₂O was somewhat unstable when removed from contact with its pyridine mother liquor. Over *ca.* four days in a closed vial the deep red crystals transformed into a pale brown solid with a strong smell of pyridine. Microanalysis suggested the stoichiometry [{Fe(dipic)(H₂O)₂}₂(μ_2 -O)] *i.e.* the coordinated pyridine ligands were displaced upon exposure to the atmosphere, equation 3.1.



Such a structure is not unreasonable as [{Fe(4-Cl-dipic)(H₂O)₂}₂(μ_2 -O)] is prepared directly in water from the diethyl ester of 4-chloropyridine-2,6-dicarboxylic acid (4-Cl-H₂dipic), iron(III) chloride hexahydrate and urea in 96 % yield.²⁶

3.4.2 Quinaldic Acid Complexes of Iron

Another structural relative of Hp_{ic} is quinaldic acid (2-quinolinecarboxylic acid, Hquin), which functions as an *N,O* chelate to iron(II) in its monoanionic form

quin⁻.^{30,31} We have observed a notable difference between the reactivity of Hquin and Hpic. Whereas iron(III) nitrate nonahydrate reacted with Hpic to give [Fe(pic)₃] (Chapter Two), the corresponding reaction with Hquin in methanol at room temperature gave a μ₂-hydroxy bridged diiron(III) complex [Fe₂(μ₂-OH)₂(quin)₄], by comparison with literature data, equation 3.2.³⁰ Presumably steric constraints precluded tris(chelation) of quin⁻ at an octahedral iron(III) centre.



Hquin reacted with iron powder under identical conditions to those used to synthesise [Fe(pic)₂(py)₂] to give [Fe(quin)₂(py)₂] as a slightly air sensitive red solid, soluble in pyridine and dmf, for which ν_{COO} (1652, 1361 cm⁻¹) are slightly higher than [Fe(pic)₂(py)₂] (1645, 1348 cm⁻¹), equation 3.3. Microanalytical data concurred with calculated values although FAB⁺ MS contained no peaks assignable to M⁺ or daughter fragments.



3.4.3 Pyridine Dicarboxamide Complexes of Iron(III)

Mascharak has investigated the coordination chemistry of H₂L¹¹ with first row transition metals. Whereas copper(II) and cobalt(II,III) are coordinated in a pentadentate fashion by the three pyridine rings and two deprotonated carboxamide nitrogen atoms of (L¹¹)²⁻,^{13,32} with iron(III) the bis(chelate) complex [Fe(L¹¹)₂]⁻ was obtained,³³ in which the nitrogen atom of the central pyridyl ring and the deprotonated carboxamide groups were bound to the iron(III) centre. Similarly the dianion of H₂L¹⁰ gives [Fe(L¹⁰)₂]⁻, while N₃ tridentate coordination by the (L^{Ph})²⁻ dianion was observed in [Et₄N][Fe(L^{Ph})₂], where H₂L^{Ph} = N,N'-bis(phenyl)pyridine-2,6-dicarboxamide.³⁴ The disparity between iron(III) and both copper(II) and cobalt(II,III) was attributed to “the exceptional stability

provided by four carboxamide nitrogen atoms.....outweighs the chelate effect of the pentadentate ligands".¹³

We have prepared a series of bis(dicarboxamide) complexes of iron(III), Na[FeL₂] by deprotonation of H₂L^{1,2,3,7,9} with sodium hydride in dmf followed by addition of [Fe(dmf)₆][ClO₄]₃ (Scheme 3.1). The complexes, obtained as deep red solids in typically 20-25 % isolated yields are presumed to be isostructural with Na[Fe(L¹⁰)₂] and Na[Fe(L¹¹)₂],³³ in which (L^{10,11})²⁻ coordinate *via* the nitrogen atoms of the central pyridyl ring and the deprotonated carboxamide groups in a *mer* arrangement, equation 3.4.

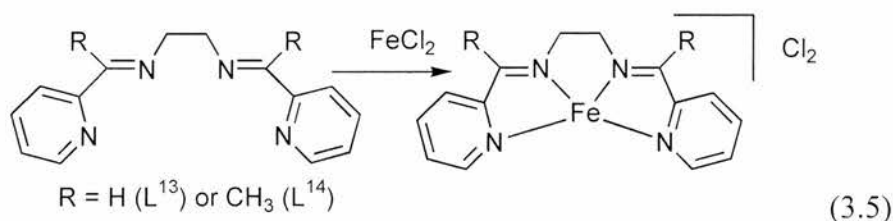


While apparently good quality crystals of several complexes were readily obtained by vapour diffusion of diethyl ether into 1:1 v/v dmf-acetonitrile solutions at room temperature, repeated attempts at X-ray crystallographic analysis failed to solve the structures. Elemental analyses suggested that the complexes crystallised from 1:1 v/v dmf/acetonitrile – diethyl ether solutions (wet solvents were used) with water of crystallisation, ES MS in some cases contained peaks corresponding to [FeL₂]. The complexes were moderately soluble in dmf, acetonitrile and methanol but decolourised in pyridine over 24-48 hrs at room temperature, indicating displacement of L²⁻ from the iron(III) coordination sphere. The complexes were appreciably soluble in water with no apparent degradation. In their IR spectra an intense ν_{CO} band appeared at *ca.* 1600 cm⁻¹ in all cases, a reduction concomitant with deprotonation of H₂L and coordination of (L)²⁻. Na[Fe(L⁷)₂] is of particular interest from a structural perspective as the 2,6-diaminopyridine unit mitigates against N₃ tridentate chelation to one metal centre in the manner of the dipic derived ligands. Microanalytical data for Na[Fe(L⁷)₂] and Na[Fe(L⁹)₂] were in reasonable agreement and fit well for a trihydrate, however no inference as to the structure of the (L⁷)²⁻ complex can be made from this.

3.4.4 Iron(II) Complexes with Imine Ligands

Recent work on iron(II)-imine complexes has demonstrated that such systems have great potential for industrially relevant catalytic processes. Thus 2,6-bis(imino)pyridine complexes are active catalysts for the oligomerisation and polymerisation of ethylene,³⁵ while α -diimine iron complexes catalysed atom transfer radical polymerisation of styrene.³⁶

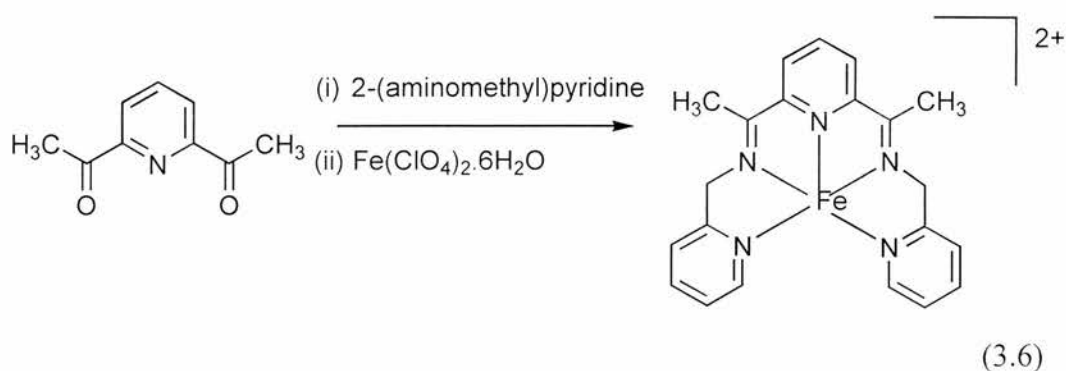
$[\text{FeL}^{13}]\text{Cl}_2$ and $[\text{FeL}^{14}]\text{Cl}_2$ were prepared by the method of Busch¹⁸ from iron(II) chloride tetrahydrate in ethanol, equation 3.5.



IR spectra for $[\text{FeL}^{13}]\text{Cl}_2$ showed bands above 3000 cm^{-1} which were assigned by Busch to ν_{OH} stretches of coordinated water molecules, although if hydrolysis of imine bonds had occurred these bands could arise from ν_{NH} vibrations. The $\nu_{\text{C=N}}$ band was at 1635 cm^{-1} , *c.f.* 1647 cm^{-1} for L^{13} . Microanalytical data for $[\text{FeL}^{13}]\text{Cl}_2$ were extremely poor (attributed in the literature to contamination by unreacted metal halide),¹⁸ the FAB^+ MS contained a peak at m/z 294 corresponding to $[\text{FeL}^{13}]^+$. From the reaction of iron(II) chloride tetrahydrate with L^{14} , two crops of material were isolated, firstly a green solid and subsequently a purple solid, in both cases their IR spectra exhibited broad bands above 3000 cm^{-1} . Notably, $\nu_{\text{C=N}}$ for $[\text{FeL}^{14}]\text{Cl}_2$ (1637 cm^{-1}) was at higher energy than the free ligand value (1631 cm^{-1}), whereas for $\text{L}^{13,15}$ coordination decreased the frequency of this band. Peaks at m/z 357 and 322 in the FAB^+ MS for $[\text{FeL}^{14}]\text{Cl}_2$ correspond to $[\text{Fe}(\text{L}^{14})\text{Cl}]^+$ and $[\text{FeL}^{14}]^+$.

$[\text{FeL}^{15}](\text{ClO}_4)_2$ was prepared from iron(II) chloride tetrahydrate, L^{15} and sodium perchlorate in methanol.³⁷ The $\nu_{\text{C=N}}$ band showed the expected bathochromic shift upon coordination, moving from 1648 cm^{-1} to 1612 cm^{-1} .

An attempt was made to prepare an iron(II) complex $[\text{FeL}^{16}][\text{ClO}_4]_2$, where $\text{L}^{16} = 2,6\text{-bis}[1\text{-}(2\text{-methylpyridylimino)ethyl}]\text{pyridine}$, from the reaction of iron(II) perchlorate hexahydrate with L^{16} generated *in situ* from 2,6-diacetylpyridine and 2-(aminomethyl)pyridine (molar ratio 1:2) in methanol, equation 3.6.³⁸



L^{16} would be expected to act as a pentadentate ligand to iron. From this reaction we isolated a purple solid and, from the filtrate, a maroon solid. For the purple solid elemental analysis was in reasonable agreement with the proposed formulation, in its IR spectrum a $\nu_{\text{C=N}}$ band appeared at 1697 cm^{-1} . The FAB^+ MS of both crops of solid contained a peak at m/z 398 corresponding to $[\text{FeL}^{16}]^+$.

During the course of this work a publication³⁹ describing the synthesis of L^{16} and *inter alia* its iron(II) bis(chelate) complex $[\text{Fe}(\text{L}^{16})_2][\text{PF}_6]_2$ appeared; characterisation data were limited to EI MS for L^{16} , microanalysis and FAB^+ MS for $[\text{Fe}(\text{L}^{16})_2]^{2+}$. L^{16} was believed to coordinate to iron(II) *via* the central pyridyl ring and imine nitrogen atoms in a tridentate mode. As $(\text{L}^{10})^{2-}$ acts as a tridentate ligand to iron(III) with the terminal pyridyl rings pendant,³³ a similar coordination mode for L^{16} is reasonable; nevertheless our isolation of a material whose elemental composition corresponded to $[\text{FeL}^{16}][\text{ClO}_4]_2$ suggests that the product formed may be sensitive to the conditions employed.

3.4.5 Complexes of Iron(II,III) with Bi-, Tri- and Tetradentate Donor Ligands

Iron(II) complexes of L¹² and pyterpy, and iron(III) complexes of TPA and bppH were prepared by literature methods. The addition of L¹² to iron(II) chloride tetrahydrate (2:1 molar ratio) gave [Fe(L¹²)₂]²⁺, which precipitated as the tetrafluoroborate salt upon addition of Na[BF₄].⁴⁰ The reaction of iron(II) perchlorate hexahydrate with two equivalents of pyterpy gave [Fe(pyterpy)₂][ClO₄]₂ in 77 % yield.⁴¹ The μ₂-oxo bridged diiron(III) complex [{Fe(bpp)(H₂O)}₂(μ₂-O)][ClO₄]₂ was prepared by reacting bppH with iron(III) perchlorate hexahydrate in the presence of triethylamine.²¹ The anion is tetradentate at iron with the amine nitrogen atom *trans*- to the μ₂-oxo bridge. This complex was recrystallised from water as a tetrahydrate. The tris(2-pyridylmethyl)amine (tpa) diiron(III) complex [{Fe(tpa)}₂(μ₂-O)][ClO₄]₄ was prepared from the reaction between tpa.3HClO₄, triethylamine and iron(III) perchlorate hexahydrate in methanol.⁴²

3.5 Summary and Conclusions

A series of pyridine dicarboxamide ligands H₂L¹⁻⁸ was prepared from reactions of H₂dipic, pyridine-2,6-dicarbonyl dichloride or 2,6-diaminopyridine with amine or carboxylic acid functionalised heterocycles. Their inability to encapsulate one metal centre owing to the requirement for four membered metallacycle formation encourages the generation of multimetallic complexes (Chapter Four). H₂L⁹⁻¹¹ crystallised with extensive hydrogen bonding networks involving pyridyl nitrogen atoms, NH groups and in some cases water of crystallisation. The carbonyl oxygen atoms play no part in the hydrogen bonding arrays. Bis(dicarboxamide) complexes Na[FeL₂] were prepared from Na₂L/[Fe(dmf)₆][ClO₄]₃ in which (L)²⁻ binds to iron(III) through the nitrogen atoms of the central pyridyl ring and the deprotonated carboxamide groups. [pyH][Fe(dipic)(Hdipic)(py)₂], containing *N,O,O'*-tridentate dipic²⁻ and *O,O'*-bidentate Hdipic⁻ ligands, was prepared from H₂dipic/iron(0) in pyridine. In air

this complex transformed into a μ_2 -oxo bridged diiron(III) species [$\{\text{Fe}(\text{dipic})(\text{py})_2\}_2(\mu_2\text{-O})$]. Hquin reacted with metallic iron to give [$\text{Fe}(\text{quin})_2(\text{py})_2$], isostructural with the complex generated using Hpic whereas [$\text{Fe}_2(\mu_2\text{-OH})_2(\text{quin})_4$] was isolated using iron(III) nitrate.

3.6 Future Work

By comparison with activated BLM, a pentadentate ligand whose iron complex possesses a free site to enable HOO to coordinate may well be the most suitable candidate for catalytic study. A hybrid ligand such as bppH is therefore just one donor atom away from this, containing both pyridyl and carboxylate functionalities in one molecule. The design and synthesis of such a ligand may therefore enable the final removal of pyridine from the Gif system and clear the way for larger scale application of this class of catalyst.

3.7 Experimental Section

General experimental conditions and instrumentation details are as described previously. H_2L^9 was prepared by a triphenylphosphite promoted condensation reaction between 2-aminopyridine and H_2dipic , H_2L^{10} and H_2L^{11} were prepared from pyridine-2,6-dicarbonyl dichloride and 2-(aminomethyl)pyridine or 2-(aminoethyl)pyridine respectively in the presence of triethylamine.^{13,14} $\text{H}_2\text{L}^9 \cdot \text{H}_2\text{O}$, H_2L^{10} and $\text{H}_2\text{L}^{11} \cdot \text{H}_2\text{O}$ were crystallised by vapour diffusion of diethyl ether into chloroform solutions of the appropriate compounds at room temperature. Pyterpy, bppH, tpa.3HClO₄ and L¹² were prepared by literature methods.^{16,17,43}

CAUTION: Although we have encountered no difficulties, perchlorate salts are potentially explosive and should be handled with care.

Pyridine-2,6-dicarbonyl dichloride: H_2dipic (5.0 g, 30.0 mmol) was added to thionyl chloride (50 cm³) and heated to reflux under dinitrogen for 6 hrs. The

reaction mixture was allowed to cool, the solvent was removed under reduced pressure and the product dried *in vacuo*. Yield 6.12 g (100 %). Selected IR bands (cm^{-1}): 1752s (ν_{CO}).

Compounds H_2L^{1-3} , H_2L^{6-8} were prepared using identical procedures on the same scale, illustrated for H_2L^7 .

Under an argon atmosphere, Hpic (4.67 g, 38 mmol) was added as a solid in one portion to a suspension of 2,6-diaminopyridine (3.0 g, 18 mmol) in pyridine (10 cm^3) and the mixture stirred at 40 °C for forty mins. Triphenylphosphite (9.5 cm^3 , 36 mmol) was added dropwise over ten mins, after which time the temperature of the mixture was increased to 90-100 °C and stirring continued for a further 4 hrs. On cooling to room temperature the colourless precipitate was filtered off, washed with water (20 cm^3), methanol (20 cm^3) and recrystallised from chloroform. Yield 4.25 g (74 %).

***N,N'*-Bis(2-thiazolyl)pyridine-2,6-dicarboxamide H_2L^1** : Yield 77 %. Found (calc. for $\text{C}_{13}\text{H}_9\text{S}_2\text{N}_5\text{O}_2 \cdot 2\text{H}_2\text{O}$): C 42.82 (42.49), H 1.59 (3.57), N 19.01 (19.06) %. δ_{H} (CDCl_3): 12.20 (br s, 2H, NH), 8.51 (d, 2H, $J = 8$, $\text{C}_5\text{H}_3\text{N}$), 8.22 (t, 1H, $J = 8$, $\text{C}_5\text{H}_3\text{N}$), 7.52 (d, 2H, $J = 4$, $\text{C}_3\text{H}_2\text{NS}$), 7.06 (d, 2H, $J = 4$ Hz, $\text{C}_3\text{H}_2\text{NS}$). Selected IR bands (cm^{-1}): 3250s (ν_{NH}), 1682s (ν_{CO}). EI MS: m/z 331, M^+ .

***N,N'*-Bis[2-(5-chloro)pyridyl]pyridine-2,6-dicarboxamide H_2L^2** : Yield 88 %. Found (calc. for $\text{C}_{17}\text{H}_{11}\text{N}_5\text{O}_2\text{Cl}_2 \cdot \text{H}_2\text{O}$): C 50.47 (50.26), H 2.48 (3.22), N 17.19 (17.24) %. δ_{H} (CDCl_3): 10.75 (br s, 2H, NH), 8.50 (d, 2H, $J = 8$, $\text{C}_5\text{H}_3\text{N}$), 8.46 (d, 2H, $J = 9$, $\text{C}_5\text{H}_3\text{NCl}$), 8.35 (d, 2H, $J = 3$, $\text{C}_5\text{H}_3\text{NCl}$), 8.18 (t, 1H, $J = 8$, $\text{C}_5\text{H}_3\text{N}$), 7.80 (dd, 2H, $J = 3$ and 9 Hz, $\text{C}_5\text{H}_3\text{NCl}$). Selected IR bands (cm^{-1}): 3268m (ν_{NH}), 1697s (ν_{CO}). EI MS: m/z 387, M^+ .

***N,N'*-Bis[2-(4-methyl)pyridyl]pyridine-2,6-dicarboxamide H_2L^3** : Yield 40 %. Found (calc. for $\text{C}_{19}\text{H}_{17}\text{N}_5\text{O}_2 \cdot \text{H}_2\text{O}$): C 62.27 (62.44), H 4.99 (5.24), N 19.33 (19.16) %. δ_{H} (CDCl_3): 10.96 (br s, 2H, NH), 8.50 (d, 2H, $J = 8$, $\text{C}_5\text{H}_3\text{N}$), 8.35 (s, 2H, $\text{CH}_3\text{C}_5\text{H}_3\text{N}$), 8.22 (d, 2H, $J = 5$, $\text{CH}_3\text{C}_5\text{H}_3\text{N}$), 8.15 (t, 1H, $J = 8$, $\text{C}_5\text{H}_3\text{N}$),

6.93 (d, 2H, $J = 5$ Hz, $\text{CH}_3\text{C}_5\text{H}_3\text{N}$), 2.42 (s, 6H, CH_3). Selected IR bands (cm^{-1}): 3299m (ν_{NH}), 1702s (ν_{CO}). EI MS: m/z 347, M^+ .

Compounds $\text{H}_2\text{L}^{4,5}$ were prepared by identical procedures, illustrated for H_2L^4 . Pyridine-2,6-dicarbonyl dichloride (5.0 g, 24.5 mmol), 2-aminopyrimidine (4.66 g, 49.0 mmol) and triethylamine (5.05 g, 50.0 mmol) were refluxed in thf (300 cm^3) for 5 hrs. Triethylamine hydrochloride was filtered off, the filtrate was evaporated *in vacuo* and the residue redissolved in acetonitrile (50 cm^3). The solution was stored at -20 °C overnight to give a colourless solid.

***N,N'*-Bis(2-pyrimidinyl)pyridine-2,6-dicarboxamide H_2L^4 :** Yield 40 %. Found (calc. for $\text{C}_{15}\text{H}_{11}\text{N}_7\text{O}_2$): C 55.60 (56.07), H 2.95 (3.45), N 24.74 (30.51) %. δ_{H} (CDCl_3): 11.07 (s, 2H, NH), 8.74 (d, 4H, $J = 5$, $\text{C}_4\text{H}_3\text{N}_2$), 8.60 (d, 2H, $J = 8$, $\text{C}_5\text{H}_3\text{N}$), 8.18 (t, 1H, $J = 8$, $\text{C}_5\text{H}_3\text{N}$), 7.12 (t, 2H, $J = 5$ Hz, $\text{C}_4\text{H}_3\text{N}_2$). Selected IR bands (cm^{-1}): 3327m (ν_{NH}), 1718s (ν_{CO}). EI MS: m/z 321, M^+ .

***N,N'*-Bis[2-(2-naphthyl)methyl]pyridine-2,6-dicarboxamide H_2L^5 :** Yield 41 %. Found (calc. for $\text{C}_{29}\text{H}_{23}\text{N}_3\text{O}_2 \cdot 0.5\text{H}_2\text{O}$): C 76.10 (76.60), H 4.93 (5.32), N 9.22 (9.24) %. δ_{H} (CDCl_3): 8.33 (m, 2H, aromatic H), 7.98-7.73 (m, 9H, aromatic H), 7.46-7.24 (m, 9H, aromatic H), 5.00 (d, 4H, $J = 6$ Hz, CH_2). Selected IR bands (cm^{-1}): 3281m (ν_{NH}), 1656s (ν_{CO}). EI MS: m/z 445, M^+ .

2,6-Bis(pyrazine-2-carboxamido)pyridine H_2L^6 : Yield 40 %. Found (calc. for $\text{C}_{15}\text{H}_{11}\text{N}_7\text{O}_2$): C 55.62 (56.07), H 3.41 (3.45), N 30.68 (30.52) %. δ_{H} (CDCl_3): 10.01 (br s, 2H, NH), 9.48 (d, 2H, $J = 1.5$, $\text{C}_4\text{H}_3\text{N}_2$), 8.79 (d, 2H, $J = 2.5$, $\text{C}_4\text{H}_3\text{N}_2$), 8.58 (dd, 2H, $J = 1.5$ and 2.5 , $\text{C}_4\text{H}_3\text{N}_2$), 8.15 (d, 2H, $J = 8$, $\text{C}_5\text{H}_3\text{N}$), 7.83 (t, 1H, $J = 8$ Hz, $\text{C}_5\text{H}_3\text{N}$). Selected IR bands (cm^{-1}): 3354s (ν_{NH}), 1702s (ν_{CO}). EI MS: m/z 321, M^+ .

2,6-Bis(pyridine-2-carboxamido)pyridine H_2L^7 : Yield 74 %. Found (calc. for $\text{C}_{17}\text{H}_{13}\text{N}_5\text{O}_2$): C 64.35 (63.94), H 3.49 (4.10), N 22.07 (21.93) %. δ_{H} (CDCl_3): 10.43 (br s, 2H, NH), 8.66 (ddd, 2H, $J = 1, 2$ and 5 , $\text{C}_5\text{H}_4\text{N}$), 8.31 (dt, 2H, $J = 1$ and 8 , $\text{C}_5\text{H}_4\text{N}$), 8.18 (d, 2H, $J = 8$, $\text{C}_5\text{H}_3\text{N}$), 7.93 (dt, 2H, $J = 1.5$ and 8 , $\text{C}_5\text{H}_4\text{N}$),

7.85 (t, 1H, $J = 8$, C₅H₃N), 7.51 (ddd, 2H, $J = 1, 5$ and 8 Hz, C₅H₄N). Selected IR bands (cm⁻¹): 3340m (ν_{NH}), 1701s (ν_{CO}). EI MS: m/z 319, M^+ .

1,3-Bis(pyridine-2-carboxamido)benzene H₂L⁸: Yield 56 %. Found (calc. for C₁₈H₁₄N₄O₂): C 67.62 (67.91), H 3.95 (4.43), N 17.48 (17.60) %. δ_H (CDCl₃): 10.11 (br s, 2H, NH), 8.61 (dd, 2H, $J = 1$ and 4, C₅H₄N), 8.29 (m, 3H, C₆H₄ + C₅H₄N), 7.90 (dt, 2H, $J = 1.5$ and 8, C₅H₄N), 7.62 (dd, 2H, $J = 1.5$ and 8, C₆H₄), 7.48 (ddd, 2H, $J = 1, 5$ and 8, C₅H₄N), 7.39 (t, 1H, $J = 8$ Hz, C₆H₄). Selected IR bands (cm⁻¹): 3242s (ν_{NH}), 1666s (ν_{CO}). EI MS: m/z 318, M^+ .

***N,N'*-Bis(2-pyridyl)pyridine-2,6-dicarboxamide H₂L⁹**: Yield 85 %. Found (calc. for C₁₇H₁₁N₅O₂·H₂O): C 60.76 (60.88), H 4.28 (3.91), N 21.07 (20.90) %. δ_H (CDCl₃): 10.59 (br s, 2H, NH), 8.51 (d, 2H, $J = 8$, C₅H₄N), 8.44 (d, 2H, $J = 8$, C₅H₃N), 8.35 (dd, 2H, $J = 1$ and 4, C₅H₄N), 8.15 (t, 1H, $J = 8$, C₅H₃N), 7.77 (dt, 2H, $J = 2$ and 8, C₅H₄N), 7.10 (dd, 2H, $J = 5$ and 8 Hz, C₅H₄N). Selected IR bands (cm⁻¹): 3293m (ν_{NH}), 1698s (ν_{CO}). EI MS: m/z 319, M^+ .

***N,N'*-Bis[2-(2-pyridyl)methyl]pyridine-2,6-dicarboxamide H₂L¹⁰**: Yield 78 %. Found (calc. for C₁₉H₁₇N₅O₂): C 64.34 (65.69), H 4.69 (4.93), N 19.91 (20.16) %. δ_H (CDCl₃): 8.99 (br t, 2H, $J = 5$, NH), 8.46 (d, 2H, $J = 5$, C₅H₄N), 8.34 (d, 2H, $J = 8$, C₅H₃N), 8.00 (t, 1H, $J = 8$, C₅H₃N), 7.64 (dt, 2H, $J = 1.5$ and 8, C₅H₄N), 7.33 (d, 2H, $J = 8$, C₅H₄N), 7.16 (dd, 2H, $J = 5$ and 8, C₅H₄N), 4.76 (d, 4H, $J = 6$ Hz, CH₂). Selected IR bands (cm⁻¹): 3306m (ν_{NH}), 1676s (ν_{CO}). EI MS: m/z 347, M^+ .

***N,N'*-Bis[2-(2-pyridyl)ethyl]pyridine-2,6-dicarboxamide H₂L¹¹**: Yield 72 %. Found (calc. for C₂₁H₂₁N₅O₂): C 66.81 (67.18), H 5.54 (5.64), N 18.63 (18.65) %. δ_H (CDCl₃): 8.74 (br t, 2H, $J = 6$, NH), 8.48 (d, 2H, $J = 5$, C₅H₄N), 8.29 (d, 2H, $J = 8$, C₅H₃N), 7.98 (t, 1H, $J = 8$, C₅H₃N), 7.60 (dt, 2H, $J = 1.5$ and 8, C₅H₄N), 7.20 (d, 2H, $J = 8$, C₅H₄N), 7.14 (dd, 2H, $J = 5$ and 8, C₅H₄N), 3.91 (q, 4H, $J = 6$, CH₂), 3.14 (t, 4H, $J = 6$ Hz, CH₂). Selected IR bands (cm⁻¹): 3319s (ν_{NH}), 1674 (ν_{CO}). EI MS: m/z 375, M^+ .

***N,N'*-Bis(2-picoly)amine L¹²:** 2-(Aminomethyl)pyridine (5.41 g, 50 mmol) was dissolved in ethanol (15 cm³) and added dropwise over a period of 15 mins to a solution of pyridine-2-carboxaldehyde (5.38 g, 50 mmol) in ethanol (50 cm³). The mixture was stirred for 15 mins at room temperature and sodium borohydride (3.78 g, 100 mmol) was added as a solid in small portions. After complete addition the mixture was refluxed for 1 hr and afterwards cooled in an ice/salt bath and acidified to pH 2 with concentrated hydrochloric acid (12 M). The resulting white precipitate was filtered off and the filtrate evaporated under reduced pressure to give an oil. This was added to concentrated hydrochloric acid (20 cm³), ethanol (80 cm³) and diethyl ether (50 cm³). The clear solution was stored at -20 °C overnight, a white precipitate of L¹².3HCl was filtered off and dried. The trihydrochloride salt was treated with a twenty-fold excess of sodium hydroxide in water, extracted into dichloromethane (5 x 50 cm³), dried over magnesium sulfate followed by evaporation under reduced pressure yielding L¹² as a pale yellow oil. Yield 6.0 g (36 %). Found (calc. for C₁₂H₁₃N₃): C 70.05 (72.33), H 7.02 (6.58), N 21.42 (21.09) %. δ_{H} (CDCl₃): 8.52 (dd, *J* = 1 and 5, C₅H₄N), 7.60 (dt, 2H, *J* = 2 and 8, C₅H₄N), 7.32 (dd, 2H, *J* = 1 and 8, C₅H₄N), 7.11 (dd, 2H, *J* = 5 and 8 Hz, C₅H₄N), 3.94 (s, 4H, CH₂), 2.57 (s, 1H, NH). Selected IR bands (cm⁻¹): 3310s (ν_{NH}). EI MS: *m/z* 199, *M*⁺.

***N,N'*-Bis(pyridine-2-carboxaldimino)diaminoethane L¹³:** A solution of 1,2-diaminoethane (1.5 g, 25 mmol) in ethanol (15 cm³) was added dropwise over 15 mins to a solution of pyridine-2-carboxaldehyde (5.38 g, 50 mmol) in ethanol (50 cm³). The solution was stirred for 2 hrs, the solvent was evaporated under reduced pressure and the crude product was extracted with boiling 40-60 °C petroleum ether (8 x 20 cm³). Upon cooling of the combined petroleum washings to room temperature L¹³ deposited as yellow crystals. Yield 3.8 g (64 %). Found (calc. for C₁₄H₁₄N₄): C 70.66 (70.56), H 5.64 (5.92), N 23.97 (23.52) %. δ_{H} (CDCl₃): 8.72 (ddd, 2H, *J* = 1, 2 and 5, C₅H₄N), 8.52 (s, 2H, CH=N), 8.08 (dt, 2H, *J* = 1.5 and 7.5, C₅H₄N), 7.82 (dt, 2H, *J* = 1.5 and 7.5, C₅H₄N), 7.39 (ddd, 2H, *J* = 1, 5 and 7.5 Hz, C₅H₄N), 4.17 (s, 4H, CH₂). Selected IR bands (cm⁻¹): 1647s (ν_{C=N}).

***N,N'*-Bis(pyridine-2-carboxoketimino)diaminoethane L¹⁴**: A solution of 1,2-diaminoethane (0.81 g, 13 mmol) in ethanol (5 cm³) was added dropwise over 15 mins to 2-acetylpyridine (3.25 g, 27 mmol) in ethanol (20 cm³). The reaction mixture was stirred for 2 hrs, during which time the solution turned blue. The solvent was evaporated under reduced pressure, the green solid was extracted with boiling 40-60 °C petroleum ether (8 x 20 cm³). Upon cooling of the combined petroleum washings to room temperature L¹⁴ deposited as yellow crystals. Yield 2.8 g (72 %). δ_{H} (CDCl₃): 8.68 (dd, 2H, $J = 1$ and 5, C₅H₄N), 8.17 (dd, 2H, $J = 1.5$ and 7.5, C₅H₄N), 7.78 (dt, 2H, $J = 2$ and 7.5, C₅H₄N), 7.36 (ddd, 2H, $J = 1, 3$ and 7.5 Hz, C₅H₄N), 4.07 (s, 4H, CH₂), 2.53 (s, 6H, CH₃). Selected IR bands (cm⁻¹): 1631s ($\nu_{\text{C=N}}$).

***N,N',N''*-Tris-2-(pyridine-2-carboxaldimino)ethylamine L¹⁵**: Tris(2-aminoethyl)amine (0.51 cm³, 0.5 g, 3.42 mmol), 2-pyridinecarboxaldehyde (0.98 cm³, 1.10 g, 10.3 mmol) and toluene (90 cm³) were added to powdered 4 Å molecular sieves (10.0 g, activated at 300 °C *in vacuo*) and the suspension was stirred under argon at room temperature for 12 hrs. The molecular sieves were filtered off and the filtrate was evaporated *in vacuo* to give L¹⁵ as a yellow oil. Yield 1.23 g (87 %). δ_{H} (CDCl₃): 8.62 (m, 3H, C₅H₄N), 8.36 (s, 3H, CH=N), 7.93 (m, 3H, C₅H₄N), 7.70 (dt, 3H, $J = 1.5$ and 7.5, C₅H₄N), 7.24 (m, 3H, C₅H₄N), 3.80 (td, 6H, $J = 1$ and 7, CH₂), 3.02 (t, 6H, $J = 6.5$ Hz, CH₂). Selected IR bands (neat film, cm⁻¹): 1648s ($\nu_{\text{C=N}}$).

3-[Bis-(2-pyridylethyl)amine]propanoic acid (bppH): 3-Bromopropanoic acid (2.81 g, 18 mmol), *N,N'*-bis(picoly)amine (5.16 g, 26 mmol) and triethylamine (11.0 cm³, 8.0 g, 79 mmol) were heated together in ethanol (40 cm³) under dinitrogen for 30 hrs. Upon cooling of the clear orange solution to room temperature triethylamine hydrobromide precipitated out and was removed by filtration. Diethyl ether was added and the solution was kept at -20 °C. The colourless precipitate was filtered off and analysed by ¹H NMR. If the solid was found to be triethylamine hydrobromide it was collected by filtration and discarded. This process was repeated until bppH was collected as an off-white solid. Yield 1.51 g (31 %). δ_{H} (D₂O): 8.51 (d, 1H, $J = 5$, C₅H₄N), 7.85 (t, 1H, J

= 8, C₅H₄N), 7.44 (m, 2H, C₅H₄N), 4.45 (s, 2H, C₅H₄NCH₂N), 3.45 (t, 1H, *J* = 6, NCH₂CH₂), 2.62 (t, 1H, *J* = 6 Hz, CH₂CH₂COOH). Selected IR bands (cm⁻¹): 2493m,br (ν_{OH}), 1706s (ν_{CO}). EI MS: *m/z* 271, *M*⁺.

Synthesis of Metal Complexes

[FeL¹³]Cl₂: L¹³ (0.67 g, 2.8 mmol) in ethanol (10 cm³) was added to iron(II) chloride tetrahydrate (0.56 g, 2.8 mmol) in ethanol (5 cm³), immediately giving a purple mixture which was stirred for 15 mins. Addition of diethyl ether (200 cm³) gave a purple solid. Yield 1.06 g (98 %). Found (calc. for C₁₄H₁₄Cl₂FeN₄): C 42.65 (46.15), H 4.59 (3.88), N 13.58 (15.39) %. Selected IR bands (cm⁻¹): 3395s (ν_{NH} or ν_{OH}), 1595s (ν_{C=N}). FAB⁺ MS: *m/z* 294, [FeL¹³]⁺.

[FeL¹⁴]Cl₂: L¹⁴ (0.32 g, 1.22 mmol) suspended in ethanol (10 cm³) was added to iron(II) chloride tetrahydrate (0.24 g, 1.22 mol) in ethanol (5 cm³). The reaction solution immediately turned purple and a precipitate formed which redissolved upon complete addition of L¹⁴. The deep purple mixture was allowed to stand for 90 mins, after which the addition of diethyl ether (200 cm³) precipitated a green solid. The filtrate was reduced in volume to *ca.* 5 cm³, addition of diethyl ether (200 cm³) precipitated a purple solid.

Green product. Yield 0.15 g (31 %). Selected IR bands (cm⁻¹): 3414, 3218 (ν_{NH} or ν_{OH}), 1635m (ν_{C=N}).

Purple product. Yield 0.22 g (46 %). Found (calc. for C₁₄H₁₄Cl₂FeN₄): C 42.65 (46.15), H 4.59 (3.88), N 13.58 (15.39) %. Selected IR bands (cm⁻¹): 3406s, 3218s, 3107m (ν_{NH} or ν_{OH}), 1637m (ν_{C=N}). FAB⁺ MS: *m/z* 357 [Fe(L¹⁴)Cl]⁺, 322 [FeL¹⁴]⁺.

[FeL¹⁶][ClO₄]₂: 2,6-Diacetylpyridine (1.0 g, 6.1 mmol) and 2-(aminomethyl)pyridine (1.32 g, 12.2 mmol) were stirred in methanol (50 cm³) under ambient conditions, giving a yellow solution. Addition of iron(II) perchlorate hexahydrate (2.21 g, 6.1 mmol) immediately gave a purple precipitate, which was collected by filtration and washed with diethyl ether. Yield 1.7 g (47 %). Found (calc. for C₂₁H₂₁Cl₂FeN₅O₈): C 43.62 (42.17), H 3.86

(3.54), N 10.68 (11.71) %. Selected IR bands (cm^{-1}): 1697m ($\nu_{\text{C}=\text{N}}$), 1095vs, 623m ($\nu_{\text{perchlorate}}$). FAB⁺ MS: m/z 398, $[\text{FeL}^{16}]^+$. A second crop of maroon solid (0.19 g) was isolated from the filtrate upon addition of diethyl ether.

[{Fe(bpp)(H₂O)}₂(μ_2 -O)][ClO₄]₂: BppH (105 mg, 0.39 mmol) and triethylamine (0.05 cm³) were dissolved in 1:1 v/v methanol-water (1 cm³). Iron(III) perchlorate hexahydrate (207 mg, 0.45 mmol) in methanol (0.5 cm³) was added, instantly giving a red solution. The solution was left to evaporate over several days, leaving red crystals, which were washed with methanol. Yield 79 mg (21 %). Found (calc. for C₃₀H₃₂Cl₂Fe₂N₆O₁₃.4H₂O): C 38.95 (38.35), H 3.86 (4.30), N 9.04 (8.95) %.

[pyH][Fe(dipic)(Hdipic)(py)₂]: Iron powder (320 mg, 5.7 mmol) and H₂dipic (1.80 g, 10.8 mmol) were heated in pyridine (50 cm³) at 110 °C under argon for 5 hrs. The red solution was filtered anaerobically while hot to remove unreacted iron and the filtrate cooled to -20 °C. Red crystals of [pyH][Fe(dipic)(Hdipic)(py)₂].3py suitable for X-ray analysis were collected by filtration under argon, concentration of the filtrate *in vacuo* gave a second crop of complex. Yield 2.29 g (74 %). Found (calc. for C₂₄H₁₇FeO₈N₄): C 52.24 (52.87), H 3.19 (3.14), N 9.85 (10.28) %. Selected IR bands (cm^{-1}): 3435s (ν_{OH}), 1673s, 1648s, 1368s, 1350s (ν_{COO}). FAB⁺ MS: m/z 388, $[\text{Fe}(\text{dipic})]^+$.

[{Fe(dipic)(py)₂}₂(μ_2 -O)]: Under aerobic conditions [pyH][Fe(dipic)(Hdipic)(py)₂] (200 mg) was dissolved in pyridine (10 cm³) with sonication, giving a red solution with some colourless precipitate. This was filtered off, the filtrate was left open to air for 12 hrs. Deep red crystals of [{Fe(dipic)(py)₂}₂(μ_2 -O)].2py.H₂O (118 mg) suitable for X-ray analysis were collected by suction filtration. Over *ca.* 96 hrs at room temperature in a closed sample vial the crystals changed colour from dark red to beige with a strong smell of pyridine. Microanalysis suggested conversion to [{Fe(dipic)(H₂O)₂}₂(μ_2 -O)]. Found (calc. for C₁₄H₁₄Fe₂N₂O₁₃): C 31.91 (31.73), H 2.43 (2.66), N 5.24 (5.28) %. Selected IR bands (cm^{-1}): 3462s, 2923s (ν_{OH}), 1656s, 1626s, 1379s, 1366s (ν_{COO}).

[Fe(quin)₂(py)₂]: Iron powder (75 mg, 1.35 mmol) and Hquin (352 mg, 2.03 mmol) were suspended in pyridine (40 cm³) and heated at 110 °C for 3.5 hrs under argon. Unreacted iron powder was filtered off anaerobically. [Fe(quin)₂(py)₂] precipitated as a red solid upon cooling of the filtrate to room temperature and was collected by filtration under argon. Yield 370 mg (49 %). Found (calc. for C₃₀H₂₂FeN₄O₄): C 63.92 (64.53), H 3.99 (3.97), N 9.80 (10.03) %. Selected IR bands (cm⁻¹): 1652s, 1361m (ν_{COO}).

[Fe₂(μ₂-OH)₂(quin)₄]: Hquin (256 mg, 1.45 mmol) was added to iron(III) nitrate nonahydrate (194 g, 0.48 mmol) in methanol (10 cm³), giving a yellow solution. Addition of diethyl ether precipitated a yellow solid. Yield 295 mg (80 %). Found (calc. for C₄₀H₂₆Fe₂N₄O₆·2H₂O): C 55.71 (55.20), H 3.03 (3.47), N 6.37 (6.44) %. Selected IR bands (cm⁻¹): 3456m (ν_{OH}), 1663s, 1372s (ν_{COO}). FAB⁺ MS: *m/z* 802, [M⁺ - 2OH].

[Fe(dm_f)₆][ClO₄]₃: Iron(III) perchlorate hexahydrate (10.0 g, 21.6 mmol) was placed in a Schlenk flask under dinitrogen and anhydrous dm_f (30 cm³) was added. The mixture was stirred for 0.5 hrs, during which time heat was evolved and the colour changed from pink to orange-red. The solvent was evaporated *in vacuo*. Cycles of addition of fresh dm_f (30 cm³) and evaporation *in vacuo* were repeated until the product maintained a bright yellow-green microcrystalline appearance. The product was stored under dinitrogen.

Pyridine Dicarboxamide Complexes

These complexes were prepared by the same general procedures as follows: Sodium hydride (2.6 mmol, 60 % *w/w* in mineral oil) was washed with hexane (2 x 10 cm³) under dinitrogen and H₂L (2.6 mmol) was added as a solid in one portion. Upon addition of dm_f (5 cm³) the pale yellow solution effervesced for a few seconds. A solution of iron(III) hexakis(dimethylformamide) perchlorate (1.3 mmol) in dm_f (5 cm³) was added by syringe, giving a red solution. Stirring was continued for 18 hrs, the solvent was evaporated *in vacuo*, the crude red product was washed with acetonitrile (20 cm³) and collected by filtration.

Isolated yields of crude products were typically 20-25 %. Small quantities of purified material were obtained by vapour diffusion of diethyl ether into 1:1 v/v dmf-acetonitrile solutions of the complexes over several days at room temperature.

Na[Fe(L¹)₂]: Selected IR bands (cm⁻¹): 1604s (ν_{CO}). ES MS: *m/z* 714, [M].

Na[Fe(L²)₂]: ES MS: *m/z* 826, [M].

Na[Fe(L³)₂]: Found (calc. for C₃₈H₃₀FeNaN₁₀O₄·2H₂O): C 56.96 (56.66), H 3.74 (4.25), N 17.30 (17.38) %. Selected IR bands (cm⁻¹): 1595s (ν_{CO}). ES MS: *m/z* 348 [HL⁺].

Na[Fe(L⁷)₂]: Found (calc. for C₃₄H₂₂FeNaN₁₀O₄·3H₂O): C 52.39 (53.21), H 3.28 (3.68), N 17.91 (18.25) %. Selected IR bands (cm⁻¹): 1599s (ν_{CO}). ES MS: No peaks were assignable.

Na[Fe(L⁹)₂]: Found (calc. for C₃₄H₂₂FeNaN₁₀O₄·3H₂O): C 53.08 (53.21), H 3.41 (3.68), N 18.06 (18.25) %. Selected IR bands (cm⁻¹): 1596s (ν_{CO}). ES MS: *m/z* 320 [HL⁺], 342 [HL⁺ + Na].

Na[Fe(L¹⁰)₂]: Selected IR bands (cm⁻¹): 1594s (ν_{CO}).

[Fe(bipy)₃]Cl₂: 2,2'-Bipy (2.36 g, 15.1 mmol) was added to iron(II) chloride tetrahydrate (1.0 g, 5.0 mmol) in methanol (20 cm³), immediately forming a deep red solution. The solution was stirred for 10 mins and then concentrated under reduced pressure. Addition of diethyl ether induced precipitation. The crude product was recrystallised as maroon needles from methanol. Yield 2.36 g (79 %).

[Fe(L¹²)₂][BF₄]₂: Under an argon atmosphere, L¹² (1.96 g, 11.5 mmol) in ethanol (20 cm³) was added to a solution of iron(II) chloride tetrahydrate (1.08 g, 5.4 mmol) and ascorbic acid (53 mg, 0.3 mmol) in distilled water (10 cm³), turning the yellow solution to brown. Addition of sodium tetrafluoroborate (0.86

g, 7.8 mmol) in small portions precipitated the complex as a brown solid. Yield 1.64 g (50 %). Found (calc. for $C_{24}H_{26}B_2F_8FeN_6$): C 46.14 (45.90), H 3.79 (4.17), N 17.98 (13.38). Selected IR bands (cm^{-1}): 3294m (ν_{NH}), 1066vs ($\nu_{tetrafluoroborate}$). FAB⁺ MS: m/z 473, $[Fe(L^9)_2 + H_2O]$.

[Fe(pyterpy)₂][ClO₄]₂: Pyterpy (0.254 g, 0.8 moles) was added as a solid in two portions to iron(II) perchlorate hexahydrate (0.150 g, 0.4 moles) in ethanol (10 cm³). On addition of the first portion, the solution immediately turned purple. Addition of the second portion precipitated the complex. After stirring for 5 mins the purple crystalline solid was filtered off. Yield 276 mg (77 %). Found (calc. for $C_{40}H_{28}N_8Cl_2FeO_8$): C 62.67 (54.91), H 3.13 (3.23), N 14.64 (12.82) %. δ_H (CD₃CN): 9.23 (s, 2H, C₅H₂N), 9.01 (d, 2H, $J = 6$, C₅H₄N-4), 8.62 (d, 2H, $J = 8$, C₅H₄N-2), 8.25 (d, 2H, $J = 6$, C₅H₄N-4), 7.92 (t, 2H, $J = 9$, C₅H₄N-2), 7.18 (d, 2H, $J = 5$, C₅H₄N-2), 7.10 (t, 2H, $J = 7$ Hz, C₅H₄N-2). Selected IR bands (cm^{-1}): 1088s, 620m ($\nu_{perchlorate}$). FAB⁺ MS: m/z 676, $[M^+ - ClO_4]$.

[{Fe(tpa)}₂(μ_2 -O)][ClO₄]₄: Tpa.3HClO₄ (0.59 g, 1.0 mmol) was dissolved in methanol (20 cm³). Triethylamine (0.45 g, 0.63 cm³, 4.5 mmol) and iron(III) perchlorate hexahydrate (0.35 g, 0.75 mmol) were added, giving a dark green solution. After 24 hrs a dark green precipitate appeared. Yield 0.25 g (60 %). Selected IR bands (cm^{-1}): 1099vs, 623s ($\nu_{perchlorate}$).

- 1 J. Lin, J. Y. Zhang, Y. Xu, X. K. Ke and Z. Guo, *Acta Cryst.*, 2001, **C57**, 192.
- 2 D. A. Conlon and N. Yasuda, *Adv. Synth. Catal.*, 2001, **1**, 343.
- 3 H. Kurosaki, R. K. Sharma, S. Aoki, T. Inoue, Y. Okamoto, Y. Sugiura, M. Doi, T. Ishida, M. Otsuka and M. Goto, *J. Chem. Soc., Dalton Trans.*, 2001, 441.
- 4 J. Zhang, Q. Liu, C. Duan, Y. Shao, J. Ding, Z. Miao, X. You and Z. Guo, *J. Chem. Soc., Dalton Trans.*, 2002, 591.
- 5 W. H. Leung, J. X. Ma, V. V. W. Yam, C. M. Che and C. K. Poon, *J. Chem. Soc., Dalton Trans.*, 1991, 1071.
- 6 B. M. Trost and I. Hachiya, *J. Am. Chem. Soc.*, 1998, **120**, 1104.
- 7 S. R. Collinson, T. Gelbrick, M. B. Hursthouse and J. H. R. Tucker, *Chem. Commun.*, 2001, 555.
- 8 I. Huc, M. J. Krische, D. P. Funeriu and J. M. Lehn, *Eur. J. Inorg. Chem.*, 1999, 1415.
- 9 J. D. Epperson, L. J. Ming, G. R. Baker and G. R. Newkome, *J. Am. Chem. Soc.*, 2001, **123**, 8583.
- 10 E. S. Nikitskaja, V. S. Usovskaja and M. V. Rubtsov, *Zh. Obsch. Khim.*, 1958, 161.
- 11 R. L. Chapman and R. S. Vagg, *Inorg. Chim. Acta*, 1979, **33**, 227.
- 12 M. J. Upadhyay, P. K. Bhattacharya, P. A. Ganeshpure and S. Satish, *J. Mol. Catal.*, 1994, **88**, 287.
- 13 F. A. Chavez, M. M. Olmstead and P. K. Mascharak, *Inorg. Chem.*, 1996, **35**, 1410.
- 14 D. S. Marlin, M. M. Olmstead and P. K. Mascharak, *Inorg. Chem.*, 1999, **38**, 3258.
- 15 D. S. Marlin, M. M. Olmstead and P. K. Mascharak, *J. Mol. Struct.*, 2000, **554**, 211.
- 16 H. J. Hoorn, P. de Joode, W. L. Driessen and J. Reedijk, *Rec. Trav. Pays-Bas*, 1996, **115**, 191.
- 17 G. W. V. Cave and C. A. Raston, *J. Chem. Soc., Chem. Commun.*, 2000, 2199.

- 18 P. E. Figgins and D. H. Busch, *J. Am. Chem. Soc.*, 1960, **82**, 820.
- 19 A. Jantti, M. Wagner, R. Suontamo, E. Kolehmainen and K. Rissanen, *Eur. J. Inorg. Chem.*, 1998, 1555.
- 20 M. Casny and D. Rehder, *Chem. Commun.*, 2001, 921.
- 21 A. Hazell, K. B. Jensen, C. J. Mckenzie and H. Toftlund, *J. Chem. Soc., Dalton Trans.*, 1993, 3249.
- 22 M. Devereux, M. McCann, V. Leon, V. McKee and R. J. Ball, *Polyhedron*, 2002, **21**, 1063.
- 23 L. Yang, D. C. Crans, S. M. Miller, A. la Cour, O. P. Anderson, P. M. Kaszynski, M. E. Godzala, L. D. Austin and G. R. Willsky, *Inorg. Chem.*, 2002, **41**, in press.
- 24 P. Laine, A. Gourdon, J. P. Launay and J. P. Tuchagues, *Inorg. Chem.*, 1995, **34**, 5150.
- 25 J. Thich, C. C. Ou, D. Powers, B. Vasiliou, D. Mastropaolo, J. A. Potenza and H. J. Schugar, *J. Am. Chem. Soc.*, 1976, **98**, 1425.
- 26 C. C. Ou, R. G. Wollmann, D. N. Hendrickson, J. A. Potenza and H. J. Schugar, *J. Am. Chem. Soc.*, 1978, **100**, 4717.
- 27 P. Laine, A. Gourdon and J. P. Launay, *Inorg. Chem.*, 1995, **34**, 5129.
- 28 G. S. Sanyal, R. Ganguly, P. K. Nath and R. J. Butcher, *J. Indian Chem. Soc.*, 2002, **79**, 489.
- 29 J. F. Hseu, J. J. Chen, C. C. Chuang, H. H. Wei, M. C. Cheng, Y. Wang and Y. D. Yau, *Inorg. Chim. Acta*, 1991, **184**, 1.
- 30 K. Hashimoto, S. Nagatomo, S. Fujinami, H. Furutachi, S. Ogo, M. Suzuki, A. Uehara, Y. Maeda, Y. Watanabe and T. Kitagawa, *Angew. Chem., Int. Ed. Engl.*, 2002, **41**, 1202.
- 31 S. A. G. Hoegberg, K. Madan, C. Moberg, B. Sjoeborg, M. Weber and M. Muhammed, *Polyhedron*, 1985, **4**, 971.
- 32 F. A. Chavez, C. V. Nguyen, M. M. Olmstead and P. K. Mascharak, *Inorg. Chem.*, 1996, **35**, 6282.
- 33 D. S. Marlin, M. M. Olmstead and P. K. Mascharak, *Inorg. Chem.*, 1999, **38**, 3258.
- 34 M. Ray, D. Ghosh, Z. Shiriu and R. Mukherjee, *Inorg. Chem.*, 1997, **36**, 3568.

- 35 G. J. P. Britovsek, V. C. Gibson, B. S. Kimberley, S. Mastroianni, C. Redshaw, G. A. Solan, A. J. P. White and D. J. Williams, *J. Chem. Soc., Dalton Trans.*, 2001, 1639.
- 36 V. C. Gibson, R. K. O'Reilly, W. Reed, D. F. Wass, A. J. P. White and D. J. Williams, *Chem. Commun.*, 2002, 1850.
- 37 A. J. Conti, C. L. Xie and D. Hendrickson, *J. Am. Chem. Soc.*, 1989, **111**, 1171.
- 38 A. I. Kakolyri, MSc thesis, University of St Andrews, 1999.
- 39 G. Chiericato, C. R. Arana, C. Casado, I Cuadrado and H. D. Abruna, *Inorg. Chim. Acta*, 2000, **300/302**, 32.
- 40 R. J. Butcher and A. W. Addison, *Inorg. Chim. Acta*, 1989, **158**, 211.
- 41 E. C. Constable and A. M. W. C. Thompson, *J. Chem. Soc., Dalton Trans.*, 1992, 2947.
- 42 R. A. Leising, B. A. Brennan, L. Que, B. G. Fox and E. Munck, *J. Am. Chem. Soc.*, 1991, **113**, 3988.
- 43 B. G. Gafford and R. H. Holwerda, *Inorg. Chem.*, 1989, **28**, 60.

Chapter Four

Coordination Chemistry of Copper(II) with Polydentate Nitrogen Donor Ligands

4.1 Introduction

From their inception in 1983, the Gif family of oxidants employed metallic iron or iron salts for catalytic oxidation of hydrocarbons. In 1991 the GoChAgg system was added to the Gif family, utilising a copper(II) catalyst and hydrogen peroxide to oxidise saturated cyclic hydrocarbons to ketones and alcohols in an analogous fashion to its iron counterparts.¹⁻³ One notable difference between iron and copper based oxidation systems was observed with copper(II) acetate/*t*-BuOOH in pyridine-acetic acid, where cycloalkanes were dehydrogenated to cycloalkenes, whereas ketone formation occurred with iron(III)/*t*-BuOOH.⁴ A later publication reported that in addition to cyclohexene, both cyclohexanol and cyclohexanone were also formed, as well as cyclohexen-3-one and cyclohexen-3-ol.⁵ The use of copper(II) complexes for hydrocarbon oxidation under Gif conditions has received scant attention, and the factors determining catalytic activity and selectivity remain poorly understood. Can copper(II) complexes containing chelate ligands with 2-pyridyl substituents oxidise saturated cyclic hydrocarbons in the absence/presence of pyridine? The syntheses of copper(II) complexes using polydentate pyridine dicarboxamides and chelating ligands containing 2-pyridyl groups forms the focus of this Chapter.

4.2 Reactions of Pyridine Dicarboxamide Ligands with Copper(II)

Pyridine dicarboxamide ligands support a range of coordination numbers, geometries and nuclearities for copper(II),⁶⁻¹¹ the flexibility of the ligand

backbone dictating the structural motif adopted. Kurosaki *et al.*⁶ have demonstrated that ligands similar to H_2L^{11} containing histidine rather than 2-pyridyl groups reacted with copper(II) acetate monohydrate to form mononuclear complexes; X-ray crystallographic analysis confirmed deprotonation of the amide groups and chelation of the copper(II) centre by the five nitrogen atoms of the dianion. *N,N'*-bis(phenyl)pyridine-2,6-dicarboxamide (H_2L^{Ph}) in its dianionic form (L^{Ph}^{2-}) reacted with copper(II) acetate monohydrate to give $[Cu_2L^{Ph}_2(\mu-OH)]^-$, in which (L^{Ph}^{2-}) is tridentate.¹² As the ligand arms elongate by one methylene unit from H_2L^{10} to H_2L^{11} dimeric⁷ $[Cu_2(L^{10})_2]$ becomes monomeric $[CuL^{11}]$ in which (L^{11}^{2-}) is pentadentate with a distorted square pyramidal arrangement at copper(II).⁹ Also, $H[CuBr_2(S-PEPDAH)]$, where $S-PEPDAH_2 = N,N'$ -bis[*S*-1-(2-pyridyl)ethyl]pyridine-2,6-dicarboxamide, in which the anion coordinates through the nitrogen atoms of a terminal pyridine, a deprotonated carboxamide and the central pyridine, undergoes reversible conversion to a dinuclear chiral helicate $[\{Cu(S-PEPDA)\}_2]$ when treated with triethylamine.¹³ *N,N'*-Bis(8-quinolyl)pyridine-2,6-dicarboxamide selectively extracted copper(II) ions into chloroform from an aqueous phase containing several divalent ions, suggesting a potential new application for pyridine dicarboxamide ligands.¹⁴

Copper(II) complexes with pyridine dicarboxamide ligands using copper(II) acetate monohydrate and copper(II) tetrakis(pyridine) perchlorate as precursors have been prepared and as expected, there are substantial differences in the products obtained using these two complexes.

4.2.1 The Reaction of Copper(II) Acetate Monohydrate with H_2L^7

Copper(II) acetate monohydrate reacted with H_2L^7 (molar ratio 3:2) in methanol-chloroform at room temperature to give a green complex (employing an equimolar ratio led to the same product contaminated with unreacted H_2L^7). IR spectroscopy confirmed, by the absence of ν_{NH} bands, that ligand deprotonation had occurred, with ν_{CO} (1630 cm^{-1}) *ca.* 70 cm^{-1} lower than in H_2L^7 (1701 cm^{-1}),

however neither FAB⁺ MS (*m/z* 824) nor microanalytical data were readily interpreted.

X-ray crystallography revealed the complex to be a trimetallic species [Cu₃(L⁷)₂(μ₂-OAc)₂], in which two H₂L⁷ ligands are doubly deprotonated at the amidic nitrogens and span three copper atoms (Figure 4.1, Table 4.1). The complex co-crystallised from chloroform with one molecule of solvent. The internal copper centre Cu(3) is bound by the nitrogen atoms N(10) and N(40) from the central pyridyl rings of each (L⁷)²⁻ anion, while Cu(1) and Cu(2) are chelated by the carboxamide and pyridyl nitrogen atoms of each ligand arm to give two CuC₂N₂ rings per terminal metal centre. Two μ₂-acetato groups bridging adjacent copper centres [Cu(1)...Cu(3) and Cu(3)...Cu(2)] complete the molecular structure.

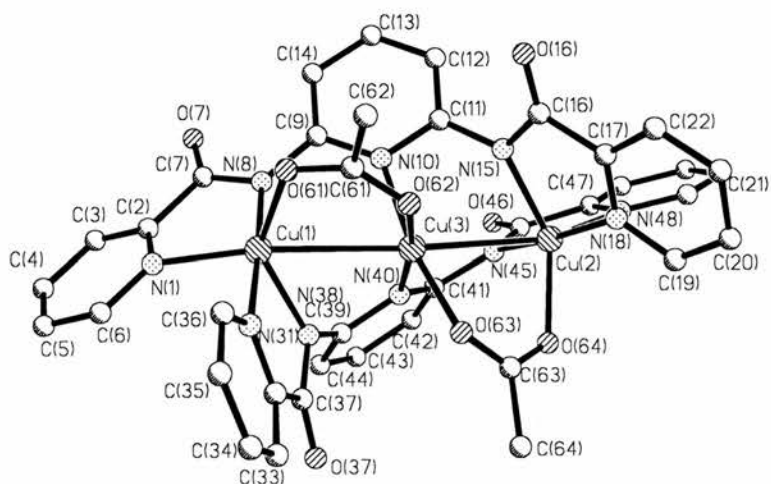


Figure 4.1: Molecular structure of [Cu₃(L⁷)₂(μ₂-OAc)₂].CHCl₃ (C-H bonds and chloroform solvate molecule omitted for clarity).

Table 4.1: Selected bond lengths (Å) and angles (°) for [Cu₃(L⁷)₂(μ₂-OAc)₂].CHCl₃ (esd's in parentheses).

Cu(1)-N(8)	1.965(11)	C(7)-N(8)	1.381(15)
Cu(1)-N(31)	2.001(10)	N(8)-C(9)	1.388(14)
Cu(1)-O(61)	2.029(9)	C(11)-N(15)	1.397(13)
Cu(1)-N(38)	2.073(9)	N(15)-C(16)	1.364(14)
Cu(1)-N(1)	2.103(11)	C(16)-O(16)	1.221(13)
Cu(2)-N(45)	1.981(9)	C(37)-O(37)	1.240(13)

Cu(2)-N(18)	2.000(9)	C(37)-N(38)	1.345(14)
Cu(2)-O(64)	2.036(8)	N(38)-C(39)	1.393(15)
Cu(2)-N(15)	2.065(9)	C(41)-N(45)	1.441(14)
Cu(2)-N(48)	2.160(11)	N(45)-C(46)	1.347(15)
Cu(3)-O(62)	1.941(7)	O(61)-C(61)	1.252(15)
Cu(3)-O(63)	1.958(7)	O(63)-C(63)	1.286(14)
Cu(3)-N(40)	1.979(9)	C(63)-O(64)	1.227(15)
Cu(3)-N(10)	2.001(9)	C(61)-O(62)	1.256(14)
N(8)-Cu(1)-N(31)	178.6(4)	N(18)-Cu(2)-N(15)	80.5(4)
N(8)-Cu(1)-O(61)	92.9(4)	O(64)-Cu(2)-N(15)	136.3(4)
N(31)-Cu(1)-O(61)	88.4(4)	N(45)-Cu(2)-N(48)	79.6(4)
N(8)-Cu(1)-N(38)	99.9(4)	N(18)-Cu(2)-N(48)	94.3(5)
N(31)-Cu(1)-N(38)	79.4(4)	O(64)-Cu(2)-N(48)	115.3(4)
O(61)-Cu(1)-N(38)	131.0(4)	N(15)-Cu(2)-N(48)	108.1(4)
N(8)-Cu(1)-N(1)	81.9(4)	N(45)-Cu(2)-Cu(3)	82.3(3)
N(31)-Cu(1)-N(1)	97.2(4)	N(18)-Cu(2)-Cu(3)	103.2(3)
O(61)-Cu(1)-N(1)	118.5(4)	O(64)-Cu(2)-Cu(3)	79.9(2)
N(38)-Cu(1)-N(1)	110.1(4)	N(15)-Cu(2)-Cu(3)	61.1(3)
N(8)-Cu(1)-Cu(3)	79.9(3)	N(48)-Cu(2)-Cu(3)	156.9(3)
N(31)-Cu(1)-Cu(3)	100.8(3)	O(62)-Cu(3)-O(63)	87.7(3)
O(61)-Cu(1)-Cu(3)	77.8(3)	O(62)-Cu(3)-N(40)	167.8(4)
N(38)-Cu(1)-Cu(3)	58.7(3)	O(63)-Cu(3)-N(40)	91.7(3)
N(1)-Cu(1)-Cu(3)	156.1(3)	O(62)-Cu(3)-N(10)	93.2(3)
N(45)-Cu(2)-N(18)	173.8(4)	O(63)-Cu(3)-N(10)	167.3(4)
N(45)-Cu(2)-O(64)	92.9(4)	N(40)-Cu(3)-N(10)	90.1(4)
N(18)-Cu(2)-O(64)	90.9(4)	O(62)-Cu(3)-Cu(2)	114.9(2)
N(45)-Cu(2)-N(15)	100.0(4)	O(63)-Cu(3)-Cu(2)	77.2(3)
N(40)-Cu(3)-Cu(2)	76.8(3)	N(40)-Cu(3)-Cu(1)	91.5(2)
N(10)-Cu(3)-Cu(2)	90.9(3)	N(10)-Cu(3)-Cu(1)	78.6(3)
O(62)-Cu(3)-Cu(1)	77.7(2)	O(63)-Cu(3)-Cu(1)	113.9(3)

The $(L^7)^{2-}$ ligands have what can loosely be described as a helicity, which is best illustrated by a consideration of N-Cu-Cu-N torsion angles; N(1)-Cu(1)-Cu(3)-N(10) and N(10)-Cu(3)-Cu(2)-N(18) are -62° and $+72^\circ$, while N(31)-Cu(1)-Cu(3)-N(40) and N(40)-Cu(3)-Cu(2)-N(48) are $+70^\circ$ and -60° respectively. This twisting of the ligand framework about the amide groups curtails electron delocalisation through the entire π -system of $(L^7)^{2-}$. Ligand helicity is also observed in $[Cu_2(L^{10})_2]$,⁷ generated from copper(II) perchlorate hexahydrate and Na_2L^{10} in methanol, the methylene groups of $(L^{10})^{2-}$ allowing greater conformational flexibility of the ligand backbone but with no potential for electron delocalisation.

Cu(1) and Cu(2) possess distorted trigonal bipyramidal $[N_4O]$ donor sets, with N(8) and N(31) for Cu(1) [N(18) and N(45) for Cu(2)] as the axial apices, Cu(1) and Cu(2) lying 0.08 and -0.07 Å respectively out of the $[N_2O]$ planes. The *cis* angles within the $[N_2O]$ equatorial planes span the range $108.1(4)$ - $136.3(4)^\circ$, the *cis* angles between axial and equatorial atoms are from $79.6(4)$ - $100.0(4)^\circ$. Cu(3) has approximately square planar *cis*- $[N_2O_2]$ geometry with *cis* and *trans* angles of $87.7(3)$ - $91.7(3)^\circ$ and $164.36(6)$ - $167.8(4)^\circ$ respectively. The two Cu_2N_2 chelates formed by each $(L^7)^{2-}$ ligand at Cu(1) and Cu(2) exhibit an unexpected asymmetry. Examining the $(L^7)^{2-}$ ligand labelled N(1)-C(22), the Cu(1)-N(8) and Cu(2)-N(15) (Cu- N_{amide}) distances are 1.965(11) Å and 2.065(9) Å respectively, while Cu(1)-N(1) and Cu(2)-N(18) (Cu- $N_{pyridyl}$) are 2.103(11) Å and 2.000(9) Å *i.e.* within each chelate ring there is one long and one short Cu-N distance, the order reversing from one half of $(L^7)^{2-}$ to the other. The $(L^7)^{2-}$ ligand labelled N(31)-C(52) behaves similarly. Inspecting the Cu- $O_{acetate}$ distances, Cu(3)-O(62) and Cu(3)-O(63) [1.941(7), 1.958(7) Å] are *ca.* 0.07 Å shorter than Cu(1)-O(61) or Cu(2)-O(62) [2.029(9), 2.036(8) Å], as a result of the different coordination geometry at Cu(3). The tricopper(II) axis is obtuse [$164.36(6)^\circ$] with intercopper distances [Cu(1)...Cu(3) 2.953(2), Cu(3)...Cu(2) 2.900(2) Å] longer than found in $[Cu_3(dpa)_4Cl_2].H_2O$ [2.471(1) Å, $dpaH = 2,2'$ -dipyridylamine]¹⁵ or $[Cu_2(OAc)_4].2H_2O$ (2.64 Å). There are no significant intermolecular contacts within the structure.

4.2.2 The Reaction of Copper(II) Acetate Monohydrate with H_2L^6

The reaction of copper(II) acetate monohydrate with H_2L^6 (3:2 molar ratio) gave $[Cu_3(L^6)_2(\mu_2-OAc)_2]$, which X-ray crystallography confirmed was isostructural with $[Cu_3(L^7)_2(\mu_2-OAc)_2]$ (Figure 4.2, Table 4.2). There are two independent molecules of the trimetallic complex in the unit cell (labelled molecules 1 and 2), the lengths and angles for the second molecule are given in square brackets in Table 4.2. Cu(1), Cu(2) and Cu(3) in molecule 1 are Cu(4), Cu(5) and Cu(6) respectively in molecule 2, for the remaining ligand atoms, atomic descriptors are sixty higher than in molecule 1, *e.g.* N(8) in molecule 1 is N(68) in molecule 2. Acetonitrile and water molecules co-crystallise with the complex. A notable difference between the structures of the $(L^7)^{2-}$ and $(L^6)^{2-}$ complexes is that in the latter there is no alternation of Cu-N_{pyridyl} and Cu-N_{amide} lengths from one half of the molecule to the other – the bonds to N_{amide} are always shorter. Otherwise the remaining bond lengths and angles are largely similar. The Cu(1)-O(23) [1.979(4), 1.987(4) Å in molecules 1 and 2] and Cu(2)-O(53) [2.018(3), 1.985(4) Å in molecules 1 and 2] lengths are marginally shorter than the $(L^7)^{2-}$ complex [2.029(9) and 2.036(8) Å], the Cu...Cu distances [2.7979(10)-3.0346(10) Å] and tricopper axis [159.97(13)^o, 163.74(3)^o] being very similar to $[Cu_3(L^7)_2(\mu_2-OAc)_2]$.

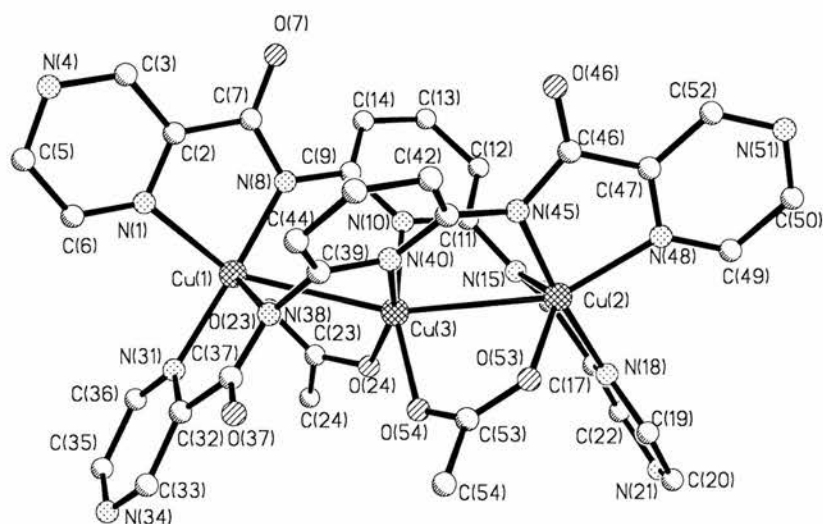


Figure 4.2: Molecular structure of $[Cu_3(L^6)_2(\mu_2-OAc)_2]$ (C-H bonds and solvate molecules omitted for clarity).

Table 4.2: Selected bond lengths (Å) and angles (°) for $[\text{Cu}_3(\text{L}^6)_2(\mu_2\text{-OAc})_2]$ (values for second independent molecule given in square brackets, esd's in parentheses).

Cu(1)-N(8)	1.960(4) [1.954(4)]	Cu(1)-O(23)	1.979(4) [1.987(4)]
Cu(1)-N(31)	2.038(5) [1.984(4)]	Cu(1)-N(38)	2.102(4) [2.047(4)]
Cu(1)-N(1)	2.121(5) [2.165(4)]	Cu(2)-N(45)	1.992(4) [1.983(5)]
Cu(2)-N(18)	2.015(4) [1.997(4)]	Cu(2)-O(53)	2.018(3) [1.985(4)]
Cu(2)-N(15)	2.099(4) [2.034(4)]	Cu(2)-N(48)	2.108(5) [2.184(4)]
Cu(3)-O(24)	1.943(4) [1.949(4)]	Cu(3)-O(54)	1.953(3) [1.965(3)]
Cu(3)-N(10)	1.963(4) [1.991(4)]	Cu(3)-N(40)	1.988(4) [2.001(5)]
N(8)-Cu(1)-O(23)	94.24(17) [93.03(17)]		
N(8)-Cu(1)-N(31)	177.57(18) [173.38(18)]		
O(23)-Cu(1)-N(31)	86.97(17) [90.71(17)]		
N(8)-Cu(1)-N(38)	101.90(17) [101.09(17)]		
O(23)-Cu(1)-N(38)	124.63(16) [136.71(14)]		
N(31)-Cu(1)-N(38)	79.08(18) [79.76(17)]		
N(8)-Cu(1)-N(1)	81.37(18) [80.73(17)]		
O(23)-Cu(1)-N(1)	135.88(15) [121.61(15)]		
N(31)-Cu(1)-N(1)	96.29(18) [92.66(16)]		
N(38)-Cu(1)-N(1)	99.03(17) [101.09(16)]		
N(45)-Cu(2)-N(18)	173.85(19) [170.8(2)]		
N(45)-Cu(2)-O(53)	92.72(15) [95.82(18)]		
N(18)-Cu(2)-O(53)	89.76(15) [90.66(15)]		
N(45)-Cu(2)-N(15)	102.34(15) [97.82(18)]		
N(18)-Cu(2)-N(15)	79.93(15) [80.68(15)]		
O(53)-Cu(2)-N(15)	133.09(16) [142.84(16)]		
N(45)-Cu(2)-N(48)	80.96(18) [79.16(19)]		
O(53)-Cu(2)-N(48)	117.83(15) [117.37(15)]		
N(15)-Cu(2)-N(48)	108.37(16) [99.11(16)]		
O(24)-Cu(3)-O(54)	86.47(14) [89.30(14)]		
O(24)-Cu(3)-N(10)	93.68(16) [90.42(16)]		
O(54)-Cu(3)-N(10)	163.14(18) [164.76(16)]		
O(24)-Cu(3)-N(40)	161.93(19) [166.97(17)]		
O(54)-Cu(3)-N(40)	91.91(15) [93.51(15)]		
N(10)-Cu(3)-N(40)	93.03(17) [90.18(16)]		

Spectroscopic and microanalytical data were in accord with the crystallographically determined structure. One interesting difference between the two trimetallic complexes is found upon examination of the crystals under a microscope. Whereas the crystals of the $(L^7)^{2-}$ complex are green, those of the $(L^6)^{2-}$ complex appear red, even though the bulk material is green.

4.2.3 Electrochemistry of $[Cu_3(L^7)_2(\mu_2-OAc)_2]$ and $[Cu_3(L^6)_2(\mu_2-OAc)_2]$

Both the trimers $[Cu_3(L^7)_2(\mu_2-OAc)_2]$ and $[Cu_3(L^6)_2(\mu_2-OAc)_2]$ have largely similar cyclic voltammetric responses on the basis of their similar structures. They have the same arrangement of donor atoms and vary only by four atoms per molecule. Figure 4.3 shows the cyclic voltammogram recorded for $[Cu_3(L^7)_2(\mu_2-OAc)_2]$ in acetonitrile, while Figure 4.4 shows the cyclic voltammogram for $[Cu_3(L^6)_2(\mu_2-OAc)_2]$ also in acetonitrile.

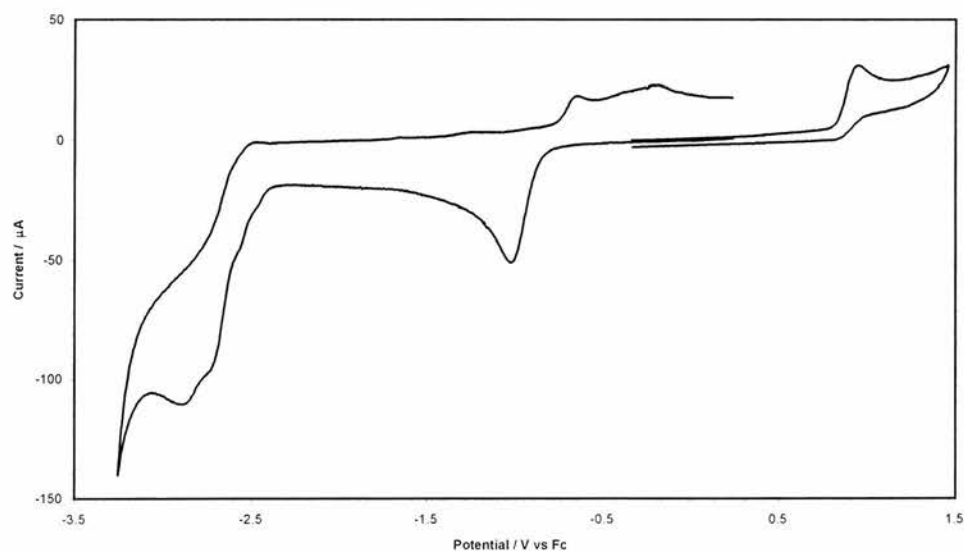


Figure 4.3: Cyclic voltammogram (100 mV s^{-1}) of $[Cu_3(L^7)_2(\mu_2-OAc)_2]$ in acetonitrile at a glassy carbon electrode (area = 0.071 cm^2). Potential referenced to ferrocene.

Both complexes display chemically irreversible reductions near $-1 \text{ V vs Fc}^{+/0}$, close to the expected potential for the copper(II/I) process. At lower temperatures ($-40 \text{ }^\circ\text{C}$), at scan rates up to 40 V s^{-1} at a platinum microelectrode

this process remained irreversible. Chronoamperometric studies (voltage stepped from 0.0 V to -1.2 V) confirmed that three electrons were involved, as in equation 4.1:

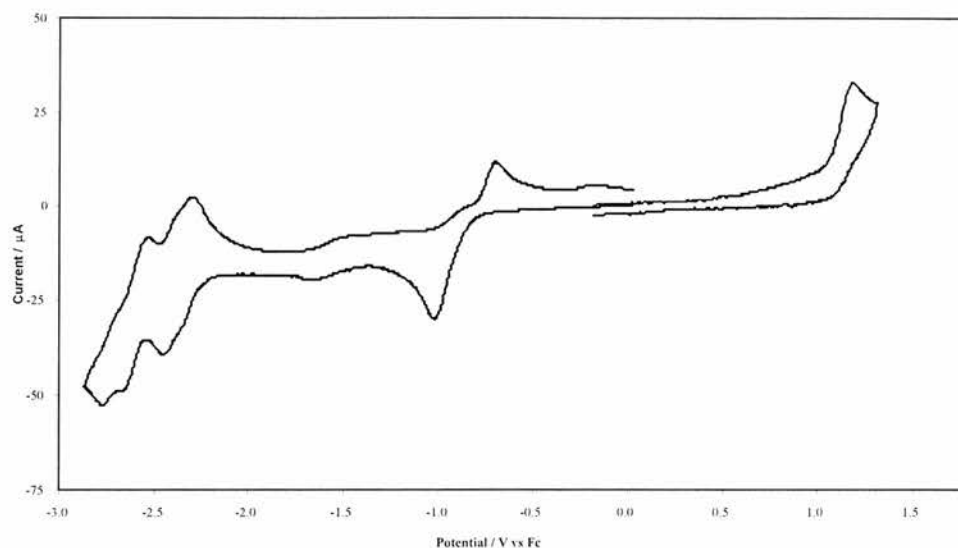
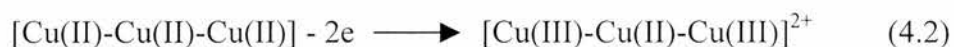


Figure 4.4: Cyclic voltammogram (100 mV s^{-1}) of $[\text{Cu}_3(\text{L}^6)_2(\mu_2\text{-OAc})_2]$ in acetonitrile at a glassy carbon electrode (area = 0.071 cm^2). Potential referenced to ferrocene.

However, it should be noted that the assignment of this process to the reduction of all three copper atoms makes the assumption that there are no following reactions which could lead to products which are themselves reducible at this potential. The reduction of $[\text{Cu}_3(\text{L}^6)_2(\mu_2\text{-OAc})_2]$ occurred at less negative potentials, as expected due to the more electron withdrawing nature of the pyrazine rings; however, again caution must be exercised, since rapid follow-up reactions can affect the position of the cathodic reduction peaks. After the copper reduction of $[\text{Cu}_3(\text{L}^7)_2(\mu_2\text{-OAc})_2]$ and $[\text{Cu}_3(\text{L}^6)_2(\mu_2\text{-OAc})_2]$ at -1 V, two new anodic peaks appear near -0.7 and -0.2 V. These peaks appear to be due to soluble species as their peak heights increase with the square root of scan rate, rather than linearly, as would be expected for a wave due to an adsorbed species. Interestingly, when using the superior solvent, dmf, the copper reduction of $[\text{Cu}_3(\text{L}^6)_2(\mu_2\text{-OAc})_2]$ was suppressed almost completely, so that the apparent

number of electrons was approximately one. We suggest that the complex may be strongly adsorbed on the electrode, perhaps *via* the pyrazine nitrogen atom, and that only one copper centre is electrochemically accessible. Other electrode surfaces (gold and platinum) exhibited similar behaviour with this solvent.

Other redox processes could be assigned as ligand-based after comparison with the free ligand cyclic voltammetric data, which on account of very poor solubility could only be measured for $[\text{Cu}_3(\text{L}^6)_2(\mu_2\text{-OAc})_2]$ in dmf and dichloromethane. The complexes also showed an irreversible, approximately two-electron oxidation process at more negative potentials than the ligand oxidation. We tentatively assign this to the oxidation of the outer copper centres, equation 4.2:



Copper in such amide environments are known to be oxidised relatively more easily.¹⁶ In principle, spectroelectrochemistry could be used to confirm this assignment but regrettably this is not possible when the oxidations are irreversible. The peak owing to the oxidation of the complex was irreversible even at scan rates up to 40 V s^{-1} at low temperature ($-40 \text{ }^\circ\text{C}$). The potentials for both this process and the copper reduction were somewhat shifted to more extreme potentials in dmf, perhaps because acetonitrile is a better solvent for the charged electrogenerated species.

The copper(II/I) reduction for $[\text{Cu}_3(\text{L}^6)_2(\mu_2\text{-OAc})_2]$ occurs at 120 mV lower than the $[\text{Cu}_3(\text{L}^7)_2(\mu_2\text{-OAc})_2]$, this is due to the electron withdrawing nature of the pyrazine groups present.

Table 4.3: Cyclic voltammetric data (100 mV s⁻¹) for trimeric copper complexes and ligands (1 mM) in 0.1 M [Bu₄N][PF₆] (V vs Fc⁺⁰) using a glassy carbon electrode (area 0.071 cm²).

Compound ^b	L ⁻²⁻	L ^{0/-}	Cu(II/I)	Cu(III/II)	L ⁺⁰
1 (dmf)	-2.865 ^c	-2.81 ^b	-1.200 ^c	-	-
1 (MeCN)	-2.623(164) ^c	-2.619 ^b	-1.148 ^c	+0.954 ^d	-
2 (dmf) ^g	-2.373 ^{c, f}	-2.373 ^{b, c}	-1.144 ^c	+0.840 ^d	-
2 (MeCN) ^h	-2.642(114)	-2.353(143)	-1.019 ^c	+1.188 ^d	+1.607 ^d

^a 1 = [Cu₃(L⁷)₂(μ₂-OAc)₂] and 2 = [Cu₃(L⁶)₂(μ₂-OAc)₂]

^b Diffusion coefficients determined to be 1.60 and 1.30 ± 0.2 × 10⁻⁵ cm² s⁻¹ for [Cu₃(L⁷)₂(μ₂-OAc)₂] and [Cu₃(L⁶)₂(μ₂-OAc)₂] respectively.

^c Cathodic peak only.

^d Anodic peak only.

^e Complex [Cu₃(L⁶)₂(μ₂-OAc)₂] was much less soluble in acetonitrile, and the cyclic voltammograms were run for this complex at half the concentration (0.5 mM).

^f Single, merged two-electron process per ligand in the complex.

^g Ligand has irreversible one-electron reductions recorded at -2.491 and -2.152 V in dmf. Oxidation at +1.397 V (irreversible; one electron process) in dichloromethane.

In order to see if the oxidation was due to the central copper [Cu(pic)₂].2H₂O was used as a model. It was found that [Cu(pic)₂].2H₂O is very insoluble in most solvents. It showed very broad CV peaks in dmf, but these sharpened up considerably in acetonitrile-1% v/v pyridine, Figure 4.5. The copper(II/I) reduction appeared at -0.987 V. Chronoamperometry confirmed this to be a one-electron reduction, and the diffusion coefficient was found to be (2.3 ± 0.2) × 10⁻⁵ cm² s⁻¹. If the potential was extended significantly more cathodically than -1.2 V than the copper(I) reduction became reversible: copper deposition occurred as evidenced by a surface wave at -2.077 V and a stripping peak at -0.509 V, followed by a broad adsorbate peak near -0.1 V. Presumably the copper(I) complex decomposes in the presence of pyridine. Cyclic voltammograms of free picH in acetonitrile or dmf showed only a reduction at *ca.* -2.5 V which was not

observed in the complex. Interestingly, the plating of copper was suppressed in the presence of dioxygen.

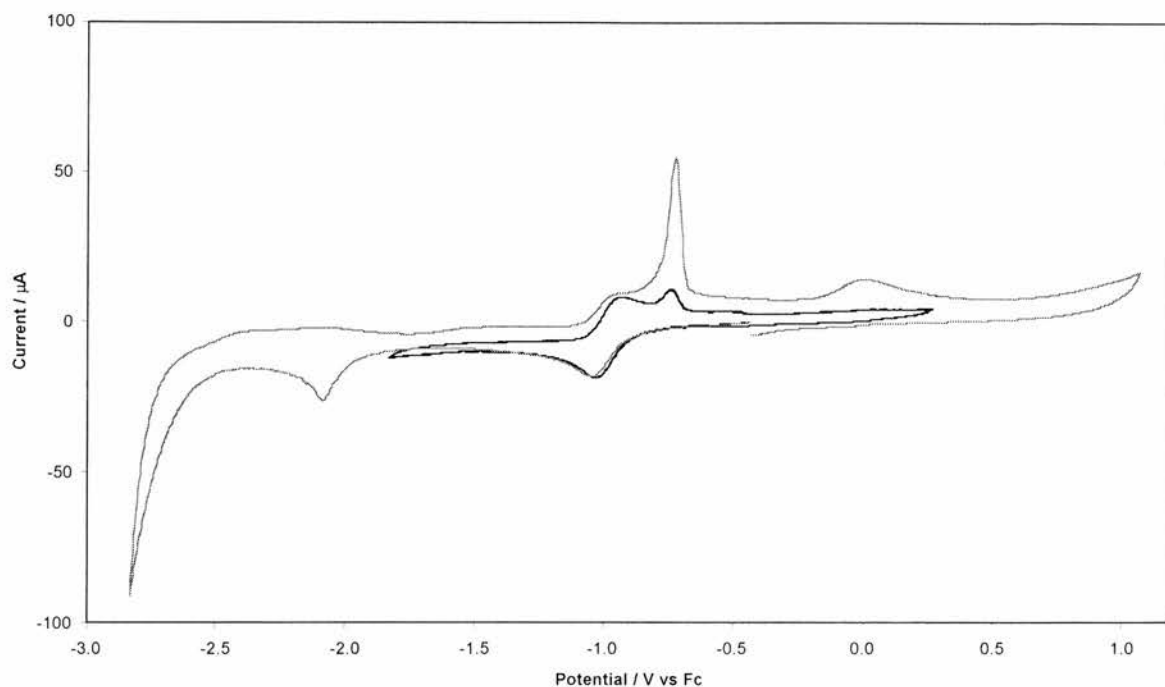


Figure 4.5: Cyclic voltammogram (100 mV s^{-1}) of $[\text{Cu}(\text{pic})_2] \cdot 2\text{H}_2\text{O}$ in acetonitrile at a glassy carbon electrode (area = 0.071 cm^2). Inner trace (bold) shows two scans between -1.8 and $+0.25 \text{ V}$. Potential referenced to ferrocene.

4.2.4 Magnetochemistry of $[\text{Cu}_3(\text{L}^7)_2(\mu_2\text{-OAc})_2]$

The magnetisation of $[\text{Cu}_3(\text{L}^7)_2(\mu_2\text{-OAc})_2]$ was measured between 1.8 and 300 K. Zero field cooled (ZFC) data was obtained in a measuring field of 200 Oe. Field cooled data was also collected, however no significant difference was observed between that and ZFC. The raw magnetisation data was converted to susceptibility using the relationship $\chi = M/H$ and adjusted to give the molar susceptibility using the mass of sample measured and the molecular weight of $[\text{Cu}_3(\text{L}^7)_2(\mu_2\text{-OAc})_2]$. The ZFC molar susceptibility data thus obtained and a best least squares fit model are shown in Figure 4.6.

The observed data were fitted to the model (equation 4.3)

$$\chi_m = \text{TIP} + C/(T + T_c) \quad (4.3)$$

where TIP is a temperature independent component to account for diamagnetism in both the sample and the sample holder, C is the Curie constant and T_c would be the Weiss or Curie temperature depending on its sense. The fit yielded the following values; TIP = 0.00589, $C = 0.42509$ and $T_c = -0.0369$ K (standard error: 0.0015097, correlation coefficient: 0.9988735). The data could be fitted using more complex models, however the fittings obtained were no better than the one given above, hence this simple model was used.

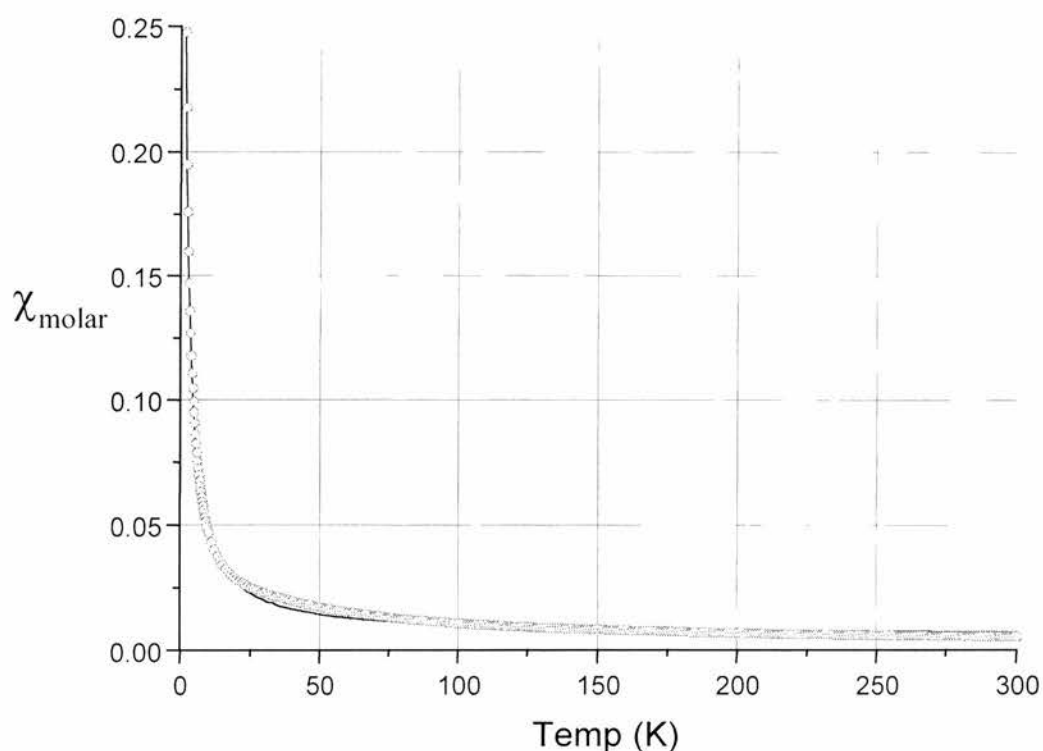
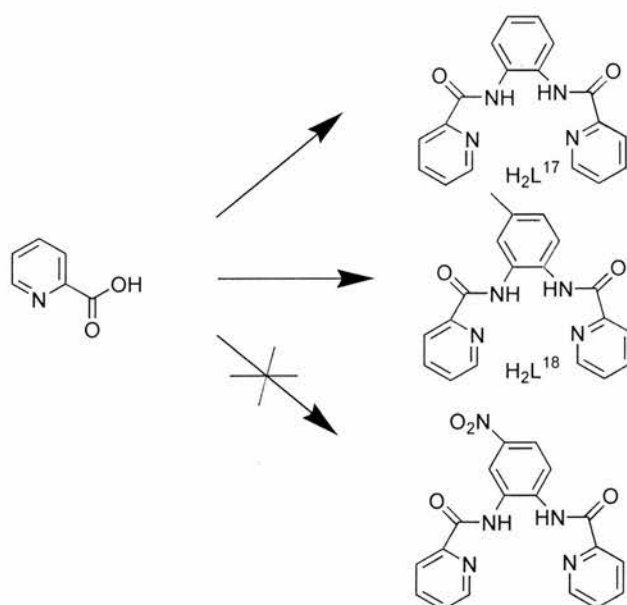


Figure 4.6: Magnetic susceptibility data for $[\text{Cu}_3(\text{L}^7)_2(\mu_2\text{-OAc})_2]$. Circles represent data points, line is best fit to model.

As Figure 4.6 demonstrates, $[\text{Cu}_3(\text{L}^7)_2(\mu_2\text{-OAc})_2]$ behaves as a simple paramagnet. Although a Weiss/Curie temperature is obtained, its value is so small that it is probably best treated with caution. These results are consistent with those of Fenton¹⁷ who noted an extremely weak antiferromagnetic interaction between adjacent copper ions $[\text{Cu}\dots\text{Cu } 3.985 \text{ \AA}]$ in another tricopper(II) complex, where direct bridging species capable of super-exchange were not present.

4.2.5 Copper(II) Complexes of Tetradentate Pyridine Dicarboxamide Ligands

The triphenylphosphite promoted condensation of 1,2-phenylenediamine with Hpic generates 1,2-bis(pyridine-2-carboxamido)benzene (H_2L^{17}) (Scheme 4.1).^{18,19} We prepared 3,4-bis(pyridine-2-carboxamido)toluene (H_2L^{18}) in 90 % yield from 3,4-diaminotoluene and Hpic by the same route. 4-Nitro-1,2-phenylenediamine did not give a corresponding dicarboxamide derivative, as the electron withdrawing influence of the nitro group deactivates the amine groups from undergoing condensation.



Scheme 4.1: Synthesis of H_2L^{17} , H_2L^{18} .

From X-ray crystallography (Figure 4.7) the pyridyl ring planes of H_2L^{18} are found to twist in opposite senses about the N-C_{tolyl} bonds relative to the toluene moiety, as seen for H_2L^{17} .⁹ Intra- and intermolecular hydrogen bonds link H(8)...O(16) (2.139 Å) and H(15)...O(7#) (2.200 Å).

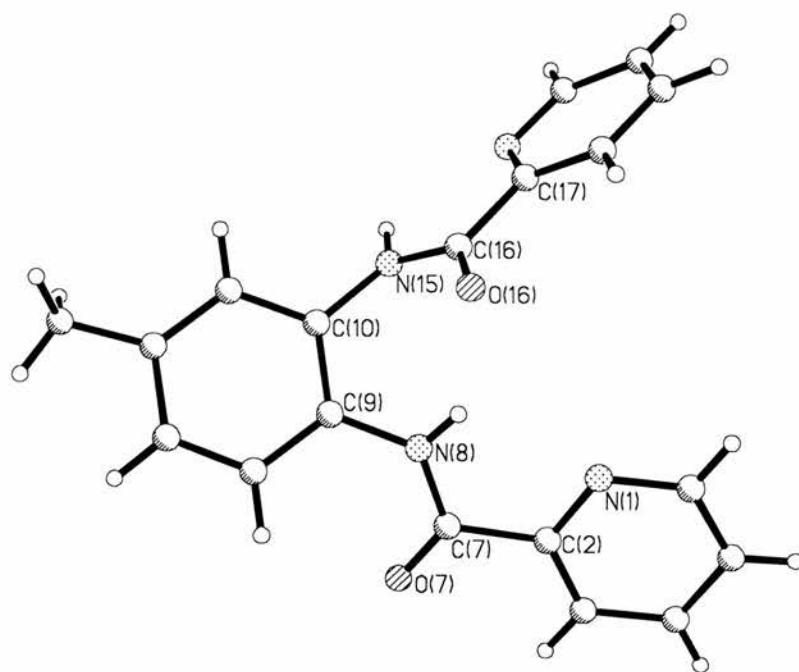


Figure 4.7: Molecular structure of H₂L¹⁸.

Table 4.4: Selected bond lengths (Å) and angles (°) for H₂L¹⁸ (esd's in parentheses).

C(7)-O(7)	1.219(4)	O(16)-C(16)	1.226(4)
C(7)-N(8)	1.356(4)	N(15)-C(16)	1.347(4)
C(16)-N(15)-C(10)	125.4(3)	C(7)-N(8)-C(9)	126.3(3)
O(7)-C(7)-N(8)	124.4(3)	O(16)-C(16)-N(15)	123.4(3)
N(8)-C(7)-C(2)	113.8(3)	N(15)-C(16)-C(17)	115.2(3)
O(7)-C(7)-C(2)	121.7(3)	O(16)-C(16)-C(17)	121.4(3)
C(10)-N(15)-C(16)-O(16)	3.5(5)	C(9)-N(8)-C(7)-O(7)	-4.2(5)
N(1)-C(2)-C(7)-O(7)	-178.5(3)		
O(16)-C(16)-C(17)-N(15)	176.5(3)		
C(10)-N(15)-C(16)-C(17)	-177.6(3)		
C(9)-N(8)-C(7)-C(2)	175.3(1)		
C(7)-N(8)-C(9)-C(14)	36.3(4)		
C(7)-N(8)-C(9)-C(10)	-143.2(3)		
C(16)-N(15)-C(10)-C(9)	-57.7(4)		
C(16)-N(15)-C(10)-C(11)	125.6(3)		

[CuL¹⁷]¹⁸ and [CuL¹⁸] were prepared in near quantitative yields by reacting copper(II) acetate monohydrate with one equivalent of the respective ligands in methanol. IR spectroscopy confirmed deprotonation as ν_{NH} bands were absent while the ν_{CO} bands (1636, 1641 cm^{-1}) were 40-50 cm^{-1} lower than in H₂L^{17,18}.

X-Ray crystallography revealed [CuL¹⁸] to have crystallographic C₂ symmetry, the methyl group having equal occupancy over two sites (Figure 4.8, Table 4.5). The coordination sphere of Cu(1) comprises pyridyl and carboxamide nitrogen atoms [N(1), N(1#) and N(8), N(8#) respectively] in a distorted square planar arrangement, with Cu-N_{amide} shorter than Cu-N_{pyridyl} [1.929(4), 1.929(3) Å vs. 2.020(4) Å]. N(1)-Cu(1)-N(1#) [111.7(2)°] is the largest *cis* angle [$\Sigma(\textit{cis}$ angles) = 360.3°], with the *trans* N(1)-Cu(1)-N(8) vector being 164.96(15)°. Although C(7)-N(8) [1.351(5) Å] is unchanged from H₂L¹⁸ [1.356(4), 1.347(4) Å] the planarity of [CuL¹⁸] permits greater electron delocalisation within the structure compared to H₂L¹⁸.

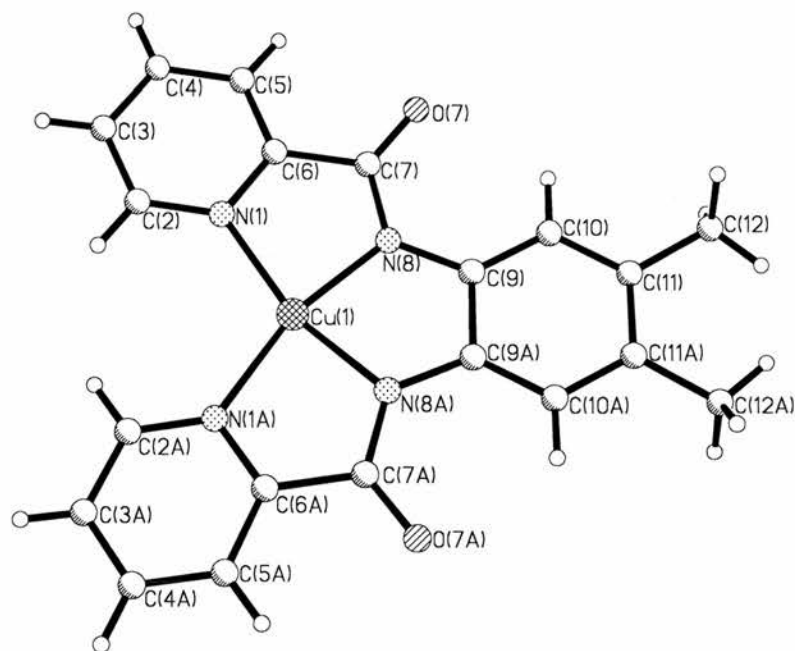
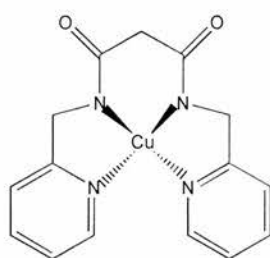


Figure 4.8: Molecular structure of [CuL¹⁸]. C(12) and C(12A) are 50 % occupancy atoms.

Table 4.5: Selected bond lengths (Å) and angles (°) for [CuL¹⁸] (esd's in parentheses).

Cu(1)-N(1)	2.020(4)	Cu(1)-N(1#)	2.020(4)
Cu(1)-N(8)	1.929(3)	Cu(1)-N(8#)	1.929(4)
C(7)-O(7)	1.239(5)	C(7)-N(8)	1.351(5)
N(8)-C(9)	1.392(5)	C(6)-C(7)	1.488(6)
<hr/>			
N(8)-Cu(1)-N(8#)	82.7(2)	N(1#)-Cu(1)-N(8#)	82.95(15)
N(1)-Cu(1)-N(8)	82.95(15)	N(1)-Cu(1)-N(1#)	111.7(2)
N(1)-Cu(1)-N(8#)	164.96(15)	N(8)-Cu(1)-N(1#)	164.96(15)
C(6)-C(7)-N(8)	111.6(4)	C(6)-C(7)-O(7)	120.2(4)
O(7)-C(7)-N(8)	128.2(4)	C(7)-N(8)-Cu(1)	117.4(3)
C(7)-N(8)-C(9)	127.1(4)	C(9)-N(8)-Cu(1)	115.4(3)

Noting the structural similarity of H₂L^{17,18} to the dioxotetraamine H₂ppO₂, which gave an isolable copper(III) complex [Cu(ppO₂)]⁺,²⁰ we investigated the electrochemistry for [CuL^{17,18}].



[Cu(ppO₂)]

The cyclic voltammetric behaviour of [CuL¹⁷] and [CuL¹⁸] in dmf were very similar (Figure 4.9, Table 4.6). Oxidation and reduction waves were observed for each complex, showing both anodic and cathodic peaks only above a scan rate of *ca.* 1 V s⁻¹. Both waves are quasi-reversible (ΔE_p greater than the 78 mV observed for ferrocene). Each wave was assigned as a one-electron process by chronoamperometry, which gave a consistent value for the diffusion coefficient. The reduction wave near -1.6 V is assigned to copper(II/I) by comparison with

[Cu(ppO₂)].²⁰ The scan-rate dependence of this wave was investigated and simulated for [CuL¹⁸] by the Digisim program²¹ using a heterogeneous rate constant of 0.01 s⁻¹ and a transfer coefficient of $\alpha = 0.75$.

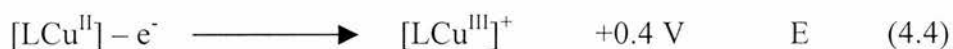
Table 4.6: Cyclic voltammetric data* (2 V s⁻¹) for [CuL^{17,18}] in 0.1 M [Bu₄N][PF₆] / dmf (V vs Fc/Fc⁺).

Compound	Cu(II/I)			Cu(III/II)	
	10 ⁵ D / cm ² s ⁻¹	E ⁰ / V	ΔE _p / mV	E ⁰ / V	ΔE _p / mV
[CuL ¹⁷]	1.70	-1.578	192	+0.438	140
[CuL ¹⁸]	1.19	-1.606	100	+0.361	130

*An additional irreversible ligand-based reduction wave is observed near -2.5 V.

The oxidation waves at +0.4 V are similar to those observed for [Cu(ppO₂)]²⁰ and are assigned as copper(III/II) processes. This was confirmed by spectroelectrochemistry of [CuL¹⁸] (Figure 4.10) which showed that the electrogenerated copper(III) species with λ_{max} at 370 and 630 nm has a UV-visible spectrum comparable to [Cu(ppO₂)]⁺. The copper(III) spectra could also be generated chemically by treatment of a dmf solution of [CuL¹⁸] with the persulfate method of Lampeka *et al.*²² Under the same conditions using EPR a reduction of the copper(II) signal upon oxidation to copper(II) was also demonstrated.

The scan rate behaviour of the copper(III/II) wave was typical for an EC reaction scheme outlined below, modelled with $k = 20 \text{ s}^{-1}$ and 5 s^{-1} for [CuL¹⁷] and [CuL¹⁸] respectively, equations 4.4-4.6.



On closer examination at lower scan rates a product wave for $[\text{CuL}^{18}]$ was identified at +0.6 V. The position of this wave does not correspond to the waves seen for the free ligand and we must therefore assign this oxidation to a new unidentified copper(II) species X arising from the reaction of $[\text{LCu}^{\text{III}}]^+$ with the solvent, equation 4.5.

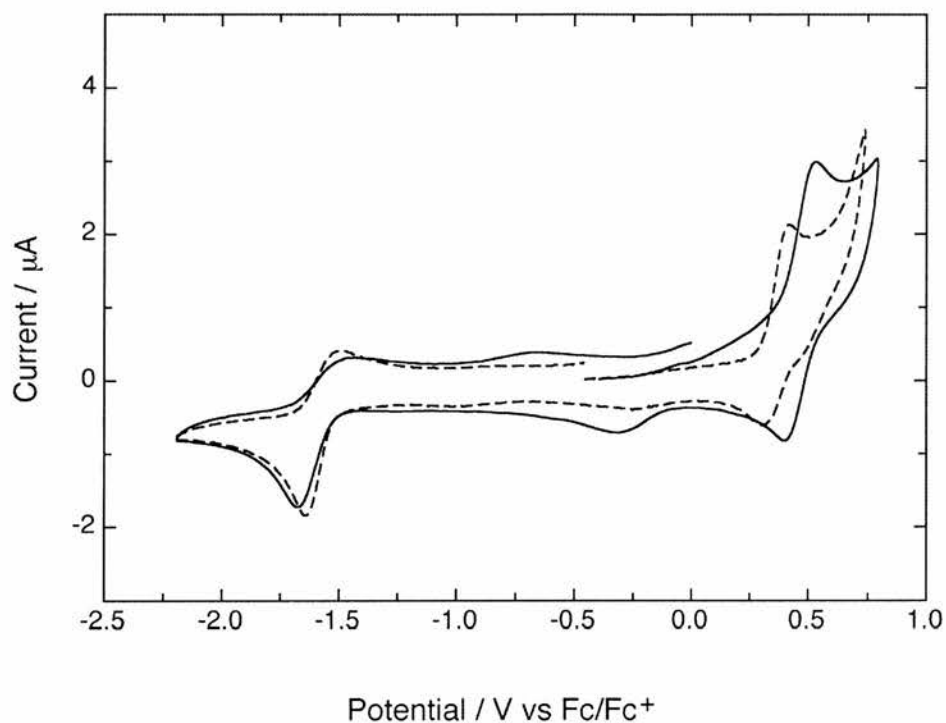


Figure 4.9: Cyclic voltammograms (2 V s^{-1}) for $[\text{CuL}^{17}]$ (full line) and $[\text{CuL}^{18}]$ (dashed line) in $0.1 \text{ M } [\text{Bu}_4\text{N}][\text{PF}_6]/\text{dmf}$ showing quasi-reversible copper(II/I) and copper(III/II) waves.

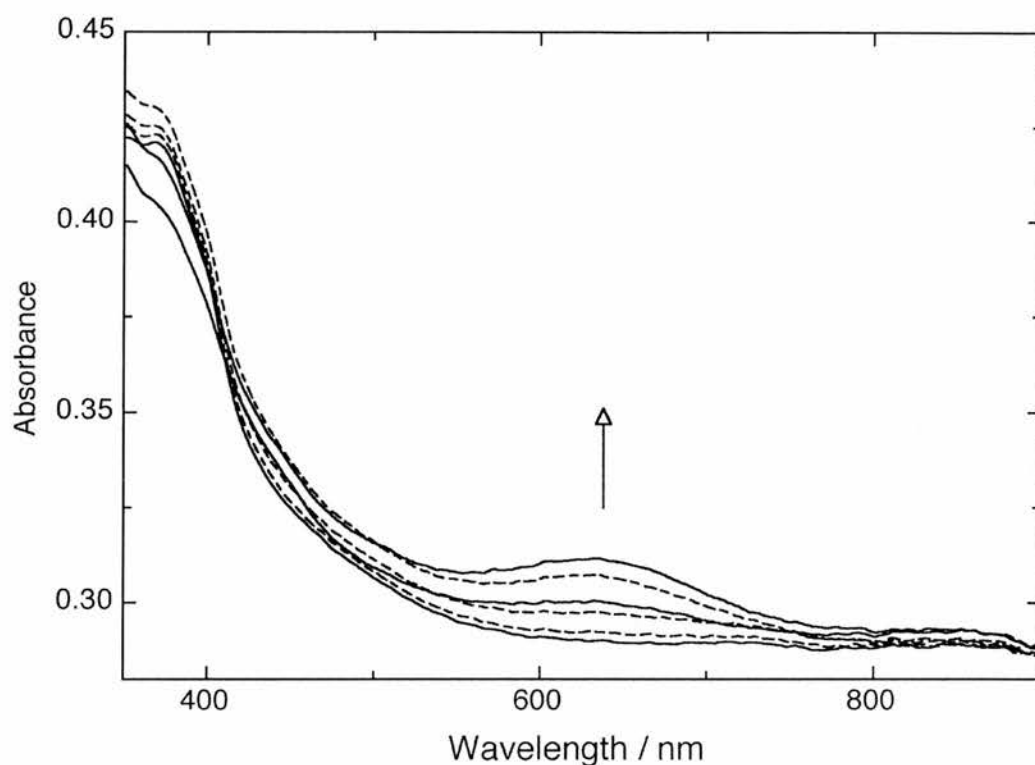


Figure 4.10: Spectroelectrochemical data during oxidation of $[\text{CuL}^{18}]$ in 0.1 M $[\text{Bu}_4\text{N}][\text{PF}_6]/\text{dmf}$ showing the reversible appearance of the copper(III) species with λ_{max} near 370 and 630 nm.

4.2.6 Reaction of Copper(II) Tetrakis(Pyridine) Perchlorate with Pyridine Dicarboxamide Ligands

The $(\text{L}^2, \text{L}^3, \text{L}^4, \text{L}^7, \text{L}^9)^{2-}$ dianions (generated from $\text{H}_2\text{L}^2, \text{H}_2\text{L}^3, \text{H}_2\text{L}^4, \text{H}_2\text{L}^7, \text{H}_2\text{L}^9$ using sodium hydride in thf) reacted with copper(II) tetrakis(pyridine) perchlorate in thf-acetonitrile to give green complexes soluble in polar organic solvents (pyridine, dmf, acetonitrile). Whereas the iron(III) complexes of $(\text{L})^{2-}$ could generally be recrystallised, it was difficult to crystallise the copper(II) complexes by any crystallisation method. Time constraints also inhibited attempts at purification by chromatographic techniques (adsorption or size-exclusion). Hence satisfactory elemental analyses could not be obtained for all of the products, which suggests contamination by unreacted ligand and

byproducts whose identities are as yet uncertain. In most cases, FAB⁺ or ES MS showed peaks corresponding to [Cu₂L₂]⁺ with the appropriate isotopic distribution, indicating that some proportion of the isolated material contained a complex with this stoichiometry.

However it was possible to crystallise [{Cu(L⁹)(OH₂)₂]₂·2H₂O from dmf-diethyl ether (Figure 4.11), selected structural parameters appear in Table 4.7. The coordination sphere of the square pyramidal Cu(1) centre comprises the nitrogen atoms of the central pyridine ring [N(10)] and the deprotonated carboxamide groups [N(7), N(16)] of one (L⁹)²⁻ ligand, a pyridyl nitrogen atom [N(1A)] from the other (L⁹)²⁻ ligand in the dimer and a water molecule. Cu(1) is displaced by 0.06 Å out of the N(16)-N(10)-N(7)-N(1A) square basal plane with O(30) the apical ligand. Upon deprotonation of H₂L⁹ both of the terminal pyridyl rings of (L⁹)²⁻ twist about the C_{pyridyl}-N_{amide} bonds, although only one is used for complexation to the second copper centre in the dimer. Despite the outward orientation of one pyridyl ring and the amide oxygen atoms from Cu(1) there are no significant intermolecular contacts within the structure.

Deprotonation leads to a very slight shortening of C(8)-O(8) [1.233(5) Å, *c.f.* O(15)-C(15) 1.246(9), 1.247(8) Å in H₂L⁹], with N(7)-C(8) [1.340(6) Å] being approximately the mean value of (C-N)_{amide} in H₂L⁹ [1.346 Å]. The *trans* N(10)-Cu(1)-N(1#) angle [169.39(14)°] is slightly narrower than for Cu(1) and Cu(2) in [Cu₃(L⁷)₂(μ₂-OAc)₂] [178.6(4)°, 173.8(4)°], which have trigonal bipyramidal [N₄O] donor sets. For [{Cu(L⁹)(OH₂)₂]₂ the Cu-N_{pyridyl} lengths [Cu(1)-N(10) 1.931(4), Cu(1)-N(1#) 1.988 Å] are shorter than Cu-N_{amide} [Cu(1)-N(16) 2.032(3), Cu(1)-N(7) 2.048(4) Å], *c.f.* the Cu-N_{amide} and Cu-N_{pyridyl} distances in [Cu₃(L⁷)₂(μ₂-OAc)₂] and [CuL¹⁸]. Within the CuN₄ plane the *cis* and *trans* N-Cu(1)-N angles are 79.13(14)°-101.44(14)° and 157.32(14)°-169.39(14)° respectively, the *cis* N-Cu(1)-O(30) angles are 86.51(13)°-105.98(14)°. Hydrogen bonding interactions within the structure exist between coordinated and solvate water molecules [H(30B)...O(31) 1.868 Å, H(31A)...O(30) 2.1 Å, H(30B)...O(15) 1.786 Å], the pendant pyridyl group and the carbonyl oxygen atoms do not participate, *c.f.* the structures of H₂L⁹⁻¹¹ (Chapter Three).

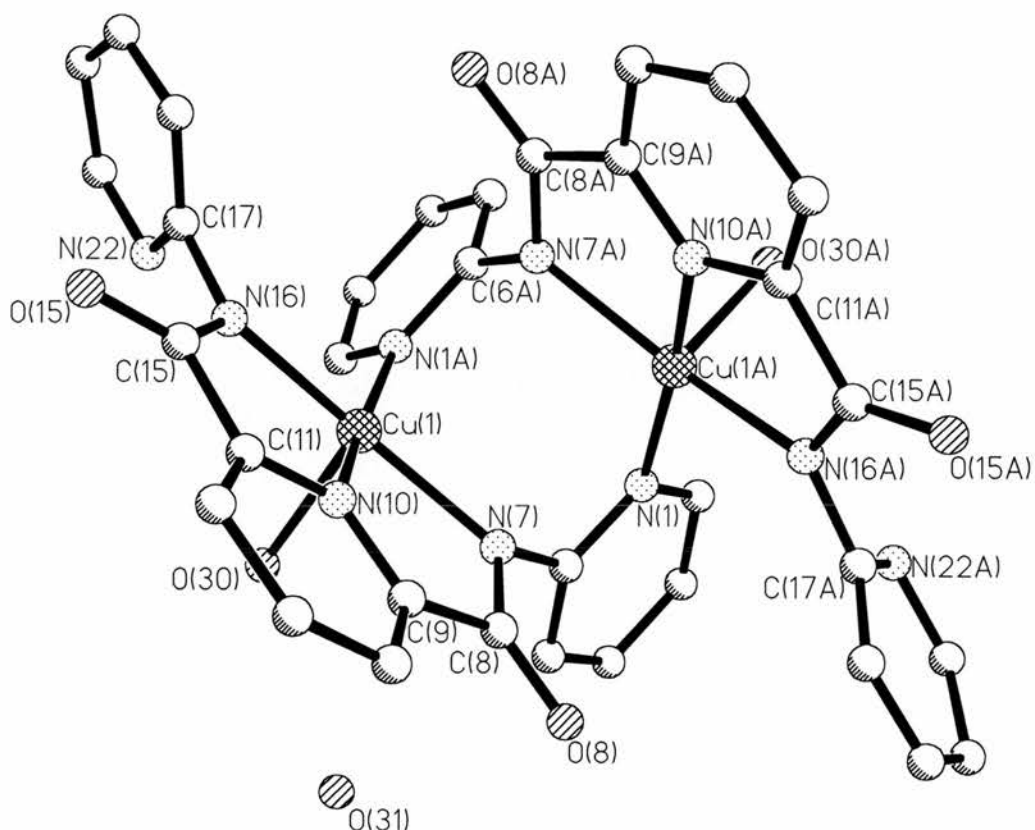


Figure 4.11: Molecular structure of $[\{\text{Cu}(\text{L}^9)(\text{OH}_2)\}_2]\cdot 2\text{H}_2\text{O}$ (C-H bonds omitted for clarity).

Whereas FAB^+ or ES MS data for the copper(II) complexes of the pyridine-2,6-dicarboxamide derived ligands were generally consistent with their formulation as bimetallic species, for the $(\text{L}^7)^{2-}$ complex we believe that the product is in fact a trimetallic species of composition $[\text{Cu}_3(\text{L}^7)_2(\text{py})_2][\text{ClO}_4]_2$, *i.e.* with a similar trinuclear axis as the copper(II) acetate derived complex of H_2L^7 . FAB^+ MS showed a prominent peak at m/z 825 for $[\text{Cu}_3(\text{L}^7)_2]^+$, with ν_{CO} at 1619 cm^{-1} in the IR spectrum, *c.f.* 1630 cm^{-1} for $[\text{Cu}_3(\text{L}^7)_2(\mu\text{-OAc})_2]$. Perchlorate bands (1085 , 624 cm^{-1}) were also apparent. The microanalytical data for the complex suggested the co-crystallisation of a molecule of pyridine. Once more $(\text{L}^7)^{2-}$ displays substantially different behaviour to the isomeric $(\text{L}^9)^{2-}$, due to the impossibility of chelation to one metal centre by the nitrogen atoms of the central pyridyl ring and the deprotonated carboxamide groups.

Table 4.7: Selected bond lengths (Å) and angles (°) for [$\{\text{Cu}(\text{L}^9)(\text{OH}_2)\}_2\} \cdot 2\text{H}_2\text{O}$ (esd's in parentheses).

Cu(1)-N(10)	1.931(4)	Cu(1)-N(1#)	1.988(4)
Cu(1)-N(16)	2.032(3)	Cu(1)-N(7)	2.048(4)
Cu(1)-O(30)	2.271(3)	C(8)-O(8)	1.233(5)
N(7)-C(8)	1.340(6)	O(15)-C(15)	1.249(5)
N(16)-C(15)	1.328(6)		
<hr/>			
N(10)-Cu(1)-N(1#)	169.39(14)	N(10)-Cu(1)-N(16)	80.22(14)
N(1#)-Cu(1)-N(16)	97.16(14)	N(10)-Cu(1)-N(7)	79.13(14)
N(1#)-Cu(1)-N(7)	101.44(14)	N(16)-Cu(1)-N(7)	157.32(14)
N(10)-Cu(1)-O(30)	99.12(13)	N(1#)-Cu(1)-O(30)	91.49(13)
N(16)-Cu(1)-O(30)	105.98(14)	N(7)-Cu(1)-O(30)	86.51(13)
C(8)-N(7)-Cu(1)	115.3(3)	C(15)-N(16)-C(17)	117.3(4)
C(15)-N(16)-Cu(1)	115.2(3)	C(17)-N(16)-Cu(1)	127.4(3)
O(15)-C(15)-C(11)	118.4(4)	N(16)-C(15)-C(11)	113.0(4)
O(8)-C(8)-N(7)	128.1(4)	O(8)-C(8)-C(9)	120.0(4)
N(7)-C(8)-C(9)	111.9(4)	O(15)-C(15)-N(16)	128.5(4)
C(6)-N(7)-Cu(1)	124.1(3)	C(8)-N(7)-C(6)	118.5(4)

To date, attempts to obtain X-ray quality crystals of $[\text{Cu}_3(\text{L}^7)_2(\text{py})_2][\text{ClO}_4]_2$ have been unsuccessful however an interesting transformation occurred during one recrystallisation from ethanol. Following addition of ethanol to the complex and standing for two days (aerobic conditions) green crystals were isolated from the orange residue. X-Ray crystallographic analysis of the green crystals revealed the complex to be a unique tetranuclear copper(II) species $[\text{Cu}_4(\text{L}^7)_2(\text{L}^7\text{-O})_2]$ (Figure 4.12, Table 4.8). There are two $(\text{L}^7)^{2-}$ and two $(\text{L}^7\text{-O})^{2-}$ ligands in the molecule, in the latter oxidation of the central pyridyl ring nitrogen atom generates an *N*-oxide. Each copper atom is bound by the nitrogen atoms of the terminal pyridyl rings and deprotonated carboxamide group from one $(\text{L}^7)^{2-}$ ligand and by the same donor atoms plus the *N*-oxo atom from an $(\text{L}^7\text{-O})^{2-}$ ligand, giving a square pyramidal $[\text{N}_4\text{O}]$ coordination sphere at the metal centre. Each *N*-oxygen atom bridges two adjacent copper centres. The central pyridyl

ring of $(L^7)^{2-}$ is too distant from any copper centre to enable it to bind, hence these ligands are tetradentate whereas $(L^7-O)^{2-}$ is pentadentate. While coordination of pyridine *N*-oxide ligands to copper(II) is common, as far as we are aware the complexation of the *N*-oxide of a 2,6-diaminopyridine derived ligand is unique.

The complex has a [2 x 2] grid structure with the $(L^7)^{2-}$ ligands being face-on to one another and perpendicular to the $(L^7-O)^{2-}$ ligands, which are themselves face-to-face. The centroids of the pyridine rings in each pair of ligands are slightly offset from one another. The frameworks of the $(L^7)^{2-}$ and $(L^7-O)^{2-}$ ligands are more planar than in $[Cu_3(L^7)_2(\mu-OAc)_2]$, suggesting greater electron delocalisation. This can be seen from the $N_{amide}-Cu-O-N_{pyridyl}$ torsion angles for the two $(L^7-O)^{2-}$ ligands. These angles are $-4.2(9)^\circ$, $19.1(8)^\circ$, $18.8(9)^\circ$ and $-6.5(9)^\circ$ for Cu(1) - Cu(4) respectively. The numbering scheme for $[Cu_4(L^7)_2(L^7-O)_2]$ is as follows; Cu(3) and Cu(1) are connected by the $(L^7)^{2-}$ ligand labelled N(31)-C(52) while Cu(4) and Cu(2) are connected by the N(91)-C(112) $(L^7)^{2-}$ ligand.

Looking at the $(L^7-O)^{2-}$ ligands, Cu(3) and Cu(4) are connected by N(61)-C(82), Cu(1) and Cu(2) by N(1)-C(22). Thus O(10) bridges Cu(1) and Cu(2), O(60) bridges Cu(3) and Cu(4). The Cu- N_{amide} lengths [1.926(13)-1.956(13) Å] are shorter than Cu- $N_{pyridyl}$ [2.052(13)-2.222(17) Å], the Cu-O distances are in the range 2.012(11)-2.087(12) Å. The sum of the angles at O(10) and O(70) is *ca.* 355° , with Cu-O-Cu approximately 137° .

$[Cu_4(L^7)_2(L^7-O)_2]$ gives a weak peak at m/z 1143 in its ES MS which corresponds to $[Cu_3(L^7)_3]^+$, a stronger peak at m/z 444 is correct for $[Cu_2(L^7)]^+$.

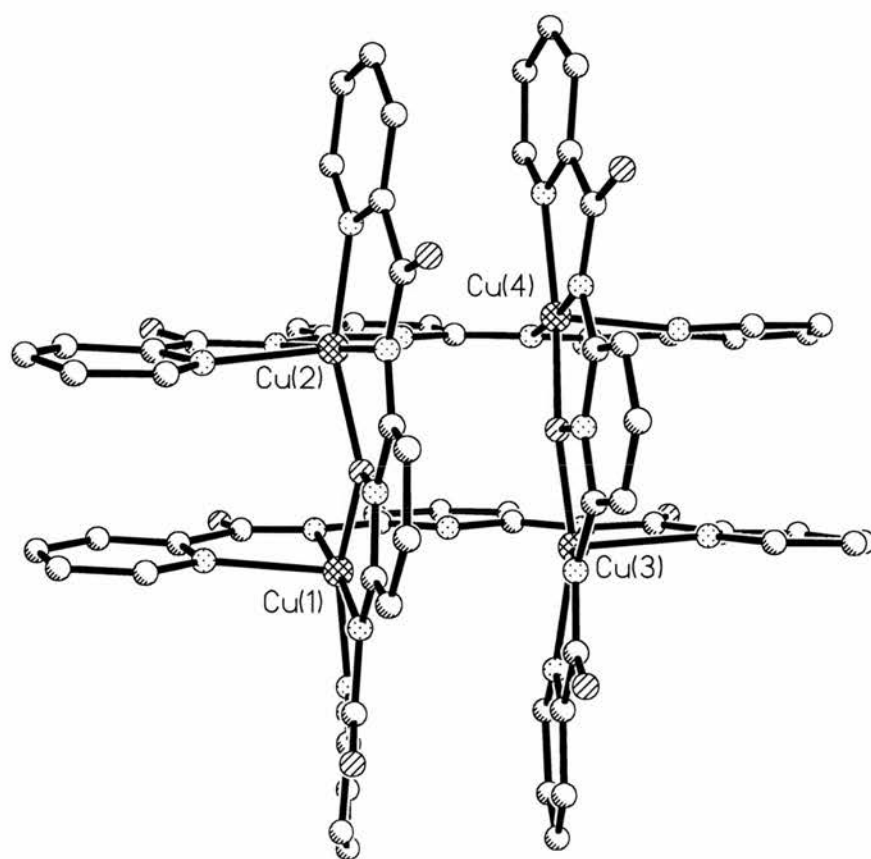


Figure 4.12: Molecular structure of $[\text{Cu}_4(\text{L}^7)_2(\text{L}^7\text{-O})_2]$ (C-H bonds and solvate molecules omitted for clarity).

A recent communication highlighted an unusual reactivity of a pyridine dicarboxamide complex of copper(II). When $[\text{Cu}(\text{dmppy})(\text{en})]$ ($\text{H}_2\text{dmppy} = N,N'$ -dimethylpyridine-2,6-dicarboxamide, $\text{en} = 1,2$ -diaminoethane) was added to a solution of en in acetonitrile, crystalline $[\text{Cu}^{\text{II}}(\text{en})_3][\text{Cu}^{\text{I}}(\text{CN})_3]$ was isolated quantitatively in addition to H_2dmppy and a methylated imidazoline derived polymer.²³ The heterolysis of acetonitrile into CH_3^+ and CN^- fragments was attributed to the highly basic nature of the dmppy^{2-} ligand. A similar chemistry may exist for selected copper(II) complexes of $\text{H}_2\text{L}^{1-11}$, however no evidence has been found for reactivity of the complexes described here towards acetonitrile or any other solvent under ambient conditions.

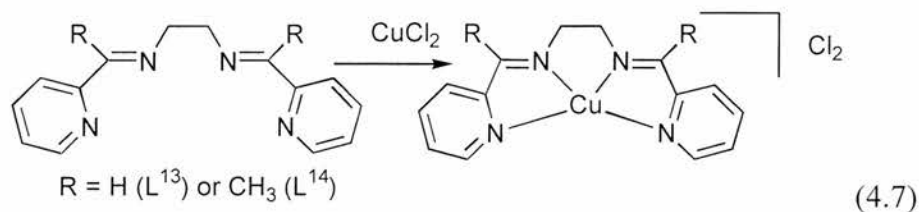
Table 4.8: Selected bond lengths (Å) and angles (°) for [Cu₄(L⁷)₂(L⁷-O)₂] (esd's in parentheses).

Cu(1)-N(38)	1.935(12)	Cu(1)-N(38)	1.950(13)
Cu(1)-O(10)	2.012(11)	Cu(1)-N(1)	2.052(13)
Cu(1)-N(31)	2.213(14)	Cu(2)-N(105)	1.932(13)
Cu(2)-N(15)	1.945(13)	Cu(2)-N(18)	2.059(13)
Cu(2)-O(10)	2.061(11)	Cu(2)-N(108)	2.209(14)
Cu(3)-N(68)	1.932(13)	Cu(3)-N(45)	1.943(12)
Cu(3)-N(61)	2.052(13)	Cu(3)-O(70)	2.087(12)
Cu(3)-N(48)	2.227(13)	Cu(4)-N(75)	1.926(13)
Cu(4)-N(98)	1.956(13)	Cu(4)-O(70)	2.069(12)
Cu(4)-N(78)	2.087(14)	Cu(4)-N(91)	2.219(13)
N(10)-O(10)	1.407(17)	N(70)-O(70)	1.376(17)
N(8)-Cu(1)-N(38)	173.8(5)	N(8)-Cu(1)-O(10)	80.8(5)
N(38)-Cu(1)-O(10)	105.3(5)	N(8)-Cu(1)-N(1)	80.2(5)
N(38)-Cu(1)-N(1)	93.9(5)	O(10)-Cu(1)-N(1)	157.5(5)
N(8)-Cu(1)-N(31)	99.9(5)	N(38)-Cu(1)-N(31)	79.1(5)
O(10)-Cu(1)-N(31)	94.9(5)	N(1)-Cu(1)-N(31)	100.3(5)
N(105)-Cu(2)-N(15)	175.4(6)	N(105)-Cu(2)-N(18)	97.2(6)
N(15)-Cu(2)-N(18)	81.6(5)	N(105)-Cu(2)-O(10)	101.7(5)
N(15)-Cu(2)-O(10)	80.5(5)	N(18)-Cu(2)-O(10)	156.9(5)
N(105)-Cu(2)-N(108)	80.4(6)	N(15)-Cu(2)-N(108)	95.5(6)
N(18)-Cu(2)-N(108)	101.2(5)	O(10)-Cu(2)-N(108)	95.0(5)
N(68)-Cu(3)-N(45)	174.3(6)	N(68)-Cu(3)-N(61)	81.4(5)
N(45)-Cu(3)-N(61)	98.1(5)	N(68)-Cu(3)-O(70)	79.3(5)
N(45)-Cu(3)-O(70)	102.6(5)	N(61)-Cu(3)-O(70)	154.9(5)
N(68)-Cu(3)-N(48)	95.5(5)	N(45)-Cu(3)-N(48)	79.1(5)
N(61)-Cu(3)-N(48)	103.0(5)	O(70)-Cu(3)-N(48)	94.8(5)
N(75)-Cu(4)-N(98)	175.0(5)	N(75)-Cu(4)-O(70)	79.1(5)
N(98)-Cu(4)-O(70)	105.8(5)	N(75)-Cu(4)-N(78)	80.2(5)
N(98)-Cu(4)-N(78)	94.8(5)	O(70)-Cu(4)-N(78)	157.3(5)
N(75)-Cu(4)-N(91)	101.2(5)	N(98)-Cu(4)-N(91)	79.6(5)
O(70)-Cu(4)-N(91)	93.8(5)	N(78)-Cu(4)-N(91)	99.2(5)

4.3 Other Complexes of Copper(II)

4.3.1 Schiff Base Complexes of Copper(II)

$[\text{CuL}^{13}]\text{Cl}_2$ and $[\text{CuL}^{14}]\text{Cl}_2$ were prepared from copper(II) chloride dihydrate in ethanol, according to equation 4.7.²⁴



During the preparation of $[\text{CuL}^{13}]\text{Cl}_2$ a green powder separated rapidly from the reaction mixture upon addition of L^{13} , and the desired blue complex precipitated from the decanted solution after 48 hrs at 25 °C. The same observations were noted in the original work,²⁴ however the authors did not identify the green compound. Microanalyses for $[\text{CuL}^{13,14}]\text{Cl}_2$ are consistently poor. As with $[\text{FeL}^{13,14}]\text{Cl}_2$, the IR spectra of $[\text{CuL}^{13,14}]\text{Cl}_2$ contained bands above 3000 cm^{-1} arising from ν_{OH} or ν_{NH} vibrations, $\nu_{\text{C=N}}$ for $[\text{CuL}^{13}]\text{Cl}_2$ (1607 cm^{-1}) was 20 cm^{-1} lower than $[\text{FeL}^{13}]\text{Cl}_2$ (1635 cm^{-1}) while the value for $[\text{CuL}^{14}]\text{Cl}_2$ (1656 cm^{-1}) was 20 cm^{-1} higher than $[\text{FeL}^{14}]\text{Cl}_2$ (1637 cm^{-1}). In their FAB⁺ MS, peaks at m/z 354 and 336 for the L^{13} complex corresponded to $[\text{Cu}(\text{L}^{13})\text{Cl}(\text{H}_2\text{O})]^+$ and $[\text{Cu}(\text{L}^{13})\text{Cl}]^+$ respectively, for the L^{14} complex an ion at m/z 364 was assigned to $[\text{Cu}(\text{L}^{14})\text{Cl}]^+$.

In Chapter Three an iron(II) complex of 2,6-bis[1-(2-methylpyridylimino)ethyl]pyridine (L^{16}) was prepared by reacting iron(II) perchlorate hexahydrate with L^{16} prepared *in situ* from 2,6-diacetylpyridine and 2-(aminomethyl)pyridine. From an attempt to prepare an analogous copper(II) complex using copper(II) perchlorate hexahydrate under identical conditions we isolated instead $[\text{Cu}(\text{2-NC}_5\text{H}_4\text{CH}_2\text{NH}_2)_2][\text{ClO}_4]_2$, (microanalytical and IR evidence) rather than $[\text{Cu}(\text{L}^{16})_n]^{2+}$ ($n = 1$ or 2). Presumably the higher Lewis acidity of copper(II) compared to iron(II) made the coordinated imine group more prone to hydrolysis.

4.3.2 Copper(II) Bis(Picolinate)

While iron(II) bis(picolinate) is a versatile precursor to iron(II,III) ternary picolinate complexes,²⁵ copper(II) bis(picolinate) is quite inert towards displacement of pic⁻ ligands from, or expansion of, the metal coordination sphere. The addition of thiourea to [Cu(pic)₂] in ethanol gave the octahedral complex [Cu(pic)₂(thiourea)₂]²⁶ while pic⁻ displaced xanthate, dithiocarbamate or β-diketonate ligands (L-L) from [Cu(L-L)₂] to give [Cu(L-L)(pic)].^{27,28} A mixed ligand complex [Cu(dpaH)(pic)][ClO₄] (dpaH = 2,2'-dipyridylamine) was prepared directly from copper(II) perchlorate hexahydrate, dpaH and Hpic.²⁹

Copper(II) bis(picolinate) dihydrate is prepared from copper(II) chloride dihydrate and Hpic, equation 4.8. In the solid state the square planar *trans* [Cu(pic)₂] units are linked by Cu...O_{carboxylate} interactions [Cu...O 2.752(2) Å], giving pseudo-octahedral geometry at copper with the water molecules occupying interstitial positions.³⁰



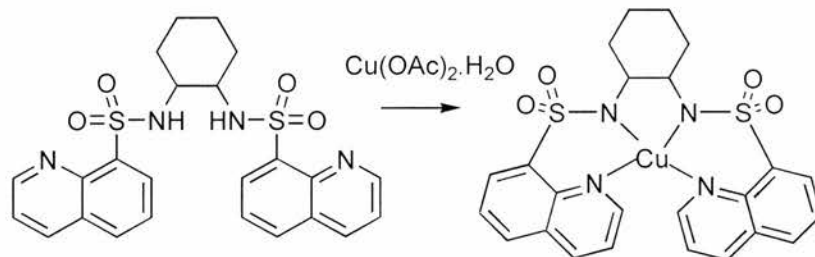
A recent publication purported to describe a different polymorph of [Cu(pic)₂].2H₂O, derived from copper(II) sulfate pentahydrate, sodium azide and α-pyridoin [2-C₅H₄NC(O)CH(OH)C₅H₄N-2],³¹ although the unit cell dimensions and molecular parameters were identical to those in the quasi-chain structure.

[Cu(pic)₂].2H₂O was prepared from copper(II) chloride dihydrate and Hpic in water, which in one instance was isolated in anhydrous form (microanalytical evidence) upon recrystallisation from water. In both hydrated and anhydrous forms the ν_{COO} vibrations in the IR spectra were identical (1638 and *ca.* 1350 cm⁻¹). Anhydrous [Cu(pic)₂] is available directly from di(2-pyridyl)ketone and copper powder in pyridine under aerobic conditions,³² although the reported ν_{COO(asym)} band (1628 cm⁻¹) is lower than observed here (1638 cm⁻¹).

4.3.3 A Sulfonamide Complex of Copper(II)

The acidity of the amine proton in sulfonamides (-SO₂NH- linkage) is increased by the adjacent sulfonyl group, hence they can be *N*-metallated in a similar way to carboxamides. Copper(II) complexes of sulfonamide ligands are much rarer than carboxamide complexes. Copper(II) complexes of *N,N'*-ditosyl-1,2-phenylenediamine, *N*-tosyl-2-aminopyridine and *N,N'*-bis(pyridine-2-sulfonyl)cyclohexane-1,2-diamine have been crystallographically characterised, the Cu-N_{sulfonyl} distances being 1.94-2.04 Å.^{33,34,35} For the third of these ligands the dianion is tetradentate through the four nitrogen atoms, structurally analogous to [Cu(L^{17,18})], Section 4.2.5.

N,N'-Bis(8-quinolinesulfonyl)cyclohexane-1,2-diamine (H₂L¹⁹) reacted with copper(II) acetate monohydrate to give a mononuclear species [CuL¹⁹] in which (L¹⁹)²⁻ coordinates to copper(II) *via* the four nitrogen atoms, equation 4.9, giving five- and six membered chelate rings.



(4.9)

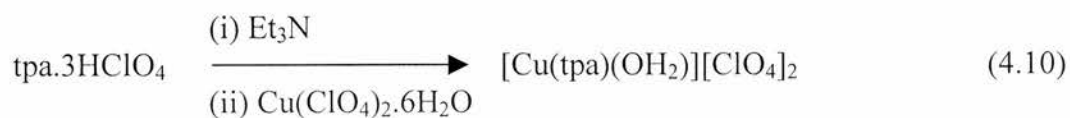
Crystals of [CuL¹⁹] grown from 1:1 *v/v* methanol/acetonitrile – diethyl ether by solvent diffusion were submitted for X-ray crystallographic analysis, however refinement of the structure was impossible as twelve independent molecules of [CuL¹⁹] were found in the unit cell. Nevertheless IR, FAB⁺ MS and microanalytical data corroborate this formulation. No ν_{NH} bands were apparent in the IR spectrum of the complex, the FAB⁺ MS contained a peak at *m/z* 559 for [M⁺ + H]. [CuL¹⁹] is the first copper(II) complex containing the (L¹⁹)²⁻ ligand.

[CuL¹⁹] is reduced by one electron at -1.174 V to the copper(I) complex in an irreversible reduction with characteristics in terms of wave shape which were very similar to those of [CuL^{17,18}] (Figure 4.13). The number of electrons was determined from the wave height and confirmed using chronoamperometry, which gave a diffusion coefficient of $1.3 \pm 0.2 \text{ cm}^2 \text{ s}^{-1}$. In addition, adsorption pre-waves were observed near -0.9 V (whose relative heights varied with scan rate). On the return scan there was an anodic wave at -0.816 V, which appeared from its scan rate dependence to be due to a soluble product of the reduction. Again, the waves were much broader in dmf, indicating perhaps strong adsorption onto the electrode from this solvent. The copper(II/I) wave was also somewhat broader and shifted on platinum electrodes.

Scanning the potential more negative revealed a broad, irreversible wave at -2.333 V corresponding to 2 electrons by chronoamperometry. Experiments on the free ligand in acetonitrile showed two irreversible one-electron reductions at -2.001 and -1.908 V, the first of which appeared to be totally irreversible.

An irreversible one-electron oxidation of [CuL¹⁹] occurred with an anodic peak at +0.880 V. This was assigned to the copper(III/II) redox reaction. Further oxidation processes at *ca.*+1.40 V were at similar potentials to those observed in the ligand voltammograms (at *ca.*+1.40 V), and are therefore assigned to ligand oxidations.

The tris(2-pyridylmethyl)amine (tpa) copper(II) complex [Cu(tpa)(OH₂)](ClO₄)₂ was prepared from tpa.3HClO₄, triethylamine and copper(II) perchlorate hexahydrate by a literature method, equation 4.10.³⁶



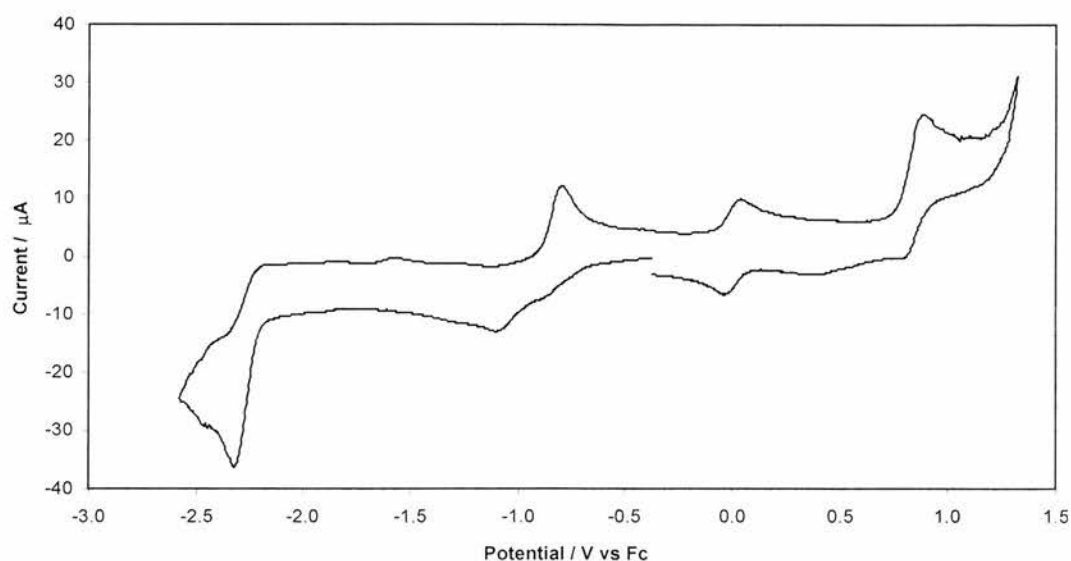


Figure 4.13: Cyclic voltammogram (100 mV s^{-1}) of $[\text{CuL}^{19}]$ in acetonitrile at a glassy carbon electrode (area = 0.071 cm^2). Potential referenced to ferrocene (reversible peak at 0.0 V).

4.4 Summary and Conclusions

The structure directing properties of pyridine dicarboxamide ligands can be exploited to prepare a range of topologies for copper(II) complexes. H_2L^6 and H_2L^7 reacted with copper(II) acetate monohydrate to give $[\text{Cu}_3\text{L}_2(\mu_2\text{-OAc})_2]$ which are the first crystallographically characterised metal complexes prepared containing a dicarboxamide ligand derived from 2,6-diaminopyridine. $[\text{CuL}^{17,18}]$ are oxidised electrochemically to copper(III) species which react further with solvent to give new copper(II) products. Copper(II) tetrakis(pyridine) perchlorate reacted with dianions of pyridine dicarboxamide ligands in acetonitrile-thf to give binuclear complexes for ligands containing the pyridine-2,6-dicarboxamide unit and a trimetallic structure for $(\text{L}^7)^{2-}$.

4.5 Future Work

The diversity of structures for copper(II) complexes containing pyridine dicarboxamide ligands suggests that synthesis of multimetallic complexes can be performed in a controlled fashion using such ligands. The grid-like structure of

the tetracopper complex $[\text{Cu}_4(\text{L}^7)_2(\text{L}^7\text{-O})_2]$ in which copper centres are directly linked by $\mu_2\text{-O}$ units is expected to lead to extremely interesting magnetic and electrochemical properties. If its preparation is indeed reproducible in good yield then other ligands containing 2,6-diaminopyridine units may exhibit similar reactivity to give oligometallic frameworks. In contrast to iron(III), the chemistry of copper(II)-pyridine dicarboxamide systems is unexpectedly complicated. This poses the question - other *d*-block metals behave similarly, particularly if co-ligands such as acetate are present?

4.6 Experimental

General experimental conditions and instrumentation details are as described previously. Syntheses of pyridine dicarboxamide and Schiff base ligands were given in Chapter Three. H_2L^{17} was prepared by a literature method,¹⁹ H_2L^{19} was a generous gift from Dr M. L. Clarke (University of St Andrews). Cyclic voltammetry and chronoamperometry for $[\text{Cu}_3(\text{L}^7)_2(\mu_2\text{-OAc})_2]$ and $[\text{CuL}^{17,18}]$ were performed using a PC-controlled EG & G PAR 273A potentiostat, with a three electrode cell comprising a platinum disc working electrode (0.5 mm diameter), a platinum wire auxiliary electrode and a silver wire quasi-reference electrode which was standardised against the wave of added ferrocene. Spectroelectrochemistry for $[\text{CuL}^{18}]$ was performed with a 0.5 mm thick optically-transparent thin layer electrode (OTTLE) cell with a platinum gauze electrode.

CAUTION: Although we have encountered no difficulties, perchlorate salts are potentially explosive and should be handled with care.

1,2-Bis(pyridine-2-carboxamido)benzene H_2L^{17} : Found (calc. for $\text{C}_{18}\text{H}_{14}\text{N}_4\text{O}_2$): C 67.91 (67.91), H 4.43 (4.21), N 17.76 (17.60) %. δ_{H} (CDCl_3): 10.25 (br s, 2H, NH), 8.55 (ddd, 2H, $J = 1, 2$ and 5, $\text{C}_5\text{H}_4\text{N}$), 8.30 (dt, 2H, $J = 1$ and 8, $\text{C}_5\text{H}_4\text{N}$), 7.88 (m, 4H, $\text{C}_5\text{H}_4\text{N} + \text{C}_6\text{H}_4$), 7.45 (ddd, 2H, $J = 1, 5$ and 8 Hz,

C₅H₄N), 7.29 (m, 2H, C₆H₄). Selected IR bands (cm⁻¹): 3316s (ν_{NH}), 1677s (ν_{CO}). EI MS: *m/z* 318, *M*⁺.

3,4-Bis(pyridine-2-carboxamido)toluene H₂L¹⁸: Hpic (2.22 g, 0.018 mol) was suspended in dry pyridine (10 cm³) under argon. 3,4-Diaminotoluene (4.64 g, 0.038 mol) was added and the mixture was stirred for 40 mins at 40 °C. Initially a white precipitate appeared, which finally formed an emulsion. Triphenylphosphite (9.5 cm³, 0.036 mol) was added dropwise, the temperature of the reaction mixture was increased to 90-100 °C and the mixture stirred for 5 hrs. After cooling to room temperature overnight methanol (20 cm³) and water (20 cm³) were added, the colourless precipitate was filtered off and recrystallised from chloroform-diethyl ether. Yield 5.38 g (90 %). Crystals suitable for X-ray analysis were grown from chloroform–diethyl ether at –20 °C. Found (calc. for C₁₉H₁₆N₄O₂): C 69.76 (68.66), H 4.53 (4.85), N 17.22 (16.86) %. δ_H (CDCl₃): 10.25 (br s, 1H, NH), 10.16 (br s, 1H, NH), 8.54 (m, 2H, C₅H₄N), 8.29 (m, 2H, C₅H₄N), 7.87 (m, 2H, C₅H₄N), 7.73 (d, 1H, *J* = 1.5, C₆H₃), 7.69 (d, 1H, *J* = 8.5, C₆H₃), 7.43 (m, 2H, C₅H₄N), 7.09 (dd, 1H, *J* = 1.5 and 8.5 Hz, C₆H₃), 2.38 (s, 3H, CH₃). Selected IR bands (cm⁻¹): 3302s (ν_{NH}), 1690s, 1660s (ν_{CO}). EI MS: *m/z* 332, *M*⁺.

***N,N'*-Bis(8-quinolinesulfonyl)cyclohexane-1,2-diamine (H₂L¹⁹)**: Found (calc. for C₂₄H₂₄N₄O₄S₂): C 57.37 (58.05), H 4.73 (4.87), N 11.00 (11.28) %. δ_H (CDCl₃): 9.01 (dd, 2H, *J* = 2 and 4, quinoline), 8.35 (dd, 2H, *J* = 1.5 and 7, quinoline), 8.23 (dd, 2H, *J* = 2 and 8, quinoline), 8.02 (dd, 2H, *J* = 1.5 and 8, quinoline), 7.62 (dd, 2H, *J* = 7 and 8, quinoline), 7.53 (dd, 2H, *J* = 4 and 8, quinoline), 6.37 (d, 2H, *J* = 5 Hz, NH), 3.04 (m, 2H, CH), 1.79 (m, 2H, CH₂), 1.40 (m, 2H, CH₂), 1.01 (m, 4H, CH₂). Selected IR bands (cm⁻¹): 3309m, 3254m (ν_{NH}), 1166s, 1141s (ν_{SO}). EI MS: *m/z* 209, [C₉H₆NSO₂NH₂]⁺.

[Cu(py)₄][ClO₄]₂: Copper(II) perchlorate hexahydrate (10.0 g, 27.0 mmol) was dissolved in pyridine (100 cm³), giving a purple solution with the evolution of some heat. The solution was evaporated to dryness and the crude product recrystallised from nitromethane as purple needles. Yield 12.50 g (80 %).

Found (calc. for $C_{20}H_{20}Cl_2CuN_4O_8$): C 41.80 (41.50), H 2.86 (3.48), N 9.60 (9.68) %.

[Cu₃(L⁶)₂(μ₂-OAc)₂]: A suspension of copper(II) acetate monohydrate (279 mg, 1.40 mmol) and H₂L⁶ (300 mg, 0.93 mmol) in 1:1 v/v methanol-chloroform (40 cm³) was heated at reflux for 2 hrs under aerobic conditions. The solution was filtered and the filtrate taken to dryness *in vacuo* to give a green solid. Yield 0.43 g (96 %). Dark green needles suitable for X-ray analysis were grown by diffusion of diethyl ether vapour into an acetonitrile solution of the complex. Found (calc. for $C_{34}H_{24}Cu_3N_{14}O_8$): C 43.03 (43.11), H 2.39 (2.55), N 20.55 (20.77) %. Selected IR bands (cm⁻¹): 1629s (ν_{CO}). ES MS: *m/z* 829, [Cu₃(L⁶)₂]⁺.

[Cu₃(L⁷)₂(μ₂-OAc)₂]: Under aerobic conditions, a solution of copper(II) acetate monohydrate (0.94 g, 4.6 mmol) in methanol (15 cm³) was added dropwise over five mins to H₂L⁷ (1.0 g, 3.1 mmol) in hot chloroform (60 cm³), giving an olive green solution. The reaction mixture was stirred overnight and the solution was concentrated under reduced pressure to *ca.* 5 cm³. Addition of diethyl ether (100 cm³) afforded an olive green solid. Yield 1.20 g (83 %). Dark green needles of [Cu₃(L⁷)₂(μ₂-OAc)₂].CHCl₃ suitable for X-ray analysis were grown by vapour diffusion of diethyl ether into a chloroform solution of the complex. Found (calc. for $C_{38}H_{28}Cu_3N_{10}O_8.CHCl_3$): C 44.36 (44.08), H 2.46 (2.75), N 13.20 (13.18) %. Selected IR bands (cm⁻¹): 1630s (ν_{CO}). FAB⁺ MS: *m/z* 824, [Cu₃(L⁷)₂]⁺.

[CuL¹⁷] and [CuL¹⁸]: These were prepared by reaction of stoichiometric amounts of copper(II) acetate monohydrate with H₂L^{17,18} in methanol at room temperature and recrystallised from acetonitrile as golden-brown solids in 90-95 % isolated yields. X-Ray quality crystals of [CuL¹⁸] were grown by evaporation of a dmf solution of the complex.

[CuL¹⁷]: Found (calc for $C_{18}H_{12}CuN_4O_2$): C 56.91 (56.56), H 2.75 (3.18), N 14.68 (14.75) %. Selected IR bands (cm⁻¹): 1636s (ν_{CO}). FAB⁺ MS: *m/z* 380, *M*⁺.

[CuL¹⁸]: Found (calc. for C₁₉H₁₄CuN₄O₂): C 56.57 (57.94), H 2.89 (3.58), N 13.94 (14.22) %. Selected IR bands (cm⁻¹): 1641s (ν_{CO}). FAB⁺ MS: *m/z* 394, *M*⁺.

[CuL¹⁹]: A solution of copper(II) acetate monohydrate (106 mg, 0.53 mmol) and H₂L¹⁹ (262 mg, 0.53 mmol) in methanol (20 cm³) was stirred for 2 hrs, giving a blue-green solution. The solution was evaporated to dryness, the crude product was extracted into 1:1 *v/v* methanol-acetonitrile (7 cm³), vapour diffusion of diethyl ether into this solution afforded a blue-green solid. Yield 74 mg (25 %). Found (calc. for C₂₄H₂₂CuN₄O₄S₂.H₂O): C 50.16 (50.03), H 3.54 (4.20), N 9.54 (9.73) %. Selected IR bands (cm⁻¹): 1102s (ν_{SO}). FAB⁺ MS: *m/z* 559, [*M*⁺ + H]

Pyridine Carboxamide Complexes

These complexes were prepared by the same general procedure as follows.

Sodium hydride (57 mg, 2.4 mmol, 60 % in mineral oil) was washed with hexane (2 x 10 cm³) under dinitrogen and then H₂L (1.2 mmol) was added as a solid in one portion. Thf (15 cm³) was added then a solution of copper(II) tetrakis(pyridine) perchlorate (70 mg, 1.2 mmol) in acetonitrile (40 cm³) was added *via* cannula, instantly giving a green suspension. Stirring was continued for 18 hrs, after which time the dark green product was filtered off, washed with acetonitrile (50 cm³) and air-dried.

Isolated yields of crude products were typically 30-80 %. Crystals of [Cu(L⁹)(OH₂)₂].2H₂O suitable for X-ray crystallographic analysis were grown by vapour diffusion of diethyl ether into a dmf solution of the complex.

[Cu(L²)(H₂O)₂].H₂O: Found (calc. for C₃₄H₂₂Cl₄Cu₂N₁₀O₆.H₂O): C 42.72 (42.82), H 1.90 (2.54), N 14.44 (14.68) %. Selected IR bands (cm⁻¹): 1626 or 1610s (ν_{CO}). FAB⁺ MS: *m/z* 899 [Cu₂(L²)₂]⁺, 923 [Cu₂(L²)₂ + Na]⁺.

[Cu(L³)(H₂O)₂]: Selected IR bands (cm⁻¹): 1610s (ν_{CO}). ES MS: *m/z* 817 [Cu₂(L³)₂]⁺, 409 [Cu(L³)]⁺.

[{Cu(L⁴)(H₂O)}₂]: Found (calc. for C₃₀H₂₂Cu₂N₁₄O₆·3H₂O): C 42.29 (42.10), H 3.11 (3.30), N 22.52 (22.91) %. Selected IR bands (cm⁻¹): 3387s (ν_{OH}), 1608s (ν_{CO}).

[Cu₃(L⁷)₂(py)₂](ClO₄)₂·py: Found (calc. for C₄₄H₃₂Cl₂Cu₃N₁₂O₈·C₅H₅N): C 46.06 (46.65), H 2.56 (2.96), N 15.11 (14.43) %. Selected IR bands (cm⁻¹): 1619s (ν_{CO}), 1085m, 624m (ν_{perchlorate}). FAB⁺ MS: *m/z* 825 [Cu₃(L⁷)₂]⁺, 320 [HL⁷]⁺.

[{Cu(L⁹)(H₂O)}₂]: FAB⁺ MS: *m/z* 764, [Cu₂(L⁹)₂]⁺. Selected IR bands (cm⁻¹): 1608s (ν_{CO}).

[CuL¹³]Cl₂ Copper(II) chloride dihydrate (0.36 g, 2.1 mmol) in ethanol (5 cm³) was added to a solution of L¹³ (0.51 g, 2.1 mmol) in ethanol (5 cm³), giving a deep blue-green suspension. Upon standing a green precipitate settled, from which the solution was decanted. After *ca.* 48 hrs [CuL¹³]Cl₂ precipitated from the decanted solution as a blue solid and was collected by filtration. A second crop precipitated from the filtrate after 48 h. Yield 0.36 g (46 %). Found (calc. for C₁₄H₁₄Cl₂CuN₄): C 34.74 (45.11), 3.72 (3.78), N 14.78 (15.03) %. Selected IR bands (cm⁻¹): 3402s, 3269s (ν_{NH} or ν_{OH}), 1607s (ν_{C=N}). FAB⁺ MS: *m/z* 354 [Cu(L¹³)Cl(H₂O)]⁺, 336 [Cu(L¹³)Cl]⁺.

[CuL¹⁴]Cl₂ A suspension of L¹⁴ (0.29 g, 1.1 mmol) in ethanol (10 cm³) was added to a solution of copper(II) chloride dihydrate (0.185 g, 1.1 mmol) in ethanol (5 cm³). The reaction mixture instantly became green and eventually turned blue with the deposition of [CuL¹⁴]Cl₂ as a blue solid. Yield 0.43 g (98 %). Found (calc. for C₁₆H₂₀Cl₂CuN₄): C 41.44 (47.70), H 3.83 (5.00), N 12.40 (13.91) %. Selected IR bands (cm⁻¹): 3418s (ν_{NH} or ν_{OH}), 1656s (ν_{C=N}). FAB⁺ MS: *m/z* 364, [Cu(L¹⁴)Cl]⁺.

Attempted preparation of [CuL¹⁶][ClO₄]₂: 2,6-Diacetylpyridine (1.0 g, 6.1 mmol) and 2-(aminomethyl)pyridine (1.32 g, 12.2 mmol) were stirred in methanol (50 cm³) for 1 hr at 25 °C, giving a yellow solution. Copper(II)

perchlorate hexahydrate (2.27 g, 6.1 mmol) in methanol (20 cm³) was added, a pale purple solid precipitated immediately, which was collected by filtration and washed with diethyl ether. The solid was found to be [Cu(2-NC₅H₄CH₂NH₂)₂][ClO₄]₂. Yield 2.0 g (68 %). Found (calc. for C₁₂H₁₆Cl₂CuN₄O₈): C 30.55 (30.11), H 2.54 (3.37), N 11.51 (11.70) %. Selected IR bands (cm⁻¹): 3329m, 3272m (ν_{NH}), 1084vs, 623s (ν_{perchlorate}).

[Cu(pic)₂].2H₂O: Hpic (1.23 g, 10 mmol) was added to a solution of copper(II) chloride dihydrate (0.85 g, 5 mmol) in water (150 cm³), instantly giving a purple precipitate, which was collected by filtration. Yield 1.6 g (94 %). Found (calc. for C₁₂H₈CuN₂O₄.2H₂O): C 42.19 (41.93), H 2.91 (3.51), N 8.11 (8.15) %. Selected IR bands (cm⁻¹): 1638s, 1347s (ν_{COO}).

Recrystallisation of a sample from boiling water gave [Cu(pic)₂]. Found (calc. for C₁₂H₈CuN₂O₄): C 46.03 (46.83), H 2.43 (2.62), N 8.75 (9.10) %. Selected IR bands (cm⁻¹): 1638s, 1350s (ν_{COO}).

[Cu(tpa)(H₂O)][ClO₄]₂: Under aerobic conditions tpa.3HClO₄ (2.04 g, 3.45 mmol) was dissolved in methanol (50 cm³). Triethylamine (1.57 g, 2.2 cm³, 15.5 mmol) and copper(II) perchlorate hexahydrate (1.28 g, 3.45 mmol) were added and the blue solution was stirred for 45 mins. Diethyl ether (75 cm³) was added and the solution cooled to -20 °C overnight, giving a blue solid. Yield 1.60 g (81 %). Selected IR bands (cm⁻¹): 3548w, 3108w (ν_{OH}), 1090s, 624m (ν_{perchlorate}). ES MS: *m/z* 353 [Cu(tpa)]⁺, 452 [Cu(tpa) + ClO₄]⁺.

- 1 D. H. R. Barton, N. C. Delanghe and H. Patin, *Tetrahedron*, 1997, **53**, 16017.
- 2 D. H. R. Barton, E. Csukai, D. Doller and Y. V. Geletii, *Tetrahedron*, 1991, **47**, 6561.
- 3 D. H. R. Barton, S. D. Beviere, W. Chavisiri, E. Csukai and D. Doller, *Tetrahedron*, 1992, **48**, 2895.
- 4 D. H. R. Barton, S. D. Beviere, W. Chavisiri, D. Doller and B. Hu, *Tetrahedron Lett.*, 1992, **34**, 567.
- 5 U. Schuchardt, R. Pereira and M. Rufo, *J. Mol. Catal. A*, 1998, **135**, 257.
- 6 H. Kurosaki, R. K. Sharma, S. Aoki, T. Inoue, Y. Okamoto, Y. Sugiura, M. Doi, T. Ishida, M. Otsuka and M. Goto, *J. Chem. Soc., Dalton Trans.*, 2001, 441.
- 7 D. S. Marlin, M. M. Olmstead and P. K. Mascharak, *Inorg. Chim. Acta*, 2001, **323**, 1.
- 8 J. M. Rowland, M. M. Olmstead and P. K. Mascharak, *Inorg. Chem.*, 2000, **39**, 5326.
- 9 F. A. Chavez, M. M. Olmstead and P. K. Mascharak, *Inorg. Chem.*, 1996, **35**, 1410.
- 10 J. M. Rowland, M. L. Thornton, M. M. Olmstead and P. K. Mascharak, *Inorg. Chem.*, 2001, **40**, 1069.
- 11 D. S. Marlin, M. M. Olmstead and P. K. Mascharak, *Inorg. Chem.*, 2001, **40**, 7003.
- 12 A. K. Patra, M. Ray and R. Mukherjee, *Polyhedron*, 2000, **19**, 1423.
- 13 T. Yano, R. Tanaka, T. Nishioka, I. Kinoshita, K. Isobe, L. J. Wright and T. J. Collins, *Chem. Commun.*, 2002, 1396.
- 14 K. Hiratami and K. Taguchi, *Bull. Chem. Soc. Jpn.*, 1990, **63**, 3331.
- 15 L. P. Wu, P. Field, J. Morrissey, C. Murphy, P. Nagle, B. Hathaway, C. Simmons and P. Thornton, *J. Chem. Soc., Dalton Trans.*, 1990, 3835.
- 16 J. Hanss, A. Beckmann, H. J. Kruger, *Eur. J. Inorg. Chem.*, 1999, 163.
- 17 N. A. Bailey, D. E. Fenton, Q. Y. He, N. Terry, W. Haase and R. Werner, *Inorg. Chim. Acta*, 1995, **235**, 273.
- 18 R. L. Chapman and R. S. Vagg, *Inorg. Chim. Acta*, 1979, **33**, 227.

- 19 M. J. Upadhyay, P. K. Bhattacharya, P. A. Ganeshpure and S. Satish, *J. Mol. Catal.*, 1994, **88**, 287.
- 20 T. Sakurai, J. I. Hongo, A. Nakahara, and Y. Nakao, *Inorg. Chim. Acta*, 1980, **46**, 205.
- 21 Cyclic voltammograms were simulated using the Digisim 3.0 program (Bioanalytical Systems Inc, West Lafayette, Indiana).
- 22 Y. D. Lampeka and S. P. Gavrish, *Polyhedron*, 2000, **19**, 2533.
- 23 D. S. Marlin, M. M. Olmstead and P. K. Mascharak, *Angew. Chem., Int. Ed. Engl.*, 2001, **40**, 4752.
- 24 P. E. Figgins and D. H. Busch, *J. Am. Chem. Soc.*, 1960, **82**, 820.
- 25 S. Kiani, A. Tapper, R. J. Staples and P. Stavropoulos, *J. Am. Chem. Soc.*, 2000, **120**, 7503.
- 26 E. G. Cox, W. Wardlaw and K. C. Webster, *J. Chem. Soc.*, 1936, 775.
- 27 R. N. Murty, R. N. Dash and D. V. R. Rao, *J. Indian Chem. Soc.*, 1984, **61**, 943.
- 28 M. K. Purohit and D. V. R. Rao, *J. Indian Chem. Soc.*, 1981, **58**, 78.
- 29 T. Murokami, S. Hatakeyama, S. Igarashi and Y. Yukawa, *Inorg. Chim. Acta*, 2000, **310**, 96.
- 30 P. R. Faure, H. Loiseleur and G. Thomas-David, *Acta Cryst.*, 1973, **B29**, 1890.
- 31 J. H. Luo, M. C. Hong, Q. Shi, Y. C. Liang, Y. J. Zhao, R. H. Wang, R. Cao and J. B. Weng, *Transition Met. Chem.*, 2002, **27**, 311.
- 32 G. Speier and Z. Tyeklar, *J. Chem. Soc., Dalton Trans.*, 1988, 2663.
- 33 H. Y. Cheng, P. H. Cheng, C. F. Lee and S. M. Peng, *Inorg. Chim. Acta*, 1991, **181**, 145.
- 34 P. H. Cheng, H. Y. Cheng, C. C. Lin and S. M. Peng, *Inorg. Chim. Acta*, 1990, **169**, 19.
- 35 A. Nanthakumar, J. Miura, S. Diltz, C. K. Lee, G. Aguirre, F. Ortega, J. W. Ziller and P. J. Walsh, *Inorg. Chem.*, 1999, **38**, 3010.
- 36 R. R. Jacobson, Z. Tyeklar, K. D. Karlin and J. Zubieta, *Inorg. Chem.*, 1991, **30**, 2035.

Chapter Five

Catalytic Studies of Iron and Copper Complexes Under Gif^{IV} Conditions

5.1 Introduction

Within the Gif family of oxidants the Gif^{IV} system [iron(II)/zinc(0)] is the most efficient for the oxygenation of saturated cyclic hydrocarbons using atmospheric dioxygen.¹ The currently accepted mechanistic interpretation of this reaction is of a radical-based pathway,^{1,2} rather than Barton's proposal of iron(V)-oxo species.^{3,4} An added interest in this system concerns a possible relevance to biological oxygenations using dioxygen, in modelling non-heme based oxidation enzymes such as sMMO.^{5,6}

While comparative studies with different metals have the potential to provide useful mechanistic insights, there have been few studies of Gif catalyst systems based on metals other than iron. Within the Gif family of oxidants the GoChAgg system is based upon copper(II).⁷ However, oxidations using copper are never as effective as when an iron catalyst is tested since dioxygen generation takes preference over ketonisation in the former. Barton has also investigated cobalt(II), ruthenium(III) and nickel(II) in a study of the oxidation of cyclododecane by hydrogen peroxide in mixed solvent systems.⁸ His general finding that the highest yield, *ca.* 25 % of alkane conversion and 10 % efficiency for hydrogen peroxide was found for pyridine-acetonitrile mixtures, underlines the dependency for pyridine in these oxygenation reactions. Gold complexes have also recently been applied for oxygenation of cyclohexane in acetonitrile with hydrogen peroxide.⁹

Powell *et al*¹⁰ have studied polynuclear ruthenium carboxylate complexes $[\text{Ru}_3(\mu_3\text{-O})(\mu_2\text{-OAc})_6(\text{py})_2\text{L}]$ (L = CO or py) and $[\text{Ru}_2(\mu_2\text{-O})(\mu_2\text{-OAc})_2(\text{py})_6]$ in Gif^{dV} systems, achieving TON's of up to 360 after 5.5 hrs, with termination of the reaction after *ca.* 8 hrs when all of the zinc had been consumed. A comparison between the mixed-valent iron and ruthenium Gif^{dV} systems $[\text{M}_3(\mu_3\text{-O})(\mu_2\text{-OAc})_6(\text{py})_3]$ confirmed that both metals acted *via* the same general mechanism, but the appearance of alcohol much earlier in the reaction for the ruthenium complex resulted from the slower formation of the species responsible for the ketonisation step, consequently the ketone:alcohol ratio was lower than for iron.¹¹ The finding that *trans*- $[\text{Fe}(\text{OAc})_2(\text{py})_4]$ was the most successful Gif^{dV} oxygenating agent proved that M(II) was the key complex formed when the trimetallic complexes were in solution. A sensitivity of TON and ketone:alcohol ratio to stirring speed was also apparent, with TON increasing for the iron catalyst but decreasing for ruthenium as stirring rate increases.

It is known that the products of oxidation arise *via* an alkyl hydroperoxide intermediate,¹² since iron(III) chloride under $\text{GoAgg}^{\text{III}}$ conditions catalyses the conversion of cyclohexyl hydroperoxide to cyclohexanone on a similar time scale (hrs) to the latter stages for oxygenation of cyclohexane. However when Gif^{dV} reactions are carried out it is not possible to directly identify the peroxide species. Shul'pin reports a method for the estimation of the peroxide content of the reaction mixture.¹³ His method is based on the quantitative amounts of ketone and alcohol achieved before and after the reaction mixture is treated with a reductant such as triphenylphosphine. It is typically seen in these reactions that the amount of ketone exceeds that of the alcohol that is produced, but on treatment with a reductant the amount of ketone is significantly reduced and the product total remains the same. It is thought that on injection of triphenylphosphine the alkyl hydroperoxide reduces to give mainly the alcohol.

As already commented upon in this thesis, a major shortcoming of Gif chemistry is its intrinsic dependence on pyridine to give high yields of oxygenated products. To overcome the reliance of Gif systems on this solvent we investigated whether incorporating pyridyl groups into ligand structures would

firstly enhance the catalytic activity and secondly lead to the ultimate removal of dependency on pyridine as solvent. We have synthesised mono- and binuclear iron(II,III) and copper(II) complexes with ligands containing 2-pyridyl substituents (Chapters Three and Four) and in this Chapter have investigated their catalytic oxygenating activities using cyclohexane as substrate, in pyridine as solvent or in some cases acetonitrile with poly(vinylpyridine) (PVP) as the source of pyridine. Product profiles have been analysed using gas chromatography. Also, a time-dependent study of the oxygenation of cyclohexane by picolinate complexes of iron and copper has been conducted, to complement the UV-vis and EPR kinetic studies for the $[\text{Fe}(\text{pic})_3]$ -hydrogen peroxide ($\text{GoAgg}^{\text{III}}$) system reported in Chapter Two.

5.2 A Survey of Comparative Studies in Gif Chemistry

Numerous research groups worldwide have investigated the Gif^{dV} system, however only in a few cases have any attempts been made to standardise the reaction conditions employed in these catalytic experiments. A summary of the experimental conditions used in a number of studies appears in Table 5.1.

It is apparent that the ratio of substrate and catalyst employed, the presence or absence of water, even the shape and volume of the reaction vessel are variable parameters. While it may at first seem that these factors should not be too critical to catalytic activity, yields (TON's) and selectivities are not strictly comparable under non-standardised conditions. For example, it has been observed that the rate of stirring can influence greatly the product profile during and at the end of the reaction, a consequence of the heterogeneous nature of the system.¹¹ Adamantane or cyclohexane are the most commonly used substrates. Barton reported that the particle size of the zinc, and not its purity, was more important in determining catalytic efficiency.¹⁴ The partial pressure of dioxygen was also critical, as was the presence of pyridine, since the effect of using ring-substituted pyridines or other nitrogen-containing heterocycles was to reduce yields of oxygenated products by a factor of up to a hundredfold.¹⁴

The number of variables in any Gif reaction means that optimisation of reaction conditions cannot be done intuitively, however one solution has recently been published. A study by Martell¹⁵ used the Plackett-Burman experimental design (a statistically designed experiment) to optimise catalytic oxidation of adamantane in acetonitrile-pyridine by a binuclear iron(III) complex of a hexaazadiphenol macrocyclic ligand in the presence of hydrogen sulfide. This work highlighted that using the Plackett-Burman design, successful prediction of experimental conditions provided the required selectivity and high TON's without the need to perform large numbers of experiments. Moreover, control of the reaction did not require an intimate knowledge of the mechanism.

Schuchardt found that under a nitrogen monoxide atmosphere, oxidation of cyclohexane with hydrogen peroxide gave no change in activity or selectivity, from which it was concluded that triplet dioxygen was neither formed nor required in the oxidation.¹⁶

Table 5.1: A comparison of the Gif^{IV} oxygenation conditions employed by other Groups.¹⁷⁻¹⁹

	Barton	Schuchardt	Carvel	Powell	Marr
Iron catalyst	7 μmol	7 μmol	25 μmol	1 μmol	14 μmol
Cyclohexane	2 mmol	10 mmol	1.9 mmol	10 mmol	20 mmol
Pyridine	28 cm^3	28 cm^3	80 cm^3	28 cm^3	56 cm^3
Acetic acid	2.3 cm^3	2.3 cm^3	10 cm^3	2.3 cm^3	4.6 cm^3
Zinc powder	20 mmol	20 mmol	76 mmol	20 mmol	40 mmol
Water	-	-	3 cm^3	1.85 cm^3	-
Reaction vessel	125 cm^3 conical flask	125 cm^3 conical flask	1 dm^3 conical flask	100 cm^3 conical flask	100 cm^3 round bottomed flask

We have employed the ratio of reactants used by Schuchardt in his catalytic study for our experiments, with 100 cm^3 round bottomed flasks (B24 neck) rather than conical flasks, a constant stirring speed (1000 rpm) throughout and zinc powder activated with dilute hydrochloric acid prior to use. No attempt was

made to stabilise the temperature, all reactions are assumed to have taken place under ambient conditions at 20 °C.

5.3 Results and Discussion

5.3.1 Results of Catalytic Testing

Using the conditions described in Section 5.6 for the catalytic reactions and product analyses, Table 5.2 lists the catalysts used and the yields of oxygenated products after a 12 hr period. A number of trends are immediately apparent from an examination of the data.

(i) Both $[\text{Fe}(\text{pic})_2]_n$ and $[\text{Fe}(\text{pic})_2(\text{py})_2]$ gave almost identical ketone:alcohol ratios (*ca.* 4.7) and TON's (*ca.* 183), indicating that the polymeric complex undergoes solvolysis to the bis(pyridine) bis(picolate) iron(II) complex almost immediately in pyridine. The TON for $[\text{Fe}(\text{quin})_2(\text{py})_2]$ (144) is lower than $[\text{Fe}(\text{pic})_2(\text{py})_2]$ (TON 182), which may be due to steric effects.

(ii) From the data obtained there does not appear to be a marked difference in activity between iron(II) and iron(III) catalysts. For example the tpa and bpp complexes [iron(III)] have the highest activities (TON 285 and 293), but $[\text{Fe}(\text{L}^{12})_2][\text{BF}_4]_2$ [iron(II)] is almost as active (TON 261). The highest turnover number was noted for the hybrid pyridyl-carboxylate ligand bpp. There is little correlation between the coordination number or donor set at iron and TON. For example, $[\text{Fe}(\text{L}^{12})_2]^{2+}$ and $[\text{Fe}(\text{acac})_3]$ have equivalent TON's despite possessing $[\text{FeN}_6]$ and $[\text{FeO}_6]$ donor sets respectively. The iron(II) picolate complexes $[\text{Fe}(\text{pic})_2(\text{H}_2\text{O})_2]$, $[\text{Fe}(\text{pic})_2(\text{py})_2]$ and $[\text{Fe}(\text{pic})_2]_n$ have similar TON's (161-184) to the iron(III) complexes $[\text{pyH}][\text{Fe}(\text{pic})_2\text{Cl}_2]$ and $[\text{Fe}(\text{pic})_3]$ (TON 164, 167).

(iii) In comparison to the iron complexes the copper(II) complexes investigated display little or no catalytic activity towards oxygenation of cyclohexane, with turnover numbers barely reaching double figures. It is noted

that $[\text{Cu}(\text{pic})_2]$ gave the highest ketone:alcohol ratio of all of the catalysts examined.

(iv) The ketone:alcohol ratio is always greater than unity, ranging from 2.1 to 9.3 in these reactions. This is in accord with previously documented catalytic studies on the Gif^{dV} system.¹⁴ The highest ratio is noted for one of the least efficient catalysts, $[\text{Cu}(\text{pic})_2]$ (TON 10); discarding this result, the highest ratios are observed with the binuclear tpa and bpp complexes, which also exhibit the highest TON's.

(v) Studies using $[\text{Fe}(\text{pic})_n]$ ($n = 2$ or 3) or $[\text{Cu}(\text{pic})_2]$ in acetonitrile with PVP demonstrated that pyridine is indeed an irreplaceable component of the Gif^{dV} manifold. For example, whereas $[\text{Fe}(\text{pic})_3]$ catalysed oxygenation of cyclohexane in pyridine with a TON of 167, using PVP (fiftyfold excess over catalyst) in acetonitrile under identical conditions led to no detectable quantities of oxygenated products after 12 hrs. The same finding was apparent for each of the three complexes used under these conditions. PVP is not soluble in acetonitrile.

Table 5.2: GC analysis of product mixtures from Gif^{IV} oxygenation reactions^{a,b}

Catalyst	Ketone (mmol)	Alcohol (mmol)	Ketone/Alcohol ratio	Total Oxidation Products (mmol)	TON
[Fe(pic) ₂ (H ₂ O) ₂]	0.92	0.21	4.3	1.13	161
[Fe(pic) ₃]	0.94	0.22	4.3	1.16	167
[Fe(terpy) ₂]Cl ₂	0.89	0.18	4.8	1.07	153
[Fe(bipy) ₃]Cl ₂	0.875	0.17	5.3	1.05	149
[Fe(pic) ₂] _n	1.06	0.23	4.6	1.29	184
[Fe(pic) ₂ (py) ₂]	1.06	0.22	4.7	1.28	182
[Fe(quin) ₂ (py) ₂]	0.83	0.18	4.4	1.01	144
Na[Fe(L ⁹) ₂]	0.91	0.25	3.7	1.16	165
[pyH][Fe(pic) ₂ Cl ₂]	0.93	0.22	4.2	1.15	164
[Fe(pyterpy) ₂][ClO ₄] ₂	0.89	0.27	3.3	1.17	167
FeCl ₂	0.31	0.04	7.8	0.35	25
[Fe(py) ₄ Cl ₂]	0.21	0.05	4.2	0.46	33
[Fe(acac) ₃]	1.53	0.28	5.5	1.81	259
[Fe(L ¹²) ₂][BF ₄] ₂	1.51	0.27	5.8	1.83	261
[Fe ₂ (μ ₂ -OMe) ₂ (pic) ₄]	1.47	0.20	7.2	1.67	237

Table 5.2(cont.): GC analysis of product mixtures from Gif^{IV} oxygenation reactions^{a,b}

Catalyst	Ketone (mmol)	Alcohol (mmol)	Ketone/Alcohol ratio	Total Oxidation Products (mmol)	TON
[{Fe(tpa)} ₂ (μ ₂ -O)][ClO ₄] ₄	1.79	0.21	8.6	2.00	285
[{Fe(bpp)} ₂ (H ₂ O)} ₂ (μ ₂ -O)][ClO ₄] ₂	1.83	0.22	8.4	2.05	293
[Cu(py) ₄][ClO ₄] ₂	0.06	0.03	2.1	0.09	13
[Cu(pic) ₂].2H ₂ O	0.06	6.45 x 10 ⁻³	9.3	0.07	10
[Cu(pyCH ₂ NH ₂) ₂][ClO ₄] ₂	-	-	-	-	-
[Cu ₃ (L ⁷) ₂ (μ ₂ -OAc) ₂]	0.06	0.01	5.6	0.07	10
[Cu(tpa)(H ₂ O)][ClO ₄] ₂	-	-	-	-	-
[CuL ¹⁷]	-	-	-	-	-

^a TON = (moles of product)/(moles of catalyst). ^b An entry given as ‘-’ indicates that amounts of this product were too small to quantify. Reaction conditions are given in Section 5.2.

Overall, the catalytic activities for the iron species are similar in range to the values for $[\text{Fe}_3(\mu_3\text{-O})(\mu_2\text{-OAc})_6(\text{py})_3]$ (TON 133) and *trans*- $[\text{Fe}(\text{OAc})_2(\text{py})_4]$ (TON 239) for cyclohexane oxygenation. However they fall well short of the TON of *ca.* 2000 reported by Barton for the oxidation of adamantane using $[\text{Fe}_3(\mu_3\text{-O})(\mu_2\text{-OAc})_6(\text{py})_3]$.²⁰ This may in part be due to the higher volatility of cyclohexane compared to adamantane, leading to appreciable loss of the substrate by evaporation through the neck of the flask during the course of the reaction.

5.3.2 Time Dependent Study of Cyclohexane Oxidation Using Metal-Picolinate Complexes

We have monitored the progress of cyclohexane oxygenation as a function of time using $[\text{Fe}(\text{pic})_3]$, $[\text{Fe}(\text{pic})_2]$ and $[\text{Cu}(\text{pic})_2]\cdot 2\text{H}_2\text{O}$ in pyridine. Reactions were conducted as described above. At 2 hr intervals a 2 cm³ aliquot of the reaction mixture was removed using a Gilson pipette, quenched with H₂SO₄ and worked up in the usual manner. The total quantity of oxidised product *versus* reaction time is plotted in Figure 5.1. As expected, the iron-picolinate complexes displayed higher oxygenating ability compared to $[\text{Cu}(\text{pic})_2]$, with preferential ketone formation over alcohol. For the iron systems, the bis(picolinate) complex gives marginally higher yields of ketone, although the alcohol content is approximately equal in both cases. An anomalously low set of data for the quantities of oxidised products at 12 hrs is attributed to some error in sampling of the reaction mixtures, which will be commented upon later. Yields of alcohol and ketone for the iron complexes became approximately constant after *ca.* 12 hrs, increasing only slightly over the course of the next 12 hrs, reflecting catalyst deactivation due to decomposition. For $[\text{Cu}(\text{pic})_2]$, ketone formation is observed only after 24 hrs, if any cyclohexanol is formed then it is present in too small a quantity to be detected by GC methods. The zinc in this system exhibited a peculiar effect, that of complete dissolution in 4 hrs and then re-appearance after 15 hrs. In contrast, for the iron systems the zinc was fully dissolved after 10 hrs and remained so during the remainder of the reaction.

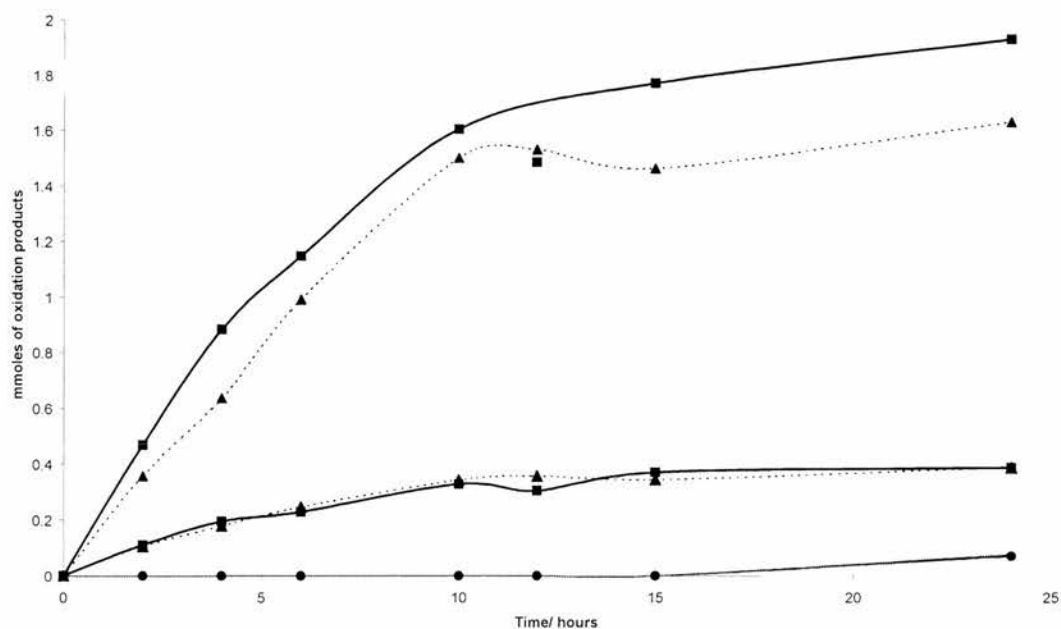


Figure 5.1: Product formation as a function of time for cyclohexane oxygenation in pyridine using metal picolinate complexes. — = $[\text{Fe}(\text{pic})_2]$, = $[\text{Fe}(\text{pic})_3]$. The two uppermost traces represent ketone concentrations, the middle two lines are those for cyclohexanol, the lowermost line represents the ketone formation for $[\text{Cu}(\text{pic})_2]$.

5.4 Summary and Conclusions

A series of iron and copper complexes of ligands containing 2-pyridyl groups were tested under Gif^{IV} conditions in pyridine for the oxygenation of cyclohexane to cyclohexanol and cyclohexanone. The highest activity was achieved using $[\{\text{Fe}(\text{bpp})(\text{H}_2\text{O})\}_2(\mu_2\text{-O})][\text{ClO}_4]_2$, the bpp^- ligand containing both pyridyl and carboxylate functionalities. For the iron complexes the TON lies within a range of 149-293, whereas the copper complexes generally have a TON below ten. The activities for the iron-picolinate complexes (TON 161-184) is independent of oxidation state of iron in the catalyst itself, which suggests that similar catalytic species may be formed in solution in all cases.

5.5 Future Work

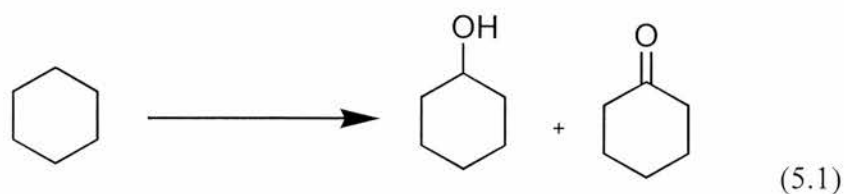
For the complexes examined, the upper limit to TON appears to be *ca.* 300. Since we have not discerned any apparent trends in TON as a function of, say, the donor atoms at iron or nuclearity of the catalyst, the factors affecting catalytic activity remain poorly understood. However, we note that (commercially available) [Fe(acac)₃] exhibits a catalytic activity almost as high as that of any of the iron complexes which required synthesis, but an order of magnitude larger than iron(II) chloride, which is important from an economic perspective. We must still determine if oxygenation activity is restricted solely to pyridine. Although metal picolinate complexes [M(pic)_n] (M = Cu or Fe) do not catalyse oxygenation of cyclohexane in acetonitrile with PVP, the activity in a pyridine-acetonitrile solvent system requires examination.

A factor that we cannot quantify is the incomplete recovery of the oxygenated products from the reaction extracts during work-up. Another intangible is the quantity of pyridine (b.p. 115 °C) and cyclohexane (b.p. 81 °C) which evaporate from the reaction vessel, the flask of course being open to air throughout the catalytic run. Neither cyclohexanol (b.p. 160 °C) nor cyclohexanone (b.p. 155 °C) is expected to evaporate under ambient conditions. The combined effect of these factors is a perpetual under-estimation of TON.

5.6 Experimental Section

5.6.1 Analysis of Cyclohexane Oxidation Products under Gif^{dV} Conditions using Gas Chromatography

Aerobic oxidation of cyclohexane catalysed by iron complexes under Gif^{dV} conditions gives two oxygenated products, equation 5.1.



5.6.2 Solution Sampling

The Gif^{dV} reactions were run in 100 cm³ round bottomed flasks (B24 neck) and stirred with a 2 cm long rugby ball shaped stirring bar at 20 °C. The mixture, consisting of catalyst (7 μmol), cyclohexane (1.07 cm³, 10 mmol) and glacial acetic acid (2.3 cm³, 40 mmol) in pyridine (28 cm³), was stirred at 1000 rpm. The reaction was initiated by the addition of activated zinc dust²¹ (<10 microns mesh, 1.3 g, 20 mmol). For the duration of the reaction (12 hrs) the contents of the flask were left open to the atmosphere *via* the B24 joint and the reaction temperature was assumed to be 20 °C.

After the set reaction time stirring was stopped and a 2 cm³ aliquot of the reaction solution was removed using a Gilson pipette and neutralised with 20 % aqueous sulfuric acid (5 cm³). The organic components were extracted with diethyl ether (3 x 5 cm³), which were combined, washed with saturated aqueous sodium bicarbonate solution (5 cm³) and dried over anhydrous magnesium sulfate. A portion of the dried ethereal extract (1 cm³) was measured out into a tube in preparation for GC analysis. The reactions were carried out only once.

The temperature of the GC oven was increased stepwise according to the following protocol. The temperature was held at 50 °C for two mins, then increased at a rate of 20 °C min⁻¹ until 130 °C was reached. The temperature was held constant for 2 mins and then increased again at a rate of 20 °C min⁻¹ to 240 °C. The temperature was held at 240 °C for 6 mins. Using GC a clear separation of alcohol and ketone peaks (retention times 5.03 and 5.51 min respectively) was observed, enabling quantitative analysis of Gif^{dV} reaction products.

The catalytic reactions of $[\text{Fe}(\text{pic})_n]$ ($n = 2$ or 3), $[\text{M}(\text{pic})_2(\text{H}_2\text{O})_2]$ ($\text{M} = \text{Fe}$ or Cu) and $[\text{FeX}_2(\text{py})_2]$ ($\text{X} = \text{pic}^-$ or quin^-) ($7 \mu\text{mol}$) and PVP (50 fold molar excess over complex, $1.4 \times 10^{-4} \text{ mol}$) in acetonitrile (28 cm^3) were performed over a 12 hr time period and analysed under exactly analogous conditions to the pyridine reactions.

5.6.3 Calibration Curves for Cyclohexanol and Cyclohexanone

Sets of standard solutions of cyclohexanone and cyclohexanol in pyridine were prepared to devise calibration curves to allow quantitative analysis of the reaction products. The solutions were prepared using the ratios of compounds given in Table 5.3.

Table 5.3: Standard solution concentrations for GC analysis

Standard	Cyclohexanone/mM	Cyclohexanol/mM
1	16.3	2.34
2	11.4	1.42
3	2.58	1.00
4	1.29	0.489
5	0.346	0.2

Five standard solutions containing varying ratios of cyclohexanone and cyclohexanol of the range of concentrations expected from the Gif reactions were prepared (Table 5.3). The amount of alcohol and ketone for each standard was dissolved in pyridine (28 cm^3) and extracted according to the procedure described in Section 5.2.1. A 2 cm^3 aliquot of each standard mixture was removed and subjected to the same extraction method as described for the reaction samples. Calibration curves were then constructed for the sample analysis to allow quantification of the products achieved from the oxidation processes as detailed below.

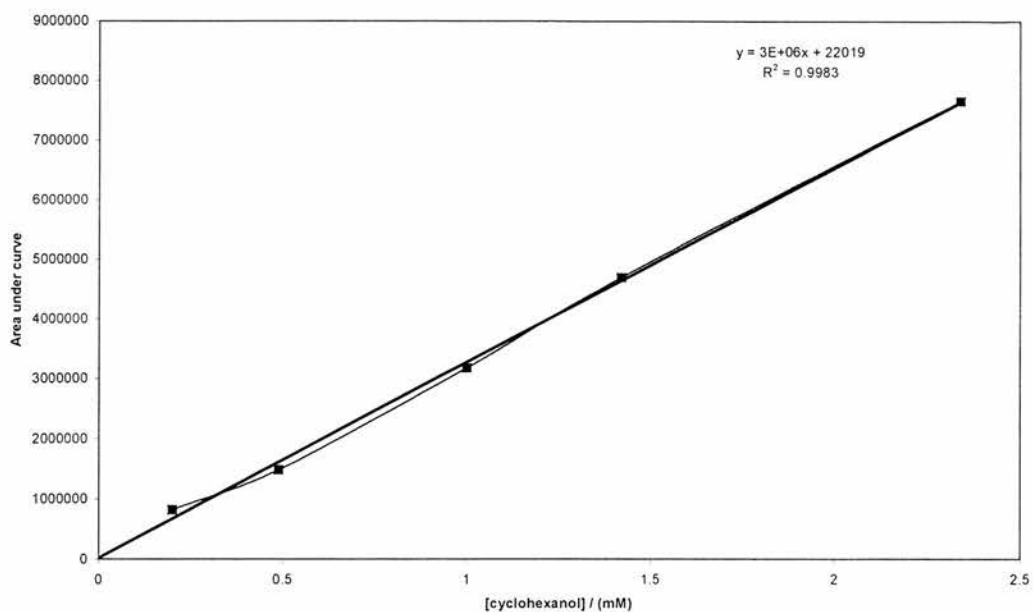


Figure 5.2: Calibration curve for cyclohexanol

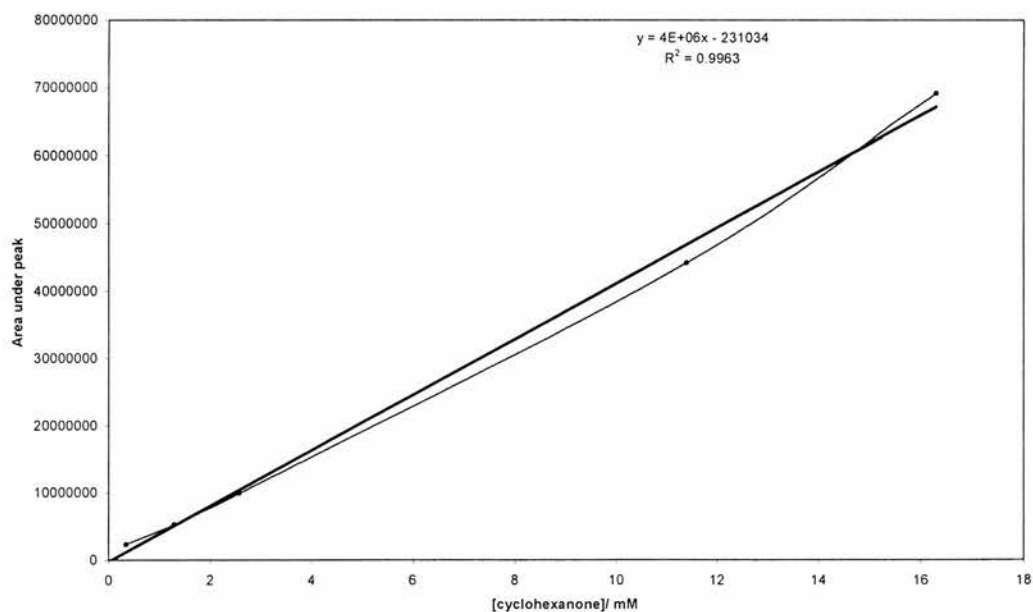


Figure 5.3: Calibration curve for cyclohexanone

To make a meaningful quantitative analysis of the cyclohexanone / cyclohexanol content of the test solutions, it was necessary to evaluate the efficiency of the diethyl ether extraction procedure. Errors may also be introduced by evaporation of the diethyl ether. Thus known mixtures of cyclohexanone and cyclohexanol under Gif^{IV} conditions in 10:1 v/v pyridine – acetic acid solution were prepared

and subjected to the same work-up and extraction procedure as described above. The concentrations of compounds present in these standard mixtures were chosen to reflect those likely to be formed during the Gif^{V} catalytic reactions. The standard solutions were analysed using the same GC conditions described and the obtained values for the two compounds were plotted against the actual values which were present in the 2 cm^3 test solution to form an “extraction efficiency curve”. These curves are shown in Figures 5.2 and 5.3. These calibration curves fitted experimental data satisfactorily with correlation coefficients of 0.998 and 0.996 for the ketone and alcohol respectively. There is an error associated with sample evaporation, but this was assumed to be constant for all samples.

- 1 P. Stavropoulos, R. Celenligil-Cetin and A. E. Tapper, *Acc. Chem. Res.*, 2001, **34**, 745.
- 2 F. Gozzo, *J. Mol. Catal. (A)*, 2001, **171**, 1.
- 3 D. H. R. Barton, *Tetrahedron*, 1998, **54**, 5805.
- 4 D. H. R. Barton and D. Doller, *Acc. Chem. Res.*, 1992, **25**, 504.
- 5 D. H. R. Barton and D. K. Taylor, *Pure Appl. Chem.*, 1996, **68**, 497
- 6 D. H. R. Barton, E. Csuhai, D. Doller, N. Ozbalik and G. Balavoine, *Proc. Natl. Acad. Sci. USA*, 1994, **87**, 3401.
- 7 D. H. R. Barton, N. C. Delanghe and H. Patin, *Tetrahedron*, 1997, **53**, 16017.
- 8 D. H. R. Barton, D. Doller and Y. V. Geletii, *Mendeleev Commun.*, 1991, 115.
- 9 G. B. Shul'pin, A. E. Shilov and G. Suss-Fink, *Tetrahedron Letters*, 2001, **42**, 7253.
- 10 G. Powell, D. T. Richens and L. Khan, *J. Chem. Res. (S)*, 1994, 506.
- 11 S. B. Marr, R. O. Carvel, D. T. Richens, H. J. Lee, M. Lane and P. Stavropoulos, *Inorg. Chem.*, 2000, **39**, 4630.
- 12 S. B. Marr and D. T. Richens, *ACH Models in Chemistry*, 1998, **135**, 821.
- 13 G. B. Shul'pin, *Chemistry Preprint Server, Article CPS: orgchem/0106003*.
- 14 D. H. R. Barton, J. Boivin, W. B. Motherwell, N. Ozbalik and K. M. Schwartzentruber, *Nouv. J. Chim.*, 1986, **10**, 387.
- 15 J. Perutka and A. E. Martell, *Anal. Chim. Acta*, 2001, **435**, 385.
- 16 U. Schuchardt, M. J. D. M. Mannini, D. T. Richens, M. C. Guerreiro and E. V. Spinace, *Tetrahedron*, 2001, **57**, 2685.
- 17 S. B. Marr, PhD thesis, University of St Andrews, 1997.
- 18 R. O. Carvel, MPhil thesis, University of St Andrews, 1993.
- 19 G. Powell, PhD Thesis, University of St Andrews, 1991.
- 20 D. H. R. Barton, M. J. Gastiger and W. B. Motherwell, *J. Chem. Soc., Chem. Commun.*, 1983, 731.
- 21 D. D. Perrin and W. L. F. Armerago, "Purification of Laboratory Chemicals", Third Edition, Pergamon Press, 1988.

Chapter Six

Polyaza Macrocycles And Their Iron(II)/(III) Complexes

6.1 Introduction

We have made a preliminary examination of some polyaza macrocycles and their iron(II,III) complexes. The chemistry of macrocyclic ligands often differs dramatically from acyclic structural analogues due to the enhanced thermodynamic stability of their metal complexes. The coordination chemist can exploit this stability to assemble macrocyclic ligands around a metal ion (templation) to prepare complexes which might otherwise be inaccessible by conventional synthetic routes. The free macrocycle can subsequently be obtained by reduction of, and decomplexation from, the metal complex. The metal ion can preorganise the ligand stereochemistry to favour one geometric isomer over another. An alternative but more involved approach to macrocycle synthesis, often applied to oxa-, thia- and selenacrown ethers, is the stepwise elongation of acyclic precursors in the absence of a metal ion and, in the final step, ring closure to give the macrocycle. Templation, where possible, is thus the preferred option.

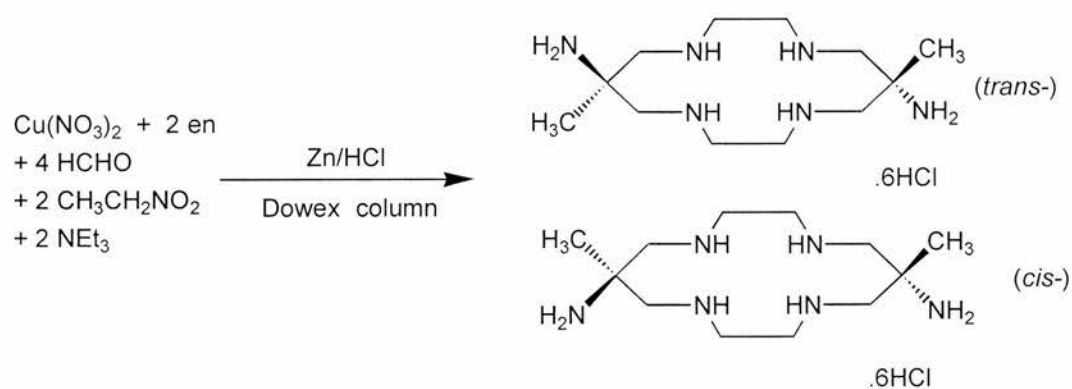
Oxidation of saturated hydrocarbons in a manner similar to the Gif family of systems can be mediated by iron complexes of polyaza macrocycles. Martell has described studies on 24-membered macrocyclic mono- and binuclear complexes of iron(II) and iron(III).¹ Hexaazadiphenol macrocycle diiron(III) complexes catalysed the hydroxylation of adamantane to 1-adamantanol and 2-adamantanol in the presence of hydrogen sulfide as a two electron reductant, small amounts of adamantanone were also generated. Oxidation of cyclohexane to cyclohexanol by *t*-BuOOH was catalysed by a μ_2 -hydroxo diiron(II) complex of a dioxatetraaza eighteen membered macrocycle with pendant 2-pyridylmethyl

groups.² Using acetonitrile as solvent, a turnover number of 160 was found after twenty minutes. The use of macrocycle complexes of iron for hydrocarbon oxidation thus has some precedent but still remains poorly investigated.

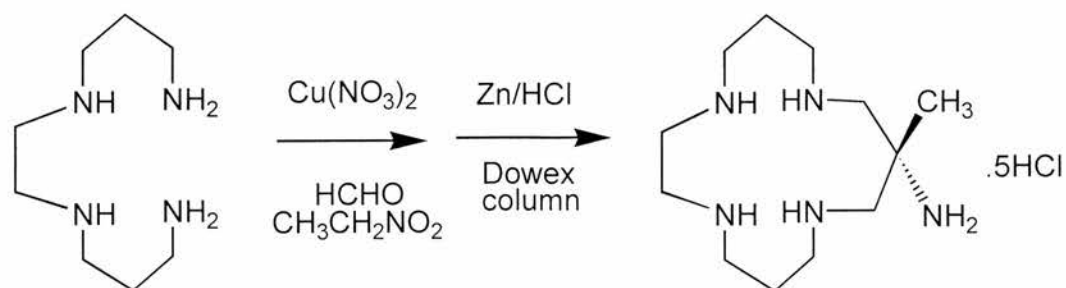
In this Chapter we examine two tetraaza fourteen membered macrocycles with exocyclic amine substituents, 10-methyl-10-amino-1,4,8,12-tetraazacyclopentadecane (monoammac) and *trans*-6,13-dimethyl-6,13-diamino-1,4,8,11-tetraazacyclotetradecane (*trans*-diammac). We describe our attempts to prepare Schiff base derivatives of these macrocycles and their subsequent coordination to iron.

6.2 Monoammac and Diammac

Two tetraazamacrocyclic ligands possessing pendant primary amino groups *trans*-diammac^{3,4} (in free base form) and monoammac⁵ (as the pentahydrobromide salt) were available according to Schemes 6.1, 6.2.



Scheme 6.1: Preparation of *trans*-diammac.



Scheme 6.2: Preparation of monoammac.

Diammac is synthesised in a multicomponent reaction involving copper(II) nitrate hydrate, 1,2-diaminoethane (en), formaldehyde and nitroethane in the presence of triethylamine. The first complex formed, $[\text{Cu}(\text{en})_2]^{2+}$, undergoes Mannich condensation with nitroethane and formaldehyde, *via* an open chain intermediate, to give the macrocyclic complex $[\text{Cu}(\text{dinemac})]^{2+}$, where dinemac = 6,13-dimethyl-6,13-dinitro-1,4,8,11-tetraazacyclotetradecane. Treatment of $[\text{Cu}(\text{dinemac})]^{2+}$ with zinc-hydrochloric acid simultaneously reduces the complex and demetallates the ligand, affording diammac.6HCl, which is isolated by ion exchange chromatography on Dowex resin. Separation of the *cis*- and *trans*-forms is achieved by fractional crystallisation from water of the isomeric hexahydrochlorides, whereupon neutralisation with sodium hydroxide liberates the free base.

Monoammac is available by a qualitatively similar templation route to diammac, commencing from copper(II) nitrate hydrate and 1,4,7,11-tetraazaundecane. Ring closure of the copper(II)-tetraamine complex using formaldehyde and nitroethane, followed by zinc-hydrochloric acid reduction and ion exchange chromatography affords monoammac.5HCl. Neutralisation of the pentahydrochloride salt with sodium hydroxide generates monoammac.

The molecular structure of *trans*-diammac.6HCl.2H₂O, obtained by X-ray crystallography on crystals deposited from hydrochloric acid (Figure 6.1), has been determined. The crystal structure of *trans*-diammac.4HClO₄.6H₂O has previously been reported⁶ but the hexahydrochloride has not. There are no significant differences in the bond lengths between these two molecules. The *trans* configuration of the structure can be seen clearly with pendant amine groups on opposite faces of the macrocycle. The macrocycle nitrogen atoms are each involved in two hydrogen-bonding interactions. In the case of N(1), the hydrogen bond distances to Cl(1) and Cl(3) are the same [2.01(4) Å] but shorter than for N(2) to Cl(1) and Cl(2) [2.10(4), 2.11(4) Å]. N(3) is bound to Cl(2) and Cl(3) and these interactions represent the weakest hydrogen bonding in this structure. One molecule of water is hydrogen bonded to two chloride anions and one of the pendant amine groups. The O-H...Cl distances are 2.27(5)–2.46(5) Å, the H(18)...O(1) distance is 1.73(5) Å. In contrast, in *trans*-

diammac.4HClO₄.6H₂O the shortest hydrogen bond distances are between amine hydrogens and the oxygen atoms of water molecules [H...O 1.61-2.14 Å] rather than to the perchlorate counterions [H...O 2.19-2.68 Å].

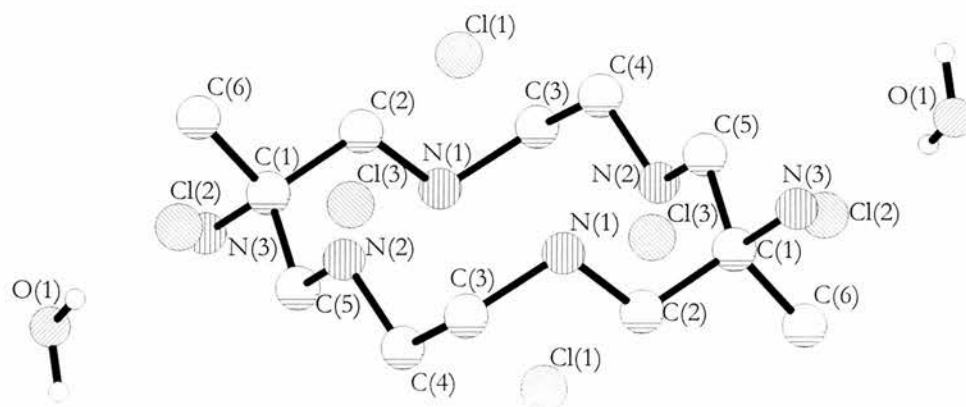


Figure 6.1: Molecular structure of *trans*-diammac.6HCl.2H₂O (hydrogen atoms of macrocycle omitted for clarity).

Table 6.1: Selected bond lengths (Å) and angles (°) for *trans*-diammac.6HCl.2H₂O (esd's in parentheses).

N(1)-C(2)	1.494(4)	N(1)-C(3)	1.519(5)
N(2)-C(4)	1.502(4)	N(2)-C(5)	1.499(4)
N(3)-C(1)	1.508(5)	C(1)-C(2)	1.531(5)
C(1)-C(5)	1.535(5)	C(1)-C(6)	1.530(1)
C(3)-C(4)	1.517(5)		
N(3)-C(1)-C(6)	107.2(3)	C(2)-C(1)-C(6)	106.9(3)
N(1)-C(2)-C(1)	116.6(3)	N(2)-C(4)-C(3)	113.8(3)
C(4)-N(2)-C(5)	113.2(3)	C(2)-N(1)-C(3)	113.5(3)
N(3)-C(1)-C(2)	109.0(3)	N(3)-C(1)-C(5)	105.6(3)
C(2)-C(1)-C(5)	115.1(3)	C(5)-C(1)-C(6)	112.8(3)
N(1)-C(3)-C(4)	115.4(3)	N(2)-C(5)-C(1)	113.0(3)

Table 6.2: Hydrogen bonding distances (Å) and angles (°) for *trans*-diammac.6HCl.2H₂O (esd's in parentheses). The hydrogen bond donor atoms are denoted as *D* and the acceptors as *A*.

	<i>D</i> -H	H... <i>A</i>	<i>D</i> ... <i>A</i>	<i>D</i> -H... <i>A</i>
O(1)-H(19)...Cl(1)	0.84(5)	2.46(5)	3.198(4)	147(5)
O(1)-H(20)...Cl(2)	0.86(5)	2.27(5)	3.110(4)	166(5)
N(1)-H(12)...Cl(1)	1.10(4)	2.01(4)	3.096(3)	169(3)
N(1)-H(13)...Cl(3)	1.00(3)	2.01(4)	3.003(3)	168(3)
N(2)-H(14)...Cl(1)	0.99(4)	2.11(4)	3.081(4)	165(3)
N(2)-H(15)...Cl(2)	0.96(4)	2.10(4)	3.058(4)	171(3)
N(3)-H(16)...Cl(2)	0.98(5)	2.19(5)	3.115(4)	157(4)
N(3)-H(17)...Cl(3)	0.88(3)	2.33(3)	3.158(4)	156(3)
N(3)-H(18)...O(1)	1.05(5)	1.73(5)	2.756(5)	162(4)

6.3 Coordination Chemistry of Monoammac and Diammac

Diammac and monoammac possess six and five amine nitrogen atoms respectively. Both *trans*- and *cis*-diammac form hexacoordinate metal complexes in which all of the exocyclic and macrocycle nitrogen atoms bind to an octahedral metal ion such as cobalt(III), chromium(III), nickel(II) and iron(II,III).⁷⁻⁹ Pentadentate and tetradentate coordination modes have been observed when one or both pendant amine groups have been protonated.^{3,10} One interesting complex is [Fe(*trans*-diammac)]²⁺,⁷ in which the two primary amine donors are mutually *trans*, a rare example of a low-spin iron(II) complex with saturated amine ligands. Octahedral chromium(III) and cobalt(III) complexes of monoammac were synthesised by Lawrance.^{11,12} Pentadentate coordination by monoammac was confirmed by crystallographically, the sixth ligand being chloride. Kinetic studies of the aquation and outer-sphere redox reactions of [M(monoammac)]³⁺, M = chromium or cobalt, have been conducted.^{13,14}

6.3.1 Reaction of *Trans*-Diammac with Iron(II) Chloride

Trans-diammac and iron(II) chloride tetrahydrate were stirred in methanol at 0 °C to give the iron(III) complex $[\text{Fe}(\textit{trans}\text{-diammac})]^{3+}$ in 46 % yield, Figure 6.2. Addition of a three-fold excess of lithium chloride to the filtrate did not give increased yields. While Lawrance initially reported that the reaction of *trans*-diammac with iron(II) sulfate afforded a yellow iron(III) complex,¹⁵ a more recent publication⁷ reports the isolation of $[\text{Fe}(\textit{trans}\text{-diammac})]^{2+}$ as a blue solid under rigorously anaerobic conditions. The IR spectrum of $[\text{Fe}(\textit{trans}\text{-diammac})]^{3+}$ showed ν_{NH} absorptions at 3454 and 3031 cm^{-1} , *c.f.* free *trans*-diammac (3367, 3261 cm^{-1}).

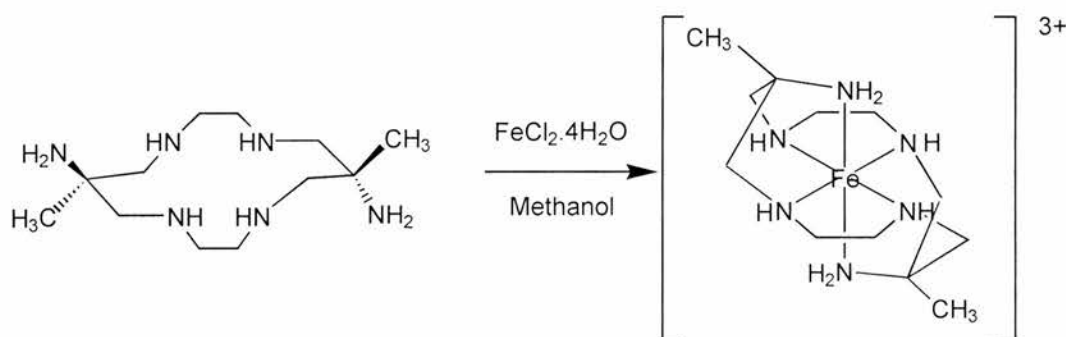


Figure 6.2: Reaction of *trans*-diammac with iron(II) chloride tetrahydrate.

6.3.2 Reaction of Monoammac with Iron(II) Chloride

There are no published iron complexes of monoammac. Monoammac and iron(II) chloride tetrahydrate were stirred in methanol at 0 °C to give a yellow solution. At -20 °C the solution became an intense green colour overnight, from which a green solid was precipitated upon addition of sodium perchlorate. The colour change points to oxidation from iron(II) to iron(III) during the work-up procedure. Strong bands at 1108 and 626 cm^{-1} in the IR spectrum confirmed that the product was a perchlorate salt, a ν_{NH} band appeared at 3414 cm^{-1} . A proposed structure for the complex is shown in Figure 6.3.

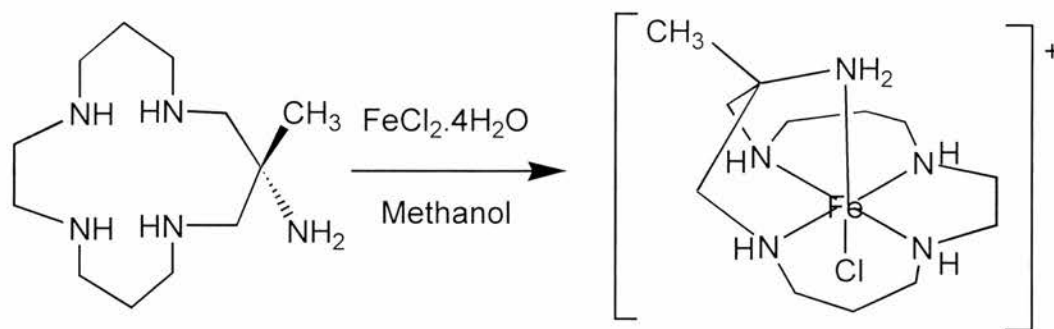


Figure 6.3: Proposed structure of iron(II)-monoammac complex.

6.4 Reaction of *Trans*-Diammac and Monoammac with Pyridine-2-Carboxaldehyde

Trans-diammac and monoammac were both treated with pyridine-2-carboxaldehyde in dehydrative condensation reactions in the expectation of generating the pendant pyridyl imine substituted macrocycles *trans*-6,13-bis(2-pyridylmethyleneimino)-6,13-dimethyl-1,4,8,11-tetraazacyclotetradecane (L^{20}) and 10-methyl-10-(2-pyridylmethyleneimino)-1,4,8,12-tetraazacyclopentadecane (L^{21}). The aim was to increase the denticity of the ligands by adding further nitrogen donor atoms. Comba has recently reported the template synthesis of 6,13-bis(2-pyridinyl)-1,4,8,11-tetraazacyclotetradecane (pypymac), in which the pendant amine groups of diammac are replaced by 2-pyridyl rings.¹⁶ Both *cis*- and *trans*- isomers of pypymac coordinate through all six nitrogen atoms to copper(II), cobalt(III) and nickel(II) ions to give octahedral $[MN_6]^{n+}$ complexes. For the *trans*-pypymac complexes the pyridyl nitrogen atoms occupy the axial positions of the coordination sphere whereas for the *cis*-pypymac complexes these donors bind to one axial and one equatorial coordination site, as established by X-ray crystallography.

6.4.1 Synthesis of L^{20} From *Trans*-Diammac

Trans-diammac was reacted with two equivalents of pyridine-2-carboxaldehyde in anhydrous acetonitrile in order to synthesise a diimine ligand L^{20} containing

two pendant pyridyl groups. L^{20} was anticipated to have the structure shown in Figure 6.4 retaining the original *trans*-stereochemistry of the diammac precursor.

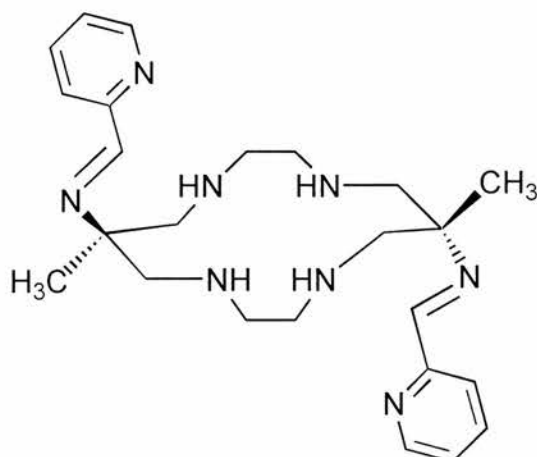


Figure 6.4: Expected structure for L^{20}

Crystals isolated from the reaction filtrate were suitable for X-ray crystallographic determination of the molecular structure, which showed that the molecule exists exclusively in the ring closed tautomeric form, Figure 6.5. ¹H and ¹³C{¹H} NMR spectroscopy subsequently showed that this intramolecular cyclisation is retained in solution, Figure 6.7. This is believed to be due to the retention of the intramolecular hydrogen-bonding present within the structure of the ring-closed tautomer. The structure has a plane of symmetry distinguished by the atoms labelled A.

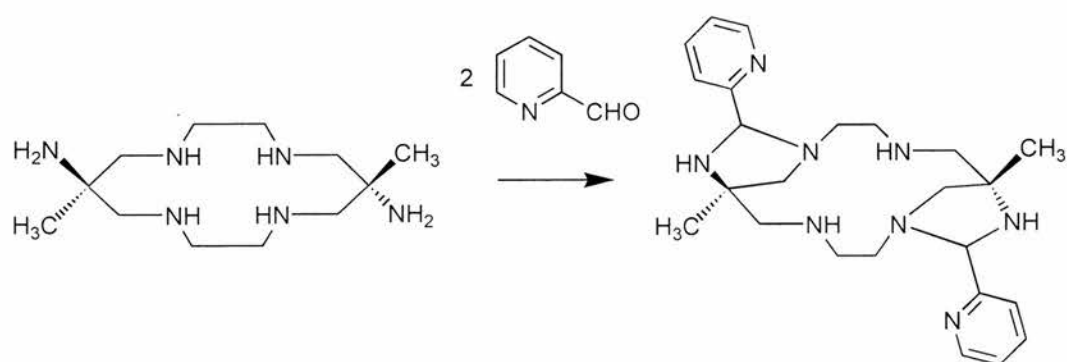


Figure 6.5: L^{20} formation from *trans*-diammac.

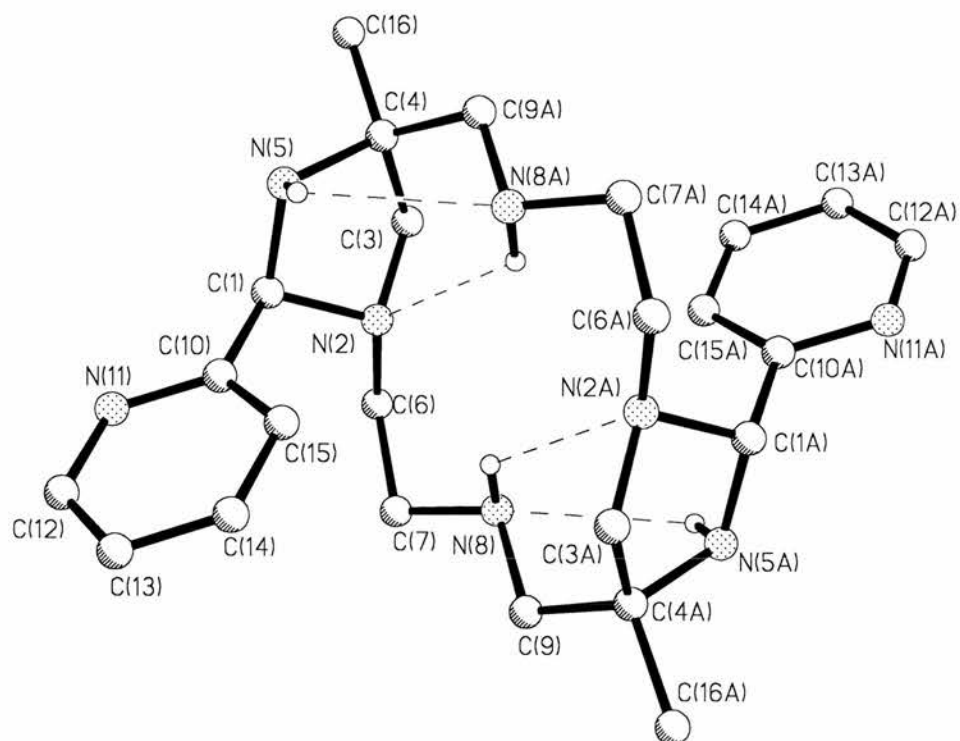


Figure 6.6: Molecular structure of L^{20} (C-H bonds omitted for clarity).

The molecule has a fourteen membered ring with two fused five membered rings at either side. Of the four macrocycle nitrogen atoms, two are shared with the five membered rings. The five membered rings have two nitrogen atoms, [N(5) and the shared N(2)] and a pendant pyridyl ring. The pyridyl ring does not appear to have any intramolecular hydrogen bonding interactions with the rest of the molecule. The N(5)-H(5N)...N(8) and N(8)-H(8N)..N(2)#1 distances are 2.44(5) and 2.36(4) Å respectively.

A comparison of the structures of *trans*-diammac.6HCl and L^{20} reveals only small differences in molecular parameters upon ring closure of the intermediate diimine. Thus the exocyclic C-N length becomes 1.496(7) Å in L^{20} compared to 1.508(5)Å in diammac, unchanged within statistical error. The internal C-N lengths in *trans*-diammac [1.456(6), 1.454(7) Å] lengthen slightly in L^{20} [1.502(4), 1.499(4) Å]. Selected bond lengths and angles for L^{20} are shown in Table 6.3.

Table 6.3: Selected bond lengths (Å) and angles (°) for L²⁰ (esd's in parentheses).

C(1)-N(5)	1.471(7)	C(7)-N(8)	1.456(6)
C(1)-C(10)	1.483(7)	N(8)-C(9)	1.454(7)
C(1)-N(2)	1.489(6)	C(9)-C(4)#1	1.516(8)
N(2)-C(3)	1.441(6)	C(10)-N(11)	1.352(7)
N(2)-C(6)	1.454(7)	C(10)-C(15)	1.354(7)
C(3)-C(4)	1.520(8)	N(11)-C(12)	1.339(7)
C(4)-N(5)	1.496(7)	C(12)-C(13)	1.342(8)
C(4)-C(9)#1	1.516(8)	C(13)-C(14)	1.362(9)
C(4)-C(16)	1.531(7)	C(14)-C(15)	1.375(8)
C(6)-C(7)	1.508(7)		
N(5)-C(1)-C(10)	111.9(5)	C(1)-N(5)-C(4)	107.3(5)
N(5)-C(1)-N(2)	103.6(4)	N(2)-C(6)-C(7)	113.7(5)
C(10)-C(1)-N(2)	114.1(4)	N(8)-C(7)-C(6)	107.9(4)
C(3)-N(2)-C(6)	114.2(5)	C(9)-N(8)-C(7)	115.1(4)
C(3)-N(2)-C(1)	101.0(4)	N(8)-C(9)-C(4)#1	113.3(4)
C(6)-N(2)-C(1)	115.5(4)	N(11)-C(10)-C(15)	122.3(6)
N(2)-C(3)-C(4)	104.6(5)	N(11)-C(10)-C(1)	115.0(5)
N(5)-C(4)-C(9)#1	111.0(5)	C(15)-C(10)-C(1)	122.7(6)
N(5)-C(4)-C(3)	102.4(4)	C(12)-N(11)-C(10)	116.3(5)
C(9)#1-C(4)-C(3)	112.4(5)	C(13)-C(12)-N(11)	124.6(6)
N(5)-C(4)-C(16)	110.1(5)	C(12)-C(13)-C(14)	118.3(6)
C(9)#1-C(4)-C(16)	109.2(5)	C(13)-C(14)-C(15)	119.3(6)
C(3)-C(4)-C(16)	111.7(5)	C(10)-C(15)-C(14)	119.3(6)

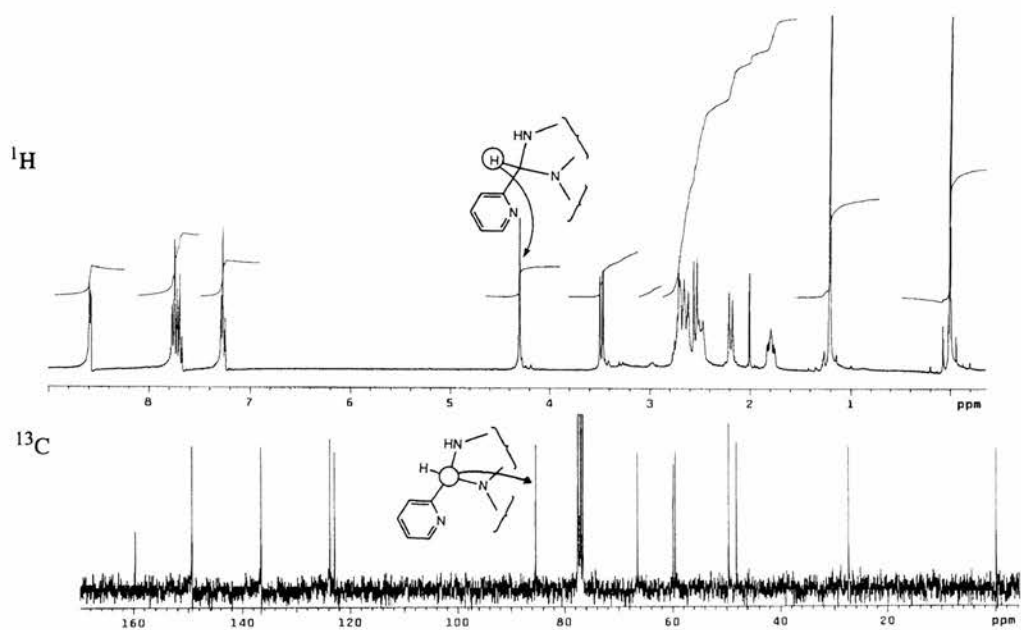


Figure 6.7: ^1H and $^{13}\text{C}\{^1\text{H}\}$ NMR spectra of L^{20} (CDCl_3 solution).

6.4.2 Synthesis of L^{21} from Monoammac

Monoammac was reacted with one equivalent of pyridine-2-carboxaldehyde in acetonitrile at room temperature, giving L^{21} as an oil. We believe that L^{21} exists as a ring closed species similar to L^{20} , Figure 6.8. The ^1H NMR spectrum of L^{21} is more complex than that of L^{20} and cannot be fully assigned with certainty, reflecting the formation of a mixture of isomeric compounds.

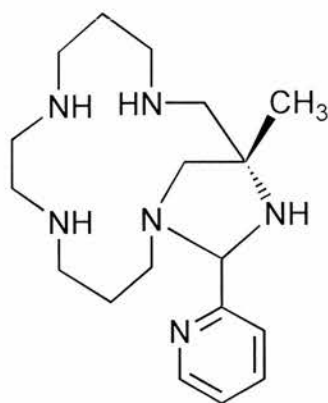


Figure 6.8: Proposed structure for L^{21}

While L²¹ needs to be purified to gain more informative spectroscopic data, it was nonetheless decided to react impure L²¹ with iron(II,III) salts in the hope that the resulting metal complexes would be simpler to purify.

6.4.3 Reaction of L²⁰ with Iron(II) Chloride

We anticipated that on reaction of L²⁰ with iron(II/III) salts a binuclear complex might result, given the number of nitrogen donor atoms (eight) present. Initial reports by McLellan suggested that binuclear iron(III) and copper(II) complexes could be prepared using a Schiff base ligand derived from *trans*-diammac and salicylaldehyde.¹⁷ Treatment of a solution of L²⁰ with iron(II) chloride tetrahydrate in methanol at 0 °C gave a red solution which turned brown overnight at -20 °C. Addition of sodium perchlorate precipitated the complex as a brown solid, whose elemental analysis is in good agreement for [FeL²⁰][ClO₄]₂. It has been suggested¹⁸ that the ring-closed tautomeric form is retained in these molecules upon complexation. The IR spectrum of the complex showed absorptions at 1093 and 625 cm⁻¹ from the perchlorate counterion.

6.4.4 Reaction of L²¹ with Iron(II) Chloride

Iron(II) chloride tetrahydrate was added to a solution of L²¹ in methanol under an argon atmosphere. The initial yellow solution turned green upon storage at -20 °C overnight and a green solid precipitated upon addition of sodium perchlorate. Microanalytical data for the crude product did not fit well with any predicted structure. This reaction should be repeated and both yellow and green products be isolated and characterised.

6.5 Summary

Attempts to prepare imine derivatives of *trans*-diammac and monoammac using pyridine-2-carboxaldehyde were unsuccessful as intramolecular attack of ring

nitrogen atom(s) upon the C=N bond(s) gave five membered ring(s) fused to the macrocycle. Complexation of the parent macrocycles and L^{20,21} with iron(II) gave products sensitive to aerial oxidation, only for L²⁰ was a solid obtained whose elemental analysis was appropriate for an iron(II) complex.

6.6 Further Work

While *trans*-diammac and monoammac react readily with pyridine-2-carboxaldehyde, ¹H NMR spectroscopy and X-ray crystallography have demonstrated that Schiff bases are not isolated, due to intramolecular attack of an NH group on the carbon atom of the imine bond. Despite not possessing the expected exocyclic imine substituents L^{20,21} can still complex to iron, through the amine and pyridyl nitrogen atoms. Although L^{20,21} are not the desired products, certainly L²⁰ is readily purified by crystallisation and investigations into its coordination chemistry are worthwhile. L²¹ requires a reliable and clean synthesis for its chemistry to develop further. Since both ligands have large numbers of donor atoms (eight for L²⁰, six for L²¹) the possibility of forming bimetallic complexes cannot be ruled out.

6.7 Experimental

General experimental conditions and instrumentation details are as in Chapter Two. Reactions were performed using dried and degassed solvents under argon. *Trans*-diammac and monoammac pentahydrobromide were prepared by literature methods.³⁻⁵

***Trans*-diammac:** δ_{H} (CDCl₃): 2.77-2.48 (m, 16H, CH₂), 1.87 (br s, 8H, NH₂ and NH), 1.08 (s, 6H, CH₃). δ_{C} (CDCl₃): 27.53 (CH₃), 48.93, 51.48 (quaternary), 61.01. Selected IR bands (cm⁻¹): 3367s, 3262s (ν_{NH}), 1589m (δ_{NH}), 1471m (δ_{CCH_3}). EI MS: m/z 258 M^+ , 241 [M^+ - NH₃].

Monoammac: Monoammac pentahydrobromide (2.0 g, 3.13 mmol) was dissolved in warm water (*ca.* 6 cm³, 70 °C) and then cooled in ice. The resultant slurry was treated with excess sodium hydroxide (2.5 g, 62.5 mmol) and extracted with dichloromethane (5 x 50 cm³). The combined extracts were dried over anhydrous sodium sulfate for 2 hrs and the solvent was evaporated under reduced pressure to give a colourless solid. Yield 0.54 g (96 %). δ_{H} (CDCl₃): 2.72 (m, 4H, NH), 2.57 (d, 2H, *J* = 11, CH), 2.34 (d, 2H, *J* = 11, CH), 1.84 (br s, 2H, NH₂), 1.67 (quintet, 4H, *J* = 2 Hz, CH₂-CH₂-CH₂), 1.04 (s, 3H, CH₃). δ_{C} (CDCl₃): 5.95 (CH₃), 27.00, 28.90, 49.32, 50.11. Selected IR bands (cm⁻¹): 3267s (ν_{NH}), 1544m (δ_{NH}), 1477m (δ_{CCH_3}), 1417 ($\nu_{\text{C-N}}$). EI MS: *m/z* 244 [*M*⁺ + H].

Reaction of *Trans*-Diammac With Iron(II) Chloride Tetrahydrate: A solution of iron(II) chloride tetrahydrate (0.77 g, 0.38 mmol) in methanol (30 cm³) was added over 1 h to *trans*-diammac (0.1 g, 0.38 mmol) in methanol (40 cm³) at 0 °C. Initially the solution appeared yellow, after the reaction was left overnight at -20 °C the mixture turned red and an orange solid precipitated. Yield 86 mg (46 %). Found (calc for C₁₂H₃₀Cl₃FeN₆): C 31.06 (34.27), H 7.29 (7.19), N 17.20 (19.99) %. Selected IR bands (cm⁻¹): 3454s, 3031s (ν_{NH}), 1617 (δ_{NH}).

Reaction of Monoammac With Iron(II) Chloride Tetrahydrate: A solution of iron(II) chloride tetrahydrate (0.3 g, 0.15 mmol) in methanol (30 cm³) was added over 1 h to monoammac (0.1 g, 0.15 mmol) in methanol (40 cm³) at 0 °C. Initially the solution appeared yellow, after the reaction was left overnight at -20 °C the solution became an intense green colour. Addition of sodium perchlorate (0.05 g, 6.0 mmol) precipitated a green solid. Selected IR bands (cm⁻¹): 3414 (ν_{NH}), 1087s ($\nu_{\text{perchlorate}}$).

Reaction of *Trans*-Diammac with Pyridine-2-Carboxaldehyde – Synthesis of L²⁰: Pyridine-2-carboxaldehyde (0.268 g, 2.15 mmol) in acetonitrile (150 cm³) was added dropwise to a solution of *trans*-diammac (0.324 g, 1.25 mmol) in acetonitrile (150 cm³). The solution was stirred at room temperature overnight,

turning cloudy yellow in appearance. On cooling the solution to 5 °C overnight L^{20} precipitated and was collected by filtration, washed with cold acetonitrile and dried. Yield 0.299 g (55 %). Storage of the filtrate at -20 °C overnight gave clear plates (0.027 g) suitable for X-ray crystallography. δ_H ($CDCl_3$): 8.57 (d, 2H, $J = 5$, C_5H_4N), 7.74 (d, 2H, $J = 8$, C_5H_4N), 7.68 (dt, 2H, $J = 2$ and 7, C_5H_4N), 7.25 (m, 2H, C_5H_4N), 4.28 (s, 2H, NH), 3.45 (d, 2H, $J = 9$, CH), 2.74-2.43 (m, 12H, CH_2), 2.16 (d, 2H, $J = 10$, CH_2), 1.78 (dt, 2H, $J = 4$ and 12 Hz, CH_2), 1.18 (s, 6H, CH_3). δ_C ($CDCl_3$): 27.40 (CH_3), 48.15, 49.58, 59.49, 59.91, 66.55 (CH_2), 85.35 (CH), 122.95, 123.77, 136.62, 149.36 (aromatics). Selected IR bands (cm^{-1}): 3306s (ν_{NH}). EI MS: m/z 436 M^+ , 330 [M^+ - py CH_2N].

Reaction of Monoammac with Pyridine-2-Carboxaldehyde - Synthesis of

L^{21} : Pyridine-2-carboxaldehyde (0.134 g, 1.25 mmol) in acetonitrile (150 cm^3) was added dropwise to monoammac (0.3 g, 1.25 mmol) in acetonitrile (150 cm^3). The solution turned cloudy yellow upon stirring at room temperature overnight. The solvent was removed under reduced pressure rendering an oil. L^{21} was used for complexation without further purification. δ_H ($CDCl_3$): 8.51 (dd, 1H, $J = 1$ and 4, C_5H_4N), 7.67 (dt, 1H, $J = 2$ and 8, C_5H_4N), 7.48 (d, 1H, $J = 8$, C_5H_4N), 7.18 (ddd, 1H, $J = 1$, 5 and 8, C_5H_4N), 4.19 (s, 1H), 3.56 (d, 1H, $J = 9$, CH), 3.20 (br s, 3H), 2.94-2.52 (br m, 6H), 2.40-2.21 (br m, 3H), 2.08 (d, 1H, $J = 9$ Hz), 1.80-1.72 (br m, 2H), 1.16 (s, 3H, CH_3). EI MS: m/z 332 M^+ .

Reaction of L^{20} With Iron(II) Chloride Tetrahydrate: A solution of iron(II) chloride tetrahydrate (0.0468 g, 0.22 mmol) in methanol (30 cm^3) was added over 1 h to a solution of L^{20} (0.1 g, 0.23 mmol) in methanol (40 cm^3) at 0 °C. This gave a red solution, which on storage overnight at -20 °C turned brown. Addition of sodium perchlorate (0.08 g, 6.7 mmol) in methanol (5 cm^3) precipitated a brown solid. Yield 0.108 g (71 %). Found (calc. for $C_{24}H_{36}Cl_2FeN_8O_8$): C 41.32 (41.69), H 4.92 (5.25), N 15.23 (16.21) %. Selected IR bands (cm^{-1}): 1637 (ν_{CN}), 1093 ($\nu_{perchlorate}$).

Reaction of L^{21} with Iron(II) Chloride Tetrahydrate: A solution of iron(II) chloride tetrahydrate (0.078 g, 0.39 mmol) in methanol (30 cm^3) was added over

1 h to L²¹ (0.13 g, 0.39 mmol) in methanol (40 cm³) at 0 °C. This gave a yellow solution, which on storage overnight at –20 °C turned green. Addition of sodium perchlorate (0.14 g, 1.17 mmol) in methanol (5 cm³) precipitated a green solid. Yield 0.123 g. Found: C 27.91, H 4.00, N 10.03 %. Selected IR bands (cm⁻¹): 1617 (ν_{CN}), 1087, 625 ($\nu_{\text{perchlorate}}$)

- 1 D. Kong, A. E. Martell and R. J. Motekaitis, *Ind. Eng. Chem. Res.*, 2000, **39**, 3429.
- 2 J. M. Vincent, S. Bearnais-Barbry, C. Pierre and J. B. Verlhac, *J. Chem. Soc., Dalton Trans.*, 1999, 1913
- 3 P. V. Bernhardt, T. W. Hambley and G. A. Lawrance, *J. Chem. Soc., Dalton Trans.*, 1989, 1059.
- 4 P. Comba, N. F. Curtis, G. A. Lawrance, A. M. Sargeson, B. W. Skelton and A. H. White, *Inorg. Chem.*, 1986, **25**, 4260.
- 5 G. A. Lawrance, M. A. O'Leary, B. W. Skelton, F. H. Woon and A. H. White, *Aust. J. Chem.*, 1988, **41**, 1533.
- 6 P. V. Bernhardt, T. W. Hambley and G. A. Lawrance, *Aust. J. Chem.*, 1990, **43**, 699.
- 7 H. Borzel, P. Comba, H. Pritzkow and A. F. Sickmuller, *Inorg. Chem.*, 1998, **37**, 3853.
- 8 P. Comba, *Inorg. Chem.*, 1994, **33**, 4577.
- 9 P. V. Bernhardt, P. Comba and T. W. Hambley, *Inorg. Chem.*, 1993, **32**, 2804.
- 10 Y. Baran, G. A. Lawrance and E. N. Wilkes, *Polyhedron*, 1997, **16**, 599.
- 11 G. A. Lawrance, T. M. Manning, M. Maeder, M. Martinez, M. A. O'Leary, W. C. Patalinghug, B. W. Skelton and A. H. White, *J. Chem. Soc., Dalton Trans.*, 1992, 1635.
- 12 G. A. Lawrance, M. Martinez, B. W. Skelton and A. H. White, *J. Chem. Soc., Dalton Trans.*, 1992, 823.
- 13 F. Benzo, P. V. Bernhardt, C. Gonzalez, M. Martinez and B. Sienra, *J. Chem. Soc., Dalton Trans.*, 1999, 3973.
- 14 M. Martinez and M. A. Pitarque, *J. Chem. Soc., Dalton Trans.*, 1995, 4107.
- 15 P. V. Bernhardt, P. Comba, T. W. Hambley and G. A. Lawrance, *Inorg. Chem.*, 1991, **30**, 942.
- 16 P. Comba, S. M. Luther, O. Maas, H. Pritzkow and A. Vielfort, *Inorg. Chem.*, 2001, **40**, 2335.

- 17 S. A. McLellan, Senior Honours Project Report, University of St Andrews, 1998.
- 18 P. V. Bernhardt, personal communication.

Appendix One

Crystal Structure Data

X-ray crystallographic analyses were performed by Dr Alexandra M. Z. Slawin, Dr Phil Lightfoot and Miss Heather L. Milton (University of St Andrews). X-Ray diffraction studies were performed using a Bruker SMART-CCD diffractometer with graphite-monochromated Mo-K α radiation or a Rigaku Mercury diffractometer with Cu-K α radiation. All data were corrected for Lorentz polarisation and long term intensity fluctuations. The structures were solved by direct methods, non-hydrogen atoms were refined with anisotropic displacement parameters, hydrogen atoms bound to carbon were idealised and fixed (C-H 0.95 Å). Amine protons were located using ΔF maps and allowed to refine subject to a distance constraint, water bound O-H protons were fixed (O-H 0.98 Å). Structural refinements were by the full-matrix least-squares method on F^2 using the program SHELXTL-PC.¹

The parameters $R1$, $wR2$ and goodness-of-fit on F^2 are defined as follows

$$R1 = \frac{\sum ||F_o| - |F_c||}{\sum |F_o|}$$
$$wR2 = \left[\frac{\sum [w(F_o^2 - F_c^2)^2]}{\sum [w(F_o^2)^2]} \right]^{1/2}$$
$$\text{goodness-of-fit on } F^2 = \left[\frac{\sum [w(F_o^2 - F_c^2)^2]}{(M - N)} \right]^{1/2}$$

where M = number of reflections, N = number of parameters refined.

For *trans*-diammac.6HCl.2H₂O the structure was solved using the teXsan crystal structure analysis package,² for which $wR2$ is defined as

$$wR2 = \left[\frac{\sum w(|F_o| - |F_c|)^2}{\sum wF_o^2} \right]^{1/2}$$

Details of X-ray data collections and structure refinements for [Fe(pic)₃], [pyH][Fe(pic)₂Cl₂] and [Fe₂(μ₂-OMe)₂(pic)₄].H₂O

	[Fe(pic) ₃]	[pyH][Fe(pic) ₂ Cl ₂]	[Fe ₂ (μ ₂ -OMe) ₂ (pic) ₄].H ₂ O
Empirical formula	C ₁₈ H ₁₂ FeN ₃ O ₆	C ₁₇ H ₁₄ Cl ₂ FeN ₃ O ₄	C ₂₆ H ₂₄ Fe ₂ N ₄ O ₁₁
<i>M</i>	422.16	451.06	680.19
<i>T/K</i>	293(2)	125(2)	293(2)
<i>λ/Å</i>	0.71073	0.71073	0.71073
Crystal system	Monoclinic	Monoclinic	Monoclinic
Space group	<i>P2(1)/n</i>	<i>P2(1)/n</i>	<i>P2(1)/n</i>
<i>a/Å</i>	9.7374(4)	7.4088(14)	12.628(4)
<i>b/Å</i>	16.4919(7)	35.191(7)	17.887(6)
<i>c/Å</i>	11.6760(4)	14.181(3)	13.593(5)
<i>α/°</i>	90	90	90
<i>β/°</i>	101.999(1)	95.321(4)	108.566(6)
<i>γ/°</i>	90	90	90
<i>U/Å³, Z</i>	1834.06(13), 4	3681.3(12), 8	2910.6(17), 4
<i>D_c/Mg m⁻³</i>	1.529	1.628	1.552

μ/mm^{-1}	0.863	1.139	1.062
$F(000)$	860	1832	1392
Crystal size/mm	0.13 x 0.1 x 0.1	0.20 x 0.20 x 0.10	0.12 x 0.1 x 0.01
θ range/ $^\circ$	2.17 – 23.33	1.55 – 23.41	1.92 – 23.37
Reflections collected	7860	16082	12191
Independent reflections (R_{int})	2630 (0.054)	5272 (0.0758)	4094 (0.2155)
Data / restraints / parameters	2630 / 0 / 253	5272 / 2 / 496	4094 / 0 / 366
Goodness-of-fit on F^2	0.938	0.845	1.006
$R1, wR2 [I > 2\sigma(I)]$	0.0384, 0.0700	0.0451, 0.0806	0.1430, 0.3165

Details of X-ray data collections and structure refinements for $\text{H}_2\text{L}^9 \cdot \text{H}_2\text{O}$, H_2L^{10} , $\text{H}_2\text{L}^{11} \cdot \text{H}_2\text{O}$, $[\text{pyH}][\text{Fe}(\text{dipic})(\text{Hdipic})(\text{py})_2] \cdot 3\text{py}$ and $[\{\text{Fe}(\text{dipic})(\text{py})_2\}_2(\mu_2\text{-O})] \cdot 2\text{py} \cdot \text{H}_2\text{O}$.

	$\text{H}_2\text{L}^9 \cdot \text{H}_2\text{O}$	H_2L^{10}	$\text{H}_2\text{L}^{11} \cdot \text{H}_2\text{O}$	$[\text{pyH}][\text{Fe}(\text{dipic})(\text{Hdipic})(\text{py})_2] \cdot 3\text{py}$	$[\{\text{Fe}(\text{dipic})(\text{py})_2\}_2(\mu_2\text{-O})] \cdot 2\text{py} \cdot \text{H}_2\text{O}$
Empirical formula	$\text{C}_{17}\text{H}_{15}\text{N}_5\text{O}_3$	$\text{C}_{19}\text{H}_{17}\text{N}_5\text{O}_2$	$\text{C}_{21}\text{H}_{23}\text{N}_5\text{O}_3$	$\text{C}_{44}\text{H}_{38}\text{FeN}_8\text{O}_8$	$\text{C}_{22}\text{H}_{20}\text{FeN}_4\text{O}_{5.5}$
<i>M</i>	337.34	347.38	393.44	862.67	484.27
<i>T/K</i>	293(2)	293(2)	293(2)	125(2)	293(2)
$\lambda/\text{\AA}$	0.71073	0.71073	1.54178	0.71073	0.71073
Crystal system	Orthorhombic	Monoclinic	Triclinic	Monoclinic	Orthorhombic
Space group	$P2(1)2(1)2(1)$	$I2/a$	$P(-1)$	$P2(1)/n$	$Ccca$
<i>a/\AA</i>	3.8239(4)	16.362(1)	9.140(3)	9.5494(11)	14.0035(5)
<i>b/\AA</i>	16.5567(17)	14.3991(9)	9.5051(11)	20.107(2)	25.4518(10)
<i>c/\AA</i>	24.640(3)	14.4267(9)	13.026(5)	21.744(3)	12.2416(5)
$\alpha/^\circ$	90	90	81.99(6)	90	90
$\beta/^\circ$	90	91.266(1)	81.50(7)	98.873(2)	90
$\gamma/^\circ$	90	90	63.11(5)	90	90

$U/\text{\AA}^3, Z$	1560.0(3), 4	3398.1(4), 8	994.9(5), 2	4124.0, 8	4363.1(3), 4
$D_c/\text{Mg m}^{-3}$	1.436	1.358	1.313	1.389	1.474
μ/mm^{-1}	0.103	0.092	0.740	0.430	0.736
$F(000)$	704	1456	416	1792	2000
Crystal size/mm	0.13 x 0.1 x 0.1	0.3 x 0.1 x 0.1	0.15 x 0.1 x 0.1	0.14 x 0.1 x 0.1	0.15 x 0.14 x 0.13
θ range $^\circ$	2.46 - 23.31	1.88 - 23.30	6.11 - 73.31	1.90 - 23.30	1.60 - 23.26
Reflections collected	7817	7218	8241	17970	10044
Independent reflections (R_{int})	2211 (0.1417)	2432 (0.0139)	3520 (0.0732)	5899 (0.0508)	1523 (0.0282)
Data / restraints / parameters	2211 / 2 / 225	2432 / 2 / 244	3520 / 4 / 279	5899 / 1 / 555	1523 / 1 / 149
Goodness-of-fit on F^2	1.008	1.014	0.959	0.939	1.077
$R1, wR2 [I > 2\sigma(I)]$	0.0774, 0.1530	0.0317, 0.0838	0.0556, 0.1349	0.0387, 0.0777	0.0641, 0.1875

Details of X-ray data collections and structure refinements for $[\text{Cu}_3(\text{L}^7)_2(\mu_2\text{-OAc})_2]\cdot\text{CHCl}_3$, H_2L^{18} , $[\text{CuL}^{18}]$, $[\{\text{Cu}(\text{L}^9)(\text{OH}_2)\}_2]\cdot 2\text{H}_2\text{O}$ and $[\text{Cu}_3(\text{L}^6)_2(\mu_2\text{-OAc})_2]\cdot 1.5\text{CH}_3\text{CN}\cdot 0.5\text{H}_2\text{O}$.

	$[\text{Cu}_3(\text{L}^7)_2(\mu_2\text{-OAc})_2]\cdot\text{CHCl}_3$	$[\{\text{Cu}(\text{L}^9)(\text{OH}_2)\}_2]\cdot 2\text{H}_2\text{O}$	$[\text{CuL}^{18}]$	H_2L^{18}	$[\text{Cu}_3(\text{L}^6)_2(\mu_2\text{-OAc})_2]\cdot 1.5\text{CH}_3\text{CN}\cdot 0.5\text{H}_2\text{O}$
Empirical formula	$\text{C}_{39}\text{H}_{29}\text{Cl}_3\text{Cu}_3\text{N}_{10}\text{O}_8$	$\text{C}_{34}\text{H}_{30}\text{Cu}_2\text{N}_{10}\text{O}_8$	$\text{C}_{19}\text{H}_{13}\text{CuN}_4\text{O}_2$	$\text{C}_{19}\text{H}_{16}\text{N}_4\text{O}_2$	$\text{C}_{37}\text{H}_{29.5}\text{Cu}_3\text{N}_{15.5}\text{O}_{8.5}$
<i>M</i>	1062.69	833.76	392.87	332.36	1017.88
<i>T/K</i>	293(2)	125(2)	125(2)	125(2)	125(2)
$\lambda/\text{\AA}$	0.71073	0.71073	0.71073	0.71073	0.71073
Crystal system	Orthorhombic	Monoclinic	Orthorhombic	Monoclinic	Triclinic
Space group	$P2(1)2(1)2(1)$	$C2/c$	$Pbcn$	$C2/c$	$P(-1)$
<i>a/\AA</i>	11.890(4)	18.377(4)	18.777(5)	24.893(5)	10.9969(14)
<i>b/\AA</i>	16.340(5)	8.9474(15)	12.749(3)	9.1295(18)	18.980(3)
<i>c/\AA</i>	22.046(7)	19.422(3)	6.8213(17)	16.445(3)	20.125(3)
$\alpha/^\circ$	90	90	90	90	101.014(2)
$\beta/^\circ$	90	93.094(5)	90	115.623(3)	101.375(2)

γ°	90	90	90	90	90	99.055(2)
$U/\text{\AA}^3, Z$	4283(2), 4	3188.8(10), 4	1633.0(7), 4	3369.8(11), 8	3958.4(9), 4	
$D_c/\text{Mg m}^{-3}$	1.648	1.737	1.598	1.310	1.708	
μ/mm^{-1}	1.727	1.408	1.359	0.088	1.674	
$F(000)$	2140	1704	800	1392	2060	
Crystal size/mm	0.1 x 0.1 x 0.05	0.20 x 0.15 x 0.06	0.30 x 0.10 x 0.10	0.30 x 0.20 x 0.20	0.14 x 0.1 x 0.01	
θ range/ $^\circ$	1.95 - 32.59	2.22 - 23.30	1.93 - 23.38	1.81 - 23.33	1.71 - 23.46	
Reflections collected	28563	7706	6437	6946	20088	
Independent reflections (R_{int})	13168 (0.1250)	2268 (0.0709)	1173 (0.0739)	2386 (0.0227)	11343 (0.1455)	
Data / restraints / parameters	13168 / 0 / 582	2268 / 4 / 261	1173 / 0 / 124	2386 / 2 / 234	11343 / 0 / 1154	
Goodness-of-fit on F^2	1.193	0.901	0.898	1.031	1.036	
$R1, wR2 [I > 2\sigma(I)]$	0.1446, 0.2152	0.0464, 0.1190	0.0428, 0.0994	0.0656, 0.1795	0.0929, 0.1741	

Details of X-ray data collections and structure refinements for $[\text{Cu}_4(\text{L}^7)_2(\text{L}^7\text{-O})_2]$, $\text{C}_2\text{H}_5\text{OH}\cdot 2\text{H}_2\text{O}$, L^{20} and *trans*-diammac. $\cdot 6\text{HCl}\cdot 2\text{H}_2\text{O}$.

	$[\text{Cu}_4(\text{L}^7)_2(\text{L}^7\text{-O})_2]$	L^{20}	<i>trans</i> -diammac
	$\cdot \text{C}_2\text{H}_5\text{OH}\cdot 2\text{H}_2\text{O}$		$\cdot 6\text{HCl}\cdot 2\text{H}_2\text{O}$
Empirical formula	$\text{C}_{70}\text{H}_{54}\text{Cu}_4\text{N}_{20}\text{O}_{13}$	$\text{C}_{24}\text{H}_{36}\text{N}_8$	$\text{C}_{12}\text{H}_{40}\text{N}_6\text{Cl}_2\text{O}_2$
<i>M</i>	1637.49	436.62	513.20
<i>T/K</i>	125(2)	293(2)	293(1)
$\lambda/\text{\AA}$	0.71073	0.71073	0.71069
Crystal system	Triclinic	Monoclinic	Orthorhombic
Space group	<i>P</i> (-1)	<i>P</i> 2(1)/ <i>c</i>	<i>Pbca</i> (#61)
<i>a</i> /\AA	12.741(3)	7.2164(15)	11.578(5)
<i>b</i> /\AA	13.793(3)	14.096(3)	19.538(8)
<i>c</i> /\AA	20.585(4)	12.193(3)	10.468(8)
$\alpha/^\circ$	93.395(4)	90	90
$\beta/^\circ$	92.971(4)	103.752(4)	90
$\gamma/^\circ$	107.026(3)	90	90
<i>U</i> /\AA ³ , <i>Z</i>	3443.8(13), 2	1204.8(4), 2	2367(2), 4

$D_c/\text{Mg m}^{-3}$	1.579	1.204	1.439
μ/mm^{-1}	1.299	0.076	0.745
$F(000)$	1668	472	1088
Crystal size/mm	0.1 x 0.03 x 0.01	0.12 x 0.11 x 0.03	0.35 x 0.30 x 0.05
θ range/ $^\circ$	1.55 - 23.31	2.25 - 23.19	
Reflections collected	17039	6701	2029
Independent reflections (R_{int})	9608 (0.0543)	1696 (0.1260)	1158 (-)
Data / restraints / parameters	9608 / 0 / 962	1696 / 2 / 154	1158 / - / 154
Goodness-of-fit on F^2	1.077	0.949	1.64
$R1, wR2 [I > 2\sigma(I)]$	0.1318, 0.3448	0.0823, 0.1877	0.031, 0.030

References

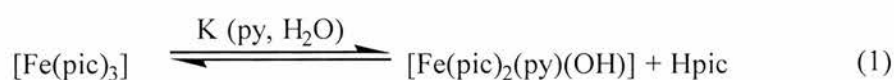
- 1 G. M. Sheldrick, SHELXTL, structure solution and determination package, Bruker AXS, Madison, WI, 1999.
- 2 TexSan, crystal structure analysis package, Molecular Structure Corporation (1985 & 1992).

Appendix 2

Kinetic Analysis of [Fe(pic)₃]/ Hydrogen Peroxide System

The following equilibria are assumed to take place when a solution of [Fe(pic)₃] in pyridine is treated with an excess of aqueous hydrogen peroxide.

In the first step (1) the dissolution of [Fe(pic)₃] in pyridine results in rapid reversible dissociation of a pic ligand from the metal co-ordination sphere and replacement by a molecule of pyridine and an HO⁻ ligand derived from water, this step is diffusion controlled. In equation (2) further reaction of this hydroxyl complex with excess hydrogen peroxide gives rise to a purple high-spin peroxy complex. The rate equation for this second step is given in equation (3), where [Fe]_T is the total concentration of iron in the solution.



$$\text{Rate} = \frac{k_1 K [\text{H}_2\text{O}_2] [\text{Fe}]_T}{K + [\text{Hpic}]} + k_{-1} \quad (3)$$

Total iron concentration is the sum of [Fe(pic)₃] and [Fe(pic)₂(py)(OH)]:

$$[\text{Fe}]_T = [\text{Fe}(\text{pic})_3] + [\text{Fe}(\text{pic})_2(\text{py})(\text{OH})] \quad (4)$$

Rearrangement of equation (1) leads to (5):

$$K = \frac{[\text{Fe}(\text{pic})_2(\text{py})(\text{OH})] [\text{Hpic}]}{[\text{Fe}(\text{pic})_3]} \quad (5)$$

Based on equation (2) the rate of formation of $[\text{Fe}(\text{pic})_2(\text{py})(\text{OH})]$ is:

$$\text{Rate} = k_1[\text{Fe}(\text{pic})_2(\text{py})(\text{OH})][\text{H}_2\text{O}_2] + k_{-1} \quad (6)$$

Substitution of (5) into equation (4) gives:

$$[\text{Fe}]_{\text{T}} = \frac{[\text{Fe}(\text{pic})_2(\text{py})(\text{OH})][\text{Hpic}]}{K} + [\text{Fe}(\text{pic})_2(\text{py})(\text{OH})] \quad (7)$$

Rearrangment of (7) gives:

$$[\text{Fe}]_{\text{T}} = \frac{[\text{Fe}(\text{pic})_2(\text{py})(\text{OH})]([\text{Hpic}] + K)}{K} \quad (8)$$

The concentration of $[\text{Fe}(\text{pic})_2(\text{py})(\text{OH})]$ from (8) is:

$$[\text{Fe}(\text{pic})_2(\text{py})(\text{OH})] = \frac{K[\text{Fe}]_{\text{T}}}{K + [\text{Hpic}]} \quad (9)$$

Substitution of (9) into (6) gives:

$$\text{Rate} = \frac{k_1 K [\text{H}_2\text{O}_2] [\text{Fe}]_{\text{T}}}{K + [\text{Hpic}]} + k_{-1} \quad (10)$$

From the experimental data:

$$\text{Rate} = k_{\text{obs}} [\text{Fe}]_{\text{T}} \quad (11)$$

Comparison of equations (10) and (11) gives rise to k_{obs} :

$$k_{\text{obs}} = \frac{k_1 K [\text{H}_2\text{O}_2]}{K + [\text{Hpic}]} + k_{-1} \quad (12)$$

Therefore a plot of k_{obs} v's $[\text{H}_2\text{O}_2]$ of slope $\frac{k_1 K}{K + [\text{Hpic}]}$ and an intercept of $\frac{k_{-1}}{[\text{Fe}]_{\text{T}}}$

If K is much larger than $[\text{Hpic}]$ the slope simplifies to k_1 .